Physiologically-based pharmacokinetic and mechanism-based pharmacodynamic modelling of monoclonal antibodies with a focus on tumour targeting

---

Saskia Fuhrmann

October 23, 2018

Published online at the
Institutional Repository of the University of Potsdam:
URN urn:nbn:de:kobv:517-opus4-418861
http://nbn-resolving.de/urn:nbn:de:kobv:517-opus4-418861

Dissertation zur Erlangung des akademischen Grades
doctor rerum naturalium (Dr. rer. nat.)

Physiologically-based pharmacokinetic and mechanism-based pharmacodynamic modelling of monoclonal antibodies with a focus on tumour targeting

Saskia Fuhrmann

1. Reviewer	Prof. Dr. Wilhelm Huisinga
2. Reviewer	Prof. Dr. Bernd Meibohm
3. Reviewer	Dr. Ekaterina Gibiansky
Supervisors	Prof. Dr. Wilhelm Huisinga and Prof. Dr. Charlotte Kloft

October 23, 2018

Saskia Fuhrmann

Physiologically-based pharmacokinetic and mechanism-based pharmacodynamic modelling of monoclonal antibodies with a focus on tumour targeting

Dissertation zur Erlangung des akademischen Grades
doctor rerum naturalium (Dr. rer. nat.), October 23, 2018
Reviewers: Prof. Dr. Wilhelm Huisinga, Prof. Dr. Bernd Meibohm and Dr. Ekaterina Gibiansky
Supervisors: Prof. Dr. Wilhelm Huisinga and Prof. Dr. Charlotte Kloft

Universität Potsdam
Mathematische Modellierung und Systembiologie
Institut für Biochemie und Biologie
Mathematisch-Naturwissenschaftliche Fakultät
Karl-Liebknecht-Str. 24/25
14476 Potsdam

Abstract

Monoclonal antibodies (mAbs) are an innovative group of drugs with increasing clinical importance in oncology, combining high specificity with generally low toxicity. There are, however, numerous challenges associated with the development of mAbs as therapeutics. Mechanistic understanding of factors that govern the pharmacokinetics (PK) of mAbs is critical for drug development and the optimisation of effective therapies; in particular, adequate dosing strategies can improve patient quality life and lower drug cost. Physiologically-based PK (PBPK) models offer a physiological and mechanistic framework, which is of advantage in the context of animal to human extrapolation. Unlike for small molecule drugs, however, there is no *consensus* on how to model mAb disposition in a PBPK context. Current PBPK models for mAb PK hugely vary in their representation of physiology and parameterisation. Their complexity poses a challenge for their applications, e.g., translating knowledge from animal species to humans.

In this thesis, we developed and validated a *consensus* PBPK model for mAb disposition taking into account recent insights into mAb distribution (antibody biodistribution coefficients and interstitial immunoglobulin G (IgG) pharmacokinetics) to predict tissue PK across several pre-clinical species and humans based on plasma data only. The model allows to *a priori* predict target-independent (unspecific) mAb disposition processes as well as mAb disposition in concentration ranges, for which the unspecific clearance (CL) dominates target-mediated CL processes. This is often the case for mAb therapies at steady state dosing.

The *consensus* PBPK model was then used and refined to address two important problems: 1) Immunodeficient mice are crucial models to evaluate mAb efficacy in cancer therapy. Protection from elimination by binding to the neonatal Fc receptor is known to be a major pathway influencing the unspecific CL of both, endogenous and therapeutic IgG. The concentration of endogenous IgG, however, is reduced in immunodeficient mouse models, and this effect on unspecific mAb CL is unknown, yet of great importance for the extrapolation to human in the context of mAb cancer therapy. 2) The distribution of mAbs into solid tumours is of great interest. To comprehensively investigate mAb distribution within tumour tissue and its implications for therapeutic efficacy, we extended the *consensus* PBPK model by a detailed tumour distribution model incorporating a cell-level model for mAb-target interaction. We studied the impact of variations in tumour microenvironment on therapeutic efficacy and explored the plausibility of different mechanisms of action in mAb cancer therapy.

The mathematical findings and observed phenomena shed new light on therapeutic utility and dosing regimens in mAb cancer treatment.

Zusammenfassung

Monoklonale Antikörper (mAK) stellen durch ihre hohe Spezifität und geringe Toxizität eine innovative Arzneistoffklasse mit großer klinischer Bedeutung in der Krebstherapie dar. Es gibt jedoch eine Vielzahl an Herausforderungen, die mit der Entwicklung von mAK als Krebstherapeutika verbunden sind. Mechanistisches Verständnis der Pharmakokinetik (PK) von mAK ist wichtig für die Arzneimittelentwicklung sowie für die Therapieoptimierung. Adäquate Dosierungsstrategien können die Lebensqualität der Patienten erhöhen und die Gesundheitskosten senken. Physiologie-basierte PK (PBPK) Modelle bieten einen physiologischen und mechanistischen Rahmen für die Extrapolation von Tiermodellen auf den Menschen. Im Gegensatz zu kleinen chemischen Molekülen besteht für die PBPK Modellierung von mAK kein Konsens: Aktuelle Modelle unterscheiden sich stark hinsichtlich Physiologie und deren Parameterisierung. Die Komplexität dieser Modelle stellt eine große Herausforderung für ihre Anwendung dar.

In der vorliegenden Arbeit entwickelten und validierten wir ein Konsens-PBPK-Modell für die mAK Disposition. Dabei wurden aktuelle Erkenntnisse zur mAK Verteilung berücksichtigt, um basierend auf Plasmadaten Vorhersagen für die PK im Gewebe verschiedener präklinischer sowie klinischer Spezies zu treffen. Das Modell erlaubt *a priori* Vorhersagen für die unspezifische (target-unabhängige) mAK Disposition als auch für die mAK Disposition in einem Konzentrationsbereich, für den die unspezifische Clearance (CL) die target-abhängige CL dominiert. Dies ist oft der Fall für mAK Therapien bei Steady-state-Dosierung.

Anschließend wurde das Konsens-PBPK-Modell genutzt und verfeinert, um zwei wichtige Aspekte näher zu untersuchen: 1) Immundefiziente Mäuse sind wichtige Tiermodelle für die Evaluierung der mAK Wirksamkeit in der Tumortherapie. Die Bindung von Antikörpern an den neonatalen Fc Rezeptor schützt diese vor dem Abbau und beeinflusst somit maßgeblich die unspezifische CL von endogenen sowie therapeutischen Antikörpern. Die Konzentration von endogenem IgG in immundefizienten Mäusen ist reduziert. Dieser Effekt auf die unspezifische mAK CL ist unbekannt, jedoch wichtig für die Extrapolation auf den Menschen in der mAK Tumortherapie. 2) Die Verteilung von mAK innerhalb eines soliden Tumors ist von großer Bedeutung. Für die umfassende Untersuchung der mAK Verteilung innerhalb des Tumorgewebes wurde das Konsens-PBPK-Modell um ein detailliertes Tumor-Verteilungsmodell, welches die mAK-Target Interaktion auf Zellebene berücksichtigt, erweitert. Wir untersuchten den Einfluss von Variationen in der Tumor-Mikroumgebung auf die klinische Wirksamkeit von mAK und untersuchten die Plausibilität verschiedener Wirkmechanismen in der mAK Tumortherapie.

Die mathematischen Ergebnisse sowie beobachteten Phänomene werfen ein neues Licht auf den therapeutischen Nutzen sowie Dosierungsschemata in der mAK Krebstherapie.

Acknowledgement

Firstly, I would like to express my sincere gratitude to my supervisor Prof. Wilhelm Huisinga for the continuous support during my PhD, his immense knowledge and enthusiasm. Wilhelm was always available and his guidance helped me in all the time of research and writing of this thesis.

I would like to thank my co-supervisor, Prof. Dr. Charlotte Kloft for introducing me into the field of pharmacometrics during my pharmacy studies and for valuable discussions and comments on my PhD project.

I am also thankful to my mentor, Dr. Hans Peter Grimm for being the best mentor one could think of. Thank you for the very fruitful discussions during my PhD — not only regularly via telephone conferences but also for allowing me to gain an insight into the work of a pharmacometrician at Roche.

I am grateful to Prof. Dr. Bernd Meibohm and to Dr. Ekaterina Gibiansky for reviewing this PhD thesis.

Furthermore, I want to thank past and present members of the PharMetrX program: In particular, Jane Knöchel for your introductions into the mathematicians' world. Thanks for the stimulating discussions and for sharing with me thoughts—both professionally and personally. Thanks to Sabine Stübler, Lena Klopp-Schulze, Ana-Marija Grišić and Iris Minichmayr for reviewing and supporting me in writing this thesis. Thank you all for all the fun we have had in the last four years.

Special thanks goes to Dr. Dana-Kristin Mah, for sharing with me the ups and downs of a PhD and for being a great friend through an important part of my life.

Last but not the least, I would like to thank my family: Besonderer Dank geht an meine Familie: Mama, Oma und Opa, die immer an mich geglaubt und mich unterstützt haben. Zum Schluss danke ich Oliver— danke für deine Unterstützung, deine unendliche Geduld und deine Liebe.

The work was funded by the Graduate Research Training Program "PharMetrX: Pharmacometrics and Computational Disease Modelling".

Publications

Part of this thesis have been published during the PhD.

A slightly different version of Chapter 4 has been published as S. Fuhrmann, C. Kloft, W. Huisinga, “Impact of altered endogenous IgG on unspecific mAb clearance”, in: *J Pharmacokinet Pharmacodyn*, 44 (2017), pp. 351-374.

Part of Chapter 2 and 5 has been published as W. Huisinga, S. Fuhrmann, L. Fronton, B.-F. Krippendorff, “Target-Driven Pharmacokinetics of Biotherapeutics”, in: *ADME Transl. Pharmacokinet. Ther. Proteins. Appl. Drug Discov. Dev.,* Eds.: H. Zhou and F.-P. Theil, Wiley, 2015, pp. 197-209.

Acronyms

ABC antibody biodistribution coefficient

ADA anti-drug antibody

ADC antibody drug conjugate

ADCC antibody-dependent cell-mediated cytotoxicity

Alb albumin

BH body height

BMI body mass index

BSA body surface area

BSB binding site barrier

BW body weight

CDC complement-dependent cytotoxicity

CI confidence interval

CL clearance

CLpla plasma clearance

CLpla_u unbound plasma clearance

$\mathrm{CLpla}_{\mathrm{BW}}$ plasma clearance per body weight

$\mathrm{CLpla}_{\mathrm{u}}\mathrm{BW}$ unbound plasma clearance per body weight

CMT compartment

CV coefficient of variation

DAR drug-to-antibody ratio

ECM extracellular tissue matrix

EGF epidermal growth factor

EGFR epidermal growth factor receptor

Fab fragment antigen binding fragment

Fc fragment fragment crystallisable

FcRn neonatal Fc receptor

FcγR Fc gamma receptor

FDA Food and Drug Administration

HER2 human epidermal growth factor receptor 2

i.v. intravenous

IFP interstitial fluid pressure

IgG immunoglobulin G

IgGendo endogenous immunoglobulin G

IIV inter-individual variability

ISF interstitial space fluid

IVIG intravenous immunoglobulin

K partition coefficient

KD equilibrium binding affinity

mAb monoclonal antibody

mPBPK minimal PBPK

MW molecular weight

NLME non-linear mixed-effects modelling approach

Obj objective function value

PBPK physiologically-based pharmacokinetics

PDE partial differential equation

PK pharmacokinetics

PNA postnatal age

POP-PK population pharmacokinetics

RME receptor-mediated endocytosis

s.c. subcutaneous

SCID severely compromised immunodeficient mice

SD single dosing

sMD small molecule drug

T-DM1 trastuzumab emtansine

TMDD target-mediated drug disposition

WT wild-type

Contents

1 Motivation and Objectives

Monoclonal antibodies (mAbs) are an innovative group of drugs with increasing clinical importance in oncology, combining high specificity with generally low toxicity [1]. There are, however, numerous challenges associated with the development of mAbs as therapeutics [2]. Mechanistic understanding of factors that govern the pharmacokinetics (PK) of mAbs is critical for drug development and the optimisation of effective therapies; in particular, adequate dosing strategies can improve patient quality life and lower drug cost.

Physiologically-based PK (PBPK) models offer a physiological and mechanistic framework, which is of advantage in the context of animal to human extrapolation. PBPK models for small molecule drugs (sMDs) are used throughout all stages of drug development [3]. However, in comparison to sMDs, for mAbs, the potential of PBPK modelling has so far not yet been fully exploited [3]. Current approaches for mAb PBPK modelling lack a consensus on the representation of physiology and its parameterisation [4]. In addition, the existing models are often over-parameterised (which potentially leads to identifiability issues), require large amounts of *in vivo* tissue distribution data to fit unknown parameters, or only allow to predict plasma PK. *"More effort is needed to use PBPK models to address critical issues in antibody development, such as subcompartment concentrations, tissue target engagement, first-in-human dose, pH-dependent FcRn or target binding, immunogenicity, and disease influence on antibody disposition."* [5, p. 171]

The overall aim of the present thesis was to establish a *consensus* PBPK model for mAb disposition that can be used to answer relevant questions within pre-clinical and clinical development of mAbs and ultimately offers a framework to reflect on therapeutic utility and treatment regimens in mAb cancer treatment.

For sMD PBPK models, the advent of methods to predict tissue-to-plasma partition coefficients significantly increased their application in drug discovery and development. With the development of antibody biodistribution coefficients (ABCs) for mAbs [6]—the analog to tissue-to-plasma partition coefficient of sMDs—, a similar advancement can be expected for mAbs. Fronton et al. [7] have derived a link between tissue partition coefficients and ABCs within a simplified PBPK model for mAb PK in mice. So far, however, ABCs have not been used in PBPK models to predict mAb PK across diverse species and strains.

ABC values and readily available physiological and drug-specific parameters for various species allow to fully specify mAb distribution; the only unknown mAb PK parameter(s) relate to clearance (CL) processes. There are two distinctive routes for the elimination of mAbs: target-mediated CL and unspecific (target-independent) CL. As mAbs bind to specific antigens with high affinity, research has largely focussed on target-mediated CL [8–13]. Conversely, unspecific elimination processes, have attracted much less attention. These CL processes, however, are important for mAb PK at typical therapeutic doses, since linear unspecific CL then dominates target-mediated CL processes.

Protection of mAbs from elimination by binding to the neonatal Fc receptor (FcRn) is known to be major pathway influencing the unspecific CL of both, endogenous and therapeutic immunoglobulin G (IgG) [14]. Experimental data of immunodeficient mouse models are most widely used to study mAb PK and examine the therapeutic response to mAbs in xenograft mice. The concentration of endogenous IgG (IgGendo) in immunodeficient mice, however, is 'by design' reduced, with unknown effect on the FcRn protection mechanism and subsequently on mAb CL, yet of great importance for the interpretation of mAb PK data. Assessment of the impact of altered IgGendo concentrations on unspecific mAb clearance is of both, pre-clinical, but also of clinical relevance, e.g., for immunosuppressed cancer patients treated with mAbs [15–17].

Im mAb cancer therapy, various factors make effective tumour targeting difficult [18]. Antibody-drug conjugates (ADC) are among the most promising classes of antibody-based cancer therapeutics [2]. In current literature [19, 20], the distribution of ADCs is claimed to be a major factor contributing to overall ADC efficacy. In addition, for mAbs competing for receptor binding with natural ligands (e.g. growth factors), the dynamics of receptor and natural ligand play a crucial role in determining mAb efficacy. Better understanding of antibody distribution within tumour tissue can be expected to aid improving the efficacy and safety of cancer therapies and gaining insights for the design of new treatment strategies.

The main objectives of this thesis were to:

- develop and validate a *consensus* PBPK model taking into account recent insights into mAb distribution (ABC values, interstitial IgG pharmacokinetics [21]) to predict common target-independent PK across several pre-clinical species and humans;
- analyse the influence of altered endogenous IgG concentrations—as present in immunodeficient mice—competing with therapeutic IgG for FcRn binding and salvage, on unspecific mAb CL;
- comprehensively investigate mAb and ligand distribution within tumour tissue and its implications on therapeutic efficacy.

Chapter 2 'Background on mAbs' provides both, the biological and modelling background that is relevant for the modelling sections within this thesis. In Chapter 3 '*Consensus* PBPK model for mAbs', we proposed a novel *consensus* PBPK model that integrates the relevant aspects of mAb target-independent PK by leveraging the concept of ABCs. The model was parameterised with parameters related to the interstitial space fluid (ISF) and tissues were modelled based on their capillary structure, which allows more realistic model-based predictions of the PK in the interstitial space. The model can be readily used in non-cross-reactive species to predict tissue PK, requiring only plasma data to fit a single unknown parameter, the unspecific plasma CL. For humans, we determined a median unspecific CL suitable to *a priori* predict mAb PK in healthy volunteers, and importantly to estimate the extent of target-mediated CL processes.

The *consensus* PBPK model was then used and refined to address two important problems:
1) In Chapter 4 'Impact of endogenous IgG on unspecific mAb clearance', we present a refinement of the *consensus* PBPK model that was used to elucidate the impact of altered IgGendo on unspecific mAb clearance in immunodeficient mice.
2) In Chapter 5 'Cell-level-based tumour PBPK model for mAbs', we coupled the *consensus* PBPK model with a detailed tumour distribution model incorporating a cell-level target-mediated drug disposition (TMDD) model to describe the dynamics of receptor and natural ligand. The model allows to study the plausibility of different mechanisms of action in mAb cancer therapy.

2 Background on mAbs

Today, mAbs are one of the largest and fastest growing classes of drugs globally [22, 23]. Due to their high specificity, mAbs play an important role in diagnostics, research and therapy. The overall aim of this thesis is to establish a *consensus* PBPK model for mAb PK that can be used to answer relevant questions within pre-clinical and clinical development of mAbs and offers a framework to study therapeutic utility and treatment regimens in mAb cancer treatment. This chapter provides the background that is relevant for the modelling sections within this thesis and is structured as follows: First, we introduce mAbs and provide an overview on the disposition of mAbs to better understand the physiological processes to be considered within mAb PBPK models. Subsequently, we provide a summary of the mechanisms of action that are relevant for the anti-cancer mAbs to be studied within this thesis and describe briefly the PK characteristics of a promising class of mAb-based cancer therapeutics—ADCs. Lastly, we introduce the modelling approaches for mAb disposition.

Part (section 2.5.3) of the present Chapter has been published as W. Huisinga, S. Fuhrmann, L. Fronton, B.-F. Krippendorff, "Target-Driven Pharmacokinetics of Biotherapeutics", in: *ADME Transl. Pharmacokinet. Ther. Proteins. Appl. Drug Discov. Dev.,* Eds.: H. Zhou and F.-P. Theil, Wiley, 2015, pp. 197-209.

2.1 Physicochemical properties

The physicochemical properties of mAbs largely influence their PK. mAbs are large hydrophilic proteins with a molecular weight (MW) of approx. 150 kDa. Their structure is similar to endogenous immunoglobulins comprising of two important regions:

- the antigen binding region (Fab fragment) determining the affinity and specificity of an antibody towards a target antigen (e.g. epidermal growth factor receptor, EGFR);
- the fragment crystallisable (Fc fragment), which contains the complement binding site and the Fc receptor binding site (important for effector functions of the antibody such as the interactions with macrophages via Fc receptors and binding to FcRn).

Figure 2.2 provides a simplified schematic representation of the structure of an antibody molecule. In mammals, there are five isotypes of Igs: IgA, IgD, IgE, IgG, and IgM. Furthermore, there are a number of subclasses, e.g., IgG consists of four subclasses, i.e., IgG1 to IgG4, which normally represent 67%, 22%, 7% and 4% of the total serum IgG concentration in humans [24]. All currently (2017) clinically used therapeutic mAbs are of IgG isotype [25, Table1] since they have very long elimination half-lives (20-21 days) compared to the other isotypes. Therapeutic mAbs are further classified by their origin into murine, chimeric, humanised and fully human. The origin is important because xenogenic parts can cause immune responses and allergic reactions.

2.2 Disposition

In the sequel, the principal properties of mAb disposition are presented to understand the relevance of processes to be incorporated into mAb PBPK models. The processes that influence mAb absorption are not reviewed in detail here, since the thesis focusses on mAb disposition processes following intravenous (i.v.) administration, which is the most common route of administration [25].

2.2.1 Distribution

General distribution processes

In general, mAb distribution is determined by

- extravasation from blood into the interstitial space of the tissue,
- distribution within the tissue and
- clearance processes.

Due to their large size and hydrophilic nature, mAb passive diffusion is limited and **extravasation from blood to tissues** occurs predominantly via convection or transcytosis across the epithelial barriers [25]. Convection is driven by a hydrostatic gradient between blood and tissue. Furthermore, convection is influenced by the sieving effect of the pores of the vascular epithelial cells. The latter effect is determined by species and drug properties, such as pore size as well as size, shape and charge of the antibody [25]. In tissues, in which extravasation via convection is limited, transcytosis, mediated via FcRn, is another important route of extravasation [25].

mAb **distribution within the tissue** depends on mAb diffusion and convection through the interstitial space of tissues and binding of the antibody to antigens. Tissue distribution can be hindered by the composition of the extracellular tissue

matrix (ECM). The fraction of ECM not available for mAb distribution is termed the exclusion volume.

mAb **clearance processes** include distributive antibody removal from interstitial space of tissues via lymphatic drainage and elimination via catabolism (for more details on IgG elimination see section 2.2.2).

The ratio of extravasation into tissues and removal via lymphatic drainage determines the unbound mAb concentrations in the interstitial fluid of tissues that are often substantially lower than in plasma [25, 26]: The concentration in the interstitial space ranges from 30% to 75% of the plasma concentration [6, 27]. The efficiency of convection from interstitial tissue space into the lymph is higher than the convection from blood into tissues due to larger pore size of tissue lymphatic capillaries compared to tissue blood capillaries [28].

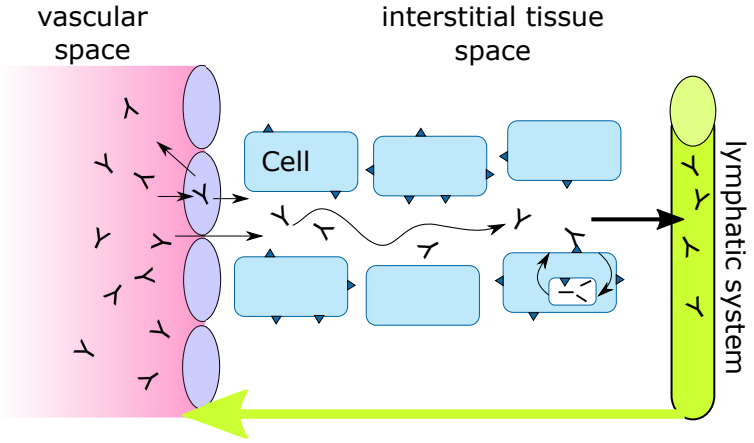

Fig. 2.1.: *Relevant processes determining mAb distribution; modified after [1, 25].*

Tumour distribution characteristics

The inefficient distribution of drugs to malignant cells within solid tumour is often discussed in the context of limiting the success of anti-cancer therapies [18, 29–31]. In this section, we highlight the main differences between healthy tissue and solid tumour tissue with impact on mAb distribution.

There are various clinical presentations of tumours: The term (i) solid tumour describes a localised mass of tissue; in contrast to (ii) tumours of the haematopoietic and lymphoid tissues. Small numbers of malignant cells can spread from the primary tumour to other parts of the body and form (iii) micrometastases. The characteristics of small pre-vascular metastases embedded in healthy tissue are more similar to healthy tissue than solid tumours whose physiology differs from healthy tissues [32].

Solid tumours are described as abnormal organs [1, 29] with the following major differences compared to healthy tissue:

- tumour vasculature:
  - abnormal blood vessels with increased branching and tortuosity [1, 30, 33]
  - blood flow velocities much slower [1]
  - high variability in blood flow leading to distinct regions within tumours, i.e., highly perfused vs. hypoxic regions [1]
  - increased vascular permeability of tumour blood vessels for large molecules [1, 33]
  - non-functional and absent lymph vessels [1]
- tumour interstitial space fluid:
  - large interstitial volume fraction [33–35]
  - high concentrations of supportive proteins and collagen (stiff stroma) [29]
  - high interstitial fluid pressure (IFP) [29, 34]

Elevated permeability of tumour blood vessels for large molecules and reduced lymphatic drainage results in an increase in tumour IFP [34]. The high IFP lowers the necessary gradient for mAb convection driven by hydrostatic pressure gradient. Whereas in healthy tissues, mAb extravasation across the capillary wall is mainly driven via convection and transcytosis, mAb **extravasation into solid tumours** is primarily mediated by passive diffusion, which is limited due to the large molecular weight of mAbs. In addition, mAb **distribution within interstitial space of solid tumours** can be retarded by their high-affinity binding to target antigens expressed on tumour cells (often referred as 'binding site barrier') [1] and by the stiff stroma creating a physical barrier for mAb distribution within tumour tissue [1, 34].

The above mentioned aspects are considered to be limiting factors for mAb distribution within large solid tumours. These limitations, however, have to be discussed in relation to the fact that 'many [antibody] molecules have demonstrated promising outcomes in the clinic' [1, p. 226]. This will be exploited in detail in Chapter 5, where intra-tumoural mAb distribution is comprehensively investigated within a developed mechanistic modelling framework.

2.2.2 Elimination

The elimination of therapeutic mAbs is often described by linear and/or non-linear clearances [36] with

- non-linear clearance typically attributed to receptor-mediated endocytosis (RME) via specific interaction between the IgG's Fab fragment and the target antigen expressed on cell surface receptors [25], and

- linear clearance resulting from antibody-target interaction in the non-saturated regimen or unspecific (not Fab-mediated) elimination following non-specific fluid-phase endocytosis into a cellular endosomal compartment or following RME via interaction between the IgG's Fc fragment and receptors expressed on phagocytic cells of the immune system, e.g., Fc gamma receptors (FcγRs) [25].

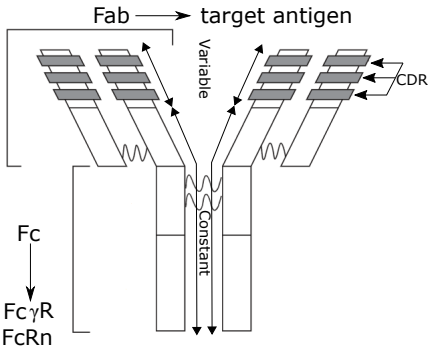

Fig. 2.2.: *Simplified schematic representation of an antibody and its clearance processes*; modified after [36]. Fab: antigen binding region, Fc: fragment crystallisable region, CDR: complement determining regions, FcRn: neonatal Fc receptor, FcγR: Fc gamma receptor.

The process of Fab-mediated RME and subsequent intracellular proteolytic catabolism of the antibody-target complex is also known as target-mediated drug disposition. TMDD is highly influenced, e.g., by the expression level of the target, the mAb dose, the affinity of the mAb for the target as well as the mAb's rate of internalisation [25]. As mAbs typically bind with high affinity to specific antigens, much research focussed on target-mediated clearance (see section 2.5.3). Following mAb concentrations resulting from therapeutic mAb doses, however, the process is often saturated and is not a major contributor to the overall mAb clearance [36]. We argue that unspecific clearance processes are important regarding mAb PK, in particular in two situations: (i) high mAb doses resulting in concentrations that saturate the target, and (ii) mAbs binding to soluble targets, since they are often present in low concentrations. mAbs binding soluble targets often exhibit linear clearance and are primarily eliminated via FcγR-mediated endocytosis [37].

IgG can be rapidly endocytosed and intracellularly degraded following engagement of FcγRs on macrophages and on other innate immune effector cells such as monocytes, dendritic cells, basophils and mast cells [38]. This process is a common pathway for endogenous and therapeutic IgG. Considering the relatively high affinity of IgG for FcγRs and the high endogenous concentrations of IgG in plasma, FcγR-mediated elimination is unlikely to be important for monomeric IgG. It may be dominant in cases where antibody is able to form soluble immune complexes containing three or more IgG molecules [39].

In addition, IgG, like other proteins found in plasma and interstitial fluid, may enter cells unspecifically in all tissues of the body via fluid-phase endocytosis (pinocytosis) [39], but particularly in tissues that are rich in capillary beds with endothelial cells. Intracellularly, a mechanism is present that protects endogenous and therapeutic IgG from unspecific degradation (see section below).

Protection from elimination via the neonatal Fc receptor

When studying mAb PK, protection from elimination by binding to FcRn is known to be a major process influencing unspecific therapeutic IgG elimination as well as the kinetics of endogenous IgG and explains its long elimination half-life [14, 40]. In the following, we present the information that is relevant for the modelling analyses within Chapter 4, where we analyse the influence of altered endogenous IgG concentrations competing with therapeutic IgG for FcRn binding and salvage, on unspecific mAb CL.

Figure 2.3 illustrates the mechanism of IgG protection via the neonatal Fc receptor. Following uptake of IgG into cells via non-specific fluid-phase endocytosis, IgG binds to FcRn in the acidified endosome. The IgG-FcRn complex is transported back to the cell surface where it is released at physiological pH into the systemic circulation. Unbound IgG is degraded within endo-lysosomes in the cell. The site of salvage is assumed to be characterised via sorting endosomes: IgG bound to FcRn is sorted into tubules leading to its return to plasma membrane, whereas unbound IgG is not sorted into tubules [41]. Albumin is protected from degradation by FcRn in a similar way, however, the albumin and IgG binding sites to FcRn are distinct [42]. The FcRn salvage mechanism is present in a wide variety of tissue types. The tissue distribution pattern of FcRn across a variety of species and tissues was qualitatively assessed for the first time by Latvala et al. in 2017 [43]. They detected FcRn in a wide variety of tissue and cell types such as endothelial cells, interstitial cells, epithelial cells as well as professional antigen-presenting cells. FcRn resides within the endosomal vesicles of these cell types. Still today, however, there is no quantitative information of FcRn abundance within human tissues. Furthermore, so far, there is very limited quantitative knowledge about the processes involved in the FcRn protection mechanism, e.g., fluid-phase endocytosis and endosomal sorting [44]. There are variations in the binding affinities of human and mouse FcRn for IgG from different species [40]. As an example, human FcRn is unable to bind to endogenous murine IgG, whereas mouse FcRn binds IgG from many different species with high affinity [40, 45]. The binding affinities towards murine FcRn, however, differ for murine and human IgG [45]. The impact of the antibody binding affinity towards FcRn on unspecific mAb clearance will be studied in more detail in Chapter 4.

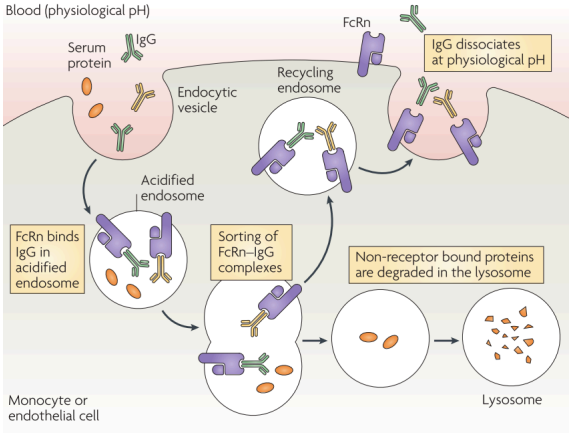

Fig. 2.3.: *Protection of IgG from degradation via the neonatal Fc receptor [40].* See text for details.

2.3 Mechanisms of action in oncology

mAbs are an innovative group of drugs with increasing clinical importance in oncology [1]. Clinically used anti-cancer mAbs often exert their therapeutic effect via multiple mechanisms; they disrupt cell signalling pathways, dampen inhibitory checkpoints, deliver toxic payloads – to name just a few [1, 46]. A detailed review of mechanisms of action of therapeutic antibodies used in oncology can be found in [46]. In this section, we only focus on the mechanisms of action that are relevant for the anti-cancer mAbs to be studied in Chapter 5.

mAbs exhibit high affinity binding to tumour specific targets. mAb **binding with their Fab region to a specific target**, e.g., can induce a specific signal blockade. As an example, trastuzumab binding to the human epidermal growth factor receptor 2 (HER2) prevents receptor dimerisation with other HER family members, and subsequently inhibits the activation of cellular downstream signalling pathways [47, 48]. Moreover, mAb target binding may also prevent receptor binding of a growth factor and thus inhibit downstream signalling pathways [1]. For example, cetuximab and panitumumab compete for binding to EGFR with the epidermal growth factor (EGF) [13].

Several targets have been validated, however, mAbs can also exert their effects via their Fc domain: **mAb binding with their Fc part or a secondary binding site** may induce multiple cytotoxic effects, e.g., recruitment of complement factors (complement dependent cytotoxicity, CDC) or recruitment of immune cells via binding to FcγRs on these cells (antibody-dependent cell-mediated cytotoxicity, ADCC) [1].

In addition, cell-killing mechanisms can result from **mAb delivery of toxic payloads to tumour cells**, e.g., delivery of small molecule cytotoxic drugs (antibody drug conjugates) or radioisotopes (antibody-radionuclide conjugates) [49].

Since clinically used mAbs often exert their therapeutic effect via multiple mechanisms, various efficacy measures may be relevant. The therapeutic efficacy of anti-cancer mAbs and the plausibility of different mechanisms of action in mAb cancer therapy will be examined in Chapter 5.

2.4 Antibody drug conjugates

ADCs are among the most-promising anti-cancer therapeutics that are developed at present with currently (late 2017) four by the Food and Drug Administration (FDA) approved ADCs and over 70 in clinical development [2, 20]. The PK and intra-tumoural distribution of ADCs (with respect to their therapeutic efficacy in cancer therapy) will be examined in Chapter 5.

ADCs are mAbs covalently attached to highly potent cytotoxic sMDs by chemical linkers [49]. The ADC approach combines the specificity of mAbs (binding a specific antigen expressed at the cell surface of tumour cells), with the potency of cytotoxic sMDs to reduce systemic toxicity (compared to standard chemotherapy). ADCs require the release of the toxic payload within the target cell for their activation [33]. Upon target binding and subsequent internalisation into the tumour cell, the ADC is trafficked to and degraded within the lysosome, which leads to liberation of the cytotoxic payload within the cell [50].

The distribution properties of conjugated mAb (ADC) and unconjugated mAb (naked mAb) are often reported to be similar owing to their similarity in size and binding kinetics [2, 19, 51, 52]. The PK of ADCs, however, is largely determined by its components and therefore much more complex compared to unconjugated mAbs [52]. ADCs represent a heterogeneous mixture of various molecules with different drug to antibody ratios (DAR) and a small amount of unconjugated mAb [52]. Location and degree of conjugation, e.g., can affect the internalisation rate and the clearance of an ADC. In addition, deconjugation is an important component of the elimination of ADCs. Deconjugation leads to a decrease in average DAR over time and subsequently impacts the PK of ADCs [52].

Linker stability, sMD potency, DAR as well as the kinetics and efficacy of ADC internalisation are important parameters for ADC development and clinical success [33]. Second-generation ADCs are characterised by an improved linker stability in the bloodstream with brentuximab vedotin and trastuzumab emtansine (T-DM1)

being approved by the FDA in 2011 and 2013 [53]. Despite these improvements, yet, major challenges in achieving consistently high clinical success rates exist [20]. It is claimed in current literature [19, 20] that intra-tumoural ADC distribution appears to be a major factor contributing to the overall ADC efficacy and that a better understanding of the relationship of ADC penetration and therapeutic efficacy is needed to improve the clinical response rates of ADCs [20].

2.5 Models of mAb disposition

Mathematical models play an important role in supporting the discovery and development of new drugs as well as the optimisation of therapies [54–56]. In the present section, we briefly describe classical compartmental modelling approaches and PBPK modelling approaches as they are relevant for the present thesis. We discuss the benefits of PBPK approaches and present the main characteristics of published PBPK models for mAbs. Furthermore, we briefly state different modelling approaches capable of analysing, simulating and inferring target-driven PK of mAbs and in particular, we highlight the advantages of the cell -level TMDD model that is applied within Chapter 5 of this thesis.

2.5.1 Classical vs. PBPK approaches

The plasma PK of mAbs is often described by **classical compartmental modelling approaches** using one or two compartment (CMT) models. Elimination is often modelled as a linear clearance or as parallel linear and non-linear clearance from the central compartment [25, 36]. Non-linear clearance reflects the elimination of the antibody via TMDD and is often described using a simple Michaelis-Menten term [36]. Importantly, both, the structure and the parameters of classical compartmental modelling approaches are based on *in vivo* drug disposition data, limiting a mechanistic and physiological interpretation. Due to their empirical nature, extrapolation beyond the investigated dose range, species and population used for model development is often limited and classical compartmental modelling is typically applied in the context of population PK analysis of clinical mAb data [36].

Whereas classical compartmental models allow to describe mAb plasma PK, **PBPK models** can be used to also predict mAb tissue concentration-time profiles and enable a more mechanistic understanding of mAb disposition processes. PBPK models are multi-compartmental models with compartments explicitly representing well-defined organs or tissues that are interconnected by blood and/or lymph flows. There is a wealth of anatomical and physiological data for various species available (see e.g. [57, 58]). In addition, during the drug discovery and development process, various drug-specific *in vitro* data are generated. PBPK models aim at integrating

such species- and drug-specific data into the modelling process and translate them into the *in vivo* context. This enables *a priori* predictions, i.e., predictions prior to any *in vivo* experiments [59], and also facilitates covariate modelling [60].

The use of PBPK models for sMDs was significantly advanced with the development of *a priori* methods to predict tissue-to-plasma partition coefficients (see [61]). Today, PBPK models for sMDs are widely applied in drug development, e.g., to predict human PK before first-in-human studies [62], to predict drug-drug interactions, and to predict PK in special populations [3]. Unlike for sMDs, there is no *consensus* on how to model mAb disposition in a PBPK context, which limits their application [3, 63]. Published PBPK models for mAbs are quite heterogeneous with respect to their representations of physiology and parameterisation of the mechanisms involved in mAb disposition (see section below).

2.5.2 mAb PBPK models: detailed vs. reduced

In the following, we briefly present the main characteristics and highlight the differences of PBPK models for mAbs.

Concerning their complexity, published PBPK models for mAbs can be categorised into

- full (also termed detailed) models, which integrate known mechanisms for mAb PK in detail, e.g., detailed tissue models to characterise mAb disposition; and
- reduced PBPK models, where the dimensionality of detailed PBPK models is reduced focussing only on the essential physiological processes.

Various detailed whole-body PBPK models for mAb PK in mice and/or men were developed [26, 64–70]. The models differ with respect to, e.g.,

- the definition of tissue distribution spaces,
- the parameterisation of the unspecific elimination involving FcRn and IgGendo,
- their extravasation models.

Within detailed PBPK models, tissues are subdivided into three sub-CMTs accounting for vascular, interstitial and cellular tissue space [64], or two sub-CMTs (vascular and interstitial tissue space) [65, 67] or the tissue model includes an additional endosomal CMT [66]. In addition, as an example, PBPK models developed by Ferl et al. [67] and Garg et al. [66] explicitly incorporate saturable binding to FcRn occurring in the vascular endothelial endosome: The authors assumed that endogenous IgG and therapeutic mAb compete for binding to FcRn in the endosome of muscle and skin [67] or in the endosomal CMT of each tissue [66]. Chen, Balthasar and co-workers [69–71] further subdivided the endosomal space using transit compartments to account for pH-dependent FcRn binding. Note that unbound

FcRn concentration was estimated (or based on unpublished FcRn-mRNA data [69]) and since it continues to be unknown, its physiological value remains questionable. Due to a lack of experimental data of the endosome and since rates of endocytotic uptake at a whole body level are difficult to measure experimentally, the reliability of such detailed models on the endosomal compartment remains questionable. Several detailed PBPK models [64, 66] include mAb extravasation across the capillary wall using a one-pore model that is a simplified version of the two-pore formalism published by Rippe and Haraldsson [72] (where large molecules extravasate through large pores being unable to pass the small pores). On the other hand, extravasation was described by both, convective and diffusive transport according to the two-pore formalism, e.g., by Baxter et al. [65].

The existing detailed PBPK models are often over-parameterised (which leads to identifiability issues) or require large amounts of *in vivo* tissue distribution data to fit unknown parameters; in addition, there is lack of a *consensus* on the representation of physiology and its adequate parameterisation. Jones et al. explicitly stated that over-parameterisation of detailed PBPK models poses a challenge for their application, e.g., for dose projections within the pharmaceutical industry [4].

To overcome this problem, Cao et al. [73, 74] took a reductionist approach and developed a minimal PBPK model that offers system-average rather than tissue-specific PK parameters in fitting of only plasma concentration versus time data. The model includes four compartments, i.e., plasma, lymph compartment and two interstitial spaces accounting for two groups of tissues classified as leaky and tight with non-specific clearance from plasma and/or from interstitial compartments. As part of their efforts, they analysed the relevance of explicitly taking into account the endothelial endosomal space and concluded that it has negligible relevance as a distributional space.

Fronton et al. [7] developed a simplified whole-body PBPK model that does allow to also predict tissue-specific mAb concentrations. This model is parameterised by a small number of parameters to allow stable parameter estimation. The model is characterised by a single ordinary differential equation for each tissue. Exchange between plasma and tissue is described in terms of the organ lymph flow, a tissue partition coefficient and vascular reflection coefficients accounting for the fact that only a fraction of plasma can move into the tissue space. It includes an extravasation rate-limited tissue distribution model. Each tissue is potentially involved in elimination with intrinsic tissue clearance in addition to a plasma clearance. Importantly, in comparison to previous described PBPK models, it only implicitly considers the endosomal space and implicitly accounts for endogenous IgG and FcRn salvage mechanism. The interstitial and endosomal spaces of each tissue are lumped due to the large uncertainty of parameters related to the endosomal space.

Through the development of those second-generation (reduced) PBPK models [7, 73], the applicability to study mAb PK was significantly advanced: While detailed PBPK models require large amounts of *in vivo* data for fitting [4], this is not the case for second generation mAb PBPK models that still enable to consider physiological and mechanistic processes of mAb disposition.

There is a strong motivation to develop more predictive models (versus data fitting) so that the typical mAb PK behaviour can be simulated [19]. A critical advance in the development of PBPK modelling for sMDs was the development of *in silico* methods to *a priori* predict tissue-to-plasma partition coefficients. With the development of ABCs for mAbs [6]—the analog to tissue-to-plasma partition coefficient of sMDs—, a similar advancement can be expected for mAbs (as in Chapter 3). Fronton et al. [7] derived a link between tissue partition coefficients and ABCs within their simplified PBPK model for mAb PK in mice. So far, however, ABCs have not been used in PBPK models to predict mAb PK across diverse species and strains.

2.5.3 Modelling target-driven mAb PK

TMDD models have been designed for drugs that bind with high affinity and to a significant extent (relative to dose) to a pharmacologic target, and as a consequence may exhibit non-linear PK behaviour [8]. Although not specifically designed for antibodies, TMDD models (and various approximations) are now widely used to study the PK of mAbs. In this section we only briefly state different modelling approaches capable of analysing, simulating and inferring target-driven PK of mAbs:

- the classical (whole-body) TMDD modelling approach,
- including its various approximations;
- and the cell-level TMDD modelling approach.

For a comprehensive review see [27]. Furthermore, we highlight the advantages of the cell-level TMDD model [13] that is applied and described in more detail within Chapter 5 of this thesis.

A generic TMDD model has been proposed in [8]; it is based on a classical two-CMT model extended by two target CMTs accounting for free and drug-bound target. Since the two target CMTs represent the concentration of the target in the entire body, we use the term 'whole-body TMDD model'. The generic whole-body TMDD model assumes the target to be present in the central compartment. For a given targeted system, the target might alternatively be assumed to be in the peripheral compartment, or in both. It is worth noticing that the generic whole-body TMDD model does not include any endogenous ligands that potentially competitively bind to the target (see also cell-level TMDD model).

It was noticed that identifiability of classical (whole-body) TMDD model parameters from PK data alone is difficult, in particular when dealing with relatively sparse clinical data, and/or if only either the free or the total drug concentration is available [10], see also [75]. One reason for this identifiability problems is the large time-scale difference between the cellular level (drug-target interaction, often on a minutes or hours time scale) and the PK level (characteristic half-lives of days or weeks).

Motivated by the problem of parameter identifiability for the full TMDD model, approximations of the full TMDD model that are characterised by less variables and parameters (see, e.g., [10, 12, 75]) are widely applied. Typically, those reduced TMDD models are used in a data-driven modelling context.

An alternative approach to resolve the problem of parameter identifiability for the full TMDD model, is to integrate prior information on the targeted system into the modelling process. This results into the so-called cell-level TMDD model that is particularly suited to translate data from *in vitro* to *in vivo*. In contrast to the whole-body TMDD model, the cell-level model is parameterised using rate constants that have been experimentally determined and validated *in vitro*, it allows to study the impact of the internalised receptor, and it allows to include the competition between natural ligand and mAb for binding to the receptor. This will be exploited in detail in Chapter 5.

3 *Consensus* PBPK model for mAbs

Unlike for sMDs, there is no *consensus* on how to model mAb disposition in a PBPK context. Consequently, the potential of PBPK modelling for mAbs has not yet been fully exploited [3]. The existing models are often over-parameterised (which potentially leads to identifiability issues), require large amounts of *in vivo* tissue distribution data to fit unknown parameters, or only allow to predict plasma PK. *"More effort is needed to use PBPK models to address critical issues in antibody development, such as subcompartment concentrations, tissue target engagement, first-in-human dose, pH-dependent FcRn or target binding, immunogenicity, and disease influence on antibody disposition."* [5, p. 171]

A critical advance in the development of PBPK modelling for sMDs was the development of *in silico* methods to *a priori* predict tissue-to-plasma partition coefficients. The absence of comparable methods for mAbs for the prediction of mAb tissue distribution has limited their application in the pharmaceutical industry [4]. Shah and Betts [6] observed a linear relationship between the plasma and various tissue concentrations of non-binding mAbs, which is generally constant irrespective of the absolute mAb concentration and animal species. The relationship was mathematically characterised using the antibody biodistribution coefficient. Those tissue-specific and species-independent ABCs can be used in PBPK models to provide a *consensus* on mAb disposition and thus have the potential to significantly increase the acceptance and therefore the application of mAb PBPK models. So far, however, this promising concept was not used in PBPK models to predict mAb PK across diverse species and strains.

We developed and validated a *consensus* PBPK model taking into account recent insights into mAb distribution (ABC values, interstitial IgG pharmacokinetics [21]) to predict common target-independent tissue PK across several pre-clinical species and humans based on plasma data only. In contrast to overparameterised more detailed mAb PBPK models, the novel *consensus* PBPK model is adapted to the complexity of the experimental data and based on a refinement of an existing second-generation mAb PBPK model—the *simplified* PBPK model [7].

This chapter is organised as follows: In the first section, we highlight the differences between the two models—the *simplified* and the *consensus* PBPK model. In sec-

tion 3.2, we describe the equations and the parameterisation of the novel *consensus* PBPK model in detail. The results are presented in section 3.3: In sections 3.3.1+ 3.3.2, we show that the developed model can be readily used in non-cross-reactive species and humans (with mAbs being dosed to saturate the targeted system) to predict tissue PK, requiring only plasma data to fit a single unknown parameter, the unspecific plasma CL. Lastly (in section 3.3.3), for humans, we determined a median unspecific CL suitable to *a-priori* predict mAb PK in healthy volunteers, and importantly to estimate the extent of target-mediated CL processes.

3.1 From the *simplified* to the *consensus* PBPK model

Fronton et al. [7] developed a *simplified* PBPK model that is (in contrast to various detailed mAb PBPK models) adapted to the complexity of the experimental data and still enables to consider physiological and mechanistic processes of mAb disposition. In comparison to the minimal PBPK model [73], it allows to also predict tissue-specific mAb concentrations. The application of the *simplified* PBPK model, however, is limited: mAb tissue PK data are necessary to estimate tissue partition coefficients K_{tis}, and the PBPK model is illustrated for mice only. Fronton et al. [7] have derived a link between tissue partition coefficients and ABCs for mAb PK in mice. So far, however, ABCs have not been used in PBPK models to predict mAb PK across diverse species and strains.

The novel *consensus* PBPK model is obtained using the *simplified* PBPK model [7] by validating the concept of ABCs for prediction of mAb tissue PK for rats as well as for humans. In contrast to [7], we parameterised the *consensus* PBPK model with parameters related to the interstitial space, e.g., interstitial volumes V_{int}, tissue partition coefficients related to the interstitial space K_{int}, and interstitial concentrations C_{int}, since they are pharmacologically more relevant than tissue concentrations C_{tis}. Furthermore, the model parameters used in the *simplified* PBPK model for prediction of mAb plasma and tissue PK in mice, were updated. In the *consensus* PBPK model, we compute tissue volumes, including interstitial and cellular space, from fractional organ weights reported in Brown et al. [57]. Cardiac output and regional blood flows are also taken from Brown et al. [57], where measurements in anaesthesised animals were excluded. In the *simplified* PBPK model [7], the lymph flows used were derived from the cardiac output stated in Baxter et al. [65]. Comparison to physiological values reviewed in Brown et al. [57] revealed that Baxter et al. used a value typical for anaesthesised mice. In the *consensus* PBPK model, we used a cardiac output typical for non-anaesthesised mice [57], which is roughly twice as large as the value used in [7, 65]. This also increased the peripheral lymph flow rates by the same factor. As a consequence, we updated the vascular reflection coefficients of the *simplified* PBPK model (for details, see section 3.2). Furthermore, the *consensus* PBPK

model is parameterised using measured residual plasma fractions $\mathrm{res}_{\mathrm{pla}}$ and interstitial volume fractions f_{int} from a single recent source, where the same experimental setting was used to determine both parameter values [21]. Previous modelling approaches were mostly referring to f_{int} and $\mathrm{res}_{\mathrm{blo}}$ [76], which is a compilation of experimental measurements of different original sources. In addition, the *consensus* PBPK model includes the recent findings based on the measurements from Eigenmann et al. [21] that interstitial antibody concentrations are highly tissue-specific and depend on their underlying vasculature. Consequently, in the *consensus* PBPK model, tissues were modelled based on different capillary structure (i.e., continuous, discontinuous or tight), which allows more realistic model-based predictions of the PK in the interstitial space. Based on the new parameterisation using information from Eigenmann et al. [21], ABCs and tissue concentrations were corrected for residual plasma/blood (for details, see section 3.2.2).

The developed *consensus* PBPK model is readily parameterised by physiological species-specific and mAb-related parameters. The latter include reflection coefficients and ABC values. Importantly, in comparison to the *simplified* PBPK model, only an unspecific clearance (in addition to mAb-specific target-related processes) needs to be estimated, which requires only plasma data. The unspecific part of mAb PK is of key relevance when target-mediated processes are saturated (which is often the case for mAbs at steady state dosing).

3.2 Development of the *consensus* PBPK model

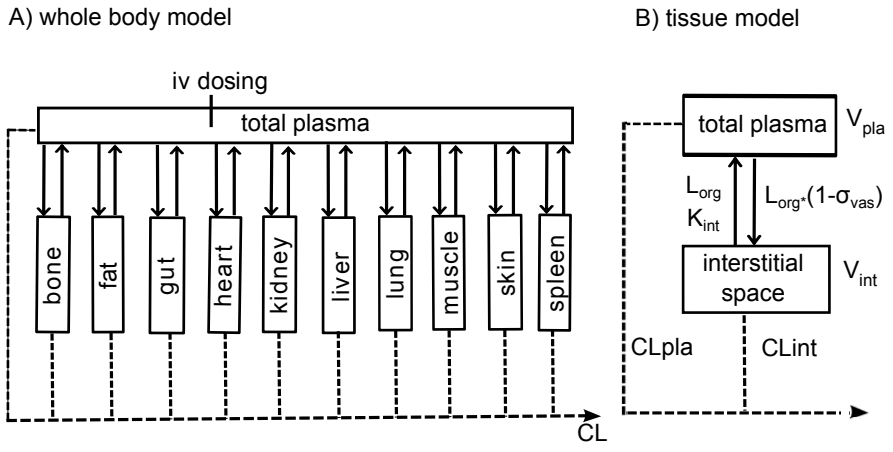

Fig. 3.1.: *Structure of the consensus PBPK model for mAb PK.* Total plasma comprises total arterial and venous plasma, including the vascular space associated with the organs. Organs are interconnected via extravasation of mAbs from plasma and the lymph flow (solid arrows). Organ compartments represent the *interstitial* space of the corresponding organs. The mAb can potentially be cleared from the plasma as well as any organ compartment (dashed arrows).

The model comprises anatomical compartments of total plasma and the interstitial spaces of lung, fat, bone, gut, heart, kidney, liver, muscle, skin and spleen. The tissue topology and model structure is shown in Figure 3.1. As in the *simplified* PBPK model [7], the plasma compartment denotes the arterial and venous as well as the vascular space associated with each organ. In contrast to [7], the *consensus* PBPK model is parameterised in terms of interstitial volumes V_{int} (in [mL] or [L]) and interstitial concentrations C_{int} (for comparison of C_{int} to experimental tissue data C_{exp}, see section 3.2.2).

3.2.1 Equations of the *consensus* PBPK model

The rates of change of the concentrations in plasma C_{pla} and in the interstitial space C_{int} (both in [nM]) of the different organs were described by the following system of differential equations:

$$\begin{aligned} V_{\mathrm{int}}\frac{\mathrm{d}}{\mathrm{dt}}C_{\mathrm{int}} &= L_{\mathrm{org}}\cdot\left((1-\sigma_{\mathrm{vas}})C_{\mathrm{pla}}-\frac{C_{\mathrm{int}}}{K_{\mathrm{int}}}\right) \\ &\quad -\mathrm{CLint}\cdot C_{\mathrm{int}}+\mathrm{TMDD}_{\mathrm{int}} \end{aligned} \tag{3.1}$$

$$\begin{aligned} V_{\mathrm{pla}}\frac{\mathrm{d}}{\mathrm{dt}}C_{\mathrm{pla}} &= \sum_{\mathrm{org}} L_{\mathrm{org}}\cdot\left(\frac{C_{\mathrm{int}}}{K_{\mathrm{int}}}-(1-\sigma_{\mathrm{vas}})\cdot C_{\mathrm{pla}}\right) \\ &\quad -\mathrm{CLpla}\cdot C_{\mathrm{pla}}+k_{\mathrm{in}}(t)+\mathrm{TMDD}_{\mathrm{pla}} \end{aligned} \tag{3.2}$$

with infusion rate $k_{\mathrm{in}}(t)$ [nmol/min]. The first equation applies to each organ.

As in the *simplified* PBPK model [7], for each organ, an extravasation rate-limited distribution model was assumed. This includes interstitial uptake by convection through large pores or discontinuous epithelia and transcytosis, and backflow into the plasma via the lymph flow or via transcytosis, see Figure 1 (B). The extravasation rate-limited distribution model is parameterised in terms of an organ lymph flow L_{org} (in [mL/min] or [L/min]) and an organ-specific vascular reflection coefficient σ_{vas}, which accounts for the fact that only a fraction (1- σ_{vas}) of the plasma concentration is accessible for extravasation (one-pore model). The apparent vascular reflection coefficient σ_{vas} is a mixed parameter, depending on drug properties, i.e., antibody size, as well as species properties such as pore size and number of pores in the vascular wall of the organ. The apparent vascular reflection coefficient is classified based on the tissue properties, such as leakiness and tightness of the vascular wall (for details see section 3.2.3). The outflowing concentration is parameterised by an organ-specific interstitial partition coefficient K_{int}, which was derived from the antibody biodistribution coefficient ABC (for details see next section). Unspecific plasma clearance CLpla and intrinsic tissue clearance CLint subsume several processes, such as Fcγ receptor-mediated clearance and unspecific endocytosis (see also [7]). In the absence of specific knowledge, the different elimination processes may be described by a single unspecific plasma clearance term.

As monoclonal antibodies typically bind with high affinity to specific antigens, much research focussed on target-mediated clearance [8–13]. In the present chapter, we focus on the target-independent part of mAb PK that is of key relevance when target-mediated processes are saturated (which is often the case for mAbs). If relevant, however, TMDD can be integrated into the *consensus* PBPK model: In this case, we considered the TMDD term to be in the plasma compartment only:

$$\mathrm{TMDD}_{\mathrm{pla}} \quad = \quad -\frac{V_{\max} \cdot C_{\mathrm{pla}}}{\mathrm{Km} + C_{\mathrm{pla}}} \tag{3.3}$$

with receptor system capacity $V_{\max}$ in [nmol/min] and Michaelis-Menten constant Km in [nM].

3.2.2 Correction for residual blood and antibody biodistribution coefficients

The amount of mAb in residual blood of tissue samples can have a marked impact on reported tissue concentrations [7]. In Shah and Betts [6], a variety of different studies were used to estimate ABC values so that these are expected to be contaminated by residual blood [6, p.203]. In the following, we denote by $\mathrm{ABC}_{\mathrm{exp}}$ the residual blood-contaminated tissue-to-plasma partition coefficients, by $\mathrm{ABC}_{\mathrm{tis}}$ the unperturbed tissue-to-plasma partition coefficients, and by $\mathrm{ABC}_{\mathrm{int}}$ the unperturbed interstitial-to-plasma partition coefficients.

Similarly to the *simplified* PBPK model, the *consensus* PBPK model is parameterised in such a way that predictions are independent of residual blood, instead correction for residual blood was a post-simulation step. Based on the derivations by Fronton et al., we corrected the ABC values and predicted residual-blood contaminated tissue concentrations C_{exp} in the *consensus* PBPK model. Based on the new parameterisation using measured residual plasma fractions $\mathrm{res}_{\mathrm{pla}}$ and interstitial volume fractions f_{int} from Eigenmann et al. [21], f_{int} was utilised to derive $\mathrm{ABC}_{\mathrm{int}}$ from $\mathrm{ABC}_{\mathrm{tis}}$, and K_{int} from $\mathrm{ABC}_{\mathrm{int}}$. In addition, we used the values for $\mathrm{res}_{\mathrm{pla}}$ to update $\mathrm{ABC}_{\mathrm{tis}}$ and C_{exp}.

We defined $\mathrm{ABC}_{\mathrm{exp}}$ by:

$$\mathrm{ABC}_{\mathrm{exp}} = \frac{C_{\mathrm{exp}}}{C_{\mathrm{pla}}},$$

as determined by Shah and Betts [6]. We corrected $\mathrm{ABC}_{\mathrm{exp}}$ for residual blood to determine $\mathrm{ABC}_{\mathrm{tis}}$ (for detailed derivation see [7, Eq. (23)]):

$$\mathrm{ABC}_{\mathrm{tis}} = \frac{C_{\mathrm{tis}}}{C_{\mathrm{pla}}} = \frac{\mathrm{ABC}_{\mathrm{exp}} - (1 - \mathrm{hct}) \cdot \mathrm{res}_{\mathrm{blo}}}{1 - \mathrm{res}_{\mathrm{blo}}}, \tag{3.4}$$

where hct refers to haematocrit. $\mathrm{res_{blo}}$ denotes the ratio of residual blood volume $V_{\mathrm{res,blo}}$ to tissue volume V_{exp} including residual blood, i.e.,

$$\mathrm{res_{blo}} = \frac{V_{\mathrm{res,blo}}}{V_{\mathrm{exp}}} \tag{3.5}$$

with $V_{\mathrm{exp}} = V_{\mathrm{tis}} + V_{\mathrm{res,blo}}$. Finally, to leverage experimental data in mice, we linked $\mathrm{res_{blo}}$ to the ratio of residual plasma volume $V_{\mathrm{res,pla}}$ to V_{exp} using hct:

$$\mathrm{res_{pla}} = (1 - \mathrm{hct}) \cdot \mathrm{res_{blo}}. \tag{3.6}$$

In [6], tissue-specific $\mathrm{ABC_{exp}}$ values were estimated from mice data and shown to be species-independent. In line with these findings, we determined $\mathrm{ABC_{tis}}$ values based on $\mathrm{res_{pla}}$ measured in mice [21] and Eq. (3.4). Corrected $\mathrm{ABC_{tis}}$, derived based on mice data and physiology, are again assumed to be constant across species, analogous to [6]. See Tables 3.2, 3.3, 3.4 and 3.5 for all parameter values.

Correction for residual blood is a post-simulation step. The residual blood-contaminated tissue concentration C_{exp} is given by

$$C_{\mathrm{exp}} = \frac{V_{\mathrm{tis}} \cdot C_{\mathrm{tis}} + V_{\mathrm{res,pla}} \cdot C_{\mathrm{pla}}}{V_{\mathrm{exp}}}. \tag{3.7}$$

For detailed derivation see [7, Eq. (21)]. Based on the simulations of C_{pla} and C_{tis} (calculated based on predicted C_{int} and interstitial volume fractions f_{int} see section below) by the *consensus* PBPK model, we can therefore directly predict C_{exp} from the above equation. For rats and humans, we assumed $\mathrm{res_{pla}}$ to be identical to the measured values in mice due to lack of more refined data.

Determining K_{int} and $\mathrm{ABC_{int}}$ from $\mathrm{ABC_{tis}}$

Interstitial volume fractions $f_{\mathrm{int}} = V_{\mathrm{int}}/V_{\mathrm{tis}}$ as experimentally determined in mice (from measured residual plasma fractions and extracellular tissue volume fractions [21]) were used to derive $\mathrm{ABC_{int}}$ from $\mathrm{ABC_{tis}}$ via the following relationship:

$$\mathrm{ABC_{int}} = \frac{C_{\mathrm{int}}}{C_{\mathrm{pla}}} = \frac{V_{\mathrm{tis}}}{V_{\mathrm{int}}} \cdot \mathrm{ABC_{tis}}. \tag{3.8}$$

For tissues with discontinuous capillaries, ISF might be assumed to be in fast equilibrium with plasma (for details, see [21]). Consequently, experimentally determined residual plasma fractions $\mathrm{res_{pla}}$ need to be interpreted with care, since they might include ISF contributions due to plasma tracer leaking into interstitial space [21]. We therefore set $\mathrm{ABC_{int}} = 1$ for liver and spleen (both having discontinuous cap-

illaries), assuming that plasma and ISF mAb concentrations are comparable. This then allowed us to estimate the interstitial volume fractions f_{int} for liver and spleen, given $\mathrm{ABC}_{\mathrm{tis}}$, and $\mathrm{ABC}_{\mathrm{int}} = 1$. f_{int} for liver and spleen were estimated based on mouse, rat and human data (where tissue data of liver and spleen were available, i.e., for rodents: [77], [78], [79], [80], [65] as well as for human female cancer patients: [81]). For estimation of f_{int} only liver and spleen tissue data were used.

For tissues with tight capillaries, e.g., brain and kidney, extracellular tissue volume fractions cannot be determined as tracers might not pass (brain) or are excreted (kidney) [21]. For kidney, in a first attempt, only a negligible amount of mAb was assumed to distribute into the interstitial space. However, following this assumption, resulting predicted C_{exp} for kidney could not describe the experimental kidney data. Thus, we assumed that some mAb can distribute into interstitial kidney space. Unlike for liver and spleen, we do not have any information on $\mathrm{ABC}_{\mathrm{int}}$ for the kidney. Therefore, f_{int} for kidney was taken from [76, Table B-I]. Since brain is not part of the *consensus* PBPK model, no action needed to be taken.

As has been observed in [6], for a given tissue the $\mathrm{ABC}_{\mathrm{exp}}$ value is approximately constant across different pre-clinical species and human. This observation greatly facilitates extrapolation between species. To conclude, tissue partition coefficients K_{int} can be determined from the readily available antibody biodistribution coefficients $\mathrm{ABC}_{\mathrm{exp}}$ [6] that were corrected for residual blood to determine the unperturbed $\mathrm{ABC}_{\mathrm{tis}}$: To derive K_{int} from $\mathrm{ABC}_{\mathrm{int}}$, we used Eq. (3.1) to determine the steady state relationship

$$(1 - \sigma_{\mathrm{vas}})C_{\mathrm{pla}} = \frac{C_{\mathrm{int}}}{K_{\mathrm{int}}}, \tag{3.9}$$

resulting in

$$K_{\mathrm{int}} = \frac{\mathrm{ABC}_{\mathrm{int}}}{1 - \sigma_{\mathrm{vas}}}. \tag{3.10}$$

See Tables 3.2, 3.3, 3.4 and 3.5 for resulting parameter values.

3.2.3 Model parameterisation

A description of the parameters of the *consensus* PBPK model is given in Table 3.1. Anatomical and physiological parameters for male immunocompetent mice (25 g body weight (BW), 9 weeks of age) are summarised in Table 3.2. Physiological and anatomical values for male immunocompetent rats (250 g, 10 weeks of age) are summarised in Table 3.3. Physiological and anatomical values for humans were mostly taken from [58]. The parameter values for a 20-50 years old male with 73 kg reference BW and a 20-50 years old female with 60 kg reference BW are summarised in Table 3.4 and Table 3.5.

Tab. 3.1.: Interpretation, units and references of the parameters of the *consensus* PBPK model.

Parameter	Unit	References	Description
V_{tis}	mL	[57] for rodents and [58] for human	tissue volume (excluding vascular space)
L_{org}	mL/min	[64, 66]	organ-specific lymph flow
σ_{vas}	-	adapted from [7] based on parameterisation [57]	organ-specific vascular reflection coefficient
$\mathrm{ABC}_{\mathrm{int}}$	-	determined from $\mathrm{ABC}_{\mathrm{tis}}$ via Eq. (3.8); $\mathrm{ABC}_{\mathrm{tis}}$ derived from $\mathrm{ABC}_{\mathrm{exp}}$ [6] that were corrected for residual blood (see Eq. (3.4)); for liver and spleen $\mathrm{ABC}_{\mathrm{int}}$ set to 1	antibody biodistribution coefficient
K_{int}	-	computed from $\mathrm{ABC}_{\mathrm{int}}$ and σ_{vas}	organ-specific partition coefficient
CLpla	mL/min	estimated	linear plasma clearance
V_{max}	nmol/min	estimated	receptor system capacity
Km	nM	estimated	Michaelis-Menten constant

For rodents, tissue volumes, residual plasma volumes, blood volume and blood flow were scaled linearly with reported BW of the study. For humans, tissue volumes, residual plasma volumes, blood volume and blood flow were scaled with lean body weight because observed inter-individual variability (IIV) in organ weight was best described by lean body weight (for details, see [60]). In addition, when no demographic information (i.e., gender and/or BW) was available, we assumed a reference BW of 25 g for mice, 250 g for rats as well as 73 kg for 20-50 years old male humans and 60 kg for 20-50 years old female humans.

The reflection coefficients σ_{vas} are based on published values by Fronton et al. [7], in which three groups of organs with different reflection coefficients were identified. In the *consensus* PBPK model, we used a cardiac output typical for non-anaesthesised mice, which is roughly twice as large as the value used in [7] based on [65]. This also increased the peripheral lymph flow rates by the same factor. As a consequence, we updated the reflection coefficients such that the fraction not reflected (1-σ_{vas}) was halved, resulting in the same extravasation rate $L_{\mathrm{org}} \cdot (1 - \sigma_{\mathrm{vas}})$. The updated reflection coefficients are: $\sigma_{\mathrm{vas}} = 0.95$ for gut, liver and spleen, $\sigma_{\mathrm{vas}} = 0.975$ for heart, kidney, lung and skin, and $\sigma_{\mathrm{vas}} = 0.99$ for bone, adipose tissue and muscle.

Tab. 3.2.: Mouse: Reference parameters

	V_{tis} [a]	V_{int} [b]	$V_{\mathrm{res,pla}}$ [c]	Q_{pla} [d]	L_{org} [f]	σ_{vas}	$\mathrm{ABC}_{\mathrm{int}}$ [h]	K_{int} [i]
Units	mL	mL	mL	mL/min	mL/min	-	-	-
Lung	0.183	0.056	0.025	10.374	0.415	0.975	0.150	5.985
Adipose	1.911	0.180	0.012	0.726	0.029	0.990	0.446	44.602
Bone	2.064	0.286	0.115	1.141	0.046	0.990	0.170	16.998
Gut	1.055[g]	0.189	0.023	1.463	0.029	0.950	0.174	3.472
Heart	0.125	0.021	0.0107	0.685	0.027	0.975	0.184	7.349
Kidney	0.418	0.093	0.045	0.944	0.038	0.975	0.240	9.605
Liver	1.373	0.0866	0.129	1.681	0.034	0.950	1	20
Muscle	9.600	1.252	0.086	1.649	0.066	0.990	0.24	24.001
Skin	4.133	1.816	0.071	0.602	0.024	0.975	0.329	13.151
Spleen	0.0875	0.0081	0.0057	0.104	0.002	0.950	1	20
Plasma	1.080[e]	-	-	10.374	-	-	-	-

[a] fractional organ weights from [57], scaled to V_{tis} with tissue density (density assumed identical to human density data see Table 3.4) and mouse body weight (25 g)

[b] computed from interstitial fractions f_{int} from [21] except for kidney (taken from [76]) and liver and spleen (estimated: $f_{\mathrm{int}} = 0.0634$ (liv); $f_{\mathrm{int}} = 0.0923$ (spl))

[c] computed from residual plasma fractions $\mathrm{res}_{\mathrm{pla}}$ from [21]

[d] $Q_{\mathrm{pla}} = Q_{\mathrm{blo}} \cdot (1 - \mathrm{hct})$ with $\mathrm{hct} = 0.40$ [82]; cardiac output from [57, Page 440] & regional blood flows from [57] (Table 24) except for adi, bon, gut and spl (taken from [83])

[e] $V_{\mathrm{pla}} = (1 - \mathrm{hct}) \cdot V_{\mathrm{blo}}$ with V_{blo} from [84], total plasma volume including vascular space of organs

[f] assumed to be 2 % and 4 % of plasma flow Q_{pla} for visceral and non-visceral organs, respectively [64, 66]

[g] gut = sum of stomach, small and large intestine

[h] $\mathrm{ABC}_{\mathrm{int}} = C_{\mathrm{int}}/C_{\mathrm{pla}}$ derived from the unperturbed antibody biodistribution coefficients $\mathrm{ABC}_{\mathrm{tis}}$ via Eq. (3.4) and interstitial volume fractions f_{int}

[i] organ-specific partition coefficients K_{int} determined from $\mathrm{ABC}_{\mathrm{int}}$ values based on Eq. (3.10)

Tab. 3.3.: Rat: Reference parameters

	V_{tis}[a]	V_{int}[b]	$V_{\mathrm{res,pla}}$[c]	Q_{pla}[d]	L_{org}[f]	σ_{vas}[h]	$\mathrm{ABC}_{\mathrm{int}}$[i]	K_{int}[j]
Units	mL	mL	mL	mL/min	mL/min	-	-	-
Lung	1.250	0.3845	0.1712	47.359	1.894	0.975	0.150	5.985
Adipose	28.930	2.7177	0.1855	3.315	0.133	0.990	0.446	44.602
Bone	14.039	1.9469	0.7847	5.778	0.231	0.990	0.170	16.998
Gut	6.750[f]	1.2103	0.1485	6.204	0.124	0.950	0.174	3.472
Heart	0.825	0.1375	0.0709	2.321	0.093	0.975	0.184	7.349
Kidney	1.825	0.4078	0.1971	6.678	0.267	0.975	0.240	9.605
Liver	9.150	0.5775	0.8601	8.240	0.165	0.950	1	20
Muscle	101.075	13.1792	0.9097	13.166	0.527	0.990	0.24	24.001
Skin	47.575	20.9020	0.8088	2.747	0.110	0.975	0.329	13.151
Spleen	0.500	0.0461	0.0325	0.947	0.019	0.950	1	20
Plasma	9.120[d]	-	-	47.359	-	-	-	-

[a] fractional organ weights from [57], scaled to V_{tis} with tissue density (density assumed identical to human density data see Table 3.4) and rat body weight (250 g)

[b] assumed to be identical to mouse values (see Table 3.2 due to lack of data.)

[c] assumed to be identical to mouse values (see Table 3.2 due to lack of data.)

[d] $Q_{\mathrm{pla}} = Q_{\mathrm{blo}} \cdot (1 - \mathrm{hct})$with $\mathrm{hct} = 0.43$ [82]; cardiac output from [57, Page 440] & regional blood flows from [57] (Table 25) except for gut and spleen from [59]

[e] $V_{\mathrm{pla}} = (1 - \mathrm{hct}) \cdot V_{\mathrm{blo}}$ with V_{blo} from [84], total plasma volume including vascular space of organs

[f] assumed to be 2 % and 4 % of plasma flow, Q_{pla}, for visceral and non-visceral organs, respectively [64, 66]

[g] gut = sum of stomach, small and large intestine

[h] assumed to be identical to mouse values (see Table 3.2)

[i] identical to mouse values due to [6]

[j] assumed to be identical to mouse values

Tab. 3.4.: Human, male, 20-50 years: Reference parameters

	$V_{\mathrm{tis}}{}^a$	$V_{\mathrm{int}}{}^b$	$V_{\mathrm{res,pla}}{}^c$	$Q_{\mathrm{pla}}{}^d$	$L_{\mathrm{org}}{}^f$	$\sigma_{\mathrm{vas}}{}^i$	$\mathrm{ABC}_{\mathrm{int}}{}^j$	$K_{\mathrm{int}}{}^k$
Units	L	L	L	L/min	L/min	-	-	-
Lung	0.500	0.1538	0.0685	3.679	0.147	0.975	0.150	5.985
Adipose	15.830	1.4870	0.1015	0.184	0.007	0.990	0.446	44.602
Bone	8.077[g]	1.1202	0.4515	0.184	0.007	0.990	0.170	16.998
Gut	1.020[f]	0.1829	0.0224	0.515	0.010	0.950	0.174	3.472
Heart	0.330	0.0550	0.0284	0.147	0.006	0.975	0.184	7.349
Kidney	0.310	0.0693	0.0335	0.699	0.028	0.975	0.240	9.605
Liver	1.800	0.1136	0.1692	0.938	0.019	0.950	1	20
Muscle	29.000	3.7813	0.2610	0.626	0.025	0.990	0.24	24.001
Skin	3.300	1.4498	0.0561	0.184	0.007	0.975	0.329	13.151
Spleen	0.150	0.0138	0.0097	0.110	0.002	0.950	1	20
Plasma	3.000[d]	-	-	3.680	-	-	-	-

[a] Tissue volumes were calculated from organ weights [58, Table 2.8] and tissue densities assuming a density of 1 kg/L for all organs except adipose [85, p.44] and bone [58, Table 2.20]
[b] assumed to be identical to mouse values (see Table 3.2 due to lack of data.)
[c] assumed to be identical to mouse values (see Table 3.2 due to lack of data.)
[d] $Q_{\mathrm{pla}} = Q_{\mathrm{blo}} \cdot (1 - \mathrm{hct})$ with hct from erythrocyte volume [58, Table 2.12] and total blood weight; cardiac output was taken from [58, Table 2.39] and blood flow Q_{blo} was derived from blood flow rates as % of cardiac output [58, Table 2.40]
[e] $V_{\mathrm{pla}} = (1 - \mathrm{hct}) \cdot V_{\mathrm{blo}}$ with V_{blo} from blood organ weight [58] assuming a density of 1 kg/L
[f] assumed to be 2 % and 4 % of plasma flow, Q_{pla}, for visceral and non-visceral organs, respectively [64, 66]
[g] gut = sum of small and large intestine
[h] bone including total bone and marrow
[i] assumed to be identical to mouse values (see Table 3.2)
[j] identical to mouse values due to [6]
[k] assumed to be identical to mouse values

Tab. 3.5.: Human, female, 20-50 years: Reference parameters (footnotes identical to Table 3.4)

	$V_{\mathrm{tis}}{}^a$	$V_{\mathrm{int}}{}^b$	$V_{\mathrm{res,pla}}{}^c$	$Q_{\mathrm{pla}}{}^d$	$L_{\mathrm{org}}{}^f$	$\sigma_{\mathrm{vas}}{}^i$	$\mathrm{ABC}_{\mathrm{int}}{}^j$	$K_{\mathrm{int}}{}^k$
Units	L	L	L	L/min	L/min	-	-	-
Lung	0.420	0.1292	0.0575	3.631	0.145	0.975	0.150	5.985
Adipose	20.742	1.9485	0.1330	0.309	0.012	0.990	0.446	44.602
Bone	6.000[g]	0.78321	0.3354	0.182	0.007	0.990	0.170	16.998
Gut	0.960[f]	0.1721	0.0211	0.581	0.012	0.950	0.174	3.472
Heart	0.250	0.0417	0.0215	0.182	0.007	0.975	0.184	7.349
Kidney	0.275	0.0615	0.0297	0.617	0.025	0.975	0.240	9.605
Liver	1.400	0.0884	0.1316	0.980	0.012	0.950	1	20
Muscle	17.500	2.2818	0.1575	0.436	0.017	0.990	0.24	24.001
Skin	2.300	1.0105	0.0391	0.181	0.007	0.975	0.329	13.151
Spleen	0.130	0.012	0.0085	0.109	0.002	0.950	1	20
Plasma	2.400[d]	-	-	3.631	-	-	-	-

3.2.4 Variability and uncertainty in PBPK parameters

Considerable inter-individual variability (IIV) has been reported for mAb PK [86]. To account for IIV, we considered variability and uncertainty in physiological and anatomical parameters:

For humans, reference values are reported for human blood volume as a function of age and gender in [87]. Haematocrit values for humans are based on erythrocyte volume from [58] with 'typically red blood cells about 43 % (42-52 %) of total blood volume in adult males and about 38 % (37-48 %) in adult females.' Thus, the following variations were taken into account: variation in blood volume ($\pm$20%) and variation in haematocrit ($\pm$10 %). Coefficient of variation (CV) for cardiac output of 23.1 % for male adults and 23.7 % for female adults were derived from mean and standard deviation stated in [87, Table 5]. To account for variations in estimated plasma clearance, we considered an IIV in linear clearance across mAbs between human patients with median CV of 30 % [36]. We included variation in $V_{\max}$ based on [36] reporting an IIV with a median CV of $\pm$34 % across the studies.

For laboratory animals, the authors in [84] report a range of means for circulating blood volume. Median and percentiles of haematocrit for mouse and rat are given in [82]. The following variations were taken into account: variation in blood volume ($\pm$ 20%) and variation in haematocrit ($\pm$ 10%). In [57, Table 24] mean and standard deviation of cardiac output in non-anaesthesised mice with CV of approximately 20 % are reported. Taking into account that pre-clinical species are expected to have a lower variation in plasma clearance, we assumed the plasma clearance to vary within $\pm$20 % for animals. To account for uncertainty and variability in organ lymph flows we assumed the lymph flow to vary within $\pm$30 % for rodents and humans.

Monte Carlo simulations were performed for 1000 virtual individuals per dose group. Due to lack of detailed information, we assumed a uniform distribution for blood volume, haematocrit and lymph flow in the above specified range. We sampled from a lognormal distribution: (i) with a CV of 20 % for rodents and humans to account for uncertainty in cardiac output, (ii) with a CV of 30 % to account for uncertainty in $V_{\max}$ and (iii) with a CV of 20 % for rodents and 30 % for humans to account for uncertainty in linear plasma clearance. To account for uncertainty in ABC values we sampled from a lognormal distribution with reported mean and standard deviation as in [6]. Furthermore we assumed the fraction accessible for extravasation f=(1 -σ_{vas}) to be log-normally distributed with 10 % CV for rodents and humans due to variations, e.g., in endothelial pore size, abundance of pores and structure of glycocalyx. To visualise the impact of parameter variability and uncertainty, we determined the 5th and 95th percentiles of mAb concentrations in plasma and tissues (see Figures 3.2, 3.3, 3.4, 3.5, 3.6 and 3.8).

3.3 Common target-independent PK of mAbs across species

The *consensus* PBPK model is fully specified by readily available physiological and drug-specific parameters for various species; only an unspecific clearance (in addition to mAb-specific target-related processes) needs to be estimated. Importantly, estimation of the unspecific clearance requires only plasma data.

3.3.1 Estimating unspecific CL and predicting tissue concentrations in non-cross-reactive animal species

The *consensus* PBPK model was used to study experimental plasma and tissue PK data in non-cross-reactive species, which means that either the mAb does not bind to the target in these species or the target is not expressed in these species. For experimental data, see section A.1.1. If not explicitly stated in the investigated publications that experimental mAb tissue PK data have already been corrected for residual blood, we assumed that the experimental tissue data include residual blood and used Eq. (3.7) for comparison of model output and data. For mice and rats, the *consensus* PBPK model in Eqs. (3.1)-(3.2) (without any TMDD term) was fitted to the rodent plasma PK data. For each mAb, only a linear plasma clearance per BW $\mathrm{CLpla_{BW}}$ was estimated as the investigated mAbs do not show any cross-reactivity to a target:

$$\mathrm{CLpla_i} = \frac{\mathrm{BW_i}}{\mathrm{BW_{ref}}} \cdot \mathrm{CLpla_{BW}}. \tag{3.11}$$

Importantly, only venous plasma data was used to estimate the linear plasma clearance. Thus, for tissue data, the model simulations are predictions rather than a fit (except for liver and spleen, as stated in section 3.2.2). Estimated $\mathrm{CLpla_{BW}}$ values are listed in Table 3.6.

For all tested mAbs in mice, as shown, e.g., in Figure 3.2, the plasma concentration-time profiles agreed well with the experimental data. In addition, experimental tissue data of different mouse strains, i.e., FcRn wild-type (WT) mice, nude and severely compromised immunodeficient (SCID) mice were accurately predicted (see Chapter 4 for details).

For all tested mAbs in rats, as shown, e.g, in Figure 3.3+Figure 3.4, the fitted plasma concentration-time profiles and predicted tissue concentration-time profiles agreed very well with the experimental data.

Fitted mAb plasma concentration-time profiles in mice and rats, not shown here, are presented in Appendix section A.1.3.

Tab. 3.6.: RODENTS: Linear plasma clearance per body weight of intact mAbs; estimated $\mathrm{CLpla_{BW}}$ and objective function values (Obj) based on the *consensus* PBPK model (Eqs. (3.1)-(3.2) without any TMDD term), see text for details.

Antibody	Subclass	Ref	$\mathrm{CLpla_{BW}}$ [L/min/kg]	Obj -
mouse				
Canakinumab	IgG1	[88]	4.20e-6	2.05e-1
RSHZ19	IgG1	[89]	3.44e-6	3.13e-1
GNbAC1 mAb	IgG4	[90]	4.23e-6	4.35e-1
anti-MUC1 mAb [a]	IgG1	[91]	4.09e-6	2.45e-1
rat				
Infliximab	IgG1	[92]	5.43e-6	9.23e-1
Bevacizumab	IgG1	[93]	6.16e-6	7.40e-2
RSHZ19	IgG1	[94]	5.10e-6	1.49e0
Rituximab	IgG1	[95]	4.24e-6	3.61e0
CNTO5825 mAb	IgG1	[96]	5.56e-6	4.04e0
mouse IgG1 [b]	IgG1	[97]	7.05e-6	4.45e-1
rat IgG1 [c]	IgG1	[97]	9.19e-6	2.47e-1
anti-IL-13 mAb	IgG1	[77]	4.17e-6	4.19e-2
rMAb425 [d]	IgG1	[78]	5.88e-6	8.98e-2

[a] huC242
[b] mouse digoxin-specific IgG1
[c] directed against mouse IgG2b and polyclonal human IgG1
[d] reshaped by combining CDRs of mMAb425 with human IgG1

To visualise the impact of residual blood on experimental tissue data, we predicted tissue concentrations with and without residual blood contamination (see Figure 3.3 and Figure 3.4). For the tissues skin, muscle and fat, we observed only little perturbations. For heart, kidney, liver, lung and spleen, however, contributions of residual blood were more pronounced. The *consensus* PBPK model captures the overall trend of the concentration-time profiles (including residual blood contribution) very well except for liver and spleen. The model predicts larger concentrations including residual blood for liver and spleen compared to experimental data. However, in human cancer patients (see previous section, Figure 3.6), the concentration-time profiles are well predicted for liver. Overprediction for liver and spleen in rat might be due to additional processes not accounted for in the model or due to errors in handling/reporting experimental data. In addition, there is a difficulty in analysing experimental data from diverse laboratories/experimental studies with a given residual plasma fraction from a different experimental study. Measured residual plasma fractions are highly influenced by harvesting and handling of tissues. In particular, for tissues with discontinuous capillaries as liver and spleen, measured residual plasma fractions might include tissue extracellular space and need to be interpreted with care.

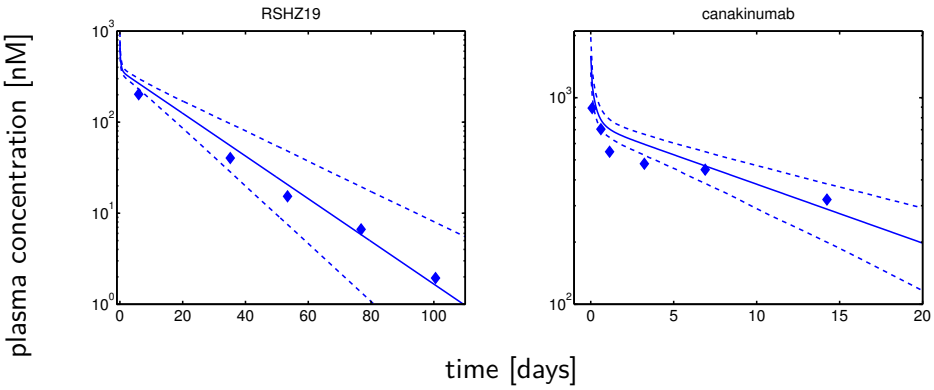

Fig. 3.2.: *Predictions of mAb* ***plasma concentration****-time profiles for* ***mice****.* Simulations are based on individually fitted plasma clearance and are compared to mean experimental data (filled diamonds) of canakinumab [88] and RSHZ19 [89] in mice. Solid lines represent the reference predictions and dashed lines the 5th and 95th percentiles.

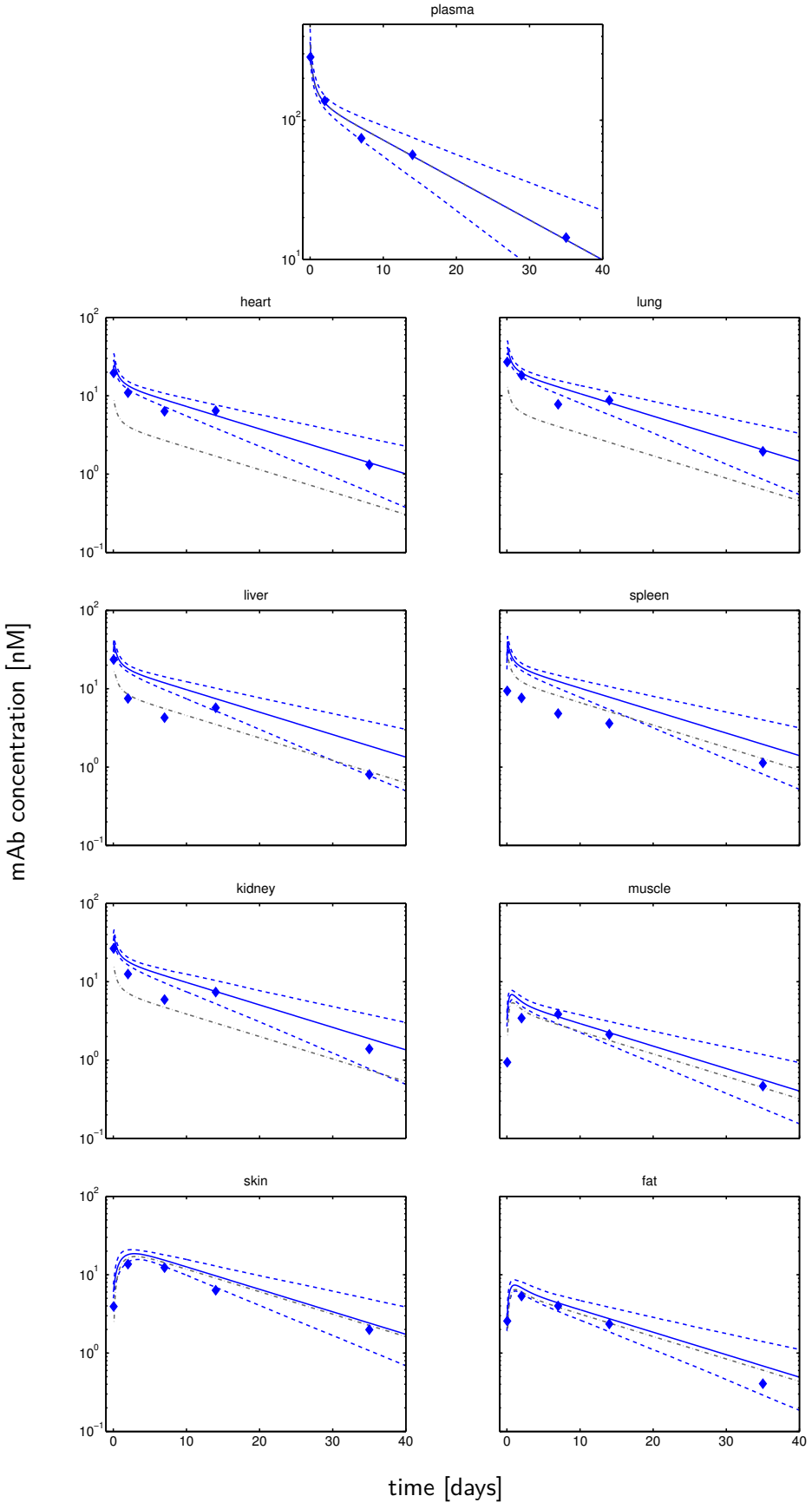

Fig. 3.3.: *Impact of residual blood contamination on anti-IL-13 mAb* ***tissue predictions*** *in* ***rats***. Simulations of concentrations **with residual blood** are based on individually fitted plasma clearance and are compared to mean experimental data (filled diamonds) of anti-IL-13 mAb in rat [77]. Solid lines represent the reference predictions and dashed coloured lines the 5th and 95th percentiles. Grey lines represent the concentration without residual blood.

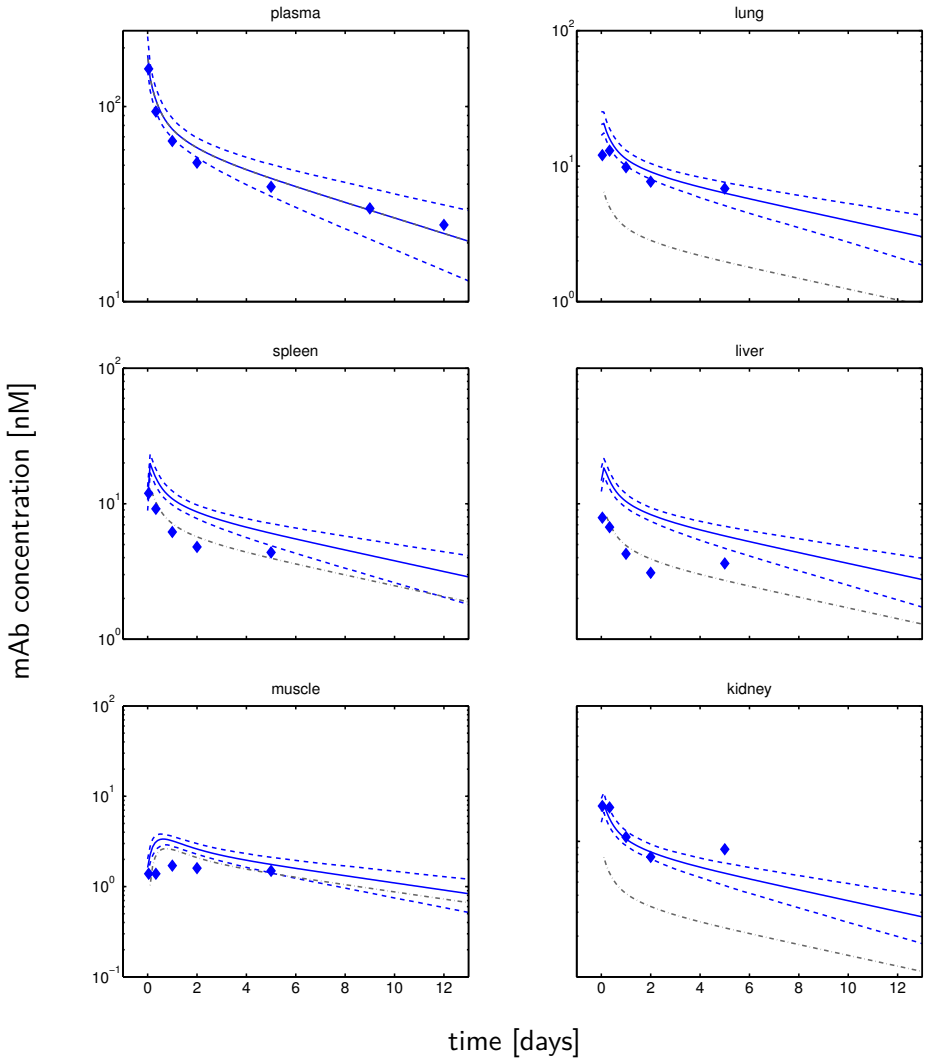

Fig. 3.4.: *Impact of residual blood contamination on rMAb 425* ***tissue predictions*** *in* ***rats***. Simulations of concentrations **with residual blood** are based on individually fitted plasma clearance and are compared to mean experimental data (filled diamonds) of rMAb 425 in rat [78]. Solid lines represent the reference predictions and dashed coloured lines the 5th and 95th percentiles. Grey lines represent the concentration without residual blood.

3.3.2 Estimating unspecific CL and predicting tissue concentrations in humans

The *consensus* PBPK model in Eqs. (3.1)-(3.2) with parallel linear and non-linear clearance was used to study plasma (and tissue) PK of different mAbs in human healthy volunteers and patients (for experimental data, see section A.1.1). If not explicitly stated in the investigated publications that experimental mAb tissue PK data have already been corrected for residual blood, we assumed that the experimental tissue data include residual blood and used Eq. (3.7) for comparison of model output and data. For humans, in all but one case (bevacizumab), the *consensus* PBPK model in Eqs. (3.1)-(3.2) without a TMDD term could describe the data (across the whole dose range) well. In these cases, only a linear clearance per body weight (see Eq. (3.11)) was estimated based on the experimental data. Estimated $\mathrm{CLpla_{BW}}$ values are listed in Table 3.7. For bevacizumab, the *consensus* PBPK model in Eqs. (3.1)-(3.2) with $\mathrm{TMDD_{pla}}$ could be used to estimate linear CLpla, $V_{\max}$ and Km. However, we used a different approach, where we only estimated $V_{\max}$ and Km, while using some median linear clearance (for details see section 3.3.3). Importantly, for estimation of clearance-related parameters, i.e., linear CLpla, $V_{\max}$ and Km, only plasma data were used. Thus, for tissue data, the model simulations are predictions rather than a fit (except for liver and spleen, as stated in section 3.2.2).

Following mg/kg dose regimen, human male and female pharmacokinetics were practically identical. In all but one case (bevacizumab), also in the presence of target, linear PK for mAbs was observed and the *consensus* PBPK model accurately captured plasma PK profiles of diverse mAb PK data. Illustrative plasma concentration-time profiles are shown in Figures 3.5 and in Appendix section A.1.4. Model predictions in Figures 3.5 are based on estimated individual linear plasma clearance, except for bevacizumab, where derived median linear plasma clearance was used and only $V_{\max}$ = 5.20e-5 nmol/min/kg BW and Km = 9.23 nM were estimated.

Due to ethical reasons, tissue PK data in humans are extremely scarce. Nevertheless, kinetics and tissue distribution data of a radiolabeled chimeric intact mAb (MOv18) were obtained from tissue biopsies in ovarian carcinoma patients [81] (for details on mAb and target, see Table 3.7). The *consensus* PBPK model successfully predicted human tissue PK in liver and skin, whereas for fat and muscle we noticed an under-prediction for the first time points (see Figure 3.6). The under-prediction in human patients may be related to inter-tissue variability (e.g., due to the difference between mAb tissue concentrations taken from biopsies and taken from whole tissue homogenates, which is often the case for rodent tissue data) or inter-individual variability.

Tab. 3.7.: HUMAN: Linear total plasma clearance per body weight of intact mAbs; estimated $\mathrm{CLpla_{BW}}$ and objective function values (Obj) based on the *consensus* PBPK model (Eqs. (3.1)-(3.2) without any TMDD term), see text for details.

Antibody	Subclass	Target	Ref	$\mathrm{CLpla_{BW}}$ [L/min/kg]	Obj -
patients					
Adalimumab	IgG1	TNFα	[98]	2.46e-6	6.37e0
Infliximab	IgG1	TNFα	[99]	2.70e-6	5.75e1
Gevokizumab	IgG2	IL-1β	[100]	1.64e-06	3.15e0
R1507 mAb	IgG1	IGF-1R	[101]	5.40e-6	2.00e1
Urtoxazumab	IgG1	E. coli SLT-2	[102]	1.40e-6	8.82e-1
Siltuximab	IgG1	IL-6	[103]	2.37e-6	4.24e0
Sirukumab	IgG1	IL-6	[104]	2.66e-6	8.20e0
Tefibazumab	IgG1	ClfA	[105]	2.22e-6	1.83e1
Pertuzumab	IgG1	HER2	[106]	4.32e-6	2.72e0
CAT354 mAb	IgG4	IL-3	[107]	1.78e-6	1.078e1
anti-IL-12 mAb	IgG1	IL-12 p40 subunit	[108]	1.37e-6	7.10e0
mAb MOv18	IgG1	FBP [a]	[81]	6.89e-6	1.32e-1
Mepolizumab	IgG1	IL-5	[109]	2.00e-06	2.53e0
AGS-1C4D4	IgG1	PSCA	[110]	1.91e-6	8.88e-1
healthy volunteers					
RSHZ19	IgG1	RSV	[89]	1.90e-6	2.39e0
TB402 mAb	IgG4	F VIII	[111]	1.88e-6	2.20e0
MEDI528	IgG1	IL-9	[112]	1.39e-6	1.16e0
CNTO5825 mAb	IgG1	IL-13	[113]	1.80e-6	1.68e1
anti-anthrax mAb	IgG1	B. anthracis PA	[114]	1.35e-6	1.58e1
GNbAC1 mAb	IgG4	MSRV-Env	[115]	1.76e-6	1.02e0
PAmAb	IgG1	B. anthracis PA	[116]	2.09e-06	2.66e0

[a] folate-binding protein

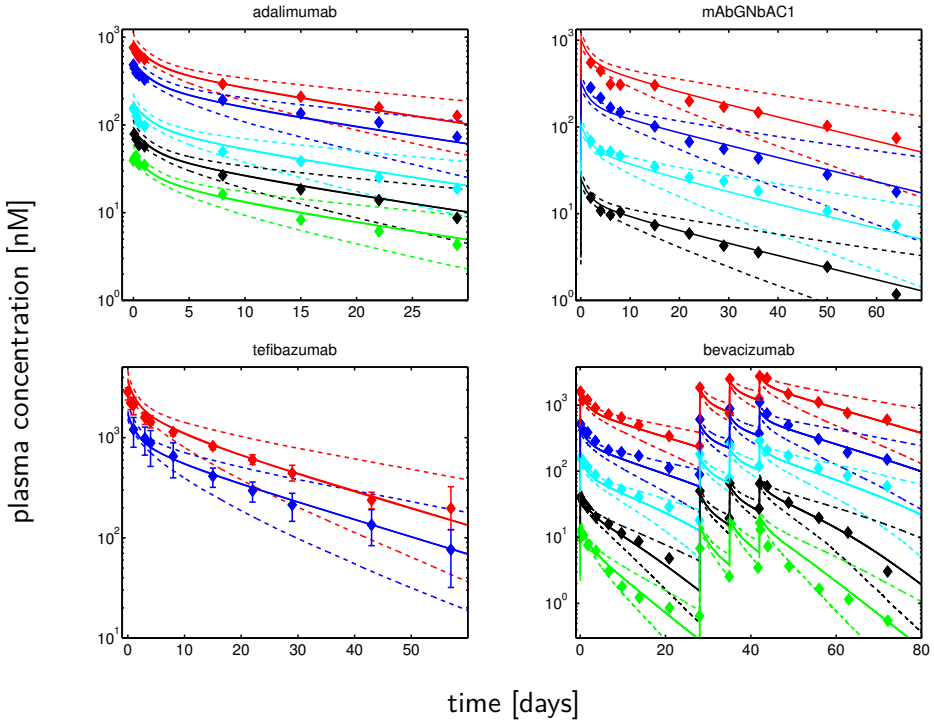

Fig. 3.5.: *Predictions of mAb plasma concentration-time profiles for* ***humans*** *based on individually* ***fitted plasma clearance****.* Simulations are compared to experimental data (filled diamonds, error bars) of different mAbs (see Table 3.7). Solid lines represent the reference predictions and dashed lines the 5th and 95th percentiles. The different colours refer to different mAb doses.

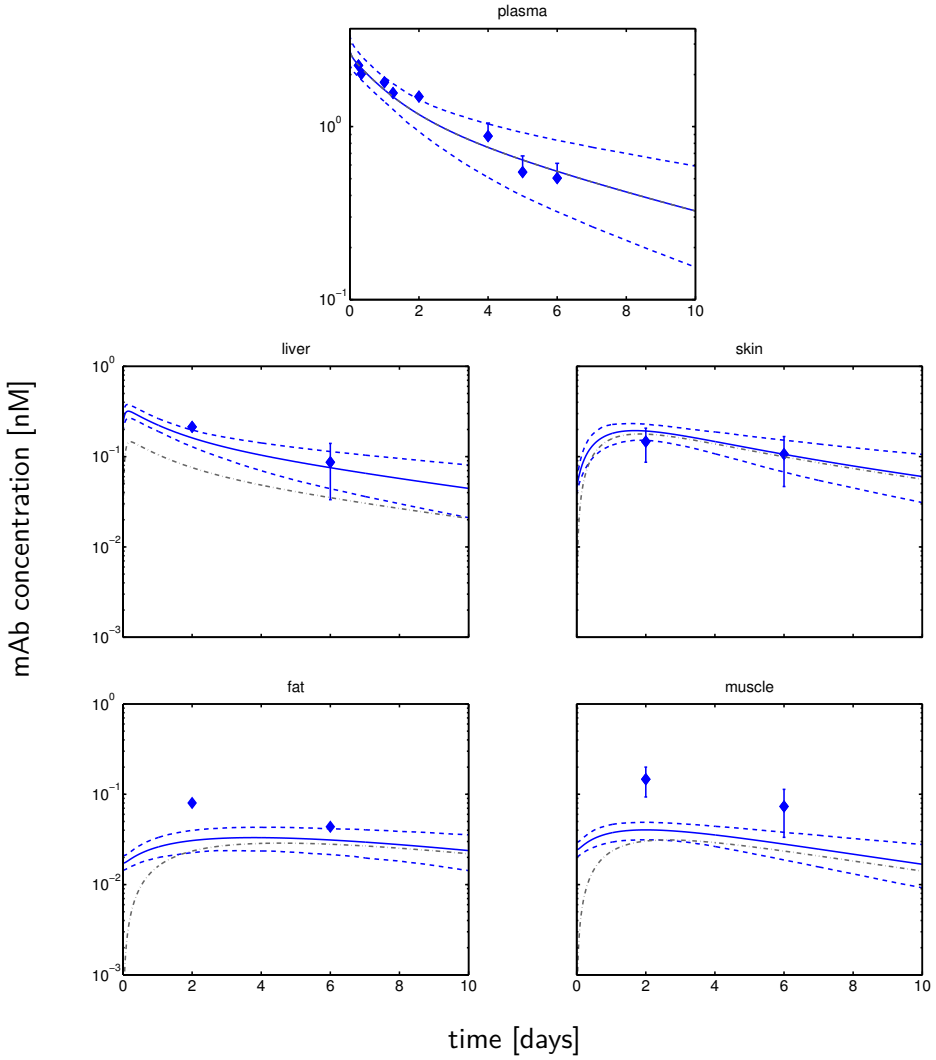

Fig. 3.6.: *Predictions of mAbMOv18 concentration-time profiles for* ***human patients*** *based on individually fitted plasma clearance.* Simulations of plasma PK and tissue of concentrations **with residual blood** are compared to experimental data (filled diamonds, error bars) of mAbMOv18 in cancer patients [81]. Solid lines represent the reference predictions and dashed lines the 5th and 95th percentiles. Grey lines represent the concentration without residual blood.

3.3.3 *A priori* prediction of clinical data using a predefined linear unspecific mAb CL

Estimated linear plasma clearances (from Table 3.7) were stratified for healthy man and human patients suffering from different diseases, and median and CV % were calculated (see Figure 3.7, top). For healthy volunteers, plasma clearance and its variation (median CLpla = 1.08e-4 L/h/kg; CV = 15.75 $\%$) is comparable to median clearance of IgGendo (1.21e-4 L/h/kg [1.11e-4, 1.42e-4]) [36, 117]. Variation of plasma clearance was estimated to be higher between human patients (median CLpla = 1.38e-4 L/h/kg, CV = 58.13 $\%$) and within the reported range for mAbs [118].

To assess the predictive capability of the *consensus* PBPK model with median plasma clearance (as in Figure 3.7, top), we plotted observed vs. predicted plasma concentrations (blue) for 21 different mAbs in human (see Figure 3.7, bottom, blue). For reference, we also plotted observed vs. individually fitted plasma concentrations (by fitting plasma clearance individually; see Figure 3.7, bottom, red). As can be inferred from Figure 3.7, bottom, the derived median plasma clearance for healthy volunteers and human patients can very well serve as a starting point for linear total clearance to obtain good predictions for PK of mAbs in excess of target and to generate expectations of target-related processes (see Figure 3.8).

For bevacizumab (see Figure 3.8), dose levels of 1-10 mg/kg are accurately *predicted* using the derived median linear plasma clearance for patients, while for the lower dose levels of 0.3 and 0.1 mg/kg, an increased clearance is observed. The difference in prediction and observation can be used to study the impact of target-related processes. Our observation is in agreement with [119], who observed linear PK of bevacizumab across the dose range 1 to 20 mg/kg and faster clearance at doses of 0.1 and 0.3 mg/kg (for more details, see Discussion).

3.4 Discussion

The *consensus* PBPK model was successfully used to study the PK of different mAbs in various strains of mice and rats as well as human patients and healthy volunteers. The model is readily parameterised by physiological and anatomical species-specific as well as mAb-related parameters. The latter include reflection coefficients and ABC values. Only an unspecific clearance (in addition to mAb-specific target-related processes) needs to be estimated. Importantly, estimation of the unspecific clearance requires only plasma data.

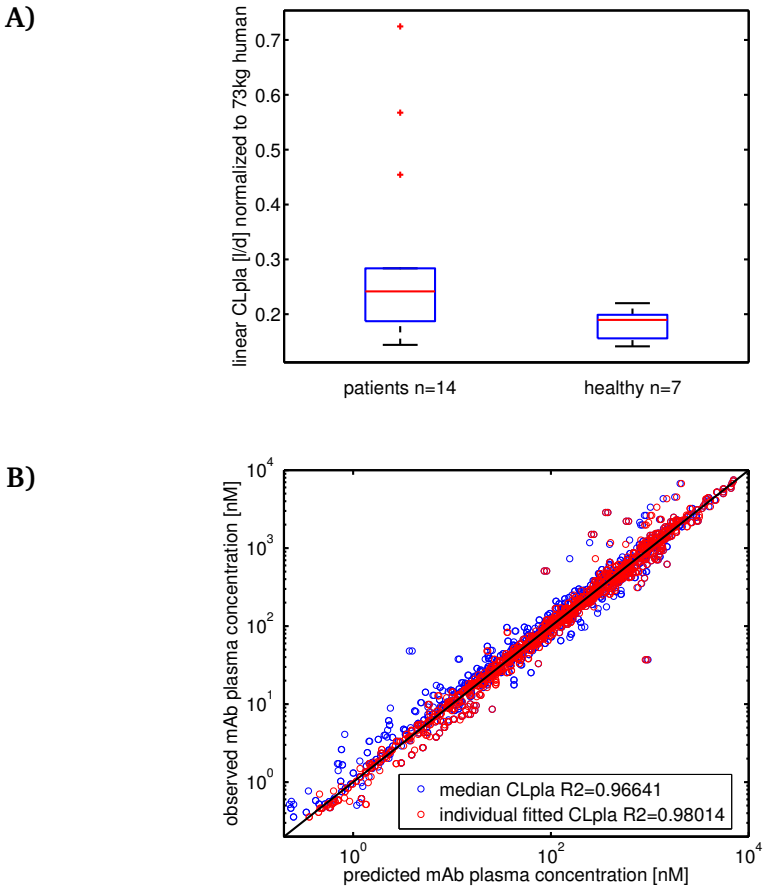

Fig. 3.7.: **A)** *Median and range of human fitted linear plasma clearance stratified for patients and healthy volunteers.* Outliers from top to down are: mAbMOv18, R1507, pertuzumab. **B)** *Comparison of observed and model predicted concentrations based on the consensus PBPK model* with individually fitted and median plasma clearance.

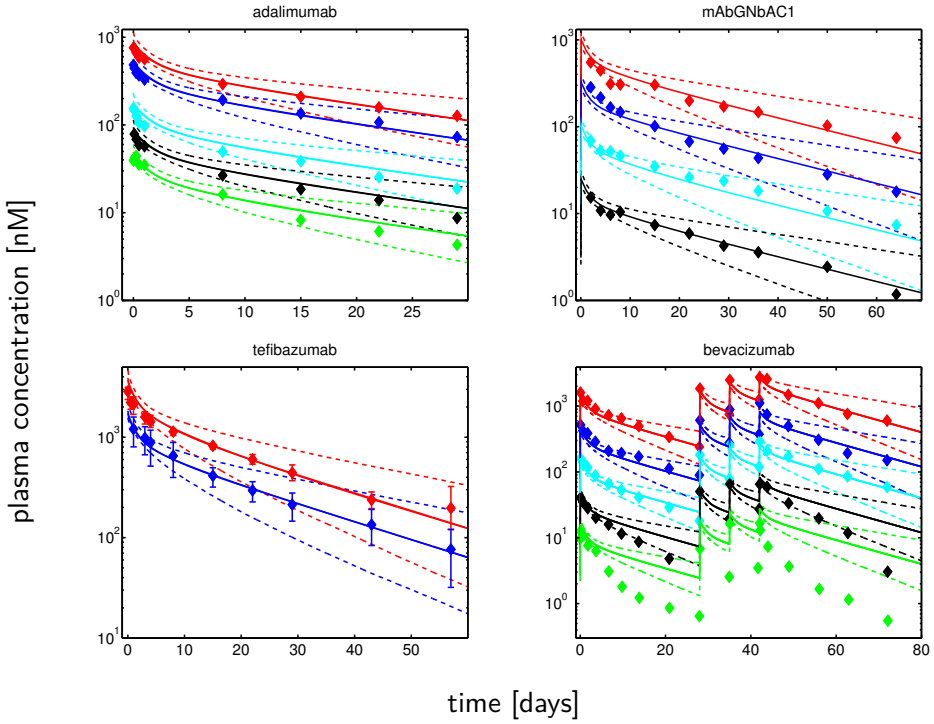

Fig. 3.8.: *A priori predictions of mAb plasma concentration-time profiles for based on* ***median plasma clearance*** *for* ***healthy volunteers and patients****.* Simulations are compared to experimental data (filled diamonds, error bars) of different mAbs (see Table 3.7). Solid lines represent the reference predictions and dashed lines the 5th and 95th percentiles. For fitted curves rather than *a priori* predictions, see Figure 3.5. The different colours refer to different mAb doses.

A main advantage in comparison to existing modelling approaches, such as the minimal PBPK model [73, 74] or empirical PK models, is the ability to predict tissue concentrations using known tissue-specific parameters that have been validated against a large data set of diverse species and mAbs. When additionally using the derived median plasma clearance per BW, the model can be used to *a priori* predict the target-unrelated part of mAb PK. This is of relevance in non-cross-reactive species, but also in humans, e.g., when clinical data and *in silico* predictions without a target are compared to estimate the impact of target-related processes. Given pre-clinical or clinical data, the *consensus* PBPK model can also be used to estimate the magnitude of unspecific and target-related clearance processes. For the common situation of mAbs being dosed to saturate the targeted system, only a single parameter (unspecific clearance) needs to be estimated from clinical data. For lower doses, also TMDD processes may be relevant and can be estimated in a convenient way.

It is known that disease status including co-medications or anti-drug antibodies (ADAs) may affect the PK of mAbs. These factors might be reasons for the outliers in human patient prediction (see Figure 3.7 (A), outliers from top to down are mAbMOV18, R1507, pertuzumab). Elevated inflammatory status, a syndrome often associated with cancer, results in an increased protein turnover rate in patients with cancer compared to healthy individuals and impacts the catabolism of immunoglobulins [25]. This may explain the estimated larger mAb clearance (in comparison to median plasma clearance) for cancer patients receiving mAbMOV18, R1507 and pertuzumab. In addition, the increased clearance for mAb R1507 may also be due to the development of anti-drug antibodies, which were detected in the serum from patients in the dose groups 1 mg/kg and 9 mg/kg [101]. Besides disease and anti-drug antibodies, the target type and the analytical method used to determine PK of mAbs, greatly impacts mAb clearance and PK. For bevacizumab, we could only estimate a linear CL for high doses of 1-10 mg/kg. At lower doses of 0.1-0.3 mg/kg, however, linear clearance was not sufficient to describe the data. This observation is in agreement with [119], which observed linear PK of bevacizumab across the larger dose range 1-20 mg/kg and faster clearance for lower doses of 0.1-0.3 mg/kg doses. Our observed non-linearity in bevacizumab CL for lower dose levels from data in [120] may also be related to the analytical method used to determine mAb PK. In [120], free and partially bound mAb was detected based on an ELISA assay. For dose level 0.1 mg/kg, the mAb concentration fell below limit of detection and high target concentration in the analytical assay may have interfered with the mAb concentration. This problem was also reported in [37], as for mAbs binding to soluble targets, high circulating antigen levels may interfere with the measurement of therapeutic mAbs by ELISA, in particular if free or partially bound mAb forms are measured. Furthermore, the authors in [121] observed elevated free bevacizumab levels in vitreal samples after prolonged frozen storage, which may be

due to dissociation of mAb-target complex. Unfortunately, in [120], the stability of bevacizumab after frozen storage was not reported.

We assumed an apparent clearance from the plasma compartment due to lack of detailed knowledge on the extent of mAb tissue metabolism in rat and human. In case of subcutaneous (s.c.) administration, the bioavailability would need to be accounted for. As stated in [122], 's.c. bioavailability for currently marketed products is in the range of 24% to 95% in human.' It is also reported that the injection site for s.c. administration can be seen as a local compartment, where crystallisation processes can occur. Additional factors to catabolism are believed to influence s.c. absorption, in particular (i) skin morphology, (ii) presence of an Fc receptor at injection site, (iii) target interactions, (iv) formulation and (v) mode of administration [122]. As soon as a more detailed quantitative understanding becomes available, such factors can easily be integrated in the presented *consensus* PBPK model.

For mAbs binding to soluble antigens, we assumed that mAb PK is not altered upon binding to the soluble ligand, which is often the case for mAbs that are directed against soluble ligands present at low endogenous concentrations [37]. Mostly, soluble ligands, such as TNFα or VEGF, are present at small endogenous concentrations, and mAbs binding to those ligands often exhibit linear dose-proportional PK, where PK remains unaltered at elevated target levels (e.g., adalimumab). The small free soluble ligand 'normally' exhibits a faster clearance compared to the free mAb, however, upon binding to the antibody, the ligand adopts the distribution and clearance properties of the antibody leading to an increase in measurable target concentrations. 'Normal' disposition processes of the ligand, such as diffusion, renal filtration or receptor-mediated endocytosis, are prevented when binding to the mAb, which leads to the formation of immune complexes. The antibody-ligand complexes are primarily cleared through Fcγ receptor-mediated endocytosis by cells throughout the body, a pathway, which is often non-specific and linear.

In summary, we believe that the presented PBPK model can serve as a consensus approach and convenient starting point to study mAb disposition in human in detail, including first-in-man studies and target-specific investigation, e.g., to assess the impact of physiological factors, such as FcRn concentration and endogenous IgG on unspecific mAb clearance (see Chapter 4) and tumour tissue on mAb PK in xenograft mice and its extrapolation to human (see Chapter 5).

4 Impact of endogenous IgG on unspecific mAb clearance

When studying mAb PK, protection from elimination by binding to FcRn is known to be a major process influencing unspecific, i.e., target-independent mAb clearance as well as the kinetics of endogenous IgG [14]. Following endocytosis, both, endogenous IgG and therapeutic mAb compete for binding to the limited capacity FcRn protection system. The neonatal Fc receptor is normally not saturated at therapeutic mAb concentrations and the unspecific mAb clearance is generally low and constant across therapeutic dose ranges [36]. The concentration of endogenous IgG under immunodeficient conditions, however, is reduced, and this effect on the FcRn protection mechanism and on unspecific mAb clearance is unknown, yet of great pre-clinical and clinical importance.

Experimental data from immunodeficient xenograft mice are most widely used to study mAb PK and examine therapeutic response to mAbs. An important characteristic of these mouse models is their impaired immune system resulting in low endogenous IgG concentrations. Hence, it is of great relevance to elucidate whether the low endogenous IgG concentrations in these animal models should be considered in the interpretation of mAb PK data from immunodeficient mouse models. Moreover, immunosuppressed cancer patients [15–17] and diseased patients (e.g., myotonic dystrophy [123]) have low concentration of endogenous IgG, while patients with liver cirrhosis have elevated concentrations of immunoglobulins, mainly IgG [124].

The objective of this chapter was to analyse the influence of altered endogenous IgG concentrations—as present in immunodeficient mice—competing with therapeutic IgG (i.e., mAb and intravenous immunoglobulin (IVIG)) for FcRn binding and salvage, on unspecific mAb clearance.

This chapter is organised as follows: First, we present different modelling approaches to explicitly include the competition of endogenous and therapeutic IgG (i.e. mAb and IVIG) for binding to FcRn in the *consensus* PBPK model. The known influence of IVIG therapy leading to increased total IgG concentration *in vivo* can be used to study the impact of altered IgG on unspecific mAb clearance. Therefore, the analysis of mAb PK data of FcRn WT mice following IVIG therapy based on the *consensus* PBPK model in section 4.3 is used to validate our model assumptions. Furthermore,

to study the impact of antibody binding affinity towards FcRn on unspecific mAb clearance, we examine whether different model scenarios can predict the influence of IVIG therapy on mAb PK in section 4.4. Finally, the impact of altered IgG due to lower endogenous IgG in immunodeficient mice on unspecific mAb clearance is studied in section 4.5. It is also investigated under which conditions the limitations of the different modelling approaches become apparent. In section 4.6, we summarise the obtained results and give a general answer to the question 'When to expect linear unspecific clearance in immunodeficient mice?'.

4.1 Modelling of FcRn-IgG interaction in PBPK models

Published mAb PBPK modes are quite heterogeneous, e.g., regarding the importance to explicitly account for endogenous IgG and with respect to the FcRn salvage mechanism (whether to explicitly account for the IgG-FcRn interaction and whether to use an equilibrium model or detailed binding kinetics, whether to account for pH-dependent binding). For a brief overview of the differences between mAb PBPK models, see Chapter 2. Still today, there is very limited quantitative knowledge about the processes involved in fluid-phase endocytosis and endosomal sorting [44]. Furthermore, quantitative information about the FcRn concentration in the different tissues is still lacking. As a consequence, parameter values related to the endosomal compartment in existing detailed mAb PBPK models are always fitted to experimental mAb tissue PK data and detailed PBPK models suffer from over-parameterisation. In contrast to over-parameterised PBPK models, Fronton et al. [7] developed a simplified mAb PBPK model that is adapted to the complexity of the experimental data and does allow to also predict tissue-specific mAb concentrations in opposition to the minimal PBPK model developed by Cao et al. [73]. We believe that through the development of those second-generation PBPK models [7, 73], the applicability to study mAb PK was significantly advanced.

The *simplified* PBPK model implicitly accounts for endogenous IgG and competition of endogenous and therapeutic IgG for binding to FcRn. Under the assumption and physiological condition that endogenous IgG concentrations are constant in time and markedly higher than therapeutic mAb concentrations following clinically relevant doses, unspecific elimination is only a function of endogenous IgG concentrations and hence, unspecific mAb clearance is linear. This can generally be expected to be the case in immunocompetent mouse models with the notable exception of IVIG therapy. It might, however, not hold for immunodeficient mouse models.

The *consensus* PBPK model that is obtained from the *simplified* mAb PBPK model [7] (for more details, see Chapter 3) allows to predict tissue mAb concentrations on plasma data and ABCs only, and can serve as a starting point, e.g., to assess the

impact of physiological factors, such as FcRn concentration and endogenous IgG on unspecific mAb clearance.

4.2 *Consensus* PBPK model to study the impact of altered endogenous IgG on unspecific mAb CL

To study the impact of altered endogenous IgG concentrations $\mathrm{IgG}_{\mathrm{endo}}$ on the unspecific plasma clearance, we explicitly included the competition of endogenous and therapeutic IgG $\mathrm{IgG}_{\mathrm{therapeutic}}$ (i.e., mAb and IVIG) for binding to FcRn in the *consensus* PBPK model. The experimental data of mice species are presented in Appendix section A.2.1. To avoid impact of target-mediated clearance processes, we focussed on mAbs without affinity to a target antigen in these mice. Required physiological and drug-related parameter values are presented in detail in Table 3.2.

To model the binding of IgG to FcRn in the endosomes of vascular endothelial cells, we considered the IgG plasma concentration as a surrogate for the corresponding endosomal concentration. This assumption is supported by the large number of empirical mAb PK compartment models that parameterise the linear clearance in terms of the central (plasma) concentration (for relaxation of this assumption, see Appendix section A.2.3). IgG not bound to FcRn in endosomes is degraded within the endo-lysosomes and thus, changes in fraction unbound $\mathrm{fu}_{\mathrm{IgG}}$ of IgG can explain changes in unspecific plasma clearance.

We parameterised the unspecific plasma clearance in terms of a 'maximal' unbound unspecific clearance $\mathrm{CLpla}_{\mathrm{u}}$ and $\mathrm{fu}_{\mathrm{IgG}}$ as follows:

$$\mathrm{CLpla} = \mathrm{CLpla}_{\mathrm{u}} \cdot \mathrm{fu}_{\mathrm{IgG}}. \tag{4.1}$$

To account for the competition, we defined the unbound fraction

$$\mathrm{fu}_{\mathrm{IgG}} = \frac{\mathrm{IgG}_{\mathrm{u}}}{\mathrm{IgG}} \tag{4.2}$$

as a function of the total IgG concentration

$$\mathrm{IgG}_{\mathrm{tot}} = \mathrm{IgG}_{\mathrm{endo}} + \mathrm{IgG}_{\mathrm{therapeutic}}. \tag{4.3}$$

The differential equations of the *consensus* PBPK model without TMDD term (section 3.2.1), describing the rates of change of the concentrations in plasma C_{pla} and in the interstitial space C_{int} (both in [nM]) of the different organs

$$V_{\mathrm{int}}\frac{\mathrm{d}}{\mathrm{dt}}C_{\mathrm{int}} = L_{\mathrm{org}}\cdot\left((1-\sigma_{\mathrm{vas}})C_{\mathrm{pla}}-\frac{C_{\mathrm{int}}}{K_{\mathrm{int}}}\right) \tag{4.4}$$

$$V_{\mathrm{pla}}\frac{\mathrm{d}}{\mathrm{dt}}C_{\mathrm{pla}} = \sum_{\mathrm{org}}L_{\mathrm{org}}\cdot\left(\frac{C_{\mathrm{int}}}{K_{\mathrm{int}}}-(1-\sigma_{\mathrm{vas}})\cdot C_{\mathrm{pla}}\right) - \mathrm{CLpla}\cdot C_{\mathrm{pla}}+k_{\mathrm{in}}(t) \tag{4.5}$$

applied to all therapeutic IgG species (e.g., mAb and IVIG); with infusion rate $k_{\mathrm{in}}(t)$ [nmol/min]. The first equation applies to each organ.

For endogenous IgG, the inflow rate k_{in} is a zero-order rate describing the endogenous IgG synthesis rate k_{syn} in mice. The endogenous IgG synthesis rate k_{syn} was parameterised in terms of baseline endogenous plasma concentration $\mathrm{IgG}_{\mathrm{endo,baseline}}$ as follows:

$$k_{\mathrm{syn}} = (\mathrm{CLpla}_{\mathrm{u}}\cdot \mathrm{fu}_{\mathrm{IgG,baseline}})\cdot \mathrm{IgG}_{\mathrm{endo,baseline}}, \tag{4.6}$$

where $\mathrm{fu}_{\mathrm{IgG,baseline}}$ is the unbound fraction of $\mathrm{IgG}_{\mathrm{endo,baseline}}$ in the absence of any therapeutic IgG. For WT mice, we used a baseline plasma concentration of $\mathrm{IgG}_{\mathrm{endo,baseline}}$=1.47e4 nM, which corresponds to 2.2e3 μg/mL (scaling factor: 1e6/MW) reported in [125]. For nude mice, we used a baseline plasma concentration of $\mathrm{IgG}_{\mathrm{endo,baseline}}$=3.3e2 nM, based on Bloemmen et al. [126], who reported a serum endogenous IgG1 concentration in nude mice (6 weeks of age) of 5e-2 mg/mL (scaling factor: 1e9/MW). For SCID mice, we used an $\mathrm{IgG}_{\mathrm{endo}}$ concentration in plasma of 1e-1 μg/mL [127] corresponding to a baseline endogenous plasma IgG concentration $\mathrm{IgG}_{\mathrm{endo,baseline}}$=6.6e-1 nM (scaling factor: 1e6/MW).

In the following three subsections, we present different models to determine the unbound fraction $\mathrm{fu}_{\mathrm{IgG}}$ of IgG. These models differ in complexity and their underlying assumptions regarding the equilibrium binding affinity $\mathrm{K_D} = (\mathrm{k_{off}}/\ \mathrm{k_{on}})$ towards FcRn. For relaxation of the assumption of equilibrium binding, see Appendix section A.2.4.

4.2.1 Equilibrium binding model to determine unbound fraction of IgG

The equilibrium binding model is briefly revisited here; for a detailed derivation see, e.g., [7, Appendix]. The model is derived under the assumption that all IgG species, i.e., mAb, IVIG and $\mathrm{IgG}_{\mathrm{endo}}$ have the same binding affinity towards FcRn (for relaxation of this assumption, see section 4.2.2).

The unbound fraction of IgG was given by

$$\mathrm{fu_{IgG}} = \frac{\mathrm{K_D}}{\mathrm{K_D} + \mathrm{FcRn_u}}, \tag{4.7}$$

where the unbound FcRn concentration $\mathrm{FcRn_u}$ was defined as a function of total FcRn $\mathrm{FcRn_{tot}}$, total IgG $\mathrm{IgG_{tot}}$ and the equilibrium binding constant $\mathrm{K_D}$

$$\mathrm{FcRn_u} = \frac{1}{2}\Big(\Delta + \sqrt{\Delta^2 + 4\mathrm{K_D} \cdot \mathrm{FcRn_{tot}}}\Big) \tag{4.8}$$

with $\Delta = \mathrm{FcRn_{tot}} - \mathrm{IgG_{tot}} - \mathrm{K_D}$.

4.2.2 Equilibrium binding model with different $\mathrm{K_D}$ values to determine unbound fraction of IgG

It is well known that human and mouse FcRn have different binding affinities for IgGs from many different species [45]. We extended the equilibrium binding model to account for differences in binding affinity to FcRn. We illustrate the model derivation for murine IgG (i.e., murine mAb and endogenous IgG) and human IgG (i.e., IVIG) in mice. The unbound murine IgG ($\mathrm{mIgG_u}$) and unbound human IgG ($\mathrm{hIgG_u}$) bind to free murine FcRn, i.e., $\mathrm{FcRn_u}$ with different binding constants ($\mathrm{mK_D}$ and $\mathrm{hK_D}$) to form the corresponding IgG-FcRn complexes ('bound IgG to FcRn') $\mathrm{mIgG_b}$ and $\mathrm{hIgG_b}$:

$$\begin{aligned} \mathrm{mIgG_u} + \mathrm{FcRn_u} &\overset{\mathrm{mK_D}}{\rightleftharpoons} \mathrm{mIgG_b} \\ \mathrm{hIgG_u} + \mathrm{FcRn_u} &\overset{\mathrm{hK_D}}{\rightleftharpoons} \mathrm{hIgG_b}. \end{aligned}$$

Our aim was to determine the unbound fractions

$$\mathrm{fu_{mIgG}} = \frac{\mathrm{mIgG_u}}{\mathrm{mIgG}} \tag{4.9}$$

$$\mathrm{fu_{hIgG}} = \frac{\mathrm{hIgG_u}}{\mathrm{hIgG}} \tag{4.10}$$

as a function of the total murine and human IgG concentrations

$$\begin{aligned} \mathrm{mIgG} &= \mathrm{mIgG_u} + \mathrm{mIgG_b} \\ \mathrm{hIgG} &= \mathrm{hIgG_u} + \mathrm{hIgG_b}. \end{aligned}$$

Total IgG concentration is given by $\mathrm{IgG_{tot}} = \mathrm{mIgG} + \mathrm{hIgG}$ and total FcRn by $\mathrm{FcRn_{tot}} = \mathrm{FcRn_u} + \mathrm{FcRn_b}$. Note that $\mathrm{FcRn_b}$ is identical to the $\mathrm{IgG_b}$, thus comprises $\mathrm{mIgG_b}$ and $\mathrm{hIgG_b}$.

Assuming quasi-steady state conditions for the binding processes, exploiting the above relationships and solving for the IgG-FcRn complexes $\mathrm{mIgG_b}$ and $\mathrm{hIgG_b}$ yielded

$$\mathrm{mIgG_b} = \frac{\mathrm{FcRn_u}}{\mathrm{mK_D} + \mathrm{FcRn_u}} \cdot \mathrm{mIgG} \tag{4.11}$$

$$\mathrm{hIgG_b} = \frac{\mathrm{FcRn_u}}{\mathrm{hK_D} + \mathrm{FcRn_u}} \cdot \mathrm{hIgG}. \tag{4.12}$$

Exploiting $\mathrm{FcRn_{tot}} = \mathrm{FcRn_u} + \mathrm{FcRn_b}$ yielded

$$\mathrm{FcRn_{tot}} = \mathrm{FcRn_u} + \frac{\mathrm{FcRn_u}}{\mathrm{mK_D} + \mathrm{FcRn_u}} \cdot \mathrm{mIgG} + \frac{\mathrm{FcRn_u}}{\mathrm{hK_D} + \mathrm{FcRn_u}} \cdot \mathrm{hIgG}. \tag{4.13}$$

Solving for $\mathrm{FcRn_u}$ requires to solve a cubic equation (with three real-valued solutions, two negative ones and one positive one). The unbound FcRn concentration, defined as the positive solution of the cubic equation, is given by

$$\mathrm{FcRn_u} = 2 \cdot \sqrt[3]{\rho} \cdot \cos(\phi/3) - \mathrm{B}/3 \tag{4.14}$$

with $\rho = \sqrt{-p^3/27}$ and $\phi = \arccos(-q/2 \cdot \rho)$ and $p = (3 \cdot \mathrm{C} - \mathrm{B}^2)/3$ and $q = 2 \cdot \mathrm{B}^3/27 - (\mathrm{B} \cdot \mathrm{C})/3 - \mathrm{D}$ and $\mathrm{B} = \mathrm{mK_D} + \mathrm{mIgG} + \mathrm{hIgG} + \mathrm{hK_D} - \mathrm{FcRn_{tot}}$ and $\mathrm{C} = \mathrm{mK_D} \cdot \mathrm{hIgG} + \mathrm{hK_D} \cdot \mathrm{mIgG} + \mathrm{mK_D} \cdot \mathrm{hK_D} - \mathrm{FcRn_{tot}} \cdot \mathrm{hK_D} - \mathrm{FcRn_{tot}} \cdot \mathrm{mK_D}$ and $\mathrm{D} = -\mathrm{FcRn_{tot}} \cdot \mathrm{hK_D} \cdot \mathrm{mK_D}$.

The resulting unbound fractions of murine and human IgG are given by

$$\mathrm{fu_{mIgG}} = \frac{\mathrm{mK_D}}{\mathrm{mK_D} + \mathrm{FcRn_u}} \tag{4.15}$$

$$\mathrm{fu_{hIgG}} = \frac{\mathrm{hK_D}}{\mathrm{hK_D} + \mathrm{FcRn_u}}. \tag{4.16}$$

4.2.3 Cutoff model to determine unbound fraction of IgG

The cutoff model was originally proposed by Xiao in 2012 [128] and theoretically derived as an approximation of the detailed equilibrium binding model in [7]. For mAbs with high-affinity binding to FcRn, $\mathrm{fu_{IgG}}$ is approximated by

$$\mathrm{fu_{IgG}} = \begin{cases} 0; & \mathrm{IgG_{tot}} \leq \mathrm{FcRn_{tot}} \\ 1 - \frac{\mathrm{FcRn_{tot}}}{\mathrm{IgG_{tot}}}; & \mathrm{IgG_{tot}} > \mathrm{FcRn_{tot}}. \end{cases} \tag{4.17}$$

In the cutoff model, $\mathrm{fu_{IgG}}$ exhibits two regimes: (i) a constant zero phase for the total IgG concentration $\mathrm{IgG_{tot}}$ below FcRn and (ii) a phase of hyperbolic increase for $\mathrm{IgG_{tot}}$ above FcRn.

Figure 4.1 shows $\mathrm{fu_{IgG}}$ as a function of the total IgG concentration based on the cutoff model and the equilibrium binding model (exemplary for the parameter values FcRn = 1e5 nM and KD = 4.8 nM). Since $\mathrm{CLpla} = \mathrm{CLpla_u} \cdot \mathrm{fu_{IgG}}$, a change in fraction unbound is one way of explaining a change in unspecific mAb clearance. As both binding models result in almost identical unbound fractions of IgG on the entire range of IgG concentrations, the cutoff model seems to be a good approximation. Only in the zoomed plot, there is a difference between the cutoff and the equilibrium binding model. For total IgG being smaller than FcRn, $\mathrm{fu_{IgG}}$ and thus CLpla is set to zero in the cutoff model, whereas CLpla is approximating zero in the equilibrium binding model.

In the following analyses, both, the cutoff model and the equilibrium binding model are used to study the impact of altered IgG on unspecific mAb clearance. It will be investigated under which conditions the limitations of the cutoff model for total IgG being smaller than FcRn become apparent and the cutoff model results in no good approximation anymore. When IgG species of different origin are available, e.g., human and mouse IgG binding to murine FcRn, the equilibrium binding model with different $\mathrm{K_D}$ values (section 4.2.2) will be compared with the equilibrium binding model with identical $\mathrm{K_D}$ values (section 4.2.1).

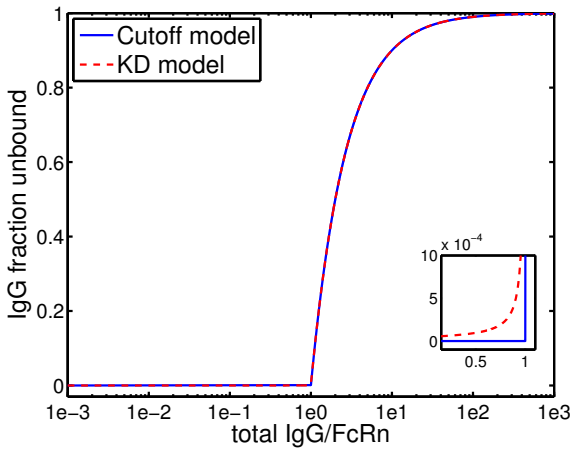

Fig. 4.1.: *IgG fraction unbound* $\mathrm{fu_{IgG}}$ *as a function of total IgG concentration (i.e., endogenous and therapeutic IgG) normalised by FcRn.* $\mathrm{fu_{IgG}}$ is predicted by the equilibrium binding model (KD model, Eq. (4.7)) and by the Cutoff model (Eq. (4.17)) exemplary for the parameters values FcRn=1e5 nM and $\mathrm{K_D}$=4.8 nM.

4.3 Prediction of mAb PK data for WT mice following IVIG therapy

Inhibition of FcRn-therapeutic mAb interaction by administration of very high doses of IVIG is known to lead to an increase in unspecific mAb clearance *in vivo* [129, 130].

Tab. 4.1.: FcRn WT mice pre-treated with IVIG: Estimated total FcRn concentration and unbound plasma clearance per body weight ($\mathrm{CLpla_u BW}$) of murine mAbs; estimated parameters, 95% confidence intervals (CI) and objective function values (Obj) based on the *consensus* PBPK model with different models to determine $\mathrm{fu_{IgG}}$, see text for details.

model	FcRn[nM] estimate [95% CI]	$\mathrm{CLpla_u BW}$ [L/min/kg] estimate [95% CI]	Obj -
model with 1 $\mathrm{K_D}$ [a] $\mathrm{hK_D}$=4.8 nM, $\mathrm{mK_D}$=4.8 nM	1.34e4 [1.31e4, 1.36e4]	3.29e-5 [2.91e-5, 3.67e-5]	5.69e-1
cutoff model	1.33e4 [1.31e4, 1.35e4]	3.26e-5 [2.91e-5, 3.66e-5]	5.69e-1

[a] PBPK model with equilibrium binding; assuming same binding affinity of $\mathrm{K_D}$=4.8 nM for murine and human IgG to mouse FcRn

The known influence of IVIG therapy leading to increased total IgG concentrations *in vivo* was used to study the impact of altered IgG on unspecific mAb clearance. Thus, the analysis of mAb PK data of FcRn WT mice following IVIG therapy based on the *consensus* PBPK model was used to validate our model assumptions.

To analyse the impact of increased total IgG concentration on unspecific mAb clearance, we used the plasma and tissue data of mAb 7E3 following IVIG therapy (mAb 7E3 following IV bolus administration of 8mg/kg to FcRn WT mice pre-treated with different doses of IVIG) [79].

We jointly fitted the *consensus* PBPK model comprising Eqs. (4.4)+(4.5) for each of the three species: therapeutic mAb, IVIG and endogenous IgG. Both, the equilibrium binding model (section 4.2.1) with $\mathrm{K_D} = 4.8$ nM [131] for therapeutic and endogenous IgG and the cutoff model (section 4.2.3) were used to perform the following analyses: For each model, we estimated $\mathrm{CLpla_u BW}$ [L/min/kg] and total FcRn concentration FcRn. For estimation, only plasma data were used. Thus, for tissue data, the model simulations are a prediction rather than a fit. For parameter estimates see Table 4.1 and for further details on the estimation method, see Appendix A.2.2.

To visualise the impact of parameter variability and uncertainty, we determined the 5th and 95th percentiles of mAb concentrations in plasma and tissues (for detailed information, see section 3.2.4). In addition to the variations assumed for parameters reported in section 3.2.4, in this chapter, we considered variations in FcRn concentration and variations in endogenous IgG concentration. Recently, Fan et al. [132] measured hFcRn tissue expression in transgenic mice with precision and bias of the analytical procedure within 20%. Diverse endogenous IgG concentrations can be found for xenograft mouse models. Endogenous IgG concentration for FcRn

WT mice is reported in [125] with coefficient of variation of 4.5% and variability in serum endogenous IgG concentration in normal human subjects is reported to be within 21.5% CV [133]. As a consequence, the following variations were taken into account: FcRn concentration ($\pm$20%, uniform distribution), endogenous IgG concentration (sampled from a log-normal distribution with CV of 5% for WT mice and 20% for nude and SCID mice).

Based on the estimated parameters, the simulated concentration-time profiles in plasma and tissues agree very well with the experimental data of mAb 7E3 in FcRn WT mice following IVIG therapy, see Figures 4.2 and 4.3. Comparable results (in terms of estimates and objective function values, see Table 4.1) are obtained using the cutoff model and the KD model (K_D=4.8 nM). For FcRn WT mice pretreated with IVIG, the cutoff model results in a good approximation of the detailed binding model.

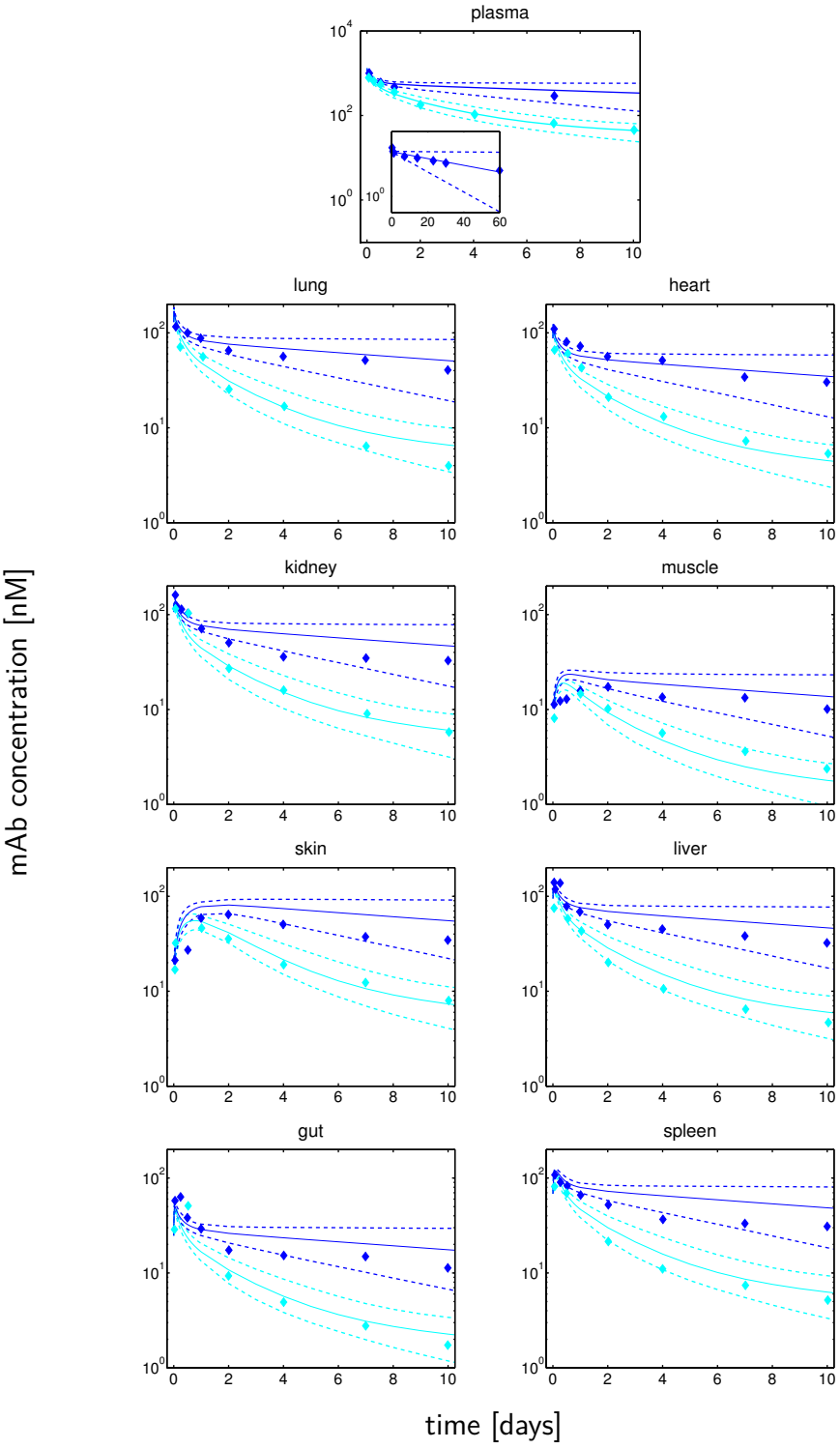

Fig. 4.2.: *Predictions of mAb 7E3 concentration-time profiles* ***(with residual blood contamination)*** *for* ***FcRn WT mice following IVIG therapy (no IVIG (top) and 2 g/kg IVIG (down))*** *based on the PBPK model with equilibrium binding* ($K_D = 4.8\,nM$) *compared to mean experimental data (diamonds) [79].* Experimental tissue data was not used for model fitting and are therefore predictions based on plasma data. Solid lines represent the reference predictions and dashed lines the 5th and 95th percentiles. For plasma, the inset shows the model fit to the experimental data up to 60 days (data only available for plasma and mice without IVIG).

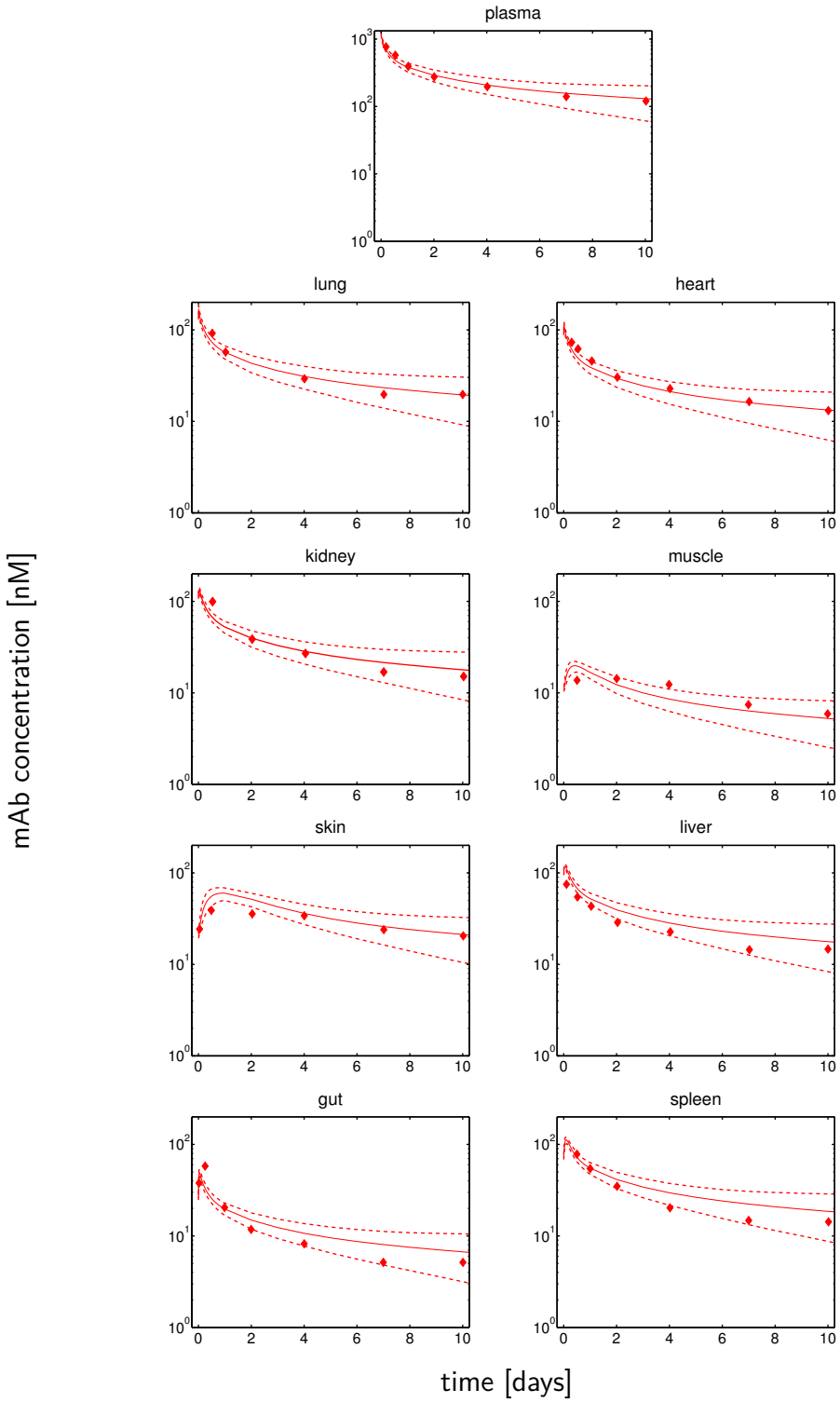

Fig. 4.3.: *Predictions of mAb7E3 concentration-time profiles* ***(with residual blood contamination)*** *for* ***FcRn WT mice following IVIG therapy (0.4 g/kg IVIG)*** *based on the PBPK model with equilibrium binding* ($K_D = 4.8\,nM$) *compared to mean experimental data (diamonds) [79].* Experimental tissue data was not used for model fitting and are therefore predictions based on plasma data. Solid lines represent the reference predictions and dashed lines the 5th and 95th percentiles.

As is shown in Figure 4.4, the simulated mAb plasma clearance changes over time as a result of the changing total IgG concentration. Total IgG concentration is drastically increased due to IVIG therapy resulting in a transient increase of IgG fraction unbound $\mathrm{fu_{IgG}}$ and thus a non-linearity of the unspecific plasma clearance. Once the total IgG concentration is dominated by endogenous IgG, the unspecific plasma clearance becomes linear again (as seen in Figure 4.4 for 0.4 g/kg IVIG (dashed line) and 2 g/kg IVIG (solid line) at approx. 15 days). Figure 4.5 shows the dependence of mAb half-life on changing total IgG concentration based on mAb 7E3 data with 2 g/kg pre-administered IVIG in WT mice. The initial sharp decrease in half-life is due to large therapeutic IgG concentrations (resulting from IVIG therapy).

In summary, the *consensus* PBPK model with explicitly included competition of endogenous and therapeutic IgG for binding to FcRn based on the cutoff model as well as on the equilibrium binding model can be used to study the impact of altered IgG on unspecific mAb clearance.

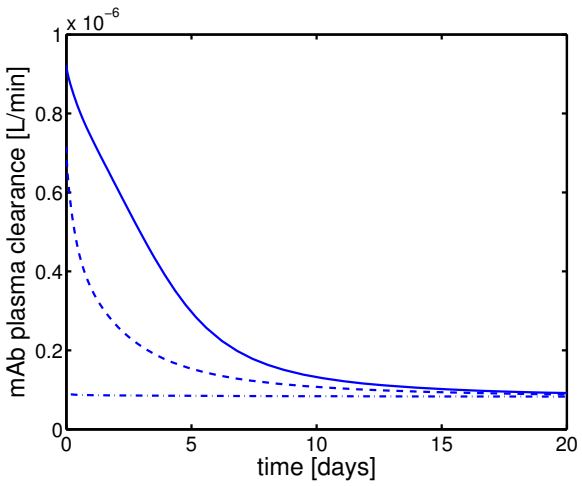

Fig. 4.4.: *Predicted unspecific mAb plasma clearance over time based on simulation of mAb 7E3 plasma PK data with pre-administered IVIG shown in Figures 4.2 and 4.3: no IVIG (dashed-dotted line), 0.4 g/kg IVIG (dashed line) and 2 g/kg IVIG (solid line).*

4.4 Impact of mAb binding affinity to FcRn on unspecific mAb CL

In the previous section, the equilibrium binding model with 1 $\mathrm{K_D}$ was used to study the impact of increased total IgG concentration on unspecific mAb clearance assuming that all IgG species (mAb, IVIG and $\mathrm{IgG_{endo}}$) have the same binding affinity ($\mathrm{K_D}$ =4.8 nM) towards FcRn. There are, however, different values reported for the equilibrium binding constant $\mathrm{K_D}$. Zhou et al. [131] report a value of $\mathrm{mK_D}$ = 750 nM for the interaction of murine IgG1 to mouse FcRn, whereas Popov

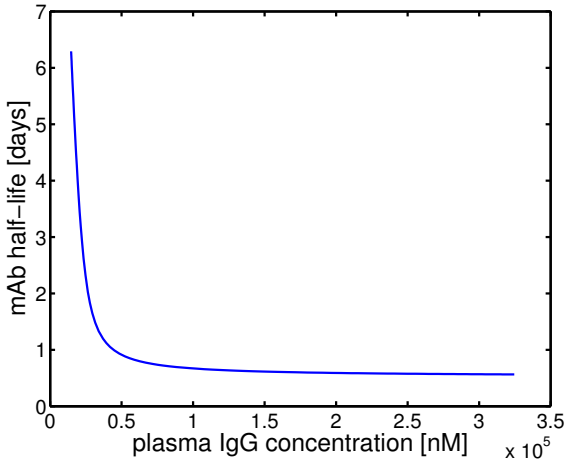

Fig. 4.5.: *Predicted mAb half-life as a function of total plasma IgG concentration based on simulation of mAb 7E3 plasma PK data with pre-administered IVIG (2 g/kg).*

et al. [134] report a value of $\mathrm{mK_D} = 4.8$ nM. In addition, differences in binding affinities between murine IgG and human IgG to mouse FcRn are reported in the literature [131, 135, 136]. Zhou et al. [131] report an almost tenfold difference in binding affinity with higher affinity of human IgG than murine IgG to mouse FcRn ($\mathrm{hK_D}$ = 82 nM vs. $\mathrm{mK_D}$ = 750 nM, respectively). Ober et al. [135, Table 1] report a twofold difference in relative binding between human and murine IgG to mouse FcRn.

To study the impact of antibody binding affinity towards FcRn on unspecific mAb clearance, we examined whether different model scenarios can predict the influence of IVIG therapy on mAb PK. To describe mAb 7E3 venous plasma and tissue data in FcRn WT mice pre-administered with IVIG, we separately fitted the equilibrium binding model with $\mathrm{K_D}$=4.8 nM or $\mathrm{K_D}$=750 nM to the WT mice data. The parameters FcRn and $\mathrm{CLpla_uBW}$ were estimated. In addition, to study the impact of different $\mathrm{K_D}$ values of murine mAb and human IVIG to murine FcRn in FcRn WT mice, we used the PBPK model with an equilibrium binding model incorporating two different $\mathrm{K_D}$ values (see section 4.2.2).

Figure 4.6 compares mAb plasma concentration-time profiles in WT mice, pre-treated with different doses of IVIG, for the different model scenarios: (i) identical values of $\mathrm{K_D}$ (either $\mathrm{K_D}$=4.8 nM or $\mathrm{K_D}$=750 nM); and (ii) a twofold difference in $\mathrm{K_D}$ values of murine IgG and human IgG to murine FcRn ($\mathrm{hK_D}$ = 375 nM vs. $\mathrm{mK_D}$ = 750 nM). Despite the large difference in equilibrium binding affinity, the predictions are almost indistinguishable up to ten days: visually (Figure 4.6), in terms of objective function values (see Table 4.2) and by comparing observed vs. predicted values (see Figure 4.7). There are, however, differences for lower doses and longer observation times. Due to lack of data for longer observation times, we

Tab. 4.2.: FcRn WT mice pre-treated with IVIG: Estimated total FcRn concentration and $\mathrm{CLpla_uBW}$ of murine mAbs; estimated parameters, 95% confidence intervals (CI) and objective function values (Obj) based on the PBPK model with equilibrium binding and different $\mathrm{K_D}$values, see text for details.

model	FcRn[nM] estimate [95% CI]	$\mathrm{CLpla_uBW}$ [L/min/kg] estimate [95% CI]	Obj -
model with 1 $\mathrm{K_D}$			
$\mathrm{hK_D}$=4.8 nM,			
$\mathrm{mK_D}$=4.8 nM	1.34e4	3.29e-5	5.69e-1
	[1.31e4. 1.36e4]	[2.91e-5, 3.67e-5]	
$\mathrm{hK_D}$=750 nM,			
$\mathrm{mK_D}$=750 nM	2.17e4	3.95e-5	1.04e0
	[1.96e4, 2.44e4]	[3.23e-5, 4.94e-5]	
model with 2 $\mathrm{K_D}$			
$\mathrm{hK_D}$=82 nM,			
$\mathrm{mK_D}$=750 nM	1.62e4	1.86e-5	1.78e0
	[1.49e4, 1.78e4]	[1.65e-5, 2.10e-5]	
$\mathrm{hK_D}$=375 nM,			
$\mathrm{mK_D}$=750 nM	1.97e4	2.96e-5	7.22e-1
	[1.82e4, 2.15e4]	[2.58e-5, 3.45e-5]	

are not able to discriminate between the different scenarios. Additional experimental data would be necessary.

Repeating the predictions with an approx. tenfold binding ratio ($\mathrm{hK_D}$ = 82 nM vs. $\mathrm{mK_D}$ = 750 nM, respectively) cannot describe the data quantitatively as accurately as the twofold difference (Figure 4.8 vs. Figure 4.6). The model with an approx. tenfold binding ratio, however, qualitatively predicts the influence of human IgG (i.e., IVIG) on murine mAb clearance and murine endogenous IgG concentrations very well. Following a higher binding affinity of IVIG to mouse FcRn, IVIG is more protected from elimination than murine mAb resulting in a lower IVIG clearance. After a significant decrease in endogenous IgG concentration, it takes time for endogenous IgG to return to baseline plasma concentration. This can be explained with the almost tenfold lower binding affinity of murine IgG to mouse FcRn resulting in a less protection by FcRn and a higher degradation within endo-lysosomes (see Figures 4.9 for kinetics of endogenous IgG and IVIG predicted by the model with twofold difference in $\mathrm{K_D}$).

Under the present data situation, following the principle of parsimony, we recommend to use the equilibrium binding model with identical $\mathrm{K_D}$ values (see section 4.2.1) instead of the equilibrium binding model with different $\mathrm{K_D}$ values to study the impact of increased total IgG concentration on mAb clearance.

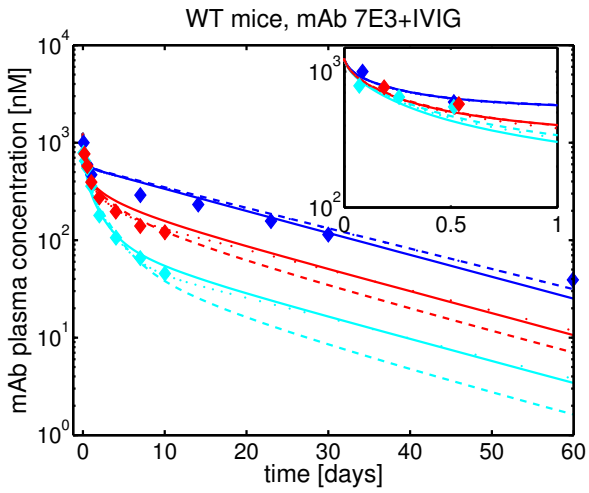

Fig. 4.6.: *Comparison of the model fit to experimental IVIG data [79] based on the PBPK model with different models to determine* $\mathrm{fu_{IgG}}$. Model fits are based on (i) identical values of $\mathrm{K_D}$ =750 nM (solid lines); (ii) identical values of $\mathrm{K_D}$ =4.8 nM (dotted lines) and (iii) $\mathrm{hK_D}$ = 375 nM vs. $\mathrm{mK_D}$ = 750 nM (dashed lines). The different colours represent mAb 7E3 data with pre-administered IVIG (from top to down): no IVIG (blue), 0.4 g/kg IVIG (red) and 2 g/kg IVIG (cyan).

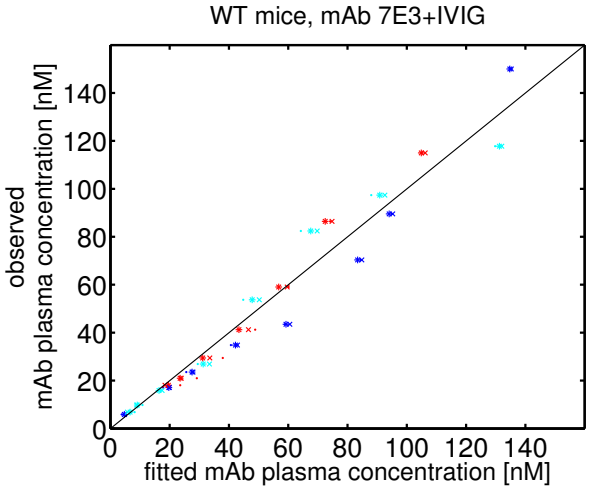

Fig. 4.7.: *Fitted vs. observed mAb plasma concentration based on the PBPK model with different models to determine* $\mathrm{fu_{IgG}}$. Model fits are based on (i) identical values of $\mathrm{K_D}$ =750 nM (circles); (ii) identical values of $\mathrm{K_D}$ =4.8 nM (asterisks) and (iii) $\mathrm{hK_D}$ = 375 nM vs. $\mathrm{mK_D}$ = 750 nM (crosses). The different colours represent mAb 7E3 data with pre-administered IVIG: no IVIG (blue), 0.4 g/kg IVIG (red) and 2 g/kg IVIG (cyan).

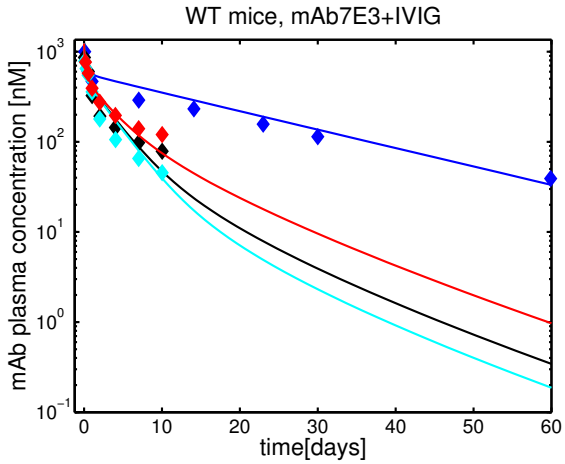

Fig. 4.8.: *mAb plasma concentration-time profiles predicted by the PBPK model with equilibrium binding with* ***approx. tenfold difference in*** K_D ***values*** *(solid lines) compared to experimental data in WT mice after i.v. bolus administration of 8 mg/kg 7E3 following different doses of IVIG [79] (from top to down): no IVIG (blue), 0.4 g/kg IVIG (red), 1 g/kg IVIG (black) and 2 g/kg IVIG (cyan).*

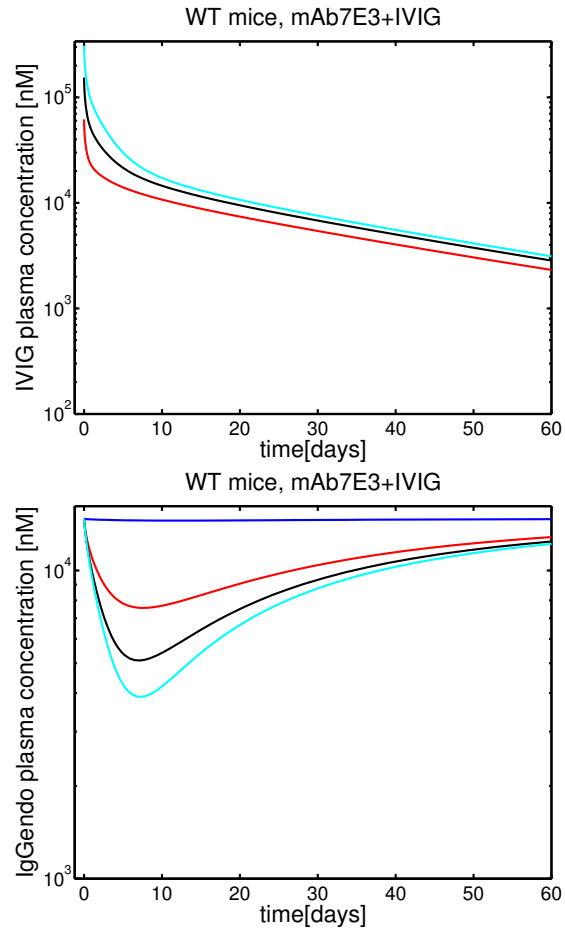

Fig. 4.9.: *Simulated IVIG plasma and endogenous IgG plasma concentration-time profiles.* Simulations are based on the PBPK model with equilibrium binding with **twofold difference in** K_D **values** and refer to WT mice after i.v. bolus administration of 8 mg/kg 7E3 following different doses of IVIG: no IVIG (blue), 0.4 g/kg IVIG (red), 1 g/kg IVIG (black) and 2 g/kg IVIG (cyan).

4.5 Prediction of mAb PK data for immunodeficient mice with low endogenous IgG

As shown in section 4.3, the *consensus* PBPK model with explicitly included competition of endogenous and therapeutic IgG for binding to FcRn can describe the impact of altered IgG concentrations due to IVIG therapy on mAb clearance. Thus it can be used to analyse the impact of altered IgG due to lower endogenous IgG in immunodeficient mice. In nude and SCID mice, the production of endogenous IgG is impaired. In nude mice, the impairment is due to non-functional T lymphocytes, while in SCID mice, impairment is due to non-functional T and B lymphocytes. To describe the mAb PK data of nude and SCID mice, we used the *consensus* PBPK model to estimate FcRn and $\mathrm{CLpla_u BW}$ (separately for nude and SCID mice). In both cases, we used the equilibrium FcRn binding model (section 4.3) with $\mathrm{K_D} = 4.8\,\mathrm{nM}$ for therapeutic and endogenous IgG as well as the cutoff model (section 4.5). The equilibrium FcRn binding model with different $\mathrm{K_D}$ values (section 4.4) is not used, since only IgG species of murine origin binding to murine FcRn are present in the experimental data of immunodeficient mice. In the following subsections, the results based on the equilibrium FcRn binding model and the cutoff model are presented.

4.5.1 Insight into parameter estimation and identifiability when using the equilibrium binding model

When using the equilibrium binding model with 1 KD (section 4.3), parameter estimation of FcRn and $\mathrm{CLpla_u BW}$ for nude and SCID mice, in contrast to IVIG data in FcRn WT mice, suffered from identifiability issues. For nude mice, no constraints of the parameter value for FcRn and only a lower constraint of the parameter $\mathrm{CLpla_u BW}$ could be obtained by log-likelihood profiling. For SCID mice, only lower constraints of the parameter values for FcRn and $\mathrm{CLpla_u BW}$ could be obtained by log-likelihood profiling. For details on log-likelihood profiling, see Appendix section A.2.2.

To resolve the identifiability problem, we considered the following two scenarios:

i) fixing the FcRn concentration to the FcRn concentration in WT mice (as given in Table 4.1 for the model with $\mathrm{K_D} = 4.8$ nM), resulting in total FcRn concentrations in nude and SCID mice that are much larger than their corresponding endogenous IgG;

ii) assuming a total FcRn concentration in nude and SCID mice much lower than the corresponding endogenous IgG concentration (e.g., two orders of magnitude below the corresponding $\mathrm{IgG_{endo}}$ concentration).

As a consequence, the remaining unknown parameter $\mathrm{CLpla_u BW}$ could be identified. For estimation, only plasma data were used. Thus, for tissue data, the model simulations are a prediction rather than a fit. See Table 4.3 for estimated parameter values.

Tab. 4.3.: Immunocompromised mice: Total FcRn concentration and estimated $\mathrm{CLpla_u BW}$ of murine mAbs; estimated $\mathrm{CLpla_u BW}$, 95% confidence intervals (CI) and objective function values (Obj) based on the PBPK model with equilibrium binding ($\mathrm{K_D}$=4.8 nM), see text for details.

	FcRn[nM] fixed	$\mathrm{CLpla_u BW}$ [L/min/kg] [a] estimate [95% CI]	Obj
nude mice	1.34e4	1.77e-2 [1.01e-2, 2.55e-2]	1.49e-1
	3.30e0	6.56e-6 [3.73e-6, 9.46e-6]	1.49e-1
SCID mice	1.34e4	2.48e-2 [2.14e-2, 2.82e-2]	2.98e0
	6.60e-3	9.14e-6 [7.86e-6, 10.47e-6]	3.17e0

[a] estimation with dose factor (see Appendix section A.2.2 for details)

In both scenarios, the resulting total plasma clearance $\mathrm{CLpla} = \mathrm{CLpla_u} \cdot \mathrm{fu_{IgG}}$, however, was practically identical and the model predictions based on parameter estimates for the two scenarios (Table 4.3) were indistinguishable. For nude mice, Figure 4.10 shows the experimental data in comparison to the simulated concentration-time profiles in plasma and tissues, respectively. The model captures the overall trend of the concentration-time profiles in the different tissues very well, with a few exceptions (kidney, gut, spleen). For example, the model predicts larger concentrations in gut compared to the experimental data in Figure 4.10. For SCID mice, the results are shown in Figure 4.11. In WT mice (Figure 4.2 and Figure 4.3) and SCID mice, the concentration-time profiles in kidney, gut and spleen are well predicted. At present, we do not know whether the difference in nude mice is due to additional processes not accounted for in the model or, e.g., due to errors in handling/reporting the experimental data. This highlights the importance of model predictions (generating expectations) when analysing experimental data.

It is worth noticing that the identifiability problems are a result of the available experimental data. It would be possible to discriminate between the two scenarios by performing in immunodeficient mice the same 'IVIG experiment' as in FcRn WT mice, i.e., administration of mAb dose of 8 mg/kg and different IVIG doses: no IVIG, 1 g/kg and 2 g/kg. In Figure 4.12, the predictions for a mAb dose of 8 mg/kg and IVIG doses of 0, 1, 2 g/kg are shown for the two above mentioned scenarios in nude mice. In scenario (i) i.e. high FcRn, the three mAb concentration-time profiles would be clearly distinguishable, while in scenario (ii), the three mAb concentration-time profiles would be superimposed. The same applies to SCID mice.

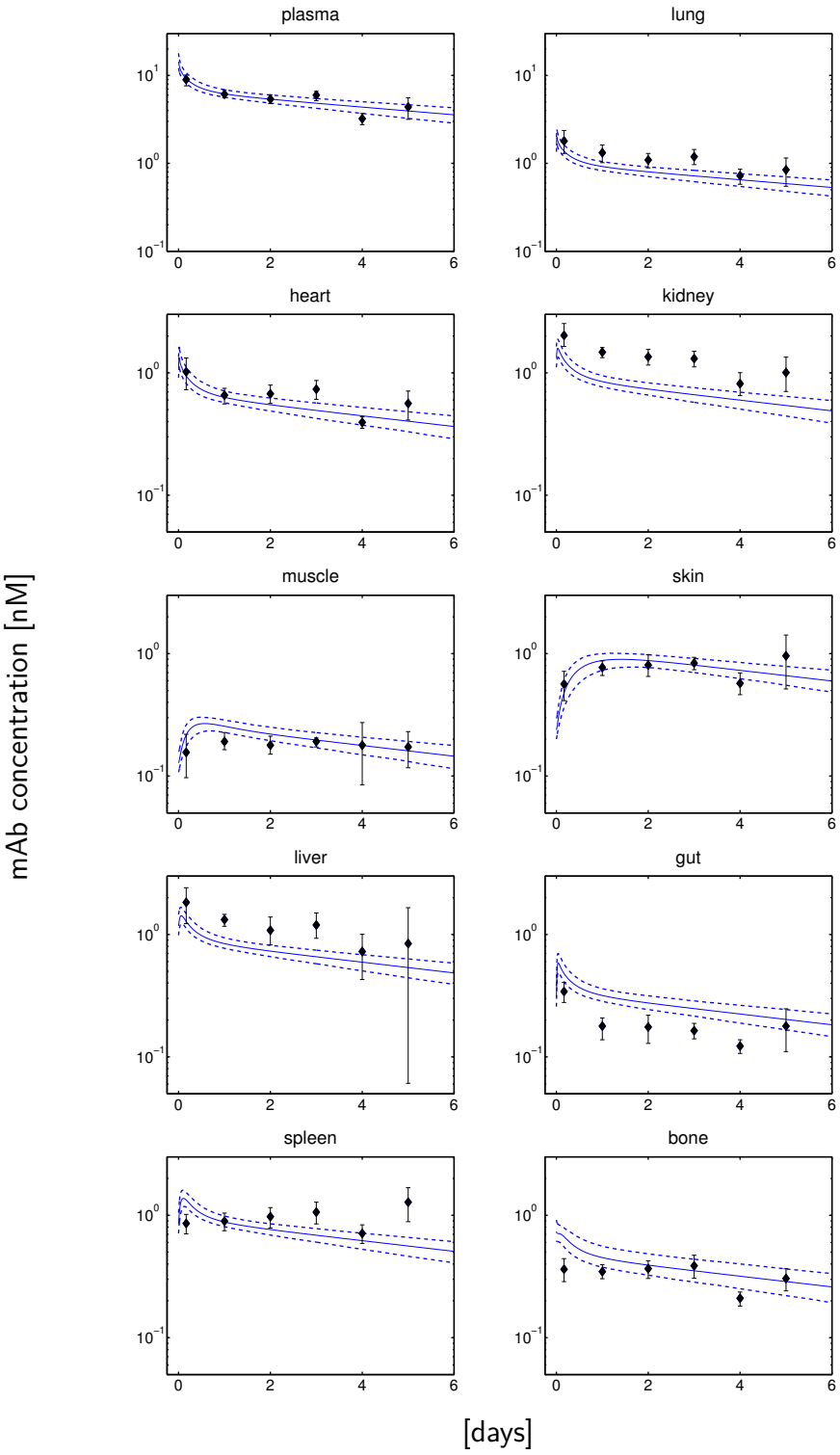

Fig. 4.10.: *Predictions of concentration-time profiles for* ***nude mice with residual blood*** *(i.v. bolus administration of 0.0038 mg MOPC21 (dose factor 0.54) based on the PBPK model with equilibrium binding* ($K_D = 4.8\,nM$) *compared to experimental data of six mice (diamonds, error bars).* Predictions are indistinguishable for parameter estimates based on the two scenarios in Table 4.3. Experimental tissue data was not used for model fitting and are therefore predictions based on plasma data. Solid lines represent the reference predictions and dashed lines the 5th and 95th percentiles.

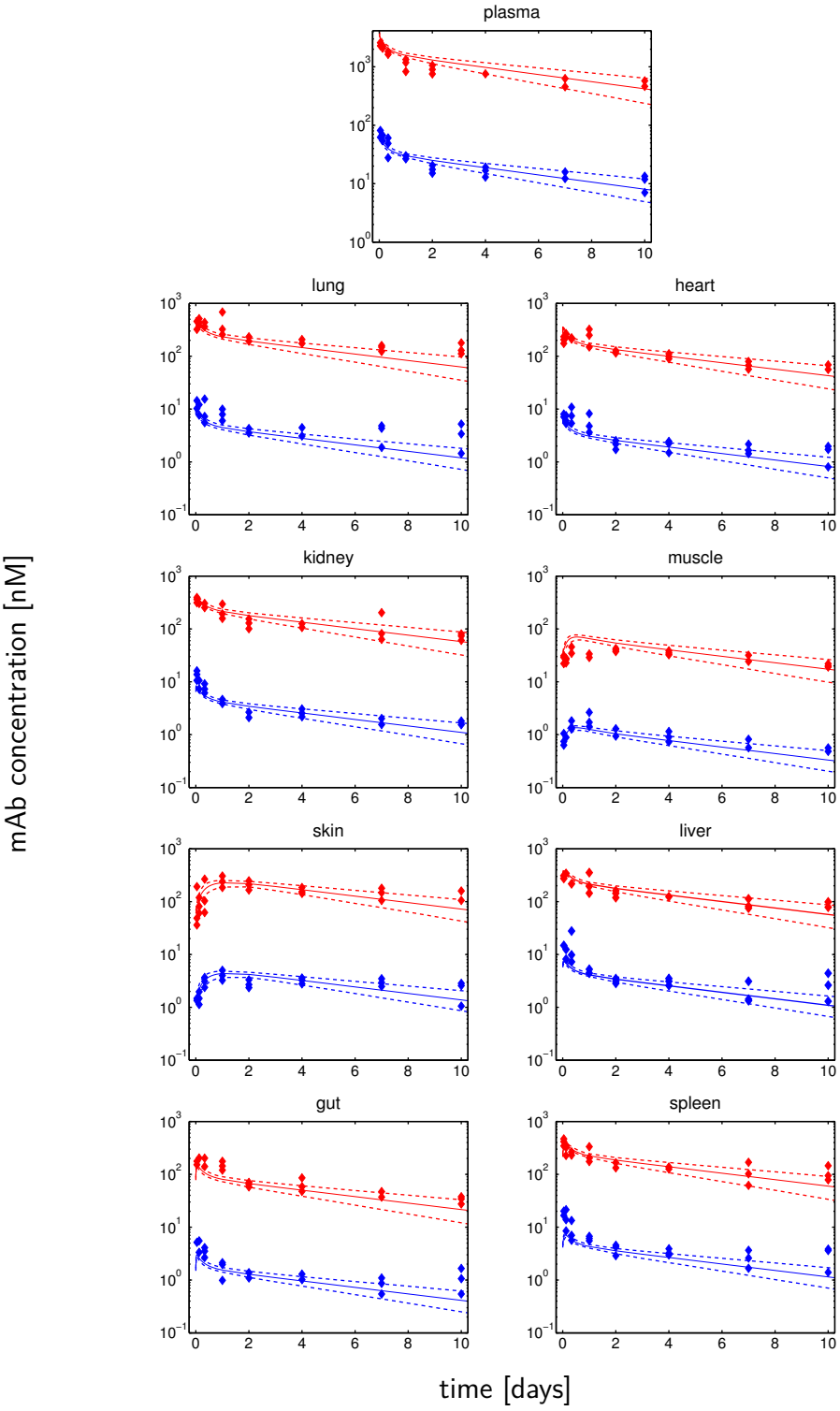

Fig. 4.11.: *Predictions of concentration-time profiles for **SCID mice with residual blood** (i.v. bolus administration of mAb 8C2 following two doses: 1 mg/kg (dose factor 0.48, blue) and 25 mg/kg (dose factor 1, red) based on the PBPK model with equilibrium binding* ($K_D = 4.8\,nM$) *compared to experimental data of three mice (diamonds).* Predictions are indistinguishable for parameter estimates based on the two scenarios in Table 4.3. Experimental tissue data was not used for model fitting and are therefore predictions based on plasma data. Solid lines represent the reference predictions and dashed lines the 5th and 95th percentiles.

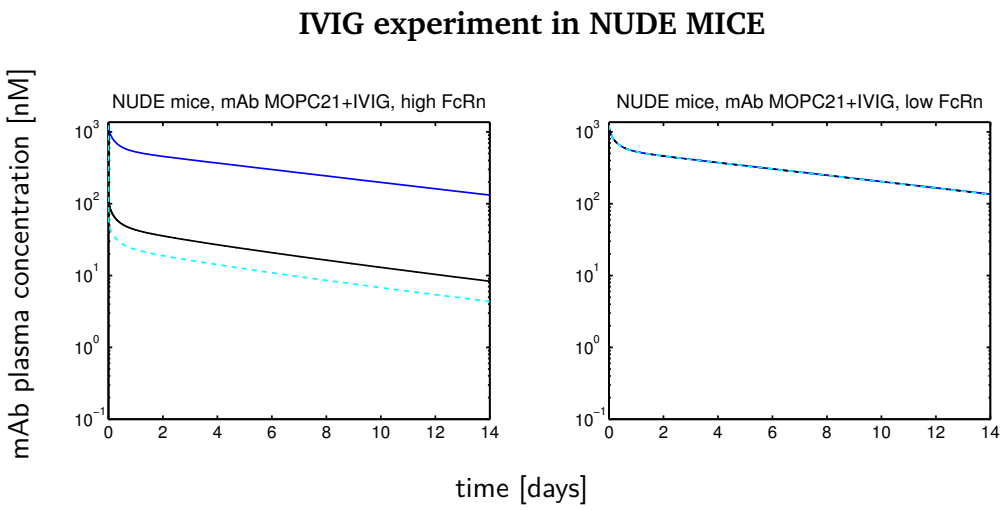

Fig. 4.12.: *Predictions of mAb plasma PK based on the PBPK model with equilibrium binding (K_D=4.8 nM) for mAb dose of 8 mg/kg and different IVIG doses: no IVIG (blue), 1 g/kg (black), 2 g/kg (cyan) in nude mice.* Simulations based on FcRn concentrations identical to WT mice (left) and based on much lower FcRn concentrations than in WT mice (and lower than the corresponding endogenous IgG concentrations, right). For estimates see Table 4.3.

4.5.2 Biased parameter estimation using the cutoff model

As both, the equilibrium binding model and the cutoff model result in almost identical unbound fractions fu_{IgG} of IgG on the entire range of IgG concentrations (see Figure 4.1), the cutoff model seems to be a good approximation of the detailed binding model. When studying mAb PK data in WT mice following IVIG therapy, parameter estimates using the cutoff model were comparable to parameter estimates using the equilibrium binding model (Table 4.1). We identified, however, important limitations of the cutoff model for total IgG concentrations being smaller than FcRn concentrations, which are of relevance for the modelling community.

The cutoff model predicts a zero unbound fraction for total IgG being smaller than total FcRn. As a consequence, the cutoff model does not allow to represent the scenario in immunodeficient mice, where FcRn concentrations are comparable to WT mice (scenario (i) in section 4.5.1), while at the same time FcRn is much larger than endogenous IgG. Using the cutoff model for estimation of total FcRn concentration and $CLpla_uBW$, we only estimated FcRn concentrations in immunodeficient mice that are lower than in WT mice. In summary, using the cutoff model, the estimation of total FcRn is biased to small values (compared to endogenous IgG) in immunodeficient mice.

4.5.3 Apparent linear CL in immunodeficient mice

Using the equilibrium binding model, different scenarios on FcRn and $\mathrm{CLpla_u}$ can be estimated for immunodeficient mice and the resulting total plasma clearance $\mathrm{CLpla} = \mathrm{CLpla_u} \cdot \mathrm{fu_{IgG}}$, was practically identical (see Table 4.3). To resolve the identifiability problems, the *consensus* PBPK model with constant linear plasma clearance (Eqs. (4.4)+(4.5), where $\mathrm{CL_{tot}} = \mathrm{CLpla}$) was used to estimate the constant plasma clearance per body weight based on nude and SCID mice data (separately). For completion, the *consensus* PBPK model with linear total plasma clearance was used to estimate $\mathrm{CLpla_{BW}}$ based on mAb 7E3 PK data in FcRn WT mice without IVIG therapy. Table 4.4 lists the estimated $\mathrm{CLpla_{BW}}$ of FcRn WT, nude and SCID mice.

For nude and SCID mice, the model predictions resulting from total constant plasma clearance were indistinguishable (visually and in terms of objective function values Table 4.3 vs. Table 4.4) from model predictions based on the two scenarios of the equilibrium binding model. Thus, under given doses, there is an apparent linear clearance in immunodeficient mice. We note that the total plasma clearance per body weight in the two immunodeficient mouse strains is larger than in WT mice.

Tab. 4.4.: Mice: Estimated linear total $\mathrm{CLpla_{BW}}$ of murine mAbs in different mice strains; estimated $\mathrm{CLpla_{BW}}$, 95% confidence intervals (CI) and objective function values (Obj) based on the *consensus* PBPK model with constant CLpla, see text for details.

	$\mathrm{CLpla_{BW}}$ [L/min/kg] estimate [95% CI]	Obj -
WT mice [a]	3.13e-6 [2.73e-6, 3.51e-6]	3.22e-1
nude mice	6.56e-6 [3.69e-6, 9.37e-6]	1.49e-1 [b]
SCID mice	9.14e-6 [7.85e-6, 10.5e-6]	3.17e0 [b]

[a] without IVIG therapy
[b] estimation with dose factor (see Appendix section A.2.2 for details)

4.6 Summary: Unspecific mAb CL as a function of endogenous IgG

In the previous sections, we analysed the impact of mAb PK based on increased total IgG in immunocompetent FcRn-WT mice pre-treated with IVIG as well as reduced endogenous IgG in immunodeficient mice. Due to the impaired immune system, typical therapeutic IgG doses may result in therapeutic IgG concentrations larger than endogenous IgG concentrations. In FcRn WT mice, such a situation resulting from IVIG doses leads to non-linear plasma clearance (see section 4.3). In SCID mice, however, we observed a linear clearance, despite the fact that therapeutic IgG concentrations (i.e., mAb concentrations) were larger than endogenous IgG concentrations. In the present section, the obtained results are summarised and a general answer to the question 'When to expect linear unspecific clearance in immunodeficient mice?' is provided.

Analysing more closely the dependence of $\mathrm{fu}_{\mathrm{IgG}}$ on total IgG, we found that the unbound fraction $\mathrm{fu}_{\mathrm{IgG}}$ is approximately constant in the following two scenarios:

i) if total IgG is below total FcRn, i.e.,

$$\mathrm{mAb} + \mathrm{IgG}_{\mathrm{endo}} = \mathrm{IgG}_{\mathrm{tot}} \ll \mathrm{FcRn}.$$

Note that only the total IgG concentration is relevant and that it is not important, whether the mAb concentration is below or above the endogenous IgG concentration.

ii) as long as total IgG is much above total FcRn, i.e.,

$$\mathrm{mAb} + \mathrm{IgG}_{\mathrm{endo}} = \mathrm{IgG}_{\mathrm{tot}} \gg \mathrm{FcRn},$$

such that the unbound fraction $\mathrm{fu}_{\mathrm{IgG}}$ is practically 1. Note that total IgG concentration may change over time. Whether or not the clearance stays linear depends on the endogenous IgG concentrations. If already endogenous IgG concentration alone results in an unbound fraction of approx. 1, then the clearance will be linear for all times, independent of the mAb concentration. If $\mathrm{IgG}_{\mathrm{endo}}$ alone results in some unbound fraction smaller than 1, then the clearance will only be linear as long as mAb concentrations and therefore total IgG concentrations are still large enough to result in an unbound fraction of 1.

Note that in FcRn WT mice (without IVIG therapy), due to larger endogenous IgG concentrations, there is a third scenario resulting in a linear clearance:

iii) $\mathrm{mAb} \ll \mathrm{IgG}_{\mathrm{endo}}$, independent of their relation to FcRn. In this scenario, the total IgG concentration stays constant, since it is practically identical to the endogenous IgG. As a result, the unbound fraction $\mathrm{fu}_{\mathrm{IgG}}$ is constant and total plasma clearance is linear.

Note that in all three above scenarios with linear clearance, we do not need to take into account the competition of endogenous and therapeutic IgG for binding to FcRn, and thus, we do not need to explicitly model endogenous IgG. To illustrate this, we used the *consensus* PBPK model with constant CLpla to model the data from nude and SCID mice (see section 4.5.2). Note that due to a constant fraction unbound $\mathrm{fu_{IgG}}$, linear total plasma clearance for nude and SCID mice can be calculated as the product of fraction unbound and corresponding unbound plasma clearance. For nude and SCID mice, the model predictions resulting from total constant CLpla were indistinguishable (visually and in terms of objective function values Table 4.3 vs. Table 4.4) from model predictions based on the PBPK model with explicitly modelled competition of endogenous and therapeutic IgG for binding to FcRn.

The dependence of $\mathrm{fu_{IgG}}$ on total IgG for the above scenarios is illustrated in Figure 4.13 showing the IgG fraction unbound $\mathrm{fu_{IgG}}$ as a function of total IgG concentration normalised by FcRn. The sharp increase of $\mathrm{fu_{IgG}}$ (Figure 4.13, 'right branch' of the curve) resulting in non-linearity of CLpla occurs when total IgG is approximately equal to total FcRn and results from large total IgG due to IVIG treatment. Without IVIG therapy, total IgG is dominated by endogenous IgG concentration in WT mice (i.e., 1.47e4 nM) resulting in constant CLpla (approx. constant $\mathrm{fu_{IgG}}$). This situation corresponds to the above scenario (iii) where $\mathrm{mAb} \ll \mathrm{IgG_{endo}}$. From the experimental data of immunodeficient mice, we inferred that endogenous IgG is slightly lower than FcRn (assuming comparable FcRn concentration for WT and immunodeficient mice), so that we are on the 'lower' left branch of the curve. For nude mice, the given mAb dose results in mAb concentrations lower than endogenous IgG and thus the maximal value of total IgG is dominated by endogenous IgG in nude mice (i.e., 3.3e2 nM) leading to constant CLpla. For SCID mice, mAb dose 25 mg/kg results in mAb concentrations larger than endogenous IgG and thus mAb concentrations dominate total IgG. However, despite mAb concentrations larger than endogenous IgG, the CLpla stays constant (approx. constant $\mathrm{fu_{IgG}}$ on the 'lower left branch' of the curve). This situation corresponds to the above scenario (i) where $\mathrm{IgG_{tot}} \ll \mathrm{FcRn}$.

In summary, via the above stated scenarios (illustrated based on the available experimental data in Figure 4.13), we can give a general answer to the question 'When to expect linear unspecific clearance in immunodeficient mice?'.

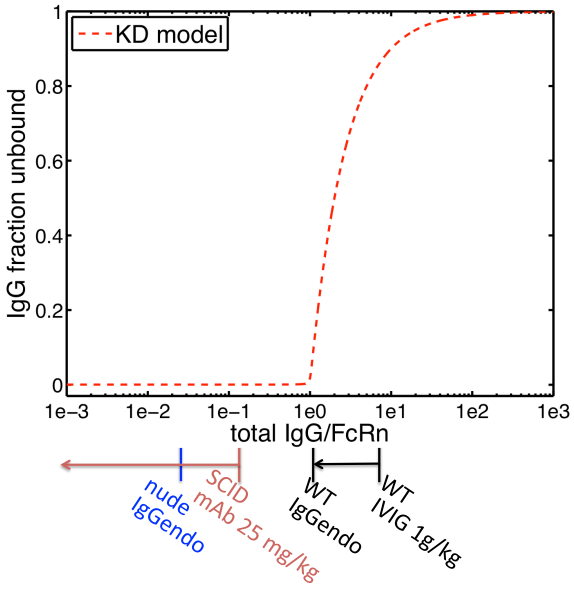

Fig. 4.13.: *IgG fraction unbound* $\mathrm{fu_{IgG}}$ *as a function of total IgG concentration (i.e., endogenous and therapeutic IgG) assuming comparable FcRn concentrations for FcRn WT mice, nude mice and SCID mice.* $\mathrm{fu_{IgG}}$ is predicted by the equilibrium binding model for FcRn=1.34e4 nM and $\mathrm{K_D}$=4.8 nM. The coloured arrows below the abscissa represent the constant total IgG value (e.g., 1.47e4 nM for WT mice and 3.3e2 nM for nude mice) or range of changing total IgG concentration for FcRn WT mice and SCID mice based on the experimental data assuming comparable FcRn concentrations.

4.7 Discussion

As is well known, target-independent (unspecific) therapeutic antibody clearance processes are important as they dominate the elimination process for high mAb doses that saturate the target. Immunocompromised mouse models are most widely used to study the efficacy of mAbs. We elucidated the impact of a compromised immune system with lower endogenous IgG concentrations competing for FcRn binding on unspecific mAb clearance. We showed that unspecific clearance often appears to be linear and exemplified situations when to expect the unspecific clearance to be non-linear. Unspecific clearance is linear, whenever mAb concentrations are lower than endogenous IgG: this holds true for many situations in healthy volunteers [137] and patients (see explanation in [7]). Unspecific clearance is also linear whenever total IgG is lower than total FcRn: a situation, which might be relevant in immunocompromised mice and special patient populations, e.g., immunocompromised cancer patients. On the other hand, unspecific clearance is non-linear whenever therapeutic IgG is larger than endogenous IgG as well as larger than total FcRn: a situation typically relevant in IVIG therapy.

Plasma and tissue data of mAb 7E3 following IVIG therapy in WT mice were used to study the impact of increased total IgG (i.e., therapeutic and endogenous IgG) on unspecific mAb clearance. The data can be described very well using the *consensus* PBPK model with equilibrium binding and equal binding affinities ($\mathrm{hK_D}$=4.8 nM, $\mathrm{mK_D}$=4.8 nM) of murine and human IgG to mouse FcRn. There are, however, different values reported in the literature for the equilibrium binding constant $\mathrm{mK_D}$ describing the binding affinity of murine IgG to mouse FcRn [131, 134, 138]. Suzuki et al. [139] report the $\mathrm{K_D}$ values of eight approved therapeutic mAbs to human FcRn ranging between 508 and 1257 nM. Gurbaxani et al. [136] examined studies that use a diverse set of methods in different model organisms. $\mathrm{K_D}$ values derived from surface plasmon resonance experiments using immobilised FcRn yield a higher avidity for IgG than the experiment, where IgG is immobilised on the chip surface [135]. Additionally the binding affinity $\mathrm{K_D}$ can be influenced by the antibody net charge and differences in mAb structure, e.g., in complementary determining regions [136, 140]. Abdiche et al. [138] confirmed that the inconsistent set of affinity constants for FcRn-IgG interaction in the literature can be attributed to experimental artefacts, in particular immobilisation artefacts. They observed, however, that FcRn-IgG interactions are independent of the IgG's variable region and they did not find a trend between an IgG's isoelectric point and its affinity to FcRn. A large difference in equilibrium binding affinity $\mathrm{K_D}$, however, results in minimal difference in PK if we compare our resulting objective function values between the equilibrium binding model ($\mathrm{hK_D}$=750 nM, $\mathrm{mK_D}$=750 nM) [131] and ($\mathrm{hK_D}$=4.8 nM, $\mathrm{mK_D}$=4.8 nM) [134] (see Table 4.2 and Figure 4.6). This is in line with Garg/Balthasar [66].

To study the impact of different $\mathrm{K_D}$ values of murine mAb and human IVIG to murine FcRn, we used the *consensus* PBPK model with equilibrium binding incorporating two different $\mathrm{K_D}$ values. Literature, however, is not unique on the magnitude of difference in binding affinity of different IgG species to FcRn. Zhou et al. [131] measure an almost tenfold higher binding affinity of human IgG1 to mouse FcRn than murine IgG1, whereas analyses by Ober et al. [135] yield only a twofold binding ratio. Abdiche et al. [138] confirmed an almost tenfold difference in equilibrium dissociation constant between the mFcRn-hIgG1 interaction and the mFcRn-mIgG1 interaction at pH 5.8 and 37°C. The mAb 7E3 data in FcRn WT mice pre-treated with IVIG, however, can be described very well using the model with a twofold difference in $\mathrm{K_D}$ (see Figure 4.6). The model with almost tenfold higher binding affinity does not describe the data quantitatively well (see Figure 4.8). Additional experimental data would be necessary to analyse the magnitude of difference in binding affinity of different IgG species to FcRn.

So far, we assume equilibrium binding with $\mathrm{K_D} = (\mathrm{k_{off}}/\ \mathrm{k_{on}})$ to model FcRn-IgG interaction (for relaxation of this assumption, see Appendix section A.2.4). The authors in [69] analysed whether mAb-FcRn binding reaches equilibrium prior to

endosomal sorting due to, e.g., rapid rates of endosomal transit and a non-instantaneous process of endosomal acidification. They propose a non-equlilibrium binding model as a more logical explanation for the lack of a clear relationship between binding affinity at pH 6 and the observed half-life of IgG antibodies. While Gurbaxani et al. [136] comments that the dissociation rate constant may be more important, Chen and Balthasar [69] conclude that the association rate is more relevant. It remains questionable, however, whether parameters such as IgG uptake rate into the endosome may be identifiable considering the lack of endosomal data.

In our analysis based on the equilibrium binding model, we compared two possible scenarios regarding the FcRn concentrations in immunodeficient mice: FcRn concentrations in immunodeficient mice are (i) lower than in FcRn WT mice; or (ii) comparable or larger than FcRn concentrations in WT mice. Possible explanations for lower FcRn concentrations in nude and SCID mice are that among other cells, FcRn is expressed in several types of professional antigen-presenting cells [141]. As B lymphocytes are also involved in presenting antigens, non-functional or absent B cells in immunodeficient mice might result in low expression of FcRn. In addition, the authors in [142] show low or undetectable FcRn concentrations in a majority of tumour cells combined with hypoalbuminemia in tumour-bearing mice. This underlines the observation that cancer patients are frequently hypoalbuminemic. The latter observation could have various reasons, e.g., TNF-alpha decreased albumin production or a high consumption of albumin in tumours with low FcRn concentrations [142]. Lower FcRn concentrations in immunodeficient mice compared to WT mice, resulted in fraction unbound $\mathrm{fu}_{\mathrm{IgG}}=1$ for immunodeficient mice due to saturation of FcRn. This is in agreement with higher total plasma clearance in the two immunodeficient mouse strains than in WT mice (see Table 4.4). To easily distinguish between the two scenarios (FcRn concentrations in immunodeficient mice (i) lower than in FcRn WT mice; or (ii) comparable or larger than FcRn concentrations in WT mice), we proposed a minimal PK study based on mAb plasma concentrations following IVIG therapy (see section 4.5.1), where it is not necessary to measure FcRn concentration in different tissues and sacrifice the animal species. Very recent findings by Latvala et al. [43] experimentally assessed qualitatively the FcRn distribution across a variety of tissues and species. The authors support our second scenario with comparable FcRn concentrations between immunodeficient and WT mice by investigating that lack of IgG in SCID mice had no negative effect on FcRn expression compared with WT mice.

The experimental data of nude mice were from a study using the residualising radioisotope Indium-111. While the marker has some influence on measured tissue concentrations, plasma concentrations are unaffected with similar blood clearance for indium- and iodine- labeled mAbs as observed in [143]. As we only estimate parameters affecting plasma concentrations, plasma clearance is not biased by the

labelling method. The mAb tissue distribution studies used in [6] to estimate and validate the antibody biodistribution coefficients employed different residualising as well as non-residualising markers. Regarding differences between labels, Shah and Betts [6] did not observe any visible trend, where residualising isotopes showed significant (within 2-fold) digression from ABC predicated tissue vs. plasma concentration profiles. This suggests that either the effect of residualising isotopes was not significant enough to be captured as a systematic deviation from the typical tissue vs. plasma concentration profiles, or the effect of residualising isotopes may be more prominent on molecules with shorter half-life than on intact mAbs with relatively longer half-lives [6]. Since in the *consensus* PBPK model, the organ-specific interstitial partition coefficient K_{int} are defined in terms of ABC values, the same applies to K_{int}.

FcRn in endosome may be accessible from vascular and interstitial space, as it is modelled, e.g., in [66]. Our predictions for mAb PK data in FcRn WT mice, nude and SCID mice based on plasma as a surrogate for endosomal concentration are indistinguishable from predictions based on the interstitial concentration as a surrogate for endosomal concentration in two groups of tissues (see Appendix section A.2.3). Following the principle of parsimony, we recommend to use plasma as the surrogate concentration. This is in line with [67], where uptake is modelled from the vascular space.

In summary, we provided a clearer understanding of the physiological processes to be explicitly considered in mAb PBPK models. The gained knowledge on the unspecific mAb clearance can also be included as a prior in the analysis of mAb data exhibiting target-mediated drug disposition, thus allowing for a more precise estimation of the target-related parameters.

5 Cell-level-based tumour PBPK model for mAbs

"Antibody drugs are widely used in cancer therapy, but conditions to maximize tumor penetration and efficacy have yet to be fully elucidated." [31, p. 1] Although being from 2011, insufficient antibody penetration in solid tumour tissues is still discussed in the context of limiting the success of anti-cancer therapies [1, 144–146].

There are various factors that make effective antibody tumour penetration difficult. As an example, mAbs have to overcome the increased interstitial fluid pressure gradients within solid tumours [18]. Moreover, heterogeneous antibody distribution within tumour tissue [18, 31, 147] is often attributed to a phenomenon called 'binding site barrier' (BSB) where "bindable mAb will be retarded in its transport throughout tumour interstitial space due to its successful binding to antigen on the tumour cell surface near entry points" [147, p. 1191]. The term 'binding site barrier' was coined by Weinstein and Fujimori [147, 148] in a study where they modelled the microdistribution of mAbs within solid tumours and compared the distribution within tumours for mAbs with different affinities. They observed that the average antibody tumour concentration does not increase linearly with affinity. Later, the BSB was confirmed *in vivo* in tumour-bearing xenograft mice by, e.g., Rudnick et al. in 2011 [31] and Glatt et al. in 2016 [149]. Thurber et al. [1] defined the BSB as a moving front rather than a physical barrier that depends on multiple factors such as antibody dose, target density and antibody internalisation rate constant.

One of the most straightforward approaches to overcome the 'binding site barrier' and to saturate tumours is to increase the antibody dose [1]. Many mAbs targeting solid tumours are administered in short intervals to human patients at relatively high doses (2-15 mg/kg, often weekly) [19, 150, 151] resulting in tumour saturation. Insufficient heterogeneous distribution of antibodies within solid tumour tissue, however, is still a current topic of debate, in particular for ADCs due to the dose-limiting toxicity of their toxic payload [19, 152]. Currently (late 2017), there are four FDA approved ADCs, yet, major challenges in achieving consistently high clinical success rates exist [20]. It is claimed in current literature [19, 20] that ADC distribution is a major factor contributing to the overall ADC efficacy and that a better understanding of the relationship of ADC penetration and therapeutic efficacy is needed to improve the clinical response rates of ADCs [20].

The objective of the present chapter was to develop a mechanistic modelling framework to comprehensively investigate antibody distribution within solid tumour tissue and its impact on therapeutic efficacy in antibody cancer therapy. Note that the parameter values of the developed model were taken from literature (i.e., not fitted to data). Since tumours are highly heterogeneous and cancer is a multifactorial disease, the parameter values of the model have to be adapted to the particular clinical setting. Nevertheless, the physiologically- and cell-level-based modelling approach allows to study in detail intra-tumoural antibody distribution and two important measures of efficacy, i.e., **antibody receptor saturation** within tumour tissue and **residual receptor activity** (arising in the case of competition of mAb and endogenous ligand for receptor binding). Based on the observed phenomena it is possible to reflect on therapeutic utility and dosing regimens in mAb cancer treatment.

The present analysis focussed on the following two scenarios in targeted cancer therapy:

i) ADC targeting receptor without known endogenous ligand;
ii) mAb targeting receptor with endogenous ligand

that allowed us to study the two above mentioned measures of efficacy.

In scenario i), we specifically chose the ADC trastuzumab emtansine T-DM1, since it is currently the only approved ADC targeting solid tumours. T-DM1 binds to HER2 that is a member of the surface receptor EGFR family (HER1-HER4) [153]. No activating ligand for HER2 has been identified [153–155]. In scenario ii), we selected mAbs competing antagonistically for binding with the epidermal growth factor to the epidermal growth factor receptor, since EGFR is a prominent target in cancer therapy. In addition, the EGF-EGFR system is also one of the best studied systems in systems biology. For an overview of the major mechanisms of action in mAb cancer therapy and ADCs, see Chapter 2.

This chapter is organised as follows: First, we present the developed mechanistic modelling framework that includes the *consensus* PBPK model, a detailed tumour distribution model (section 5.1.1) and the cell-level TMDD model (section 5.1.2). The focus in sections 5.2+5.3 is to study ADC T-DM1 tumour distribution and its impact on receptor saturation in mice and humans. In sections 5.4+5.5, the focus is to analyse the impact of ligand-mAb competition for receptor binding on therapeutic efficacy of anti-EGFR mAbs in human patients. In section 5.5, specifically the impact of changes in tumour microenvironment on therapeutic efficacy of anti-EGFR mAbs will be examined. In the sequel, we will use natural and endogenous ligand as well as the terms monoclonal antibody and antibody as synonyms.

Part (section 5.1.2) of the present Chapter has been published as W. Huisinga, S. Fuhrmann, L. Fronton, B.-F. Krippendorff, "Target-Driven Pharmacokinetics of Biotherapeutics", in: *ADME Transl. Pharmacokinet. Ther. Proteins. Appl. Drug Discov. Dev.,* Eds.: H. Zhou and F.-P. Theil, Wiley, 2015, pp. 197-209.

5.1 Development of the cell-level-based tumour PBPK model

To study mAb distribution within solid tumours, we extended the *consensus* PBPK model (see Chapter 3) by a detailed tumour model. A graphical representation of the whole-body tumour PBPK model is shown in Figure 5.1. For each organ, except tumour, we assumed an extravasation rate-limited distribution model. For all organs, except tumour, the outflowing concentration is parameterised by an organ-specific interstitial partition coefficient K_{int} that was derived from ABCs. For the present analysis, we assumed a total clearance from plasma equal to the median unspecific plasma clearance from human patients (see Chapter 3). To simulate variations in unspecific linear mAb CL, we used the derived 25th percentile and 75th percentile of clearance values from human patients. For further details and parameterisation of the *consensus* PBPK model, see Chapter 3.

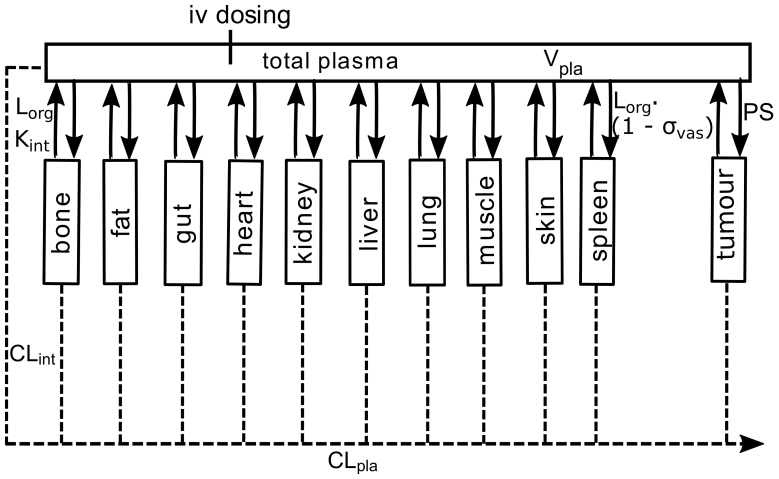

Fig. 5.1.: *Structure of the consensus tumour PBPK model for mAb PK.* Organs except tumour are interconnected via antibody extravasation from plasma and the lymph flow. Due to limited convection of mAbs into tumour tissue [1, 29, 34], only the diffusive distribution was taken into account. The mAb can potentially be cleared unspecifically from the plasma as well as any organ compartment (dashed arrows).

The rates of change of the concentrations of unbound mAb in plasma C_{pla} and in the interstitial space C_{int} of the different organs except tumour were described by the following system of differential equations:

$$V_{\mathrm{int}}\frac{\mathrm{d}}{\mathrm{dt}}C_{\mathrm{int}} = L_{\mathrm{org}}\cdot\left((1-\sigma_{\mathrm{vas}})C_{\mathrm{pla}}-\frac{C_{\mathrm{int}}}{K_{\mathrm{int}}}\right) \tag{5.1}$$

$$\begin{aligned} V_{\mathrm{pla}}\frac{\mathrm{d}}{\mathrm{dt}}C_{\mathrm{pla}} &= \sum_{\mathrm{org}} L_{\mathrm{org}}\cdot\left(\frac{C_{\mathrm{int}}}{K_{\mathrm{int}}}-(1-\sigma_{\mathrm{vas}})\cdot C_{\mathrm{pla}}\right) \\ &\quad -\mathrm{CLpla}\cdot C_{\mathrm{pla}}+k_{\mathrm{in}}(t)+\mathrm{PS}\cdot(C_1-C_{\mathrm{pla}}) \end{aligned} \tag{5.2}$$

with infusion rate $k_{\mathrm{in}}(t)$ [nmol/min], concentrations in [nM], and initial conditions $C_{\mathrm{pla}}(0) = \mathrm{dose}/V_{\mathrm{pla}}$, $C_{\mathrm{int}}(0) = 0$ for organs. The equations (5.1) and (5.2) are identical to the equations of the *consensus* PBPK model (see Chapter 3) except for the last term of equation (5.2). The exchange between plasma and the first tumour layer (with concentration C_1) was modelled in terms of the permeability surface area product PS (see section 5.1.1).

The PBPK tumour CMT was represented using a detailed tumour distribution model with krogh cylinder geometry (described in the following section).

5.1.1 Tumour distribution model

There are many different types of tumour distribution models and geometries (e.g., spherical, cylindrical geometry or a combination of both). For comparison between the cylindrical and the spherical geometry, see Appendix section A.3.2. The most common model for capturing heterogeneous distribution of drugs within solid tumour is the cylindrical vascular-tissue model, so-called krogh cylinder geometry. It has been validated for mAbs by multiple groups [19, 152, 156]. The krogh radius is the half-intercapillary distance and can be interpreted as the tumour vascular density: the larger the krogh radius, the lower the vascular density, i.e., each capillary supplies a larger area of tumour tissue [157]. As mAbs are extravasation rate-limited, changes along the blood vessel of the capillaries are typically neglected and a 1-D model with only radial flux from the capillary with radius r_{cap} towards the tumour periphery was used [19, 156]. This model is an idealised model to represent vascularised regions of a solid tumour and was described in detail by Thurber et al. [156]. We assumed that the krogh cylinder is divided into n well-stirred layers (subcompartments) that represent the tumour tissue around the blood capillary. The number of layers was chosen depending on r_{krogh}, so that at least one cell layer per subcompartment exists. A graphical illustration of the solid tumour represented by krogh cylinder geometry is shown in Figure 5.2.

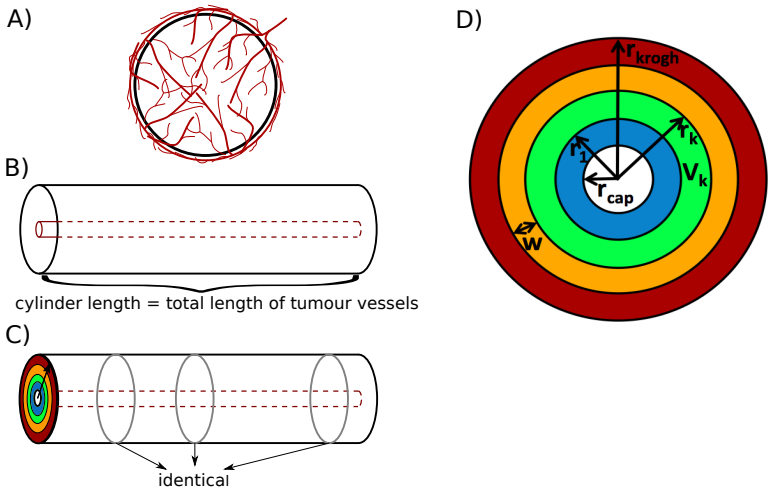

Fig. 5.2.: *Illustration of a solid tumour represented by krogh cylinder geometry.* **A)** Schematic illustration of an idealised solid tumour and its vasculature distribution. **B)** The tumour compartment was represented using krogh cylinder geometry of tumour blood vessels surrounded by tumour tissue. The length of the krogh cylinder represents the total length of tumour vessels. **C)** As mAbs are extravasation rate-limited, changes along the blood vessel of the cylinder are neglected. To describe intra-tumoural mAb distribution, a 1-D model with only radial flux from the blood vessel towards the tumour periphery was used. **D)** The radius r_{cap} is surrounded by tumour tissue with radius r_{krogh}. The tumour tissue was assumed to be divided into 4 layers with equal width.

The krogh cylinder represents total tumour volume V_{tum} comprising vascular space and total tumour tissue volume V_{tis}:

$$V_{\mathrm{tum}} = V_{\mathrm{res,tum}} + V_{\mathrm{tis}}. \tag{5.3}$$

We calculated the total tumour tissue volume V_{tis} based on total tumour volume V_{tum} and measured tumour volume fraction $f_{\mathrm{tis}} = 1 - f_{\mathrm{res,tum}}$ (from [35]).

We assumed the total tumour volume V_{tum} to be constant. An extension to tumour growth is possible: Tumour growth can be implemented into the cell-level tumour PBPK model by increasing the cylinder length that represents the total tumour capillary system. Based on the volume equation of a cylinder $V(r) = \pi \cdot r^2 \cdot \mathrm{L}$, we determined the length L as:

$$\begin{aligned} V_{\mathrm{tis}} &= V(r_{\mathrm{krogh}}) - V(r_{\mathrm{cap}}) \\ &= \pi \cdot \mathrm{L} \cdot (r_{\mathrm{krogh}}^2 - r_{\mathrm{cap}}^2) \\ \Rightarrow \mathrm{L} &= \frac{V_{\mathrm{tis}}}{\pi \cdot (r_{\mathrm{krogh}}^2 - r_{\mathrm{cap}}^2)}. \end{aligned} \tag{5.4}$$

Tumour tissue volume V_{tis} was defined as the sum of interstitial tumour V_{int} and intra-cellular tumour volume V_{cel} and divided into 'k' layers of equal width $\text{w}=(r_{\text{krogh}}-r_{\text{cap}})/\text{k}$. We calculated the tumour tissue volume of each layer V_k as:

$$\begin{aligned} V_1 &= V(r_1) - V(r_{\text{cap}}) \\ V_k &= V(r_k) - V(r_{k-1}) \end{aligned} \tag{5.5}$$

for $\text{k} \in \{2, \ldots, n\}$ and with $r_k = r_{\text{cap}} + k \cdot \text{w}$.

Each layer consists of interstitial tumour space with interstitial volume,

$$V_{k,\text{int}} = f_{\text{int}} \cdot V_k$$

and intra-cellular tumour space with cellular volume,

$$V_{k,\text{cel}} = f_{\text{cel}} \cdot V_k.$$

To study intra-tumoural mAb distribution, we assumed that mAb in plasma distributes to and from the first tumour tissue layer. Due to limited convection of mAbs into tumour tissue [1, 29, 34], only the diffusive distribution was taken into account. The exchange between plasma and tumour was modelled based on the permeability surface area product [dm^3/min] :

$$\text{PS} = \text{P} \cdot \text{SA}_{\text{cap}} \tag{5.6}$$

with capillary surface area [dm^2]:

$$\text{SA}_{\text{cap}} = 2\pi \cdot r_{\text{cap}} \cdot \text{L}. \tag{5.7}$$

The vascular permeability P [dm/min] can be interpreted as a measure of leakiness of tumour capillaries.

In each tumour layer, mAb can bind to its receptor or distribute to any adjacent layer. The surface area SA_k between the different tumour layers was calculated as:

$$\text{SA}_k = 2\pi \cdot r_k \cdot \text{L}$$

with $\text{k} \in \{1, \ldots, \text{n}-1\}$. Diffusion of free interstitial mAb between tumour layers $\text{k} \in \{2, \ldots, \text{n}\}$ was modelled via diffusion exchange [dm^3/min] that was calculated as:

$$\text{D}_{k-1,k} = \frac{\text{D}}{\text{w}} \cdot \text{SA}_{k-1} \tag{5.8}$$

where $\mathrm{D}_{k-1,k}$ [dm^3/min] denotes the diffusion exchange between the layers k-1 and k, and D represents the effective intra-tumoural diffusion coefficient [dm^2/min]. For the mathematical derivation of Eq. (5.8), see Appendix section A.3.1.

We assumed that all cells within a layer behave as a reference cell. This assumption can easily be relaxed; this, however, would require much more detailed information and is beyond the scope of the current analysis. Our assumption implied an equal distribution of receptor within the tumour. The number of cells within tumour layers was calculated via:

$$N_{k,\mathrm{cel}} = \frac{V_{k,\mathrm{cel}}}{V_{\mathrm{singlecell}}} \tag{5.9}$$

with the average volume of a single human tumour cell $V_{\mathrm{singlecell}}$ (see Table 1).

A schematic illustration of the tumour distribution model is shown in Figure 5.3 (A). More details on the tumour physiology and relevant processes of mAb transport within solid tumours can be found in Chapter 2. For parameter values, see Table 5.1. The tumour distribution model integrates a single cell-level TMDD model within each tumour layer to account for antibody-receptor-ligand interactions as well as receptor dynamics. The model equations of the *consensus* PBPK model including a cell-level-based tumour distribution model are presented in the following section.

5.1.2 Cell-level TMDD model

We use the cell-level TMDD model developed by Krippendorff et al. [13] for antibodies antagonistically inhibiting EGFR.

The cellular level is depicted in Figure 5.3 (B). In the interstitial space of the tumour layers, the natural ligand and the mAb competitively bind to the membrane-bound target (free receptor) with associate rate constants k_{onL} and k_{onC}. The ligand is synthesised per tumour cell with rate constant k_{synL}. The membrane-bound ligand-receptor complex dissociates with rate constant k_{offL} or is internalised and subsequently degraded with rate constant k_{degRL}. The membrane-bound drug-receptor complex dissociates with rate constant k_{offC} or is internalised and subsequently degraded with rate constant k_{degRC}. The free membrane-bound receptor is synthesised with rate k_{synR} and internalised with rate constant k_{degR}. The internalised free receptor is recycled to the membrane with rate constant k_{recyRi} or degraded with rate constant k_{degRi}. The number of membrane-bound ligand-receptor and drug-receptor complexes is denoted by RL and RC, and the number of free membrane-bound receptor and free internalised receptor by R and Ri, respectively. Extra-cellular ligand and mAb concentrations were assumed to have units in [nM]. The receptor species were given in [# molecules]. Thus, an additional scaling factor $\mathrm{SF}_{\mathrm{unit}} = 10^9/N_{\mathrm{avog}}$

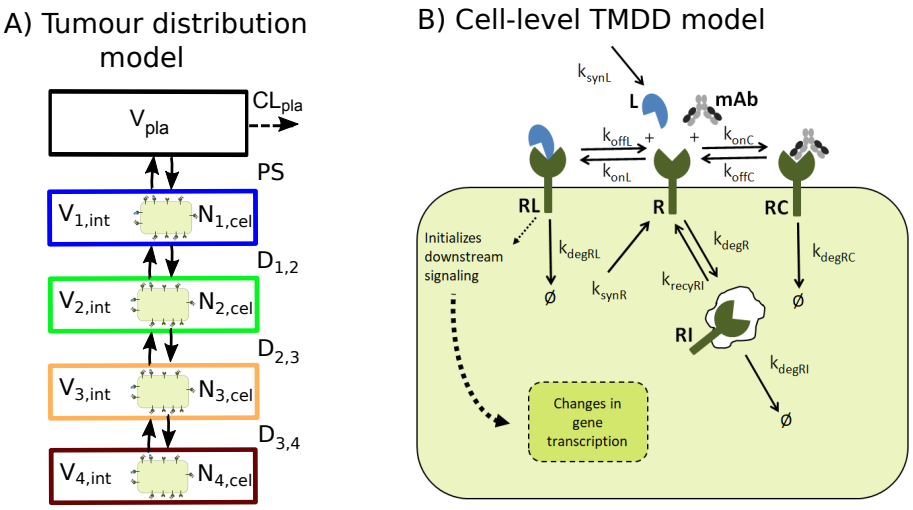

Fig. 5.3.: *Schematic illustration of the tumour distribution model integrating a single cell-level TMDD model.* **A)** The tumour compartment was divided into k=4 layers that consist of interstitial and cellular space. mAb in plasma was allowed to distribute to and from the first tumour tissue layer with the permeability surface area product PS. In each tumour layer, mAb was allowed to bind to its receptor or distribute to any adjacent layer. Diffusion of free mAb in interstitial space between tumour layers was modelled via diffusion exchange $\mathrm{D}_{k-1,k}$. **B)** The single cell-level TMDD model of receptor activation and inhibition [13] was integrated within each layer.

from [# molecules] to [nmol] was needed, where $N_{\mathrm{avog}} = 6.02 \cdot 10^{23}$ [1/mol] denotes the Avogadro constant. For a more detailed description of the cell-level TMDD model, see [13]. The cell-level TMDD model was parameterised using rate constants experimentally determined *in vitro*. For more details on the parameterisation, see Table 5.2.

The rates of change of the concentrations of unbound mAb within tumour interstitial space of the different tumour layers $C_1, \ldots, C_n$ [nM] were described by the following system of differential equations:

$$\begin{aligned}
V_{1,\mathrm{int}} \frac{\mathrm{d}}{\mathrm{dt}} C_1 &= \mathrm{PS} \cdot (C_{\mathrm{pla}} - C_1) - \mathrm{D}_{1,2} \cdot (C_1 - C_2) \\
&\quad + N_{1,\mathrm{cel}} \cdot \mathrm{SF}_{\mathrm{unit}} \cdot (k_{\mathrm{offC}} \cdot \mathrm{RC}_1 - k_{\mathrm{onC}} \cdot \mathrm{R}_1 \cdot C_1) \\
V_{k,\mathrm{int}} \frac{\mathrm{d}}{\mathrm{dt}} C_k &= \mathrm{D}_{k-1,k} \cdot (C_{k-1} - C_k) - \mathrm{D}_{k,k+1} \cdot (C_k - C_{k+1}) \\
&\quad + N_{k,\mathrm{cel}} \cdot \mathrm{SF}_{\mathrm{unit}} \cdot (k_{\mathrm{offC}} \cdot \mathrm{RC}_k - k_{\mathrm{onC}} \cdot \mathrm{R}_k \cdot C_k) \\
V_{n,\mathrm{int}} \frac{\mathrm{d}}{\mathrm{dt}} C_n &= \mathrm{D}_{n-1,n} \cdot (C_{n-1} - C_n) \\
&\quad + N_{4,\mathrm{cel}} \cdot \mathrm{SF}_{\mathrm{unit}} \cdot (k_{\mathrm{offC}} \cdot \mathrm{RC}_4 - k_{\mathrm{onC}} \cdot \mathrm{R}_4 \cdot C_4)
\end{aligned} \tag{5.10}$$

for k $\in \{2, \ldots, n-1\}$, with initial conditions $C_k(0) = 0$, and the diffusion exchange $\mathrm{D}_{k-1,k}$ [dm^3/min] from Eq. (5.8).

Denoting the concentrations of the natural ligand within the tumour interstitial space of the layers by L in [nM], the rates of changes of $\mathrm{R}_k, \mathrm{Ri}_k, \mathrm{RC}_k$ and L at the cellular level were given by:

$$\begin{aligned}
\frac{\mathrm{d}}{\mathrm{dt}}\mathrm{R}_k &= k_{\mathrm{synR}} - k_{\mathrm{onC}}\mathrm{R}_k \cdot C_k + k_{\mathrm{offC}}\mathrm{RC}_k - k_{\mathrm{degR}} \cdot \mathrm{R}_k \\
&\quad + k_{\mathrm{recyRi}} \cdot \mathrm{Ri}_k - k_{\mathrm{onL}}\mathrm{L}_k \cdot \mathrm{R}_k + k_{\mathrm{offL}}\mathrm{RL}_k \\
\frac{\mathrm{d}}{\mathrm{dt}}\mathrm{Ri}_k &= k_{\mathrm{degR}} \cdot \mathrm{R}_k - k_{\mathrm{recyRi}} \cdot \mathrm{Ri}_k - k_{\mathrm{degRi}} \cdot \mathrm{Ri}_k \\
\frac{\mathrm{d}}{\mathrm{dt}}\mathrm{RC}_k &= k_{\mathrm{onC}} \cdot C_k \cdot \mathrm{R}_k - k_{\mathrm{offC}}\mathrm{RC}_k - k_{\mathrm{degRC}} \cdot \mathrm{RC}_k \\
\frac{\mathrm{d}}{\mathrm{dt}}\mathrm{RL}_k &= k_{\mathrm{onL}}\mathrm{L}_k \cdot \mathrm{R}_k - k_{\mathrm{offL}} \cdot \mathrm{RL}_k - k_{\mathrm{degRL}} \cdot \mathrm{RL}_k \\
\frac{\mathrm{d}}{\mathrm{dt}}\mathrm{L} &= 0
\end{aligned} \tag{5.11}$$

for $k \in \{1, \ldots, n\}$. The natural ligand concentration in the extracellular space of the tumour tissue was assumed to be constant. This is an often used simplification (e.g., in [13]) when including the competition between mAb and natural ligand for receptor binding. Prior to any drug treatment, the system was assumed to be in pre-treatment steady state, resulting in some number of free receptor $\mathrm{R}{=}\mathrm{R}_{\mathrm{ss}}$, internalised receptor $\mathrm{Ri}{=}\mathrm{Ri}_{\mathrm{ss}}$ and membrane-bound ligand-receptor $\mathrm{RL}{=}\mathrm{RL}_{\mathrm{ss}}$ as well as pre-treatment ligand concentration L_{ss} (see Table 5.2). For comparison between different tumour ligand concentrations and their impact on efficacy in terms of receptor saturation and residual receptor activity, see Appendix section A.3.3.

Different measures of therapeutic mAb efficacy can be determined using the cell-level TMDD model:

- Receptor saturation by the mAb, described as the ratio of receptor-mAb complex RC to membrane-bound receptors Rm:

$$\frac{\mathrm{RC}}{\mathrm{Rm}} \tag{5.12}$$

  is often taken as a measure of the inhibitory potential of a drug.
- In case of mAbs competing for receptor binding with natural ligands, not only receptor saturation but also residual receptor activity can be an important measure for mAb therapeutic efficacy. Residual receptor activity is defined relative to the pre-treatment level $\mathrm{RL}_{\mathrm{ss}}$ of activated receptors [13]:

$$\frac{\mathrm{RL}}{\mathrm{RL}_{\mathrm{ss}}}. \tag{5.13}$$

There are different approaches of including the competition between mAb and natural ligand for receptor binding to determine residual receptor activity. Besides a constant ligand concentration within tumour, tumour ligand concentration can

dynamically change over time (in the following termed as **'Ligand dynamics'**) due to e.g., the interaction of the mAb with the receptor.

Modelling 'Ligand dynamics' within tumour: In each layer of the tumour, we assumed the ligand to be produced with rate k_{synL}, and binding to free receptor and subsequent internalisation and degradation of the receptor-ligand complex RL with rate constant k_{degRL}.

Furthermore, we assumed a ligand concentration Lpla within plasma to mimic ligand synthesis and degradation within other organs than tumour. The rate of change of ligand concentration within plasma Lpla [nM] was described by the following differential equation:

$$\begin{aligned} V_{\mathrm{pla}} \frac{\mathrm{d}}{\mathrm{dt}} \mathrm{Lpla} &= k_{\mathrm{synLpla}} \cdot V_{\mathrm{pla}} - k_{\mathrm{degLpla}} \cdot \mathrm{Lpla} \cdot V_{\mathrm{pla}} \\ &\quad -\mathrm{PS} \cdot (\mathrm{Lpla} - \mathrm{L}_1) \end{aligned} \tag{5.14}$$

with k_{synLpla} [nM/min], k_{degLpla} [1/min] and initial conditions $\mathrm{Lpla}(0) = \mathrm{Lpla}_{\mathrm{ss}}$. Similar to the mAb, the soluble natural ligand in plasma was assumed to distribute to and from the first tumour layer (with the permeability surface area product PS [dm^3/min] via Eq. (5.6)).

In any tumour layer, we assumed the ligand to bind to its receptor or to distribute to any adjacent tumour layer. The rates of change of the concentrations of the natural ligand $\mathrm{L}_1, \ldots, \mathrm{L}_n$ [nM] within the tumour interstitial space of the different layers were described by the following system of differential equations:

$$\begin{aligned} V_{1,\mathrm{int}} \frac{\mathrm{d}}{\mathrm{dt}} \mathrm{L}_1 &= \mathrm{PS} \cdot (\mathrm{L}_{\mathrm{pla}} - \mathrm{L}_1) - \mathrm{D}_{1,2} \cdot (\mathrm{L}_1 - \mathrm{L}_2) \\ &\quad + N_{1,\mathrm{cel}} \cdot \mathrm{SF}_{\mathrm{unit}} \cdot (k_{\mathrm{offL}} \cdot \mathrm{RL}_1 - k_{\mathrm{onL}} \cdot \mathrm{R}_1 \cdot \mathrm{L}_1 + k_{\mathrm{synL}}) \\ V_{k,\mathrm{int}} \frac{\mathrm{d}}{\mathrm{dt}} \mathrm{L}_k &= \mathrm{D}_{k-1,k} \cdot (\mathrm{L}_{k-1} - \mathrm{L}_k) - \mathrm{D}_{k,k+1} \cdot (\mathrm{L}_k - \mathrm{L}_{k+1}) \\ &\quad + N_{k,\mathrm{cel}} \cdot \mathrm{SF}_{\mathrm{unit}} \cdot (k_{\mathrm{offL}} \cdot \mathrm{RL}_k - k_{\mathrm{onL}} \cdot \mathrm{R}_k \cdot \mathrm{L}_k + k_{\mathrm{synL}}) \\ V_{n,\mathrm{int}} \frac{\mathrm{d}}{\mathrm{dt}} \mathrm{L}_n &= \mathrm{D}_{n-1,n} \cdot (\mathrm{L}_{n-1} - \mathrm{L}_n) \\ &\quad + N_{n,\mathrm{cel}} \cdot \mathrm{SF}_{\mathrm{unit}} \cdot (k_{\mathrm{offL}} \cdot \mathrm{RL}_n - k_{\mathrm{onL}} \cdot \mathrm{R}_n \cdot \mathrm{L}_n + k_{\mathrm{synL}}) \end{aligned} \tag{5.15}$$

for $k \in \{2, n-1\}$ and with initial conditions $\mathrm{L}_k(0) = \mathrm{L}_{\mathrm{ss}}$. The exchange between plasma and the first tumour layer was determined by the permeability surface area product PS [dm^3/min] via Eq. (5.6). The diffusion exchange [dm^3/min] was calculated via Eq. (5.8). Note that the vascular permeability P and the effective intra-tumoural diffusion coefficient D differ between mAb and natural ligand due to their differences in MW (see Table 5.1).

In the following sections, the developed modelling framework will be used to study in detail intra-tumoural antibody distribution and two important measures of efficacy, i.e., antibody receptor saturation within tumour tissue and residual receptor activity (arising in the case of competition of mAb and endogenous ligand for receptor binding).

Tab. 5.1.: Krogh cylinder simulation parameters

Parameter	Value	Unit	References	Description
r_{cap}	8.0e-5	dm	[19]	capillary radius
r_{krogh}	7.5e-4	dm	[19]	krogh cylinder radius
CLpla	2.3e-6	L/min/kg BW	Chapter 3	median unspecific mAb plasma clearance for human patients [a]
$V_{\mathrm{tum,m}}$	2.0e-4	dm^3=L	[158]	typical tumour volume xenograft mice
$V_{\mathrm{tum,h}}$	1.0e-3	dm^3=L	[159]	clinically detectable volume in solid human tumours
$V_{\mathrm{singlecell}}$	2.0e-12 [b]	L	[160]	average human tumour cell volume
f_{tis}	0.94	-	[35]	tissue volume fraction of total tumour volume
$f_{\mathrm{res,tum}}$	0.06	-	[35]	vascular volume fraction of total tumour volume
f_{int}	0.34	-	[35]	interstitial volume fraction of tissue tumour volume
f_{cel}	0.66	-	[35]	cellular volume fraction of tissue tumour volume
mAb [c]				
P	1.7e-6	dm/min	[161, Table S3], [19]	vascular permeability to tumour tissue
D	7.6e-8	dm^2/min	[161, Table S1] [d]	intra-tumoural effective diffusion coefficient
ligand				
P	2.7e-5	dm/min	[161, Figure 1C] [e]	vascular permeability to tumour tissue
D	7.8e-7	dm^2/min	[161, Figure 1A] [f]	intra-tumoural effective diffusion coefficient

[a] assumed to be identical for mice
[b] in agreement with reported mammalian cell volume of 1e-13 to 1e-11 L [162]; assumed to be identical for mice
[c] values hold for mAbs of IgG isotype with MW of approx. 150 kDa
[d] value in agreement with measured values in [163] and reported value in [19]
[e] digitised based on [161, Figure 1C] using MW of 6 kDa and a molecular radius of $r = 0.912 \cdot \mathrm{MW}^{0.333}$ [161]
[f] digitised based on [161, Figure 1A] using MW of 6 kDa and a molecular radius of $r = 0.912 \cdot \mathrm{MW}^{0.333}$ [161]

Tab. 5.2.: Parameter values for the cell-level TMDD model (EGF-EGFR system) [a] [b]

Parameter	Value	Unit	References	Description
k_{synR}	1.3e2	molecules/min	[13], orig. [164]	EGFR synthesis
k_{onL}	7.2e-2	1/(nM·min)	[13], orig. [164]	EGF-EGFR binding
k_{offL}	3.4e-1	1/min	[13], orig. [164]	EGF-EGFR unbinding
k_{degR}	3.0e-2	1/min	[13], orig. [164]	EGFR internalisation
k_{degRL}	3.0e-2	1/min	[13], orig. [164]	EGF-EGFR complex internalisation
k_{recyRi}	2.3e-1	1/min	[13]	EGFR recycling
k_{degRi}	5.50e-4	1/min	[13]	EGFR degradation
k_{synL}	1.28e2	molecules/min	calculated [c]	EGF synthesis per tumour cell
k_{synLpla}	4.10e-3	nM/min	calculated [d]	tumour-independent EGF synthesis [e]
k_{degLpla}	1.0e-2	1/min	[165]	tumour-independent EGF degradation [e]
$\mathrm{Lpla}_{\mathrm{ss}}$	4.08e-1	nM	[166] [f]	EGF pretreatment concentration in plasma [e]
L_{ss}	8.16e-1	nM	[167, 168]	EGF pretreatment concentration in solid tumour
Panitumumab				
$\mathrm{K_D}$	5.0e-2	nM	[13]	binding affinity [g]
k_{onC}	k_{onL}	1/(nM·min)	[13]	mAb-receptor binding
k_{degRC}	8.3e-5	1/min	[13, 169]	mAb-receptor complex internalisation
Zalutumumab				
$\mathrm{K_D}$	7.0e0	nM	[13]	binding affinity [g]
k_{onC}	k_{onL}	1/(nM·min)	[13]	mAb-receptor binding
k_{degRC}	8.3e-5	1/min	[13, 169]	mAb-receptor complex internalisation
Trastuzumab				
$\mathrm{K_D}$	5.0e-1	nM	[19]	binding affinity [g]
k_{onC}	4.3e-2	1/(nM·min)	[19]	mAb-receptor binding
k_{degRC}	2.0e-3	1/min	[19]	mAb-receptor complex internalisation

[a] values of receptor dynamics (k_{synR}, k_{degR}, k_{recyRi}, k_{degRi}) assumed to be identical to HER2, since HER2 is a member of the surface receptor EGFR family (HER1-HER4) [153]

[b] rate constants of ligand-receptor interaction (EGF-EGFR) assumed to be similar across species, e.g., mouse and human

[c] calculated via $k_{\mathrm{synL}} = \mathrm{RL,ss} \cdot k_{\mathrm{degRL}}$; set to zero in the cell-level model including constant EGF concentration within tumour tissue ($\frac{\mathrm{d}}{\mathrm{dt}}\mathrm{L} = 0$)

[d] calculated via $k_{\mathrm{synLpla}} = \mathrm{Lpla,ss} \cdot k_{\mathrm{degLpla}}$

[e] Lpla only used for the cell-level model including 'Ligand Dynamics'

[f] calculated from reported mean concentration of EGF in 20 healthy women [166] (with EGF MW 6 kDa and based on 7 ligands that can activate EGFR in mammals [170])

[g] corresponding values for k_{offC} calculated via $\mathrm{K_D} = k_{\mathrm{offC}}/k_{\mathrm{onC}}$ while association rate constant k_{onC} was unchanged due to the common assumption that k_{offC} is diffusion-limited [1, 13]

5.2 Tumour volume influences receptor saturation via impact of TMDD clearance on plasma PK

Heterogeneous distribution of ADCs within tumour tissue (in particular due to dose-limiting toxicity) is still a current topic of debate. It was experimentally observed in xenograft mice e.g. by Cilliers et al. [19]. ADCs require the release of the toxic payload within the target cell for their activation [33]. Thus, receptor saturation within tumour tissue is an important measure for therapeutic efficacy of ADCs. The objective of the present section was to study the distribution and receptor saturation within solid tumour tissue of the ADC T-DM1 in mice and human patients.

To do so, the cell-level tumour PBPK model was applied. We made the simplifying assumption that independent of the payload, each ADC species has the same (PK) properties as the naked mAb. We are aware that the PK can be much more complex, with differences between ADC species dependent of their DAR [52, 171].

No activating ligand for HER2 has so far been identified [153–155]. Thus, when studying tumour distribution of T-DM1 binding to HER2, no ligand was included within the single cell-level TMDD model. We assumed the tumour CMT to consist of 4 layers. Receptor saturation within each of the 4 tumour layers was calculated via Eq. (5.12) with $\mathrm{Rm} = \mathrm{RC} + \mathrm{R}$. T-DM1 plasma concentrations and total (i.e., unbound+bound) T-DM1 tumour concentrations were simulated over time for mice (25 g BW) and humans (male, BW 73 kg), respectively. Simulations were conducted following a single clinical dose of T-DM1 (i.e., 3.6 mg/kg BW [19, 172]). We assumed (pre-)clinically relevant tumour volumes for mice, i.e., V_{tum}=0.2 mL and human patients, i.e., V_{tum}=1 mL.

Figure 5.4 shows the plasma and tumour PK as well as the receptor saturation profiles for mouse with typical xenograft tumour volume at start of mAb administration (i.e., V_{tum}=0.2 mL) and human with clinically detectable tumour volume (i.e., V_{tum}=1 mL). Despite same dose per kg BW, a marked difference in plasma and tumour PK for mouse and human was observed: faster declining tumour PK as well as faster declining plasma PK profile in mouse compared to human. In mouse, our model predicted a heterogeneous receptor saturation up to 50%, which is in line with previous reports [19]. In contrast, in human after approx. 5 days receptor saturation was close to 100% throughout all layers. A detailed analysis revealed that the main reason for the observed differences is the difference in tumour volume per body weight between mouse and human (V_{tum}=8 mL/kg vs. V_{tum}=0.014 mL/kg).

The differences in receptor saturation (Figure 5.4, bottom) depending on the tumour volume can be explained as follows: The larger the tumour volume per body weight,

the larger the number of cells (with identical number of target receptors per cell) within tumour. Thus, target-mediated mAb CL is dominating over linear unspecific CL. This is the situation in mice with V_{tum}=8 mL/kg. As a result, the large target-mediated mAb CL in tumour leads to a faster declining plasma PK in xenograft mice compared to humans with clinically detectable tumour volume (i.e., V_{tum}=0.014 mL/kg) (see Figure 5.4).

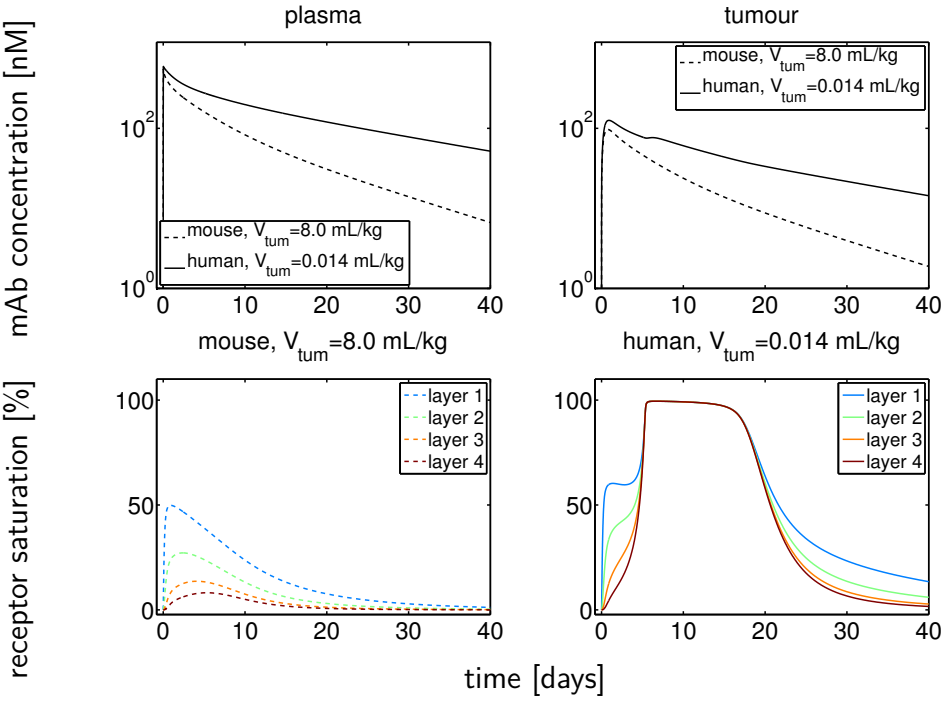

Fig. 5.4.: *Predicted impact of **different tumour volume per body weight** on mAb plasma PK (top left), tumour PK (top right) and receptor saturation for **mouse** (bottom left) and **human** (bottom right) based on the cell-level tumour PBPK model without natural ligand following **T-DM1 dose of 3.6 mg/kg BW**.*

To verify our hypothesis that tumour volume per body weight is the main reason for differences in receptor saturation between xenograft mice and humans, we conjectured that identical tumour volume per body weight for both species would result in comparable PK and receptor saturation profiles.

Figure 5.5 shows the plasma and tumour PK as well as the receptor saturation profiles for mouse and human with identical tumour volume per body weight in both species. The tumour volume in mouse (25 g BW, V_{tum}=0.2 mL, V_{tum}=8.0 mL/kg) would correspond to a large human tumour volume of 584 mL (73 kg BW, V_{tum}=8.0 mL/kg). Thus, based on identical tumour volumes per body weight in both species, the model predicted comparable plasma and tumour PK as well as similar receptor saturation profiles for mouse and human within tumour tissue. Vice versa, the clinically relevant tumour volume in human (i.e., 73 kg BW, V_{tum}=0.014 mL/kg) would correspond to a mouse tumour volume of 3.5e-4 mL (25 g, V_{tum}=0.014 mL/kg). In this case, the model also predicts comparable receptor saturation-time profiles for both species.

The fact that ultimately plasma PK determines receptor saturation (via impact of tumour volume on TMDD CL) is also supported in Figure 5.5.

In addition, the observed transient stagnation during initial increase in the human receptor saturation-time profile at approx. 2 days in particular in layers 1 and 2 (Figure 5.4, bottom right) highlights the impact of the internalised free receptor: The free receptor is initially not fully saturated due to the pool of internalised free receptor. This may be an explanation for the observed initial time-dependence in linear CL by Kågedal and Gibiansky [51]

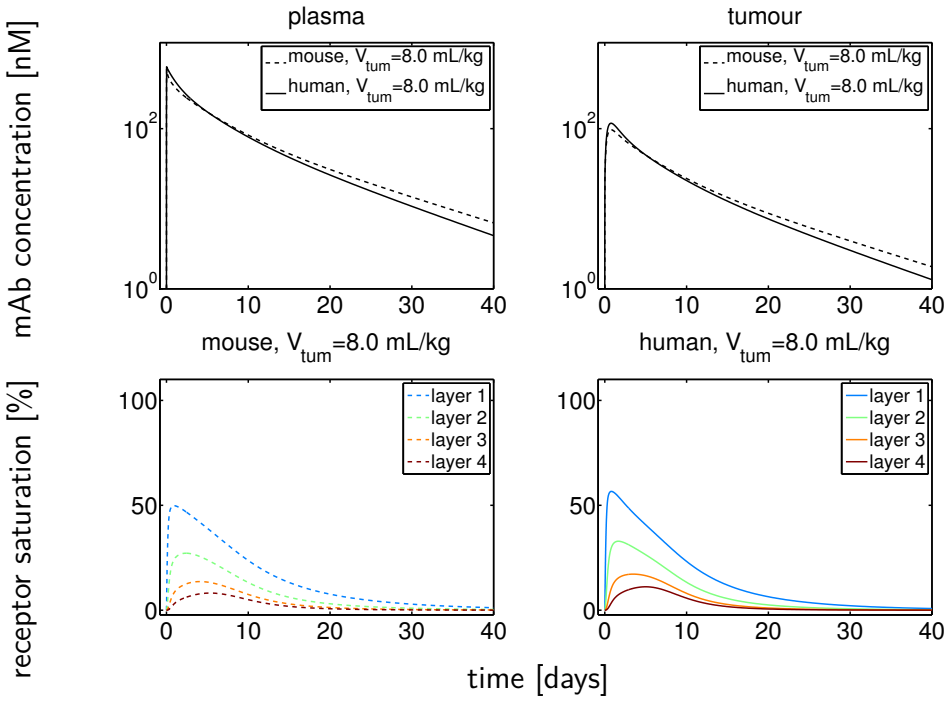

Fig. 5.5.: *Predicted impact of **identical tumour volume per body weight** on mAb plasma PK (top left), tumour PK (top right) and receptor saturation for **mouse** (bottom left) and **human** (bottom right) based on the cell-level tumour PBPK model without natural ligand following **T-DM1 dose of 3.6 mg/kg BW**.*

5.3 Impact of IIV of unspecific mAb CL and implications for dosing strategies of ADC therapy in human patients

In human patients, the model predicted receptor saturation close to 100% after approx. 5 days following single T-DM1 dose (at clinically detectable tumour volume, i.e., 1 mL). If the target-mediated clearance is saturated in human, the unspecific clearance dominates and we expect a large impact of its IIV on plasma PK and subsequently on receptor saturation. This is of relevance in cancer therapy, since

unspecific mAb clearance can be increased, e.g., due to increased turnover of proteins (as frequently observed in cachectic cancer patients) [25]. This affects the catabolism of both endogenous IgG and therapeutic IgG (i.e., therapeutic mAb).

The objective of the present section was to study the impact of IIV of unspecific clearance on PK and efficacy (in terms of receptor saturation) of ADC T-DM1 therapy in human patients. As in the previous section, the cell-level tumour PBPK model without natural ligand was applied. Simulations were conducted following the clinically approved dosing regimen of T-DM1 (i.e., 3.6 mg/kg BW q3w) [172].

Figure 5.6 shows the impact of IIV in unspecific clearance on plasma and tumour PK as well as on receptor saturation for human patients following multiple dosing of T-DM1. Based on IIV in unspecific clearance, the model predicted differences in plasma and tumour PK and differences in the duration of receptor saturation: If unspecific clearance is increased (i.e., 75th percentile of clearance vs. 25th percentile of clearance), a pronounced difference in duration of receptor saturation was observed for the first treatment cycle (before second dose). If receptor saturation is required for efficacy, this finding is relevant for patients with increased unspecific clearance resulting in suboptimal efficacy within the first treatment cycle. A strong relationship between trough plasma concentrations and receptor saturation was observed, in particular between cycle 1 minimum plasma concentration (at 21 days) and receptor saturation (see Figure 5.6 grey area). Based on this observation, we conjectured that by dose intensification (i.e, reducing the length of the dosing interval of cycle 1) the strong decrease in receptor saturation within the first treatment cycle (Figure 5.6, bottom left) can be prevented.

Figure 5.7 shows the difference between the (i) standard clinically approved dosing regimen of T-DM1 (i.e., 3.6 mg/kg BW q3w) and (ii) the dose intensification strategy within the initial treatment cycle (e.g., second dose administered after 14 days instead of 21 days) on plasma PK as well as on receptor saturation in human patients (with 75th percentile of CL). Based on scenario (ii), receptor saturation $> 98\%$ was observed throughout ADC therapy (Figure 5.7, bottom right). Thus, based on our developed modelling approach, an initial dose intensification was mechanistically supported to guarantee ADC receptor saturation from the start of treatment.

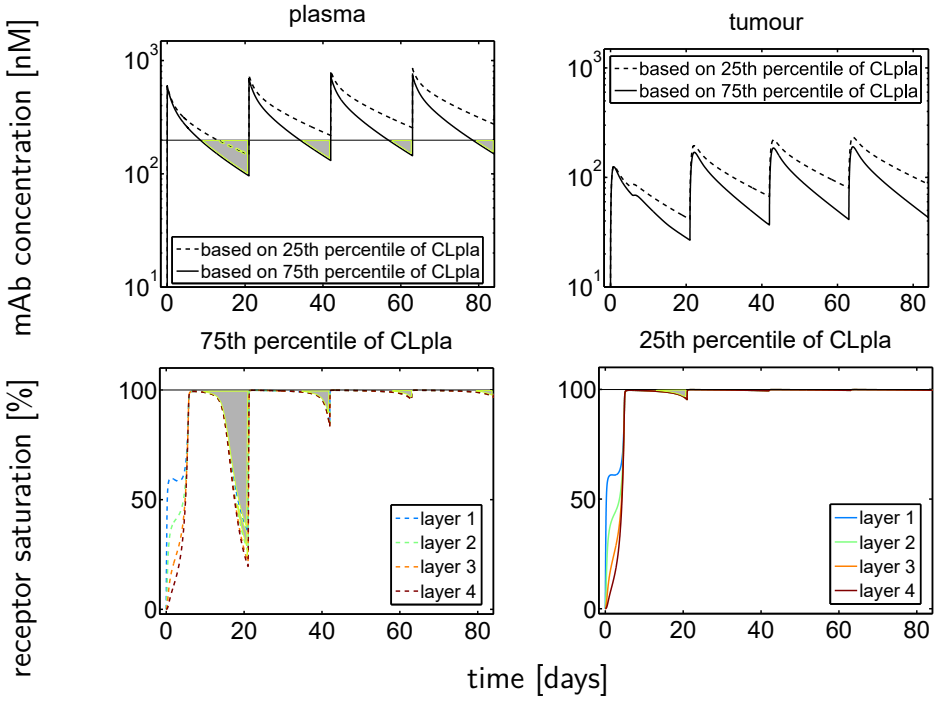

Fig. 5.6.: *Predicted impact of **IIV in unspecific plasma clearance** on T-DM1 PK and receptor saturation for **human patients** (V_{tum}=0.014 mL/kg) based on the cell-level tumour PBPK model without natural ligand.* Predicted plasma PK (top left) and total tumour PK (top right) following **T-DM1 clinically approved dosing regimen of 3.6 mg/kg BW q3w** are based on different unspecific CLpla. Predicted receptor saturation is based on 25th percentile of CLpla (bottom right) and 75th percentile of CLpla (bottom left).

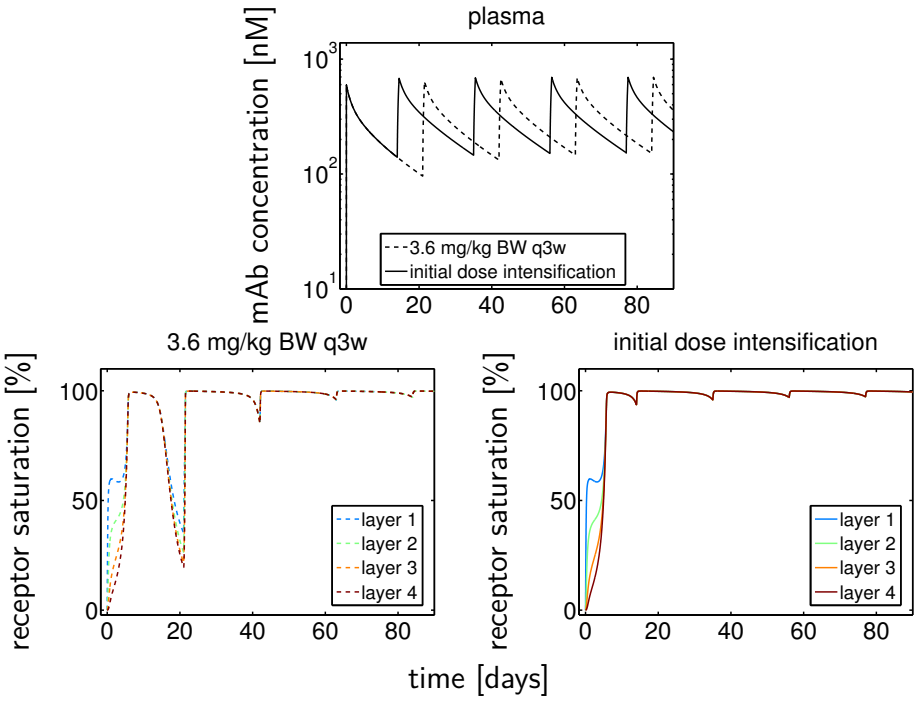

Fig. 5.7.: *Predicted impact of **initial dose intensification** on T-DM1 receptor saturation for **human patients** (V_{tum}=0.014 mL/kg) based on the cell-level tumour PBPK model without natural ligand.* Predicted plasma PK (top) is based on 75th percentile of CLpla following (i) **T-DM1 clinically approved dosing regimen of 3.6 mg/kg BW q3w vs.** (ii) **dose intensification strategy within the initial treatment cycle**. Predicted receptor saturation is shown based on scenario (i) (bottom left) and scenario (ii) (bottom right).

5.4 Impact of ligand-mAb competition for receptor binding on therapeutic efficacy of anti-EGFR mAbs in human patients

EGFR is a prominent target in cancer therapy. Anti-EGFR mAbs used as anti-cancer agents can exert their therapeutic effect via prevention of binding of EGF to EGFR. Thus, not only receptor saturation but also reduction in receptor activity can be an important measure to assess their therapeutic efficacy. In this case the ratio of affinity of mAb and ligand towards receptor is important.

The objective of this chapter was to study the impact of ligand-mAb competition for receptor binding on therapeutic efficacy and the impact of mAb properties, i.e., mAb-receptor affinity. The present analysis focussed on the following two anti-EGFR mAbs with marked differences in their affinity towards the receptor EGFR (see Table 5.2):

- panitumumab (KD=5e-2 nM): more affine than EGF (KD= 4.72e0 nM),
- zalutumumab (KD=7e0 nM): less affine than EGF.

The cell-level tumour PBPK model (including natural ligand at constant concentration within tumour $\mathrm{L_{ss}}$ = 0.816 nM) was used to study EGFR saturation and residual EGFR activity within solid tumour tissue of the two mAbs. We assumed the tumour CMT to consist of 4 layers. Anti-EGFR mAb plasma concentrations and total (i.e., unbound+bound) tumour concentrations were simulated over time for human patients (male, BW 73 kg, V_{tum}=0.014 mL/kg). EGFR saturation within tumour tissue was calculated via Eq. (5.12) with $\mathrm{Rm} = \mathrm{RC} + \mathrm{R} + \mathrm{RL}$. Residual EGFR activity over time was computed via Eq. (5.13). Initially, simulations were conducted following a single clinical dose of panitumumab (i.e., 6 mg/kg BW [150]), which has been approved in contrast to zalutumumab.

In Figure 5.8, the plasma and tumour PK profiles as well as the residual receptor activity- and receptor saturation-time profiles are shown for panitumumab and zalutumumab following single dosing (SD) of 6 mg/kg BW. Despite the marked differences in affinities between the mAbs, only minimal changes in EGFR saturation from 100% were observed (Figure 5.8, middle left). This can be explained by the fact that mAb receptor complex RC is by far the most abundant membrane-bound receptor species (see Figure 5.8, bottom). Furthermore, we observed a much larger %-residual EGFR activity for zalutumumab compared to panitumumab in terms of minimum and duration of residual EGFR activity (Figure 5.8, middle right). This can be explained by their differences in affinity towards the free receptor EGFR. The lower the mAb affinity to free EGFR, the larger the number of free EGFR where ligand EGF can bind to for inducing downstream-signalling pathways.

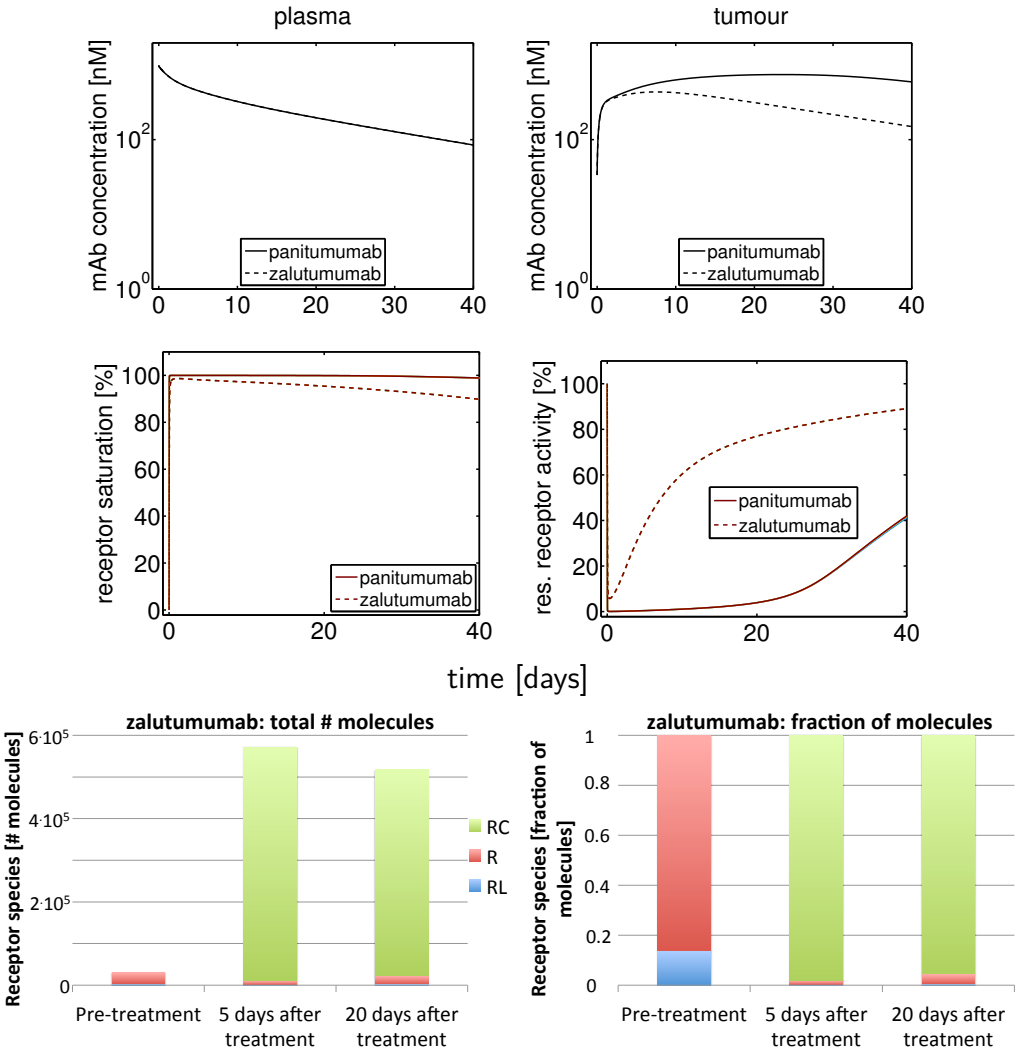

Fig. 5.8.: *Predicted impact of* ***constant natural ligand concentration*** *within tumour* (L_{ss} = *0.816 nM) competing for receptor binding with* ***panitumumab*** *or* ***zalutumumab*** *following* ***SD 6 mg/kg BW***. Simulations of plasma and tumour PK (top), receptor saturation (middle left), residual receptor activity (middle right) and dynamics of the receptor species RC, R, RL (bottom) are based on the cell-level tumour PBPK model. All four layers are superimposed.

The following simulations were based on clinically relevant dosing regimens, i.e., (i) clinically approved panitumumab dose 6mg/kg BW q2w [150] versus (ii) 16mg/kg BW qw for zalutumumab. The latter dosing scheme was based on a Phase I trial where patients received weekly doses of zalutumumab without experiencing dose limiting toxicity [173]. Figure 5.9 shows the plasma and tumour PK profiles as well as the residual receptor activity- and receptor saturation-time profiles for panitumumab and zalutumumab. Similar to the single dosing regimen, a larger %-residual EGFR activity for zalutumumab was observed compared to panitumumab (Figure 5.9, bottom right). Interestingly, both efficacy measures (receptor saturation by the mAb and residual receptor activity) largely differ. The figures clearly show that receptor saturation is almost identical between the two mAbs (Figure 5.9, bottom left) while all other 3 plots of Figure 5.9 show differences. This highlights the importance of using (mechanistic) modelling approaches to translate the binding of the drug into its inhibitory effect and to account for interactions between mAb, ligand and receptor over time.

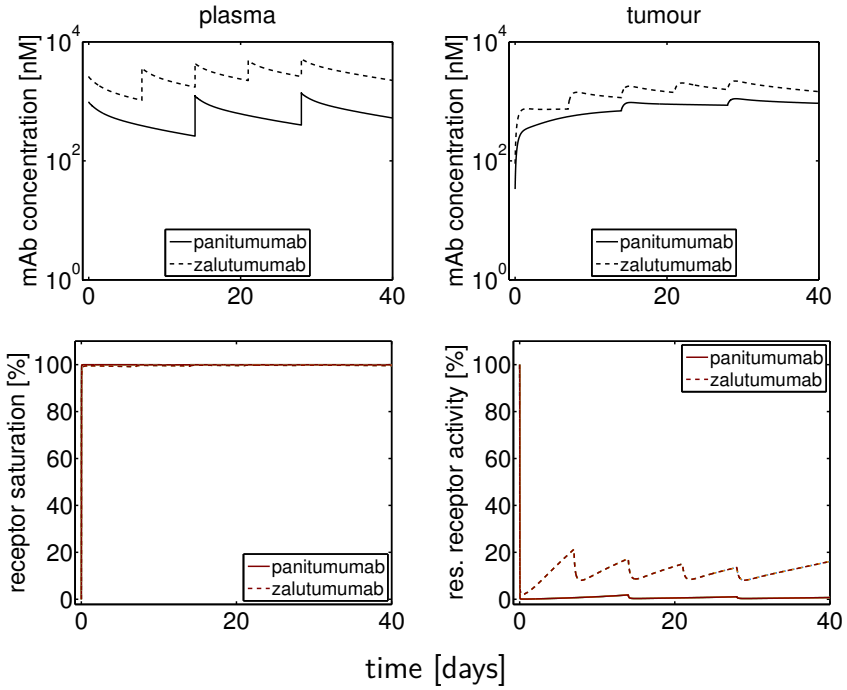

Fig. 5.9.: *Predicted impact of* ***constant natural ligand concentration*** *within tumour (L_{ss} of 0.816 nM) competing for receptor binding with* ***panitumumab*** *following* ***6mg/kg BW q2w*** *and* ***zalutumumab*** *following* ***16mg/kg BW qw***. Simulations of plasma and tumour PK (top), receptor saturation (bottom left) and residual receptor activity (bottom right) are based on the cell-level tumour PBPK model. All four layers are superimposed.

5.5 Impact of tumour microenvironment on therapeutic efficacy of anti-EGFR mAbs

So far, we assumed a constant ligand EGF concentration within tumour tissue to study the impact of ligand-drug competition for receptor binding on therapeutic efficacy of anti-EGFR mAbs in human patients. Tumour EGF concentration, however, is excepted to dynamically change over time, e.g., due to mAb-receptor interaction and/or EGF permeation between tumour and other organs/plasma. These factors may be largely influenced by the tumour microenvironment, e.g., permeability of tumour vessels and intra-tumoural diffusivity.

In the present section, the objective was to study the impact of tumour microenvironment on therapeutic efficacy of anti-EGFR mAbs by examining how changes in

A) tumour ligand EGF concentration,
B) tumour vascular permeability (affecting the exchange between capillary and tumour tissue) and
C) intra-tumoural diffusivity

influence both, mAb and ligand EGF intra-tumoural distribution.

The cell-level tumour PBPK model with natural ligand was applied. We assumed the tumour CMT to consist of 4 layers. Simulations were conducted following a single clinical dose of panitumumab (i.e., 6 mg/kg BW [150]). Panitumumab plasma concentrations and free (i.e., unbound) panitumumab tumour concentrations as well as EGF plasma and free EGF tumour concentrations were simulated over time for human patients (male, BW 73 kg, V_{tum}=0.014 mL/kg). EGFR saturation by panitumumab, and residual EGFR activity were calculated as in the previous section.

Scenario (A): Impact of tumour ligand concentration

Simulations were conducted based on constant tumour ligand concentration vs. dynamically changing tumour ligand concentration over time. Figure 5.10 shows the concentration-time profiles of EGF in plasma and free EGF in tumour tissue as well as %-residual EGFR activity and %-EGFR saturation. Based on dynamically changing tumour ligand EGF concentration, an initial accumulation of EGF within tumour tissue was observed (Figure 5.10, top right) that depends on the ratio of affinity of mAb and EGF towards EGFR as well as on the permeation of EGF into plasma. At the same time, a similar minimum residual EGFR activity for both scenarios was observed, however, the duration of residual EGFR activity differed

between the scenarios (Figure 5.10, bottom right). Note that the change in EGF plasma concentration (Figure 5.10, top left) is only minimal in comparison to the changes in free EGF tumour concentration. This can be understood by the much larger plasma volume than tumour volume. The plasma compartment acts as a 'sink' for ligand leaving the tumour tissue. The simulations show that despite changes in tumour ligand concentration, there is no change in receptor saturation and only minor changes in residual receptor activity.

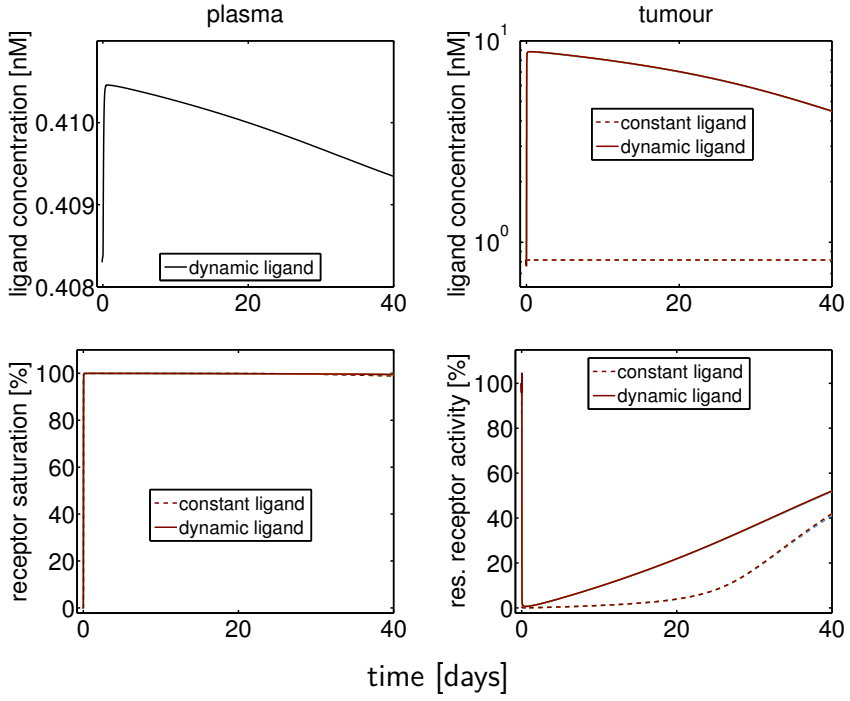

Fig. 5.10.: *Predicted impact of tumour microenvironment:* ***scenario (A) impact of tumour ligand concentration*** *for* ***panitumumab*** *following* ***SD 6 mg/kg BW***. Simulations of ligand plasma and tumour concentration (top), receptor saturation by the mAb (bottom left) and residual receptor activity (bottom right) are based on the cell-level tumour PBPK model with ligand at constant vs. dynamically changing tumour ligand concentration. All layers are superimposed.

Scenario (B): Impact of tumour vascular permeability

To examine the impact of tumour vascular permeability, the cell-level tumour PBPK model with dynamically changing tumour ligand EGF concentration was applied. In Figure 5.11, the predicted impact of changes in EGF and mAb vascular permeability to tumour tissue were illustrated based on two scenarios: In scenario 'reference P', permeability P of mAb and ligand was based on literature values (see Table 5.1). In scenario 'reduced P', permeability P of both, mAb and ligand was one order of magnitude reduced. Differences in tumour vasculature were assumed to affect vessel permeability of the mAb and the ligand in the same way. Note that the reference

vessel permeability of EGF is larger than the vessel permeability of the mAb due to lower MW of EGF.

For 'reduced P' the free tumour mAb concentration and plasma EGF concentration is reduced, while the free tumour EGF concentration is increased (see Figure 5.11). Furthermore, the %-residual EGFR activity was much larger compared to scenario 'reference P'. The increased %-residual EGFR activity can be explained, on the one hand, by the larger free tumour EGF concentration and on the other hand, by the lower free tumour mAb concentration.

Changes in vascular permeability highly influence residual receptor activity (Figure 5.11, bottom right), however, the impact on receptor saturation is minimal (Figure 5.11, bottom left). This can be explained by the fact that RC is dominating over the receptor species RL and R.

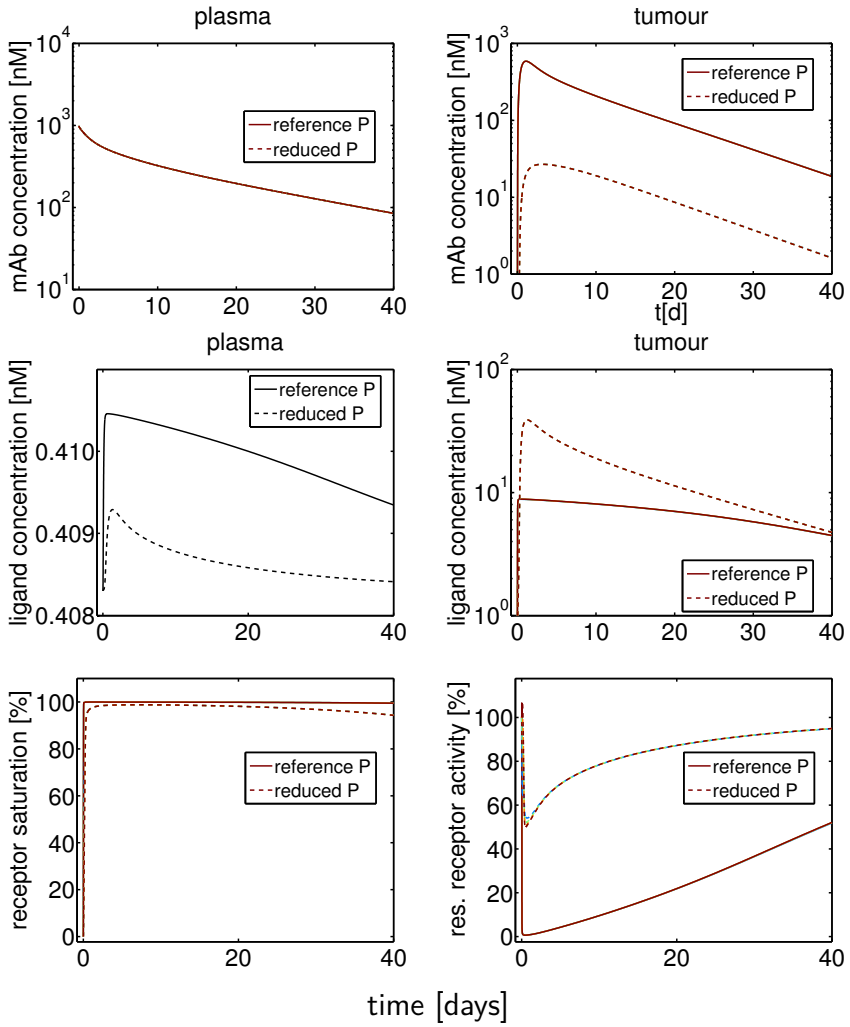

Fig. 5.11.: *Predicted impact of tumour microenvironment:* ***scenario (B) impact of tumour vascular permeability*** *following* ***panitumumab SD 6 mg/kg BW***. Simulations of mAb plasma and tumour PK (top), ligand plasma and tumour concentration (middle), receptor saturation by the mAb (bottom left) and residual receptor activity (bottom right) are based on the cell-level tumour PBPK model with ligand dynamics. In scenario 'reference P', permeability P of mAb and ligand is based on literature values (see Table 5.1). In scenario 'reduced P', P of both, mAb and ligand is one order of magnitude reduced. All layers are superimposed.

Scenario (C): Impact of intra-tumoural diffusivity

Parameter values for effective intra-tumoural diffusivity of mAb and ligand were determined experimentally primarily in mouse xenograft models [161] and assumed to be identical for human (Table 5.1). Diffusivity, however, may differ between xenograft tumours and the clinical setting, where tumours can be highly heterogeneous with inter-patient, intra-patient as well as intra-tumoural variability [20].

To examine the impact of intra-tumoural diffusivity on therapeutic efficacy of anti-EGFR mAbs, the cell-level tumour PBPK model was used and 'dynamically changing tumour EGF concentration' within tumour tissue was assumed. In Figure 5.12, the predicted impact of changes in EGF and panitumumab effective intra-tumoural diffusivity was illustrated based on two scenarios: In scenario 'reference D', diffusivity D of mAb and ligand is based on literature values (see Table 5.1). In scenario 'reduced D', intra-tumoural diffusivity D of both, mAb and ligand is three orders of magnitude reduced mimicking a stiff tumour interstitial fluid space [29]. Note that vessel permeability of mAb and ligand was set to the reference values (see Table 5.1).

Following differences between scenario 'reduced D' and 'reference D' were observed (Figure 5.12): All layers show a decreased plasma ligand concentration (Figure 5.12, middle left). Within layers 2 to 4 (layers more distant from the capillary), an increased free tumour ligand concentration (Figure 5.12, middle right) was observed. Furthermore, a decreased free tumour mAb concentration (Figure 5.12, top right) and an increased %-residual receptor activity (Figure 5.12, bottom right) compared to scenario 'reference D' can be seen. In contrast, within layer 1 (near the capillary), a decreased free tumour ligand concentration (Figure 5.12, middle right) and increased free mAb tumour concentration (Figure 5.12, top right) was observed and thus decreased %-residual receptor activity (Figure 5.12, bottom right) compared to scenario 'reference D'. The lower the effective intra-tumoural diffusivity of both, mAb and ligand, the more heterogeneous their tumour distribution and the lower the therapeutic efficacy in terms of %-EGFR receptor activity in particular for the tumour layers 2 to 4.

Due to the reduced intra-tumoural diffusivity, the free mAb concentration is highest in layer 1 being closest to the vessel and gradually declines with lowest concentration in layer 4 farthest from the vessel. Nevertheless, the mAb concentration within each tumour layer is still large enough to displace the ligand from receptor binding (see 100% receptor saturation). Ligand in layer 1 can still 'escape' via permeation into plasma. This is the main difference between layer 1 and layers 2 to 4 leading to reduced ligand concentration within layer 1 while ligand concentration within layers 2 to 4 is increased compared to scenario 'reference D'. In scenario 'reference D', the mentioned difference between layer 1 and layers 2 to 4 becomes negligible due to larger intra-tumoural diffusivity of both, mAb and ligand.

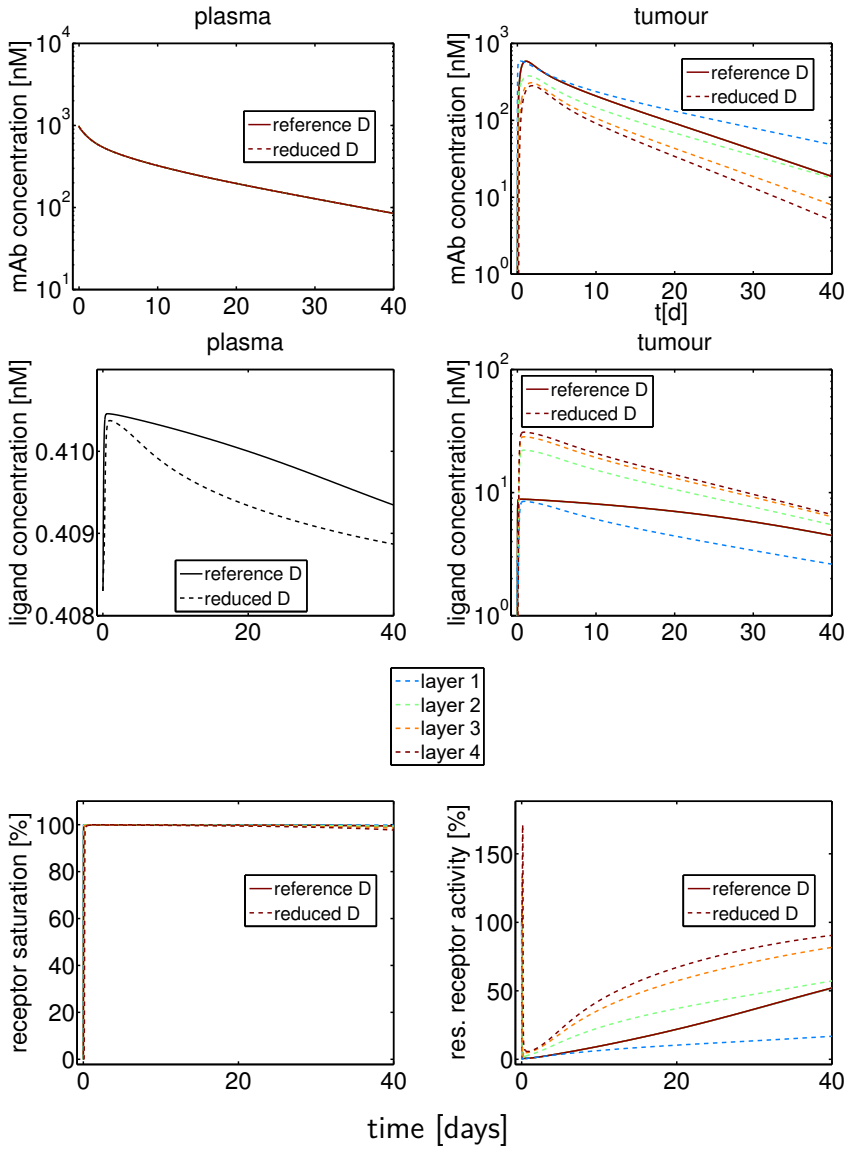

Fig. 5.12.: *Predicted impact of tumour microenvironment:* ***scenario (C) impact of intra-tumoural diffusivity*** *following* ***panitumumab SD 6 mg/kg BW***. Simulations of mAb plasma and tumour PK (top), ligand plasma and tumour concentration (middle), receptor saturation by the mAb (bottom left) and residual receptor activity (bottom right) are based on the cell-level tumour PBPK model with ligand dynamics. In scenario 'reference D', diffusivity D of mAb and ligand is based on literature values (see Table 5.1). In scenario 'reduced D', D of both, mAb and ligand is three orders of magnitude reduced.

5.6 Discussion

In this chapter, we developed a physiologically- and cell-level-based modelling approach that integrates a tumour distribution model and a cell-level TMDD model. It allows to study in detail mAb and natural ligand distribution within tumour tissue and its implications for therapeutic efficacy in cancer therapy. The model enables to study the impact of variations in parameter values such as tumour ligand concentration, vascular permeability and intra-tumoural diffusivity that may arise from changes in tumour microenvironment as well as the impact of tumour volume on intra-tumoural distribution of mAb and ligand. Furthermore, the modelling framework allows to study the interactions between mAb, ligand and receptor over time and to study the plausibility of different mechanisms of actions. The latter is important, since mAbs often exert their therapeutic effect via multiple mechanisms [1] and various efficacy measures can be related to the observed clinical effect.

In comparison to prior work, our modelling approach has several advantages: In 2016, Cilliers and Thurber et al. [19] coupled a PBPK model with a detailed tumour distribution model represented by krogh cylinder geometry. The authors used their model to analyse experimental results on the ADC T-DM1 tumour distribution in HER2-positive mouse xenografts. Antibody-receptor interaction within tumour tissue was modelled using a TMDD model, which, in contrast, does not include the internalisation of free receptor nor ligand-mAb-receptor interactions. Cilliers and Thurber et al. used partial differential equations (PDEs) to describe changes of free mAb and ADC concentration over time and space. We showed that a tumour krogh cylinder model with 4 layers leads to a layer thickness corresponding to the width of a single tumour cell. This questions a further division of the krogh cylinder model and the use of PDEs. Furthermore, our modelling framework allows to address additional questions, e.g., the extrapolation of mice to humans, the impact of internalised receptor, and the impact of the competition between mAb and ligand for receptor binding. In addition, due to the integrated single cell-level model, we believe that it is much easier to interpret and to implement. Depending on the tumour physiology and growth pattern, the geometry to represent antibody and ligand tumour distribution can be adapted (for a comparison between cylindrical and spherical geometry, see Appendix section A.3.2).

In the first part of this chapter, the impact of tumour volume on ADC T-DM1 intra-tumoural distribution and therapeutic efficacy in terms of receptor saturation was assessed. Experimentally observed heterogeneous and sub-saturating T-DM1 tumour distribution in xenograft mice following single dose [19] was supported by our developed modelling approach. In contrast, extrapolation to human patients (with clinically relevant tumour volume) yielded homogeneous T-DM1 tumour distribu-

tion and approx. 100% receptor saturation within tumour tissue. The predicted differences in receptor saturation between mouse and human can be explained by their differences in tumour volume per body weight, which affects TMDD CL and ultimately plasma PK and exposure. Plasma PK above a certain threshold is an important surrogate for therapeutic efficacy that can be used in the clinic to develop dosing strategies to guarantee receptor saturation: Our observed strong relationship between T-DM1 trough plasma concentrations and its receptor saturation, in particular for treatment cycle 1, supports studies by Chen et al. [174], where cycle 1 minimum plasma concentration was reported as an indicator for improved overall survival in T-DM1 therapy. To verify the clinical relevance of our predicted decrease in receptor saturation, our *in silico* study suggests a clinical trial, where the standard clinical dosing of T-DM1 (3.6 mg/kg BW q3w) could be compared with our proposed dose intensification strategy within the initial treatment cycle (see section 5.3). However, this also requires close monitoring in patients for adverse events, since ADCs have a relatively narrow therapeutic window [2].

ADCs represent a heterogeneous mixture of various species with different DAR and a small amount of naked antibody [52]. We made the simplifying assumption that independent of the payload, each ADC species has the same (PK) properties as the naked mAb. We are aware that the PK can be much more complex, with differences between ADC species dependent of their DAR [52, 171]. As an example, deconjugation is an important component of the elimination of ADCs, which leads to a decrease in average DAR over time and subsequently largely impacts their PK [52]. We only made this simplifying assumption to illustrate the concepts of ADC PK, tumour distribution and efficacy. A possible extension is to incorporate the deconjugation process and to model the different DAR species, although it would multiply the number of equations used in the developed modelling framework.

Heterogeneous antibody distribution within solid tumour tissue is intensively discussed as a factor limiting the therapeutic efficacy of ADCs [19]. Our analysis suggests that ADC tumour distribution may be homogeneous in humans, in contrast to the heterogeneous tumour distribution in xenograft mice (single dosing). The predicted differences are plausible due to the difference in tumour volume per body weight. After multiple dosing with shortened dosing interval (qw for mice compared to q3w in humans), the heterogeneous distribution will disappear for mice. Thus, not dose per body weight but rather exposure (e.g., AUC or Cmin) should be used for extrapolation.

In the light of our predicted homogeneous ADC tumour distribution in humans, the question remains whether heterogeneous tumour distribution is really a limiting factor to achieve consistently high clinical success rates in ADC tumour therapy. Particularly as heterogeneous antibody distribution within tumour tissue is not

always associated with lower therapeutic efficacy. Whether tumour heterogeneity of ADCs is associated with lower efficacy depends, among others, on the toxicity of the payload [19]. A highly toxic payload leads to cell death at subsaturating ADC concentrations. In this case, heterogeneous ADC tumour distribution results in an overkill of tumour cells near the blood vessels and to off-tumour cell-toxicity, while leaving cells in the tumour centre unharmed [1]. Conversely, ADCs with a low toxic payload require a saturating number of ADCs per tumour cell for tumour cell death. In this case, a saturation of receptors on tumour cells near the blood vessels has a larger efficacy than a sub-saturated homogeneous ADC distribution throughout whole tumour tissue [19].

Many monoclonal antibodies targeting solid tumours are administered in short dosing intervals at relatively high doses making it possible to approach tumour saturation. Therefore, the question arises whether and/or why antibodies targeting tumour antigens expressed on tumour cells are rarely curative by themselves [33, 175, 176]. In the initial phase of first-line therapy in cancer treatment, in particular in the neo-adjuvant setting (i.e., prior to surgery), mAbs are often administered in combination with standard chemotherapy to reduce tumour size [33, 175]. The question remains whether tumour penetration is really a limiting factor. HER2 targeted approaches have revolutionised the treatment and outcomes of breast cancer therapy. Resistance to treatment, however, remains a clinical challenge, e.g., due to mutations in the signalling pathways [176, 177] and may be a possible reason why mAbs are rarely administered as monotherapy in the initial phase of first-line therapy in cancer treatment. Furthermore, cancer is a multifactorial disease and the optimal treatment strategy depends on a large number of factors such as age, tolerance to treatment, treatment setting, performance status and co-morbidities. The influence of these factors likely has a major impact on clinical decision-making [178].

In section 5.5, we investigated the changes in ligand and mAb vascular permeability as well as effective diffusivity. We observed that the lower the vascular permeability to tumour tissue of both, mAb and ligand, the lower the therapeutic efficacy (i.e., larger EGFR residual activity). In this context, the question arises about the consequences for anti-angiogenic treatments that are intended to modify tumour microenvironment to ultimately increase drug delivery to tumour. Bevacizumab is administered to 'normalise' tumour vasculature, which may result in e.g., reduction of vascular permeability *in vivo* [1]. In this case, a reduced vascular permeability, however, may not directly result in lower therapeutic efficacy due to competing bevacizumab effects such as reduced interstitial fluid pressure, increased blood flow and increased oxygenation [1]. In addition, our observed larger *in silico* EGFR residual activity for zalutumumab in comparison to panitumumab may not automatically result in less therapeutic efficacy: The antibody therapeutic effect can also

be mediated due to indirect cytotoxic effects via recruitment of immune cells due to mAb binding to Fcγ receptors or recruitment of complement factors. In these cases, the fraction of bound mAb that is presented to the extracellular space is an important measure for therapeutic efficacy.

6 Conclusion and Outlook

We already summarised the major findings and critically discussed the assumptions of the developed modelling approach and the obtained results at the end of the three main chapters within this thesis. Thus, in the following, we highlight the major impact of our work and only briefly summarise the limitations and possible extensions of this work.

Mechanistic understanding of factors that govern the PK of mAbs is critical for drug development and the optimisation of effective therapies. PBPK models offer a physiological and mechanistic framework, which is of advantage in the context of animal to human extrapolation. PBPK models for sMDs are used throughout all stages of drug development [3]. However, in comparison to sMDs, for mAbs, the potential of PBPK modelling has so far not yet been fully exploited [3]. Current approaches for mAb PBPK modelling lack a *consensus* on the representation of physiology and its parameterisation [4]. In addition, existing mAb PBPK models are typically much more detailed requiring many assumptions or loose completely the level of individual organs. Similarly to sMD PBPK models, the advent of methods to predict tissue-to-plasma partition coefficients, also termed ABCs [6], has the potential to significantly increase the application of mAb PBPK models in therapeutic mAb discovery and development.

In this thesis, we developed a *consensus* mAb PBPK model that is of simple and comparable complexity as for sMD PBPK models. The *consensus* PBPK approach takes into account recent insights into mAb distribution (ABC values, interstitial IgG pharmacokinetics [21]) to predict common target-independent PK across several pre-clinical species and humans with only unknown parameters related to CL processes. A main advantage in comparison to existing modelling approaches, such as the minimal PBPK model [73, 74] or classical CMT models, is the ability to predict tissue concentrations (based on plasma data only). In addition, the parameters of the *consensus* PBPK model have a physiological interpretation, and equally important, variability can be incorporated mechanistically.

Therapeutic mAbs are associated with substantial mAb-to-mAb PK variability, e.g., related to drug parameters such as charge, size, glycosylation and binding affinity towards FcRn [118]. There still remain several directions of research to be investigated to explain mAb atypical PK that is not related to the target. As an example,

variation in charge of the antibody may impact tissue distribution and hence, it may impact the antibody biodistribution coefficients. To our knowledge, so far there is no quantitative information on the dependency of ABCs on isoelectric point and thus, we did not include variability between mAbs related to charge. Moreover, the *consensus* PBPK model does not take into account additional factors for mAb disposition related to the systems part, e.g., co-medication, immunogenicity or disease status. Data of more patients is necessary to stratify the derived median CL according to patient's disease and to incorporate disease status into the *consensus* PBPK model. As soon as a more detailed quantitative understanding and data becomes available, such factors can easily be integrated in the presented *consensus* PBPK model.

So far, the *consensus* PBPK model was successfully used to extrapolate mAb PK from rodents to human adults. This leads to the question whether the model is also applicable to extrapolate from human adults to paediatric patients. Physiological parameters, i.e., organ volumes as well as blood and lymph flows in children can be used for extrapolation of mAb PK from human adults to children. However, we also have to account for other physiological differences between children and adults, e.g., related to the blood brain barrier and saturable PK pathways have to be considered. For each PK process, i.e., absorption, distribution and elimination, there are considerable knowledge gaps regarding children-specific properties that influence mAb PK [179]. The impact of growth and maturation on PK parameters has not yet been well characterised for mAbs [179]. In this context, the abilities of currently available PBPK modelling approaches to predict mAb PK in paediatric populations have to be investigated. First research in this direction has been done during an internship (I2 module as part of the PharMetrX PhD program) at F. Hoffmann-La Roche Ltd., where current available empirical modelling methods to predict PK and to determine exposure in children were explored as well (see Appendix section A.4.2 'Model-based predictions of mAb clearance in paediatric populations').

We demonstrate that the *consensus* PBPK model provides valuable mechanistic understanding, e.g., to assess the impact of physiological factors, such as FcRn concentration and endogenous IgG on unspecific mAb CL. The gained knowledge is of both, pre-clinical and clinical relevance. Studying the impact of lowered endogenous IgG concentrations—as present in immunodeficient mice—on unspecific therapeutic antibody CL revealed that under therapeutic mAb doses as typically used in humans (in contrast to high dose IVIG therapy), the unspecific CL is effectively linear. This can be expected to also hold for immunosuppressed cancer patients. Knowledge on the unspecific CL can also be included as a prior in the analysis of mAb PK data exhibiting TMDD, thus allowing for a more precise estimation of the target-related parameters. In accordance with these findings, variability related to FcRn is implicitly included in the *consensus* PBPK model. Variability in binding affinity towards FcRn was shown to have minimal impact on the model fit. There

continues to be a need to understand the quantitative relationship between *in vitro* FcRn binding affinity and *in vivo* PK, where the current available literature suggests mixed results towards a correlation [118]. *In vitro* KD often overestimates the mAb affinity; most likely due to a simplified assay system, which does not represent the complex situation *in vivo* [11]. A quantitative relationship between *in vitro* KD and *in vivo* half-life has not been well-established [69, 144]. This suggests that other factors than binding to FcRn may play an important role, e.g., endosomal sorting and release into systemic circulation. However, factors determining whether IgG is recycled or transcytosed, are not yet fully understood [44]. If such data is available, the *consensus* PBPK model can also be used to answer questions related to the development of engineered mAbs with shorter half-life.

Antibody-drug conjugates are among the most promising classes of mAb-based cancer therapeutics [2]. In current literature [19, 20], the tumour distribution of ADCs is claimed to be a major factor contributing to overall ADC efficacy. In addition, for mAbs competing for receptor binding with natural ligands (e.g. growth factors), the dynamics of receptor and natural ligand play a crucial role in determining mAb efficacy. We extended the *consensus* PBPK model by a detailed tumour distribution model incorporating a single cell-level TMDD model. Our developed modelling approach offers a mechanistic framework to comprehensively investigate mAb and ligand distribution within tumour tissue and its implications on therapeutic efficacy. In comparison to whole-body TMDD models, the cell-level model integrates not only processes such as drug binding and internalisation of drug-receptor complex but also internalisation and recycling of the free receptor that is important to understand mAb PK as well. In addition, the modelling framework allows (i) to study the interactions between mAb, ligand and receptor over time and (ii) to study the impact of variations in parameter values, e.g., ligand concentration, tumour size or variations in tumour microenvironment on mAb and ligand intra-tumoural distribution. Based on the observed phenomena it is possible to reflect on therapeutic utility and dosing regimens in mAb cancer treatment. The incorporation of tumour growth and the influence of drugs (e.g. toxic payload) on tumour size would represent a highly relevant and interesting extension to our developed modelling framework.

In conclusion, this thesis contributes significantly to a future and routine use of PBPK modelling for large molecules as an integral part of their development. The developed modelling approach serves as a convenient starting point to study mAb disposition in human in detail, including first-in-man studies and target-specific investigation, e.g., to assess the impact of physiological factors, such as FcRn concentration or tumour microenvironment on antibody PK and thus, greatly enhances our mechanistic understanding.

Appendix A

A.1 *Consensus* PBPK model for mAbs

A.1.1 Experimental data

PK data of 29 different mAbs from 32 publications in mice, rats and humans (7 healthy volunteers and 14 patients) were obtained from literature. For details see Tables 3.6+3.7. The analysed mAbs are of IgG isotype, bind to diverse targets and are of different origin (human, humanised, chimeric). While for mice and rats, the investigated mAbs do not display any cross-reactivity to a target, in human patients the mAbs bind with high affinity to their target.

All experimental data were extracted from the respective publications using the software WebPlotDigitizer, version 3.8, Ankit Rohatgi. If not explicitly stated in the respective publications that experimental data have already been corrected for residual blood, we assumed that the experimental tissue data include residual blood and used Eq. (3.7) for comparison of model output and data.

A.1.2 Parameter estimation

We used MATLAB R2013a for modelling and simulation (ode15s solver). Parameter estimation was performed using the 'fminsearchbnd' based on the Nelder-Mead simplex algorithm described in Lagarias et al. [180] and a sum of squared residuals criterion (referred as objective function value = $\sum^{n} (C_{\mathrm{pred}} - C_{\mathrm{exp}})^2$) following log-transformation of experimental data C_{exp} and predictions C_{pred}.

A.1.3 Estimating unspecific CL and predicting mAb PK in non-cross-reactive animal species

In section 3.3.1, the *consensus* PBPK model was used to study experimental plasma and tissue PK data in non-cross-reactive species. For mice and rats, the *consensus* PBPK model in Eqs. (3.1)-(3.2) (without any TMDD term) was fitted to the rodent plasma PK data. For each mAb, only a linear plasma clearance per BW was estimated as the investigated mAbs do not show any cross-reactivity to a target. Estimated $\mathrm{CLpla}_{\mathrm{BW}}$ values are listed in Table 3.6. For all tested mAbs, as shown in Figures A.1+A.2 and in section 3.3.1, the plasma concentration-time profiles agreed well with the experimental data.

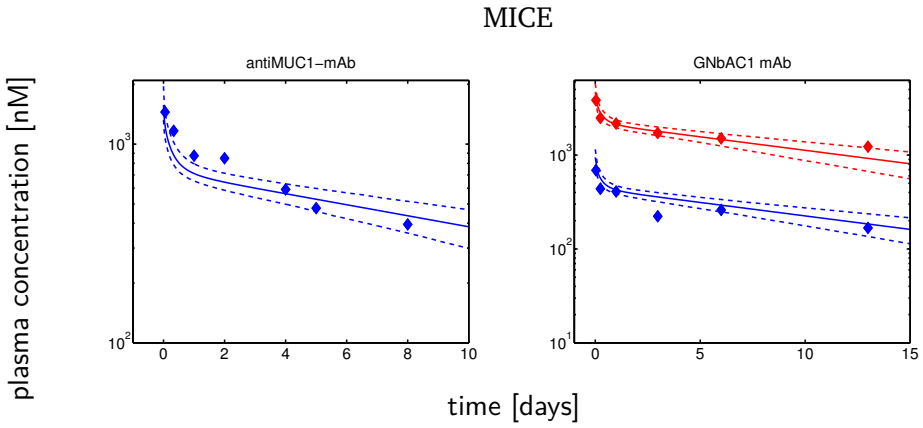

Fig. A.1.: *Predictions of mAb **plasma concentration**-time profiles for **mice**.* Simulations are based on individually fitted plasma clearance and are compared to mean experimental data (filled diamonds) of anti-MUC1 mAb [91] and GNbAC1 mAb [90] in mice. Solid lines represent the reference predictions and dashed lines the 5th and 95th percentiles. The different colours refer to different mAb doses.

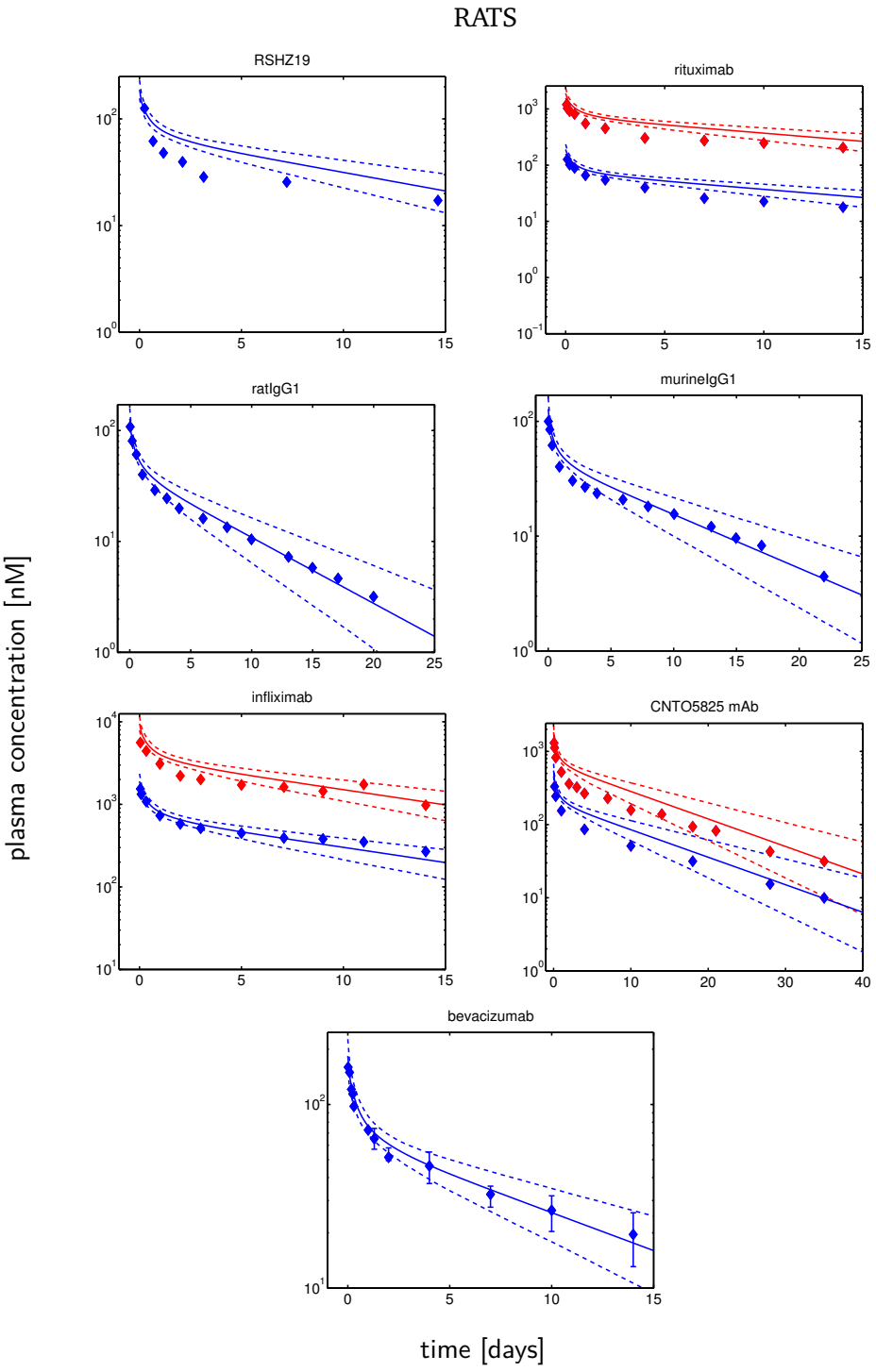

Fig. A.2.: *Predictions of mAb **plasma concentration**-time profiles for **rats**.* Simulations are based on individually fitted plasma clearance and are compared to experimental data (filled diamonds, error bars) of different mAbs (see Table 3.6) in rats. Solid lines represent the reference predictions and dashed lines the 5th and 95th percentiles. The different colours refer to different mAb doses.

A.1.4 Estimating unspecific CL and predicting mAb PK in humans

In section 3.3.2, the *consensus* PBPK model in Eqs. (3.1)-(3.2) with parallel linear and non-linear clearance was used to study plasma (and tissue) PK of different mAbs in human healthy volunteers and patients (for experimental data, see section A.1.1). In all but one case (bevacizumab), also in the presence of target, linear PK for mAbs was observed and the *consensus* PBPK model accurately captured plasma PK profiles of diverse mAb PK data. In these cases, only a linear clearance per body weight (see Eq. (3.11)) was estimated based on the experimental data. Estimated $\mathrm{CLpla}_{\mathrm{BW}}$ values are listed in Table 3.7. Illustrative plasma concentration-time profiles are shown in section 3.3.2 and Figures A.3+A.4+A.5.

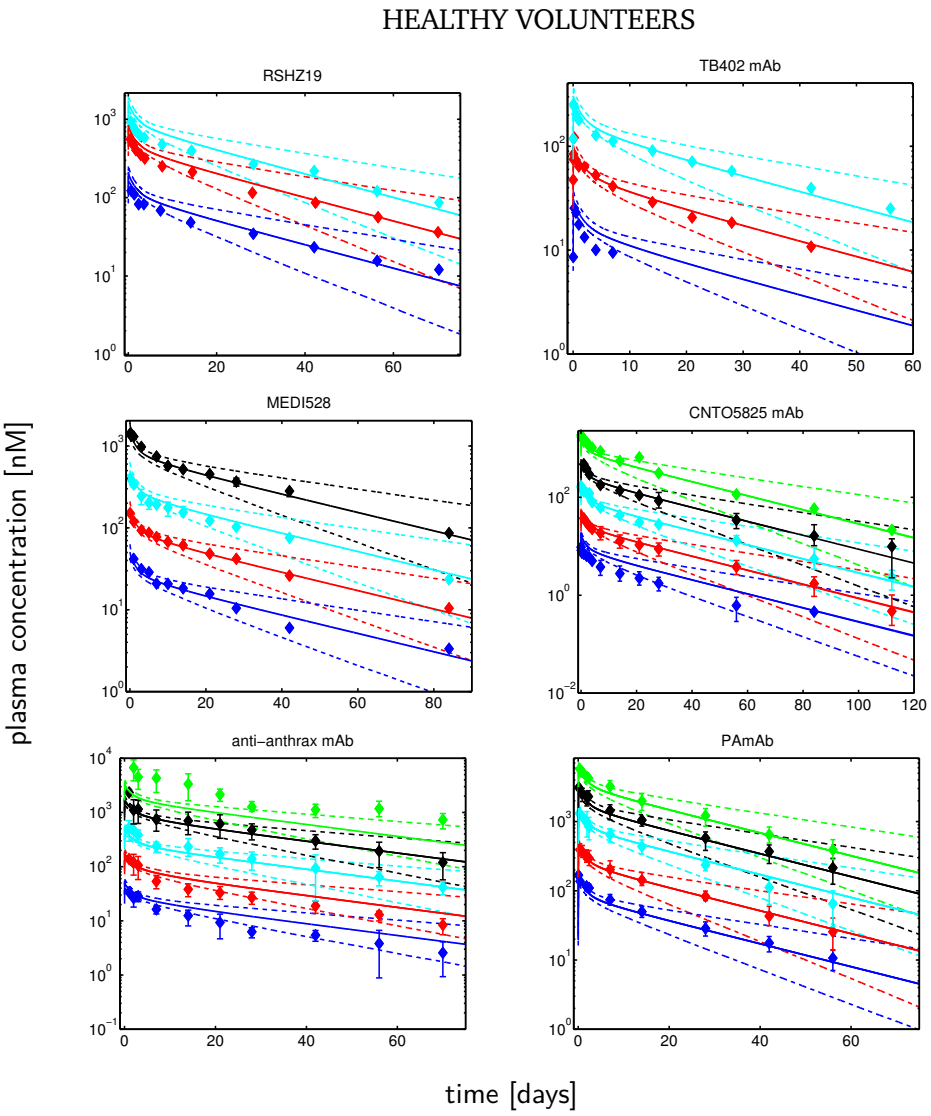

Fig. A.3.: *Predictions of mAb plasma concentration-time profiles for* ***human healthy volunteers*** *based on individually* ***fitted plasma clearance****.* Simulations are compared to experimental data (filled diamonds, error bars) of different mAbs (see Table 3.7). Solid lines represent the reference predictions and dashed lines the 5th and 95th percentiles. The different colours refer to different mAb doses.

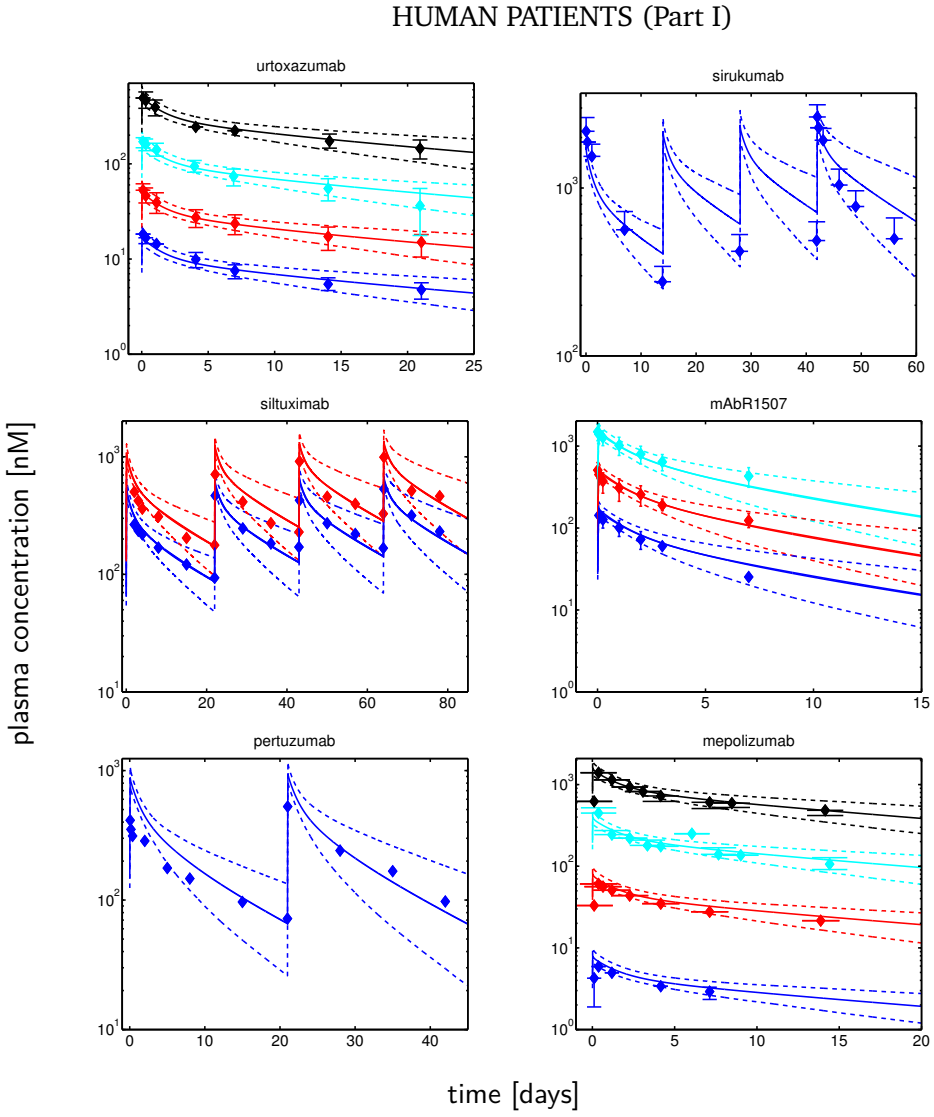

Fig. A.4.: *Predictions of mAb plasma concentration-time profiles for **human patients** based on individually **fitted plasma clearance**.* Simulations are compared to experimental data (filled diamonds, error bars) of different mAbs (see Table 3.7). Solid lines represent the reference predictions and dashed lines the 5th and 95th percentiles. The different colours refer to different mAb doses.

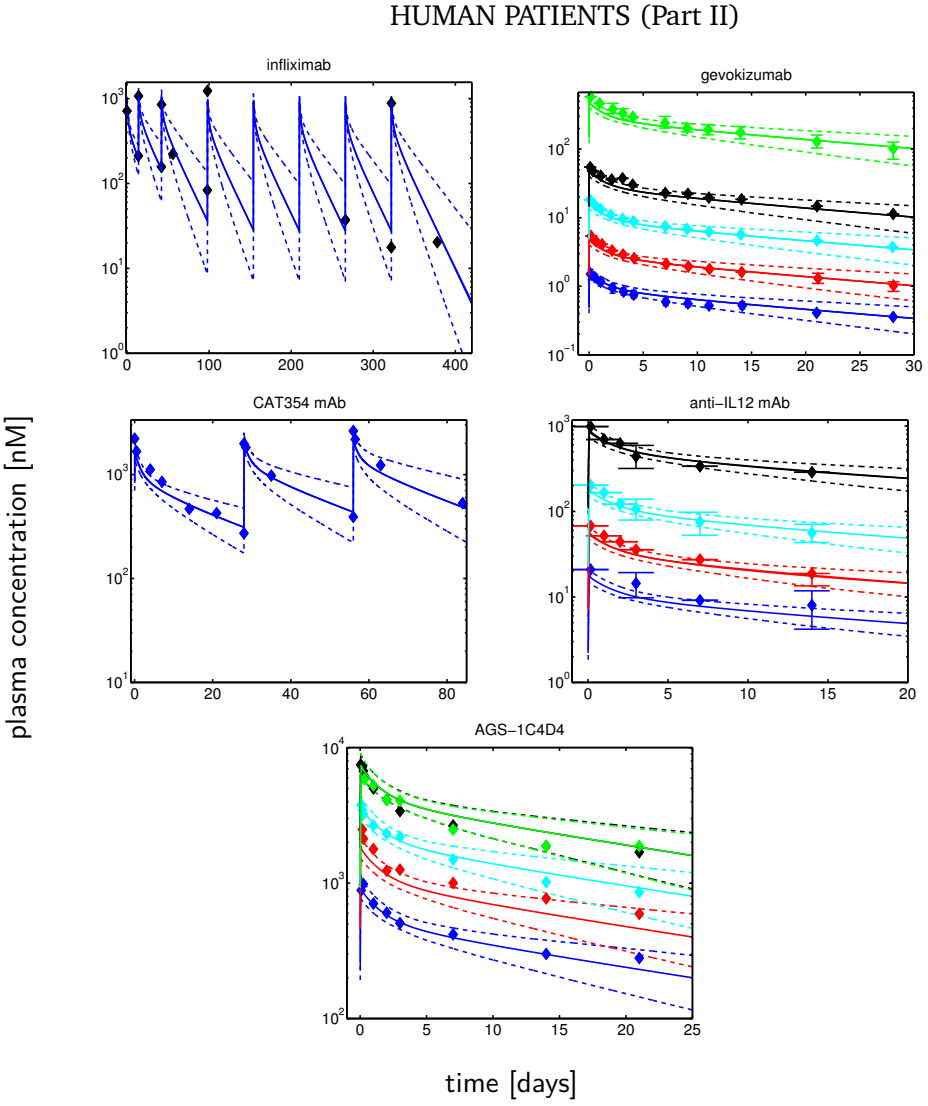

Fig. A.5.: *Predictions of mAb plasma concentration-time profiles for **human patients** based on individually **fitted plasma clearance**.* Simulations are compared to experimental data (filled diamonds, error bars) of different mAbs (see Table 3.7). Solid lines represent the reference predictions and dashed lines the 5th and 95th percentiles. The different colours refer to different mAb doses.

A.2 Impact of endogenous IgG on unspecific mAb clearance

A.2.1 Mice experimental data for model development and evaluation

For model development, experimental data of a murine monoclonal IgG1 antibody, mAb 7E3, were extracted from [79]. 7E3 is an anti-platelet mAb with high affinity for the human glycoprotein IIb/IIIa. The mAb does not bind to the murine glycoprotein IIb/IIIa [79, Chapter 3, Figure 3]. The experimental data include measurements of 125I-labeled 7E3 after a single i.v. bolus dose of 8 mg/kg BW in FcRn wild-type mice (C57BL/6J strain, 25 g BW) in the venous plasma and in lung, heart, kidney, muscle, skin, gut, spleen and liver. Different IVIG doses (0.4, 1 or 2 g/kg BW) were pre-administered intravenously to FcRn wild-type mice (n=3).

To study the influence of endogenous IgG on mAb PK in immunodeficient mice, experimental data of a murine monoclonal IgG1 antibody, mAb 8C2, were extracted from [80, Figure 8a, Figure 8b]. 8C2 is an anti-topotecan mAb without specific affinity for mouse or human antigen. The data include measurements of 8C2 after a single i.v. bolus dose of 1 mg/kg and 25 mg/kg BW in SCID mice (n=3) bearing LS174T xenografts in the venous plasma and in lung, heart, kidney, muscle, skin, gut, spleen and liver. Information on body weight was taken from growth data of SCID mice (C.B-17/ IcrHsd-Prkdc^{SCID}, 4-5 weeks of age, 19 g BW) [181]. When tumour size reached 200 – 300 mm^3, 8C2 was injected intravenously in mice at the given dose with a defined tracer amount of 125I-labeled 8C2.

To study mAb PK in nude (nu/nu) mice (n=6), experimental data of a non-specific murine IgG1 antibody, MOPC21, in plasma, bone, heart, kidney, liver, lung, muscle, skin, spleen, and GI tract were extracted from [65, Figure 1]. The data include measurements of 111-In-labeled MOPC21 after intravenous administration of 3.8 μg in female nude mice (22.15 $\pm$ 1.6 g BW) bearing T380 human colon carcinoma xenografts. T380 cells produce and secrete CEA. The tumour was grown until it reached the size of 472 $\pm$ 110 mg [65].

In [65, 80] the two mAbs were used as a control with no affinity to any tumour antigen. Consequently the tumour acts only as a distributional space and has no influence on clearance. Initial tumour volumes were reported to be $1-2\%$ of mouse body weight and approximately doubled during the experiment. Due to the negligible impact on overall volume of distribution, and lack of data for tumour

lymph flow, vascular reflection coefficient and antibody biodistribution coefficient, we decided not to include a tumour compartment into the PBPK model.

All experimental data were extracted from the respective publications using the software WebPlotDigitizer, version 3.8, Ankit Rohatgi. If not explicitly stated in the respective publications that experimental data have already been corrected for residual blood, we assumed that the experimental tissue data include residual blood and used Eq. (3.7) for comparison of model output and data.

A.2.2 Parameter estimation

We used MATLAB R2013a for modelling and simulation (ode15s solver). Parameter estimation was performed using the 'fminsearchbnd' based on the Nelder-Mead simplex algorithm described in Lagarias et al. [180] and a sum of squared residuals criterion (in the following referred as objective function value = $\sum^{n} (C_{\mathrm{pred}} - C_{\mathrm{exp}})^2$) following log-transformation of experimental data C_{exp} and predictions C_{pred}. 95% CIs were obtained using parameter log-likelihood profiling as described in [182]. Estimation was based on plasma data only.

For nude mice, and SCID mice following dose 1 mg/kg BW, a noticeable difference and strong discrepancy between measured and simulated plasma concentration with the first hours was observed. Since the model already accounts for the distribution processes within the first hours (extravasation) as can be seen, e.g., in SCID mice following 25 mg/kg BW dose (Figure 4.11, plasma, red curve, dose factor =1), we believe that the discrepancy in nude mice and in SCID mice following dose 1 mg/kg has other reasons. For experimentally used antibodies (e.g., mAb 8C2) and therapeutic mAbs the production and purification processes may differ. Furthermore, even for therapeutic standardised mAbs, differences in PK following intravenous administration can occur [183]. Such variability accounts for, e.g., differences between actual and nominal doses following intravenous administration. Thus, in our studies, we estimated a dose factor for nude mice, and SCID mice dose 1 mg/kg BW that can be interpreted as resulting from crystallisation or agglomeration processes following intravenous administration. To do so, we estimated the initial mAb plasma concentration $C_{\mathrm{pla}}(0)$ (separately for nude mice and SCID mice) jointly with the unbound plasma clearance per body weight based on the KD model with identical $\mathrm{K_D}$=4.8 nM at fixed total FcRn concentration. The dose factor was calculated by dividing the estimated initial mAb plasma concentration by the initial mAb plasma concentration without dose factor ($^{\mathrm{dose}}/_{V_{\mathrm{pla}}}$ [nmol/L]).

Tab. A.1.: Immunodeficient mice: Total FcRn concentration and estimated $\mathrm{CLpla_u BW}$ and initial plasma concentration $C_{\mathrm{pla}}(0)$ of murine mAbs; PBPK model with equilibrium binding ($\mathrm{K_D}$=4.8 nM) for murine and human IgG to mouse FcRn (estimation based on plasma data only)

	FcRn[nM] fixed	$\mathrm{CLpla_u BW}$ [L/min/kg] estimate	$C_{\mathrm{pla}}(0)$ [nmol/L] estimate	Obj -
nude mice	3.30e0	6.57e-6	14.37	1.49e-1
SCID mice	6.60e-3	9.14e-6	75.76	3.17e0

A.2.3 FcRn-dependent CL kinetically linked to interstitial fluid of organs

To explicitly model the binding of IgG to FcRn in the endosomes of vascular endothelial cells, we considered the IgG plasma concentration as a surrogate for the corresponding endosomal concentration (see Chapter 4). This is in line with the model by Ferl et al. [67], where uptake is modelled from the vascular space. FcRn in endosome, however, may be also accessible from vascular and interstitial space, as it is modelled, e.g., in [66]. In this section, we analyse, whether our assumption of IgG plasma concentration as a surrogate for the endosomal concentration is reasonable and does not provide contrary results to predictions based on interstitial organ concentrations as a surrogate for the endosomal concentration.

In order to account for FcRn-dependent clearance kinetically linked to the interstitial fluid of organs, we make use of the organ extraction ratio E_{org}. The extraction ratio is estimated for two groups of organs (separately for mAb PK data in FcRn wild-type mice, nude and SCID mice), dependent on the tightness (corresponding to organs adipose tissue, bone, muscle and skin) and leakiness (corresponding to organs liver, heart, lung, kidney, spleen and gut) of the vessel wall. Intrinsic clearance from interstitial fluid of organs $\mathrm{CLint_{int}}$ is determined by the organ extraction ratio. CLpla is calculated via total clearance $\mathrm{CL_{tot}}$ and the plasma clearance corresponding to the different intrinsic clearances from the organs as

$$\begin{aligned}\mathrm{CLpla} = \mathrm{CL_{tot}} &- \sum_{\mathrm{tight}\neq\mathrm{pla}} E_{\mathrm{org}} \cdot L_{\mathrm{org}} \cdot (1-\sigma_{\mathrm{vas}}) \\ &+ \sum_{\mathrm{leaky}\neq\mathrm{pla}} E_{\mathrm{org}} \cdot L_{\mathrm{org}} \cdot (1-\sigma_{\mathrm{vas}}).\end{aligned} \tag{A.1}$$

Note that in this case, total clearance is the sum of plasma clearance and the plasma clearance corresponding to the different intrinsic clearances from the organs. $\mathrm{CL_{tot}}$ was estimated (separately for mAb PK data in FcRn wild-type mice, nude and SCID mice) based on the *consensus* PBPK model with constant CLpla (where $\mathrm{CL_{tot}} = \mathrm{CLpla}$) and with extraction ratios E_{org} set to zero (see Table 4.4).

Fraction unbound of IgG $\mathrm{fu_{IgG}}$ is determined by Equation 4.7 of the equilibrium binding model and calculated dependent on total IgG concentration (i.e. therapeutic IgG and endogenous IgG) and FcRn concentration, both in interstitial fluid of the organs. Endogenous IgG synthesis rate k_{syn} is determined by clearance processes from plasma & interstitial fluid of organs and baseline endogenous plasma concentration $\mathrm{IgG_{endo,baseline}}$ of WT mice, nude and SCID mice:

$$k_{\mathrm{syn}} = (\mathrm{CLpla} + \sum \mathrm{CLint_{int}} \cdot \mathrm{ABC_{int}}) \cdot \mathrm{IgG_{endo,baseline}}. \tag{A.2}$$

The baseline concentration of endogenous IgG in interstitial fluid is computed from $\mathrm{IgG_{endo,baseline}}$ via $\mathrm{ABC_{int}}$:

$$\mathrm{IgG_{endo,baseline,int}} = \mathrm{IgG_{endo,baseline}} \cdot \mathrm{ABC_{int}}. \tag{A.3}$$

FcRn concentration in interstitial fluid was estimated for the two groups of tissues (separately for mAb PK data in FcRn wild-type mice, nude and SCID mice). Hence, intrinsic clearance from interstitial fluid of organs $\mathrm{CLint_{int}}$ is calculated based on total IgG:

$$\mathrm{CLint_{int}} = \mathrm{CLint_u} \cdot \mathrm{fu_{IgG}} \tag{A.4}$$

with maximal unbound clearance for two groups of tissues $\mathrm{CLint_u}$ calculated via $\mathrm{CLint_{int}/fu_{IgG}}$.

Our predictions of mAb PK data in FcRn wild-type mice, nude and SCID mice based on the equilibrium binding model with $1\mathrm{K_D}$ and plasma as a surrogate for the endosomal concentration (Figure 4.2, Figure 4.3, Figure 4.10 and Figure 4.11) are indistinguishable from predictions based on the equilibrium binding model with $1\mathrm{K_D}$ and interstitial organ concentrations as a surrogate for the endosomal concentration. Following the principle of parsimony, we recommend to use plasma as the surrogate concentration.

A.2.4 Accounting for non-equilibrium binding on unspecific CL

To study the impact of altered endogenous IgG on unspecific mAb clearance, we assumed equilibrium binding with $\mathrm{K_D} = (\mathrm{k_{off}}/\ \mathrm{k_{on}})$ to explicitly model the binding of IgG to FcRn (see Chapter 4). When using the equilibrium binding model with $1\mathrm{K_D}$ of 4.8 nM, however, we estimated a different $\mathrm{CLpla_u}$ at comparable total FcRn levels for wild-type mice and immunodeficient mice. Unbound plasma clearance was lower for wild-type mice following IVIG treatment compared to immunodeficient mice at the same total FcRn level of 1.34e4 nM (see Table 4.2 vs. Table 4.3). This may be explainable by a very slow and incomplete (non-equilibrium) binding of IgG to FcRn leading to a high amount of IgG in lysosome or unregulated sorting resulting in FcRn within endo-lysosomes.

We propose a non-equilibrium binding model (see Eq. (A.5)) to analyse whether our hypothesis of an incomplete binding of IgG to FcRn will explain the different values of unbound plasma clearance at same total FcRn between wild-type mice and immunodeficient mice. To account for non-equilibrium binding, we parameterised the unspecific plasma clearance as:

$$\mathrm{CLpla} = \mathrm{CLpla_u} \cdot \mathrm{fu_{IgG}} + \mathrm{CL_{base}} \tag{A.5}$$

with baseline clearance $\mathrm{CL_{base}} = \mathrm{fu_{base}} \cdot \mathrm{CLpla_u}$. We jointly estimated $\mathrm{CLpla_u}$, total FcRn and a baseline clearance $\mathrm{CL_{base}}$ to predict mAb PK data in FcRn wild-type mice following IVIG treatment, nude mice and SCID mice.

Following non-equilibrium binding, we obtained estimates for total FcRn (1.42e4 nM) and unbound plasma clearance per body weight (2.95e-4 L/min/kg BW) that are identical for wild-type mice and immunodeficient mice with a plausible baseline value of the fraction unbound $\mathrm{fu_{base}}$ of approx. 12% ($\mathrm{CL_{base}}$ per BW= 3.5e-6 L/min/kg BW) due to incomplete binding of IgG to FcRn.

A.3 Cell-level tumour PBPK model for mAbs

A.3.1 Derivation of the ordinary differential equations of the cylindrical tumour distribution model

I hereby acknowledge Dr. Niklas Hartung (Institute of Mathematics, University of Potsdam) for assisting me with the mathematical derivation.

In Cilliers and Thurber et al. [19, Suppl.], the common diffusion model in radial coordinates for the free (i.e., unbound) mAb and ADC concentrations $C_{(t,r)}$ within tumour tissue was given by the following partial differential equation:

$$\frac{\partial}{\partial t}C_{(t,r)} = \mathrm{D} \cdot \frac{1}{r} \cdot \frac{\partial}{\partial r}\left(r \cdot \frac{\partial}{\partial r}C_{t,r}\right), \tag{A.6}$$

where D denotes the effective diffusion coefficient.

We discretised the partial derivatives by centred differences:

$$\frac{\partial}{\partial r}\left(r \cdot \frac{\partial}{\partial r}C_{(t,r)}\right) \approx \frac{(r+\Delta r)\frac{\partial}{\partial r}C_{(t,r+\Delta r)} - (r-\Delta r)\frac{\partial}{\partial r}C_{(t,r-\Delta r)}}{\underbrace{(r+\Delta r)-(r-\Delta r)}_{=2\Delta r}}$$

and

$$\frac{\partial}{\partial r}C_{(t,r+\Delta r)} \approx \frac{C_{(t,r+2\Delta r)} - C_{(t,r)}}{\underbrace{(r+2\Delta r)-r}_{=2\Delta r}}.$$

This resulted in the following approximation of Eq. (A.6):

$$\frac{\partial}{\partial t}C_{(t,r)} = \frac{\frac{\mathrm{D}}{r} \cdot \left((r+\Delta r)\left(\frac{C_{(t,r+2\Delta r)}-C_{(t,r)}}{2\Delta r}\right) - (r-\Delta r)\left(\frac{C_{(t,r)}-C_{(t,r-2\Delta r)}}{2\Delta r}\right)\right)}{2\Delta r}.$$

Setting $\mathrm{w} = 2\Delta r$, this yields:

$$\begin{aligned}\frac{\partial}{\partial t}C_{(t,r)} \quad = \quad & \frac{\mathrm{D}}{r \cdot \mathrm{w}} \cdot \frac{r+\Delta r}{\mathrm{w}} \cdot \Big(C_{(t,r+\mathrm{w})} - C_{(t,r)}\Big) + \\ & \frac{\mathrm{D}}{r \cdot \mathrm{w}} \cdot \frac{r-\Delta r}{\mathrm{w}} \cdot \Big(C_{(t,r-\mathrm{w})} - C_{(t,r)}\Big).\end{aligned} \tag{A.7}$$

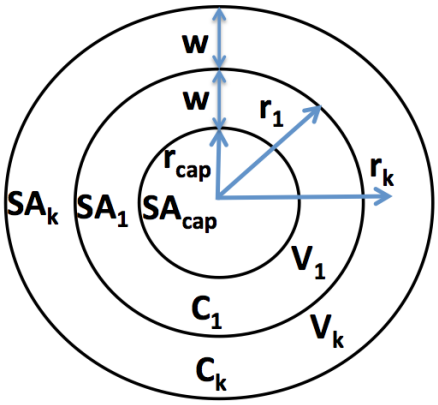

Fig. A.6.: *Schematic illustration of the cylinder disk.*

Defining the volume of some layer at radius r and width $\mathrm{w} = 2\Delta r$ by

$$\begin{aligned}
\Delta V(r) &= V(r+\Delta r) - V(r-\Delta r) \\
&= \pi \mathrm{L} \cdot \Big((r+\Delta r)^2 - (r-\Delta r)^2 \Big) \\
&= \pi \mathrm{L} \cdot \left(\underbrace{(r+\Delta r) - (r-\Delta r)}_{=2\Delta r = w} \right) \cdot \left(\underbrace{(r+\Delta r) - (r-\Delta r)}_{=2r} \right) \\
&= 2\pi \cdot \mathrm{L} \cdot \mathrm{w} \cdot r
\end{aligned}$$

and observing that

$$\mathrm{SA}(r \pm \Delta r) = 2\pi \cdot \mathrm{L} \cdot (r \pm \Delta r),$$

we obtain after multiplication of Eq. (A.7):

$$\begin{aligned}
\Delta V(r) \cdot \frac{\partial}{\partial t} C_{(t,r)} &= \frac{\mathrm{D}}{\mathrm{w}} \cdot \frac{2\pi \cdot \mathrm{L} \cdot r \cdot \mathrm{w}(r+\Delta r)}{r \cdot \mathrm{w}} \cdot \Big(C_{(t,r+\mathrm{w})} - C_{(t,r)} \Big) \\
&\quad + \frac{\mathrm{D}}{\mathrm{w}} \cdot \frac{2\pi \cdot \mathrm{L} \cdot r \cdot \mathrm{w}(r-\Delta r)}{r \cdot \mathrm{w}} \cdot \Big(C_{(t,r)} - C_{(t,r-\mathrm{w})} \Big) \\
&= \frac{\mathrm{D}}{\mathrm{w}} \cdot \mathrm{SA}(r+\Delta r) \cdot \Big(C_{(t,r+\mathrm{w})} - C_{(t,r)} \Big) + \\
&\quad \frac{\mathrm{D}}{\mathrm{w}} \cdot \mathrm{SA}(r-\Delta r) \cdot \Big(C_{(t,r)} - C_{(t,r-\mathrm{w})} \Big).
\end{aligned}$$

Discretising the radial axis as

$$r_k \coloneqq r_{\mathrm{cap}} + k \cdot \Delta \mathrm{w}, \qquad k \in \{1, \ldots, n\},$$

and using the following abbreviations:

$$\begin{aligned}
C_k(t) &\coloneqq C(t, r_k - \Delta r) \\
V_k &\coloneqq \Delta V(r_k - \Delta r) = V(r_k) - V(r_k - \mathrm{w}) \\
\mathrm{SA}_k &\coloneqq \mathrm{SA}\Big((r_k - \Delta r) + \Delta r \Big) = \mathrm{SA}(r_k),
\end{aligned}$$

we finally obtained,

$$V_k \frac{\mathrm{d}}{\mathrm{dt}} C_k(t) = \frac{\mathrm{D}}{\mathrm{w}} \cdot \mathrm{SA}_k \cdot \Big(C_{k+1}(t) - C_k(t)\Big) - \frac{\mathrm{D}}{\mathrm{w}} \cdot \mathrm{SA}_{k-1} \cdot \Big(C_k(t) - C_{k-1}(t)\Big), \tag{A.8}$$

for k $\in \{2, \ldots, n-1\}$.
For k = n, the first term is absent, while for k=1, the second term is absent and an additional term modelling the exchange with the capillary is present, resulting in the following system of ordinary differential equations:

$$\begin{aligned} V_1 \frac{\mathrm{d}}{\mathrm{dt}} C_1(t) &= \frac{\mathrm{D}}{\mathrm{w}} \cdot \mathrm{SA}_1 \cdot \Big(C_2(t) - C_1(t)\Big) + \mathrm{PS} \cdot \Big(C_{\mathrm{pla}}(t) - C_1(t)\Big), \\ V_k \frac{\mathrm{d}}{\mathrm{dt}} C_k(t) &= \frac{\mathrm{D}}{\mathrm{w}} \cdot \mathrm{SA}_k \cdot \Big(C_{k+1}(t) - C_k(t)\Big) + \frac{\mathrm{D}}{\mathrm{w}} \cdot \mathrm{SA}_{k-1} \cdot \Big(C_{k-1}(t) - C_k(t)\Big), \\ V_n \frac{\mathrm{d}}{\mathrm{dt}} C_n(t) &= -\frac{\mathrm{D}}{\mathrm{w}} \cdot \mathrm{SA}_{n-1} \cdot \Big(C_n(t) - C_{n-1}(t)\Big), \end{aligned} \tag{A.9}$$

with k $\in \{2, \ldots, n-1\}$.

A.3.2 Cylindrical vs. spherical tumour distribution model

There are many different types of tumour distribution models and geometries (e.g., spherical, cylindrical geometry or a combination of both). The PBPK tumour CMT of our developed modelling framework in Chapter 5 was represented using a detailed tumour distribution model with krogh cylinder geometry. Depending on the tumour physiology and growth pattern, the geometry to represent antibody and ligand tumour distribution can be adapted. In this section, we present a detailed tumour distribution model based on spherical geometry. Furthermore, we will compare the simulations of the *consensus* PBPK model (i) coupled to the krogh cylinder tumour model (see section 5.1.1) and (ii) coupled with the herein explained spherical tumour distribution model.

'The main difficulty in the experimental study of tumour cords is that they cannot be grown *in vitro*. This explains why much more attention, also by mathematicians, has been devoted to what are called multicellular tumour spheroids (...).' [184, p. 183].

As reported in [185], spherical tumour models were developed to represent tumour spheroids *in vitro*. Such multicellular spheroids are spherical aggregates consisting of many thousand tumour cells. To study the mAb 'binding site barrier' hypothesis within tumour, a spherical model was used by Fujimori and Weinstein [147] to simulate a small pre-vascular tumour nodule with a radius of 150 μm. In their model, the tumour was represented as a sphere with surrounding capillaries and

radial flux of mAb from capillaries towards the centre of the tumour. Note that at a radius of 150 μm, the tumour has not yet developed necrotic regions [147, 186].

Spherical models are also used to represent nodular lymphomas that grow in a nodular (also termed follicular) pattern without developing a necrotic centre [187, 188]. When growing in a nodular pattern, the malignant cells are clustered into nodules with central vessels in each nodule branching to periphery.

In summary, spherical models often represent either

i) a small primary tumour or micrometastasis (with diameter $<$ 300 μm) [186];
ii) the histology of nodular lymphomas, where the tumour consists of N nodules (each nodule has a diameter of $<$ 300 μm;) or
iii) multicellular tumour spheroids *in vitro* [147].

The nodule radius and thus the number of nodules determines the vascularisation degree of the tumour.

For modelling a 'nodular tumour model', we assumed that the tumour tissue volume V_{tis} consists of a number N of nodules (see Figure A.7 (A)). The tissue volume of each nodule V_{nodule} was calculated using the volume equation of a sphere (V(r)=$\frac{4}{3} \cdot \pi \cdot r^3$):

$$V_{\text{nodule}} = V(r) = \frac{4}{3} \cdot \pi \cdot r^3$$

with radius r=150 μm [147, 186]. The number N of nodules within whole tumour tissue was calculated via

$$\frac{V_{\text{tis}}}{V_{\text{nodule}}}. \tag{A.10}$$

To study mAb intra-tumoural distribution, each nodule was divided into n well-stirred layers with equal width and diffusion of the mAb towards the centre of the tumour nodule. The outermost layer of each nodule (i.e., layer 1) is in contact with tumour blood vessels. Equal width between layers within a nodule was defined as w=$\frac{r}{4}$. The tumour tissue volumes of the layers 'k' within each nodule were denoted by $V_1, \ldots, V_n$ and were calculated as:

$$V_k = V(r_k) - V(r_{k-1})$$

with $k \in \{1, \ldots, n\}$.

Within each nodule, each layer consists of interstitial tumour space with interstitial volume of the layers,

$$V_{k,\text{int}} = f_{\text{int}} \cdot V_k$$

and intra-cellular tumour space with cellular volume of the layers,

$$V_{k,\text{cel}} = f_{\text{cel}} \cdot V_k.$$

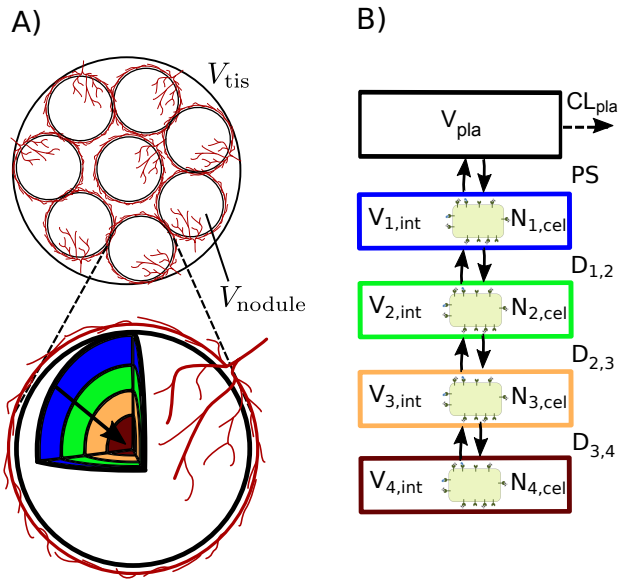

Fig. A.7.: *Illustration of a nodular tumour distribution model.* **A)** Schematic illustration of a tumour consisting of a number of nodules. To study mAb intra-tumoural distribution, each nodule is divided into 4 tumour layers. mAb diffuses towards the centre of the spherical nodule. **B)** Schematic illustration of the tumour distribution model integrating a single cell-level TMDD model. The tumour compartment is divided into 4 layers that consist of interstitial and cellular space. Monoclonal antibody in plasma is allowed to distribute to and from the first tumour tissue layer with the permeability surface area product PS. In each tumour layer, mAb can bind to its receptor or distribute to any adjacent layer.

To integrate antibody-receptor interaction with each layer at the cellular level, the number of cells within tumour layers of each nodule was calculated as

$$N_{k,\text{cel}} = V_{k,\text{cel}}/V_{\text{singlecell}}.$$

To study mAb intra-tumoural distribution, monoclonal antibody in plasma was allowed to distribute to and from the first tumour tissue layer. The exchange between plasma and the first tumour layer was modelled via the permeability surface area product $\text{PS} = \text{P} \cdot \text{SA}_{\text{cap}}$ [dm^3/min].

In each tumour layer, we assumed mAb to bind to its receptor or distribute to each adjacent layer. Diffusion of free mAb in interstitial space between tumour layers was modelled via diffusion exchange rates [dm^3/min] that were calculated as:

$$\text{D}_{k,k+1} = \frac{\text{D}}{\text{w}} \cdot \text{SA}_k$$

for $k \in \{1, \ldots, n-1\}$. $\text{D}_{k,k+1}$ denotes the diffusion exchange rate between layers k and k+1. D represents the effective intra-tumoural diffusion coefficient. The surface

area between the different tumour layers within each nodule was calculated based on the equation of a sphere:

$$\mathrm{SA}_k = 4\pi \cdot r_k^2 \tag{A.11}$$

with (k $\in \{1, \ldots, n-1\}$). SA_k [dm^2] denotes the surface area between layers k and k+1.

Finally, to account for mAb distribution throughout whole tumour tissue, the number of cells of each nodule $N_{\mathrm{cel,nodule}}$, the volumes of the layers of each nodule V_{nodule} and the surface area of each nodule $\mathrm{SA}_{\mathrm{nodule}}$ were multiplied with the whole number of nodules N within tumour tissue. For parameter values, see Table 5.1 and for model structure, see Figure A.7 (B).

We compared the simulations of the *consensus* PBPK model (i) coupled to the krogh cylinder tumour model (see section 5.1.1) and (ii) coupled with the herein explained nodular tumour model following T-DM1 single dose of 3.6 mg/kg BW in mice. Figure A.9 shows the simulated plasma and total tumour PK profiles as well as receptor saturation-time profiles in mice for both geometries. Despite same dose per kg BW and same tumour volume per BW, we observed a marked difference in plasma and tumour PK for both geometries: faster declining plasma and tumour PK profiles for spherical geometry compared to krogh cylinder geometry. For cylindrical geometry, we simulated a heterogeneous and sub-saturating T-DM1 tumour distribution in mice, whereas for spherical geometry, we simulated a homogenous T-DM1 tumour distribution with 100% receptor saturation after approx. 1 day in mice.

The pronounced differences in PK and receptor saturation-time profiles despite same tumour volume per BW and same number of cells within tumour can be explained by the different volumes and surface areas depending on the tumour geometry. For the cylindrical geometry, the mAb diffuses from the centre (capillary) towards the tumour periphery with volumes and surface areas that increase from centre towards periphery. For the spherical geometry, however, the mAb diffuses from the capillary towards the centre of the tumour with decreasing volumes. For visualisation, see Figure A.8.

Thus, the 'binding site barrier' is more pronounced using a tumour represented by cylindrical geometry, especially at high tumour volume per body weight, i.e., 8 mL/kg BW (see Figure A.9). This observation is in line with results by Weinstein and Fujimori [148].

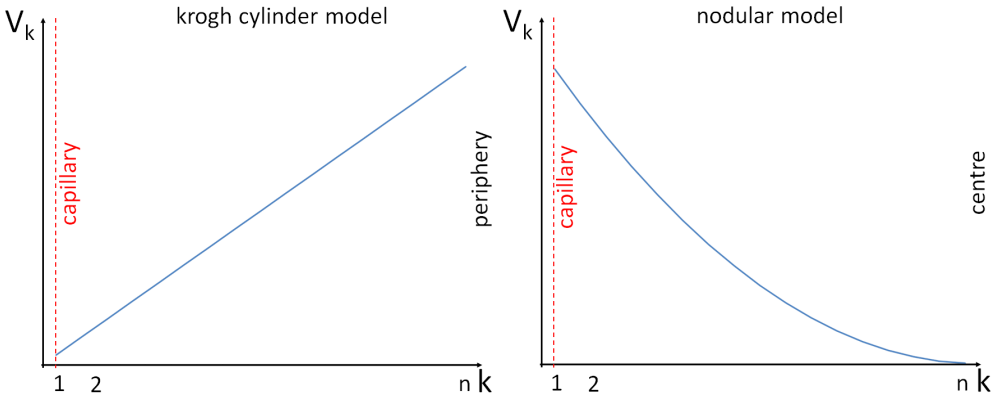

Fig. A.8.: *Schematic illustration of the volume changes for cylindrical and spherical geometry.* For the cylindrical geometry, the mAb diffuses from the centre (capillary) towards the tumour periphery with increasing volumes. For the nodular geometry, however, the mAb diffuses from the capillary towards the centre of the tumour with decreasing volumes.

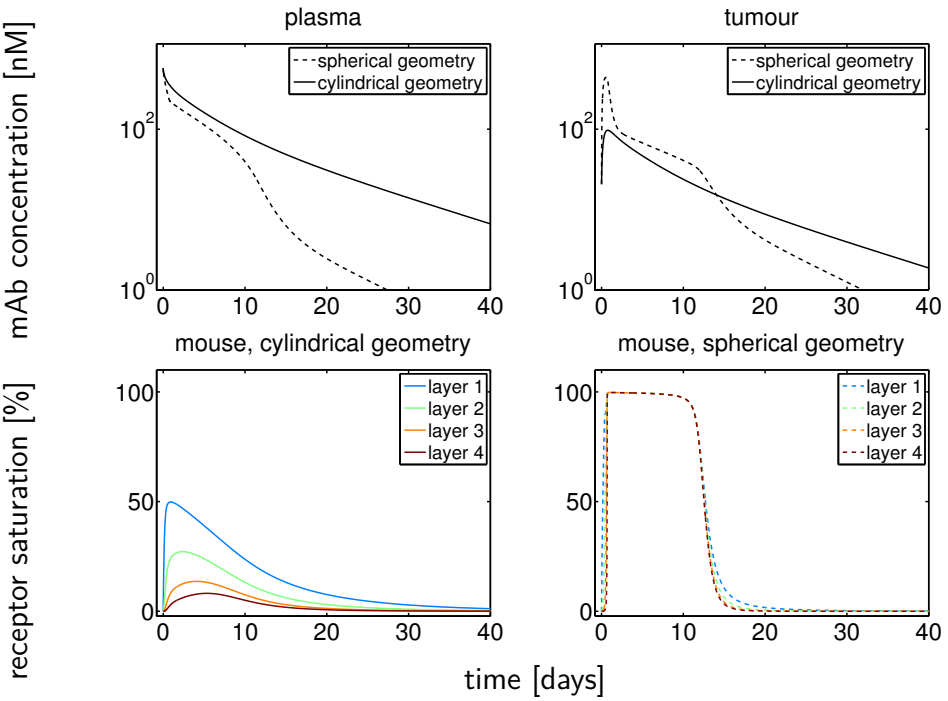

Fig. A.9.: *Predicted **impact of geometry** of the tumour distribution model, i.e., tumour represented using krogh cylinder or spherical geometry on PK and receptor saturation for **mouse** (V_{tum}=8 mL/kg BW).* Simulations are based on the cell-level tumour PBPK model without natural ligand following **T-DM1 single dose of 3.6 mg/kg BW**. The figures below display the receptor saturation (RC/(RC+R))-time profiles.

A.3.3 Impact of tumour ligand concentration on therapeutic efficacy

In section 5.4, we studied the impact of ligand-drug competition for receptor binding on therapeutic efficacy of anti-EGFR mAbs with different K_D values (zalutumumab and panitumumab). A constant ligand EGF concentration within tumour tissue (L_{ss} =8.16e-1 nM, based on EGF MW of 6 kDa) was assumed. We observed from Figure 5.8 that %-residual EGFR activity and %-EGFR saturation were not inversely correlated and %-residual EGFR activity highly differed dependent on mAb K_D. Krippendorff et al. [13], however, predicted similar %-residual EGFR activity despite manifold change in K_D assuming a lower constant tumour EGF concentration (L_{ss}=2.36e-3 nM, based on EGF MW of 133 kDa).

In this section, we present a rationale for the different values of tumour EGF concentrations that were assumed and analyse the impact of tumour EGF concentration on therapeutic efficacy of anti-EGFR mAbs.

Stated differences in EGF concentrations can, e.g., be explained by the different values of EGF MW that are reported within literature. Differences in EGF MW account for the various molecular existing forms. EGF is reported to be synthesised as a precursor form with MW of around 130-160 kDa. The precursor form is trafficked to the cell membrane and processed to the secreted mature soluble protein with MW of approx. 6 kDa [47, 189, 190]. Different organs can contain different amounts of mature protein [47]: As an example, in salivary gland, precursor EGF appears to be processed intracellularly to mature EGF, whereas kidney contains mostly unprocessed EGF with low levels of mature EGF [189]. Both forms, however, are reported to be biologically active and bind to EGFR with same affinity [47, 189].

Figure A.10 shows the simulations of %-EGFR saturation and %-residual EGFR activity for zalutumumab and panitumumab in human patients based on the cell-level tumour PBPK model with low (2.36e-3 nM [13]) tumour EGF concentration. We observed following differences in comparison with our results from section 5.4 (Figure 5.8) based on larger constant ligand EGF concentration within tumour tissue (L_{ss} =8.16e-1 nM):
In Figure 5.8, %-residual EGFR activity highly differed between panitumumab and zalutumumab, whereas in Figure A.10, we observed quite similar %-residual EGFR activity for panitumumab and zalutumumab. Furthermore, in Figure A.10, %-EGFR saturation and %-residual EGFR activity are in an inverse relationship in contrast to Figure 5.8.

The differences in predictions of mAb efficacy in terms of receptor saturation and residual receptor activity when assuming those different values of tumour ligand concentration (Figure 5.8 vs. Figure A.10) highlights the value of our developed modelling framework allowing to study different scenarios.

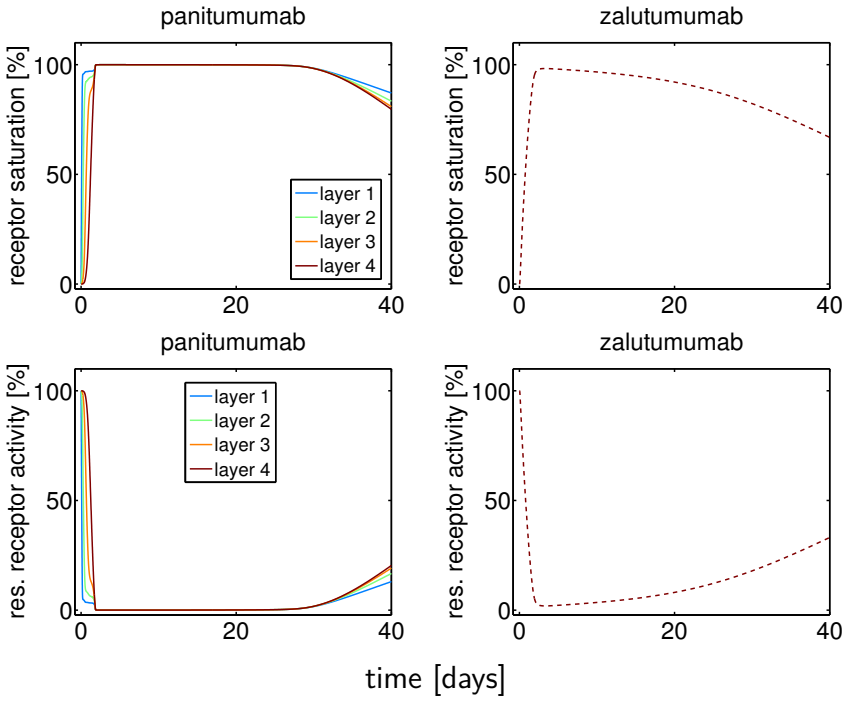

Fig. A.10.: *Predicted impact of low ligand concentration within tumour* (L_{ss} *= 2.36e-3 nM) competing with* ***panitumumab*** *or* ***zalutumumab*** *for receptor binding following* ***SD 6 mg/kg BW*** *in* ***human patients***. Simulations are based on the cell-level tumour PBPK model with constant tumour ligand concentration. For zalutumumab, all four layers are superimposed.

A.4 Model-based predictions of mAb clearance in paediatric populations

This work was conducted during an internship (I2 module) at F. Hoffmann-La Roche Ltd. (Roche Pharma Research and Early Development, Pharmaceutical Sciences, Roche Innovation Center Basel) as part of the graduate research training program PharMetrX: Pharmacometrics & Computational Disease Modelling from September - December 2016.

The FDA act 2012 requires sponsors to submit a paediatric drug development plan to the regulatory agency at the end of Phase II studies [191]. 'The stronger enforcement to obtain paediatric information by the regulatory agencies in recent years resulted in an increased number of trials in children.' [191, p. 364] Defining an adequate first dose in children is one of the main challenges in conducting clinical studies in children in spite of practical and ethical considerations [191]. For sMDs at least for children above two years of age, there are two well-established approaches to predict children PK from adult PK data [60, 192–194]:

- allometric scaling and
- physiologically-based extrapolation.

For children younger than two years, it is known that maturation processes have marked effects on PK parameters [194].

For mAbs, a few methods to predict PK and to determine exposure in children have been suggested in the literature. Mainly these methods include allometric approaches and PBPK models. Unlike for sMDs, a systematic and quantitative comparison of both approaches for mAbs is not available so far [179]. The present study aims to examine the published models that are used to characterise mAb PK in children and to compare the model-based predictions across age. In this context, the impact of growth and maturation on PK parameters has not been well-characterised for mAbs [179, 195]. For each PK process, i.e., absorption, distribution and elimination, there are considerable knowledge gaps regarding children-specific properties that influence PK [179]. Model-based comparison of mAb PK across age in paediatric populations is exemplified by using the example of CL, which is an important PK parameter to determine exposure together with the area under the curve. Our analysis will focus on the unspecific part of mAb PK that is of key relevance when target-mediated processes are saturated (which is often the case for mAbs at steady state dosing).

The present chapter is organised as follows: First, we explore the published empirical models involving paediatric populations to characterise mAb PK and/or compare exposure for various dosing regimens in children. Using these models, we quan-

titatively compare the model-based predictions of clearance (mean and spread) across age. Furthermore, we briefly summarise the abilities of currently available PBPK modelling approaches to predict mAb PK in paediatric populations and include predictions of clearance across age based on PBPK-extrapolation.

A.4.1 Empirical modelling methods to predict PK in paediatric populations - Data & Models

This analysis is based on mAb PK models involving paediatric populations (including individuals below 12 years of age) available in literature. A model from an internal report of F. Hoffmann-La Roche Ltd. was also investigated.[1]

All models aimed to characterise or evaluate the PK of mAbs in paediatric patients using non-linear mixed-effects modelling approach (NLME). NLME models facilitate the quantification of the typical model parameters in the population, their variability among individuals and the residual variability. The NLME approach can be applied to a wide variety of data including pharmacokinetic and pharmacodynamic data and enables for explanation of variability in a population using patient characteristics, also termed covariates. For mAbs, BW is often incorporated as a covariate on clearance in population PK (POP-PK) analyses. Serum albumin concentration (Alb) and ADAs have also been identified to have a large impact on the clearance of mAbs [36]. The pharmacokinetic characteristics of mAbs are reviewed in detail in Chapter 2.

As commonly reported for mAbs, the concentration-time profiles were described by one- or two-CMT models with solely linear elimination and/or non-linear elimination. Within the investigated models, BW and serum albumin concentration were the most frequent covariates on linear clearance. Furthermore, ADA status, body surface area (BSA), body mass index (BMI), sex, race, disease and co-medication were identified as significant covariates on linear clearance. Only in a single study [196], where the PK of palivizumab was analysed, an explicit age-based 'maturation' model was reported for linear clearance. In Table A.2, we provide an overview on the current (late 2016) published mAb POP-PK models where clinical data of paediatric patients was used for model development.

[1] The covariate model for the linear clearance (body surface area) is used here in comparison with similar models from public domain. This relationship is part of a POP-PK model developed at F. Hoffmann-La Roche Ltd. to characterise the PK of mAb X in a paediatric population of roughly 200 patients between 2-17 years (3 patients < 3 years). Detailed values on the clearance parameters and information on mAb X, the patient population, and the developed PK model are not disclosed.

We make use of the following definitions according to the classification of paediatric age categories by the FDA [197]:

- Neonates: Birth to 1 month,
- Infants: 1 month to 2 years,
- Children: 2 to 12 years, and
- Adolescents: 12 to < 16 years.

Tab. A.2.: Overview on the current (late 2016) published mAb POP-PK models involving clinical data on paediatric populations, see text for details

Antibody	Study	Age range of study population (number of individuals)	Covariates on unspecific CL
Palivizumab	[196]	$\leq$ 2 years (1684) & > 18 years (116)	BW, age, race, disease, ADAs
Bevacizumab	[198]	0.5 - 21 years (152)	BW, Alb, sex, disease
Canakinumab	[199]	2 - < 20 years (201)	BW, Alb
Adalimumab	[200]	6 - 17 years (189)	BW, ADAs
Omalizumab	[201]	5 - > 18 years (2155)	BW, BMI
Infliximab	[202]	6 - 76 years (692)	BW, Alb, ADAs, co-medication
mAb X	internal	2 - 17 years (188)	BSA

The different investigated models are based on data of different study populations. For sMDs, extrapolation from adults to children older than two years is possible using size-based scaling [60, 194]. For infants, maturation processes play an important role and need to be taken into account [194]. The question arises whether and to what extent this also holds true for mAbs. As can be inferred from Figure A.11, for mAbs, there is no study, which covers the whole age range, in particular including individuals below and above two years of age. Furthermore, data is generally sparse for infants with only two studies including data for infants and only four studies including data for subjects $\leq$ 3 years of age. In addition, the number of included individuals $\leq$ 3 years of age is generally very low: nine subjects for bevacizumab, 24 subjects for canakinumab and only three subjects for mAb X. The study [196], where the PK of palivizumab was analysed, was the only study including very rich data for infants, i.e., the paediatric dataset was comprised of 1684 patients $\leq$ two years of age and preterm infants were included as well.

The presented NLME models used to characterise mAb PK in children mainly include purely body weight-based scaling methods where adult pharmacokinetic parameter values are scaled to children based on size models (allometric scaling). Applying simple allometry, the typical value of linear clearance is often described as a function of individual body weight normalised by the reference body weight of 70 kg with a fixed allometric exponent of 0.75 [196, 198]:

$$\mathrm{CL} = \mathrm{CL}_{\mathrm{pop}} \cdot \left(\frac{\mathrm{BW}}{70}\right)^{0.75} \tag{A.12}$$

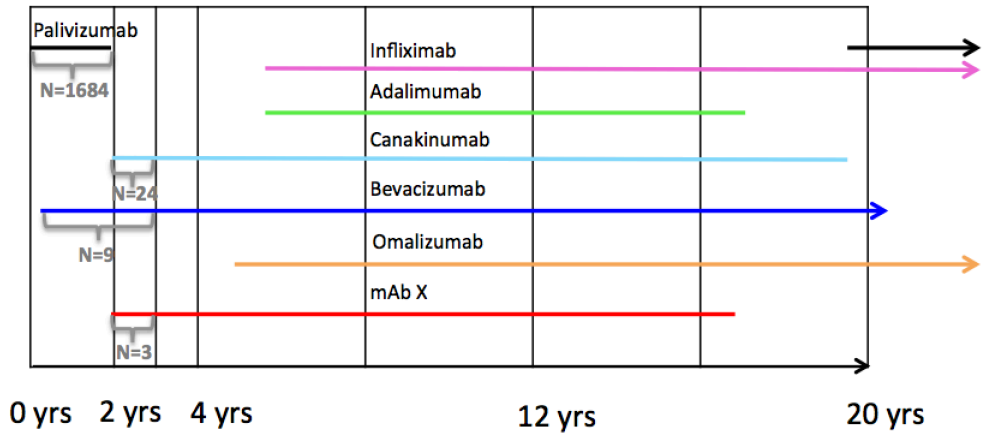

Fig. A.11.: *Age ranges of the study populations used for development of the investigated mAb POP-PK models.* The numbers of individuals N is given for children below two and three years of age that were included in the respective POP-PK analyses.

where $\mathrm{CL}_{\mathrm{pop}}$ is the typical clearance at a BW of 70 kg. The allometric scaling approach for linear clearance differed between the POP-PK models presented in Table A.2 with respect to the reference BW and the allometric exponent. In study [200], CL was normalised to the median BW of the study population and in study [199] to a BW of 33 kg. The allometric exponent was estimated and ranged from 0.48 to 0.8 in [199, 200, 202]. Allometric scaling approaches do not explicitly take into account maturation processes.

Only a single study [196] included an explicit age-based 'maturation function' to describe mAb CL in young patients < 2 years. The authors [196] aimed to characterise the population PK of palivizumab in adults and children. Palivizumab is approved starting at 35 weeks of gestational age to < 2 years. The so-called 'maturation function' is described by a covariate model that considers age in addition to body weight effects:

$$\mathrm{MF} = 1 - \beta \cdot e^{\left(-\frac{\ln(2)}{\tau_{\mathrm{CL}}} \cdot \frac{\mathrm{PAGE}-\mathrm{GA}}{4.35}\right)}, \tag{A.13}$$

where PAGE is the sum of gestational and postnatal age (PNA) in months, GA the gestational age of 40 weeks (full-term neonate), β is the fractional change in CL for a typical full-term (40-week PAGE) infant, τ_{CL} is the maturation half-life of 62.3 months, and 4.35 is the scaling factor for weeks/month. The age descriptor PAGE is also termed postmenstrual age in literature. Figure A.12 shows explicitly the impact of age on clearance using the maturation function in Eq. (A.13). The maturation function was developed based on a population PK analysis involving adult and paediatric (below two years of age) PK data. Thus, for children between 2 and 18 years, the trend of CL vs. age is solely an *a priori* prediction.

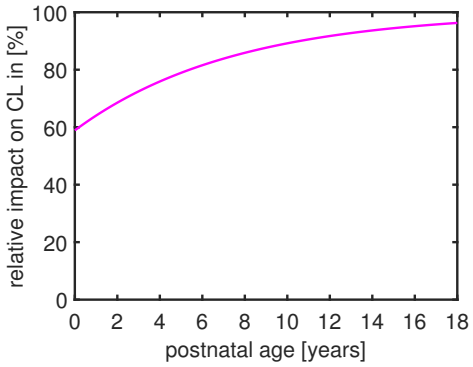

Fig. A.12.: *Explicit age impact on unspecific mAb clearance.* 'Maturation' of clearance is described by an empirical covariate model that considers age in addition to body weight effects [196]. Relative impact on CL is computed via CL=(100 % · MF) with maturation function MF from Eq. (A.13).

In three out of seven mentioned POP-PK studies, serum albumin concentration was identified as a covariate on linear CL. For example in [198], in addition to BW, serum albumin concentration was included to describe bevacizumab linear CL:

$$\mathrm{CL} = \mathrm{CL}_{\mathrm{pop}} \cdot \left(\frac{\mathrm{BW}}{70}\right)^{0.75} \cdot \left(\frac{\mathrm{Alb}}{39}\right)^{-0.3} \tag{A.14}$$

with individual serum albumin concentration normalised to the median value of the model building population (39 g/L) and an estimated exponent of -0.3. Used reference albumin concentration and estimated allometric exponent for albumin differed between the models in Table A.2.

The study population used for model development can have an impact on the estimation of CL, as nicely illustrated by study [202]. The objective of study [202] was to compare data on the PK properties of infliximab in paediatric and adult patients with moderately to severely active Crohn's disease. Fasanmade et al. [202] developed the PK models (i) based on children data only (termed in the following the 'children infliximab model'); (ii) based on adults data only; and (iii) based on children and adults data (termed in the following the 'final infliximab model'). The authors used the combined population for establishing important covariates on infliximab PK since the paediatric study lacked data to allow for a full determination of influential covariates. Covariates on infliximab CL such as ADA status and co-medication could not be determined using the paediatric study population only because almost all of the paediatric patients in the study were treated concurrently with both, infliximab and immunomodulators. Moreover, the ADA status was not detected as a significant covariate in paediatric patients as only three patients (2.8%) were positive for ADAs. Thus, the underlying study population influences the identification of covariates on CL. As an example, reference values and estimated exponents for the covariates BW and Alb differ between the three models in [202].

In addition to body weight, albumin or explicit age effect, other covariates on linear CL were identified by the authors of the different studies (see Table A.2). As an example, Han et al. [198] described the PK of bevacizumab by a linear two-CMT PK model with covariates such as body weight, albumin, gender and disease effect for clearance. Owing to limited information on, e.g., specific covariates such as disease, in our analysis, only body weight, serum albumin concentration, gender and age effects on CL were retained. Considering the diversity of study populations of the different publications (e.g., patients with different diseases within one study), the covariates such as ADA status, race, disease effect and co-medication were set to the respective reference values of a healthy caucasian individual.

For example, in our analysis bevacizumab linear clearance was described as a function of body weight and serum albumin concentration as well as gender effects:

$$\mathrm{CL} = \mathrm{CL}_{\mathrm{pop}} \cdot \left(\frac{\mathrm{BW}}{70}\right)^{0.75} \cdot \left(\frac{\mathrm{Alb}}{39}\right)^{-0.3} \cdot 1.11^{\mathrm{m}} \tag{A.15}$$

where m=0 for female and m=1 for male. 9.90 mL/h is the typical clearance ($\mathrm{CL}_{\mathrm{pop}}$) at a BW of 70 kg.

Robbie et al. [196] added covariates such as race, disease effect and ADA titer to describe the linear CL of palivizumab, however, in our analysis only body weight and explicit age effects on CL were retained (see above):

$$\mathrm{CL} = \mathrm{CL}_{\mathrm{pop}} \cdot \left(\frac{\mathrm{BW}}{70}\right)^{0.75} \cdot \left(1 - \beta \cdot e^{(-\frac{\ln(2)}{\tau_{\mathrm{CL}}}) \cdot \mathrm{PNA}}\right) \cdot e^{\eta_{\mathrm{CL}}} \tag{A.16}$$

where 197 mL/day is the typical clearance ($\mathrm{CL}_{\mathrm{pop}}$) at a BW of 70 kg, and PNA in months. Due to limited studies in pre-term infants, in our analysis, only postnatal age (PNA= PAGE-GA) was included as age descriptor on CL.

Quantitative comparison of unspecific CL - How to compare the different models?

The objective of our study was to quantitatively compare the model-based predictions of unspecific clearance (mean and spread) across postnatal age using the investigated population PK models (Table A.2). As described in the previous section, clearance was based on different covariates, e.g., BW or Alb. Following question arose: How to compare the different CL-models when they are based on different covariates? Linking the reported covariates to PNA provides a potential answer to the question (see Figure A.13).
As an example, given CL as a function of BW in study [198]:

$$\mathrm{CL(BW)} = \mathrm{CL_{pop}} \cdot \left(\frac{\mathrm{BW}}{70}\right)^{0.75}, \tag{A.17}$$

we need the relationship between BW and PNA in order to compute CL as a function of PNA:

$$\mathrm{CL(PNA)} = \mathrm{CL_{pop}} \cdot \left(\frac{\mathrm{BW(PNA)}}{70}\right)^{0.75}. \tag{A.18}$$

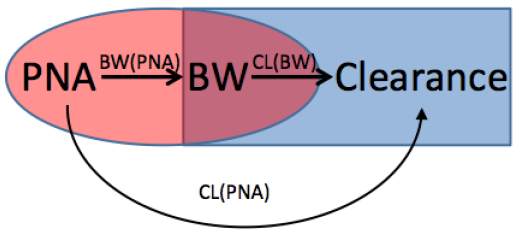

Fig. A.13.: *Linking the covariate body weight on clearance to PNA using the relationship between BW and PNA.*

To do so, we make use of the reported relationship of body weight vs. PNA and body height (BH) vs. PNA from the WHO recommended growth charts [203]. Information of both size measures is necessary to compute other covariates such as BSA or BMI as functions of PNA. Body surface area was linked to body weight and body height via the formula by Dubois & Dubois [204]:

$$\mathrm{BSA} = 0.007184 \cdot \mathrm{BH}^{0.725} \cdot \mathrm{BW}^{0.425}.$$

The advantage of using the WHO recommended growth charts, is that they provide continuous information for children from birth up to 19 years by combining the information of the 2006 WHO growth charts for children aged < 24 months and the CDC growth charts for children of 2-19 years. Note that the WHO recommended growth charts only consider healthy subjects not receiving pharmacotherapy and

lack data for premature neonates. Due to limited studies in pre-term infants, we included only postnatal age as age descriptor on CL.

Figure A.14 shows the BW vs. PNA relationship from WHO/CDC growth charts and Figure A.15 shows the BW-dependency of CL across PNA based on Eq. (A.18) with $\mathrm{CL}_{\mathrm{pop}}$ set to 100%.

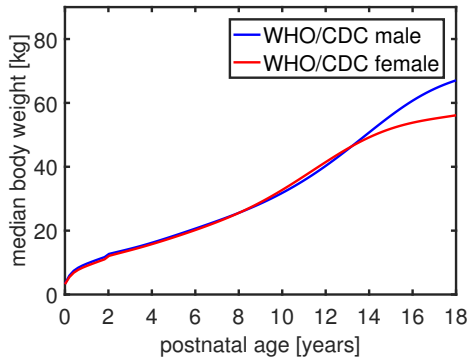

Fig. A.14.: *Median body weight vs. postnatal age relationship from WHO/CDC growth charts for male and female healthy subjects up to 18 years.*

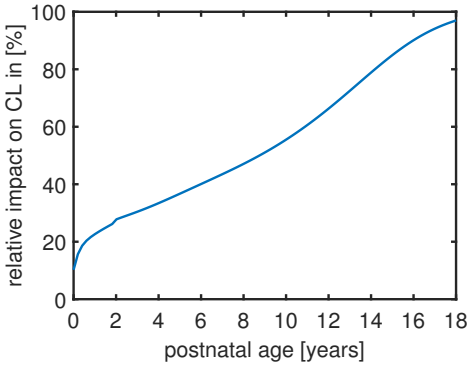

Fig. A.15.: *Body weight impact on clearance.* Predicted weight-dependency of clearance across age is based on the reported body weight vs. postnatal age relationship from WHO/CDC growth charts (Figure A.14). Relative impact on CL is computed based on Eq. (A.17) with with $\mathrm{CL}_{\mathrm{pop}}$ set to 100%.

In addition, similarly to BW, we also linked the covariate serum albumin concentration to PNA in order to compute CL as a function of albumin dependent on PNA. Quantitative changes in serum albumin concentration [g/L] across age (see Figure A.16) were computed using the function published by [205]:

$$\mathrm{Alb}(\mathrm{PNA}) = 1.1287 \cdot \log(\mathrm{PNA}) + 33.74 \tag{A.19}$$

with PNA in days.

'Maturation' of CL that considers postnatal age in addition to BW effects can be directly used to predict CL as a function of PNA (see Figure A.12).

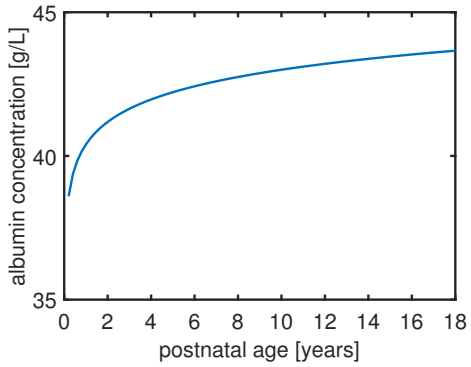

Fig. A.16.: *Ontogeny of albumin concentration.* The relationship of albumin concentration across postnatal age from healthy subjects [205] is used to predict the impact of albumin concentration on clearance.

The investigated models were developed based on different study populations in paediatric patients with different diseases, e.g., study [196] characterised the PK of palivizumab in patients with serious respiratory tract disease, the patient population in [198] suffered from primary central nervous system tumours or sarcomas, the PK of paediatric patients with Crohn's disease was analysed in [200].

As already mentioned in the previous section, disease status of the study population used for model development impacts covariates on CL such as body weight or serum albumin concentration. Both, the BW vs. PNA relationship (from WHO recommended growth charts) and the Alb vs. PNA relationship [205] are based on healthy subjects. The authors [205] present the ontogeny of albumin concentration for healthy subjects with approx. 37g/L for infants and 43 g/L for adults (see Figure A.16). In study [198] where children suffered from primary central nervous system tumours or sarcomas, albumin concentration was normalised to the median value of the model building population (0.5-21 years of age), i.e. 39 g/L with range (24-52 g/L). In this case, an albumin dependent quantification of disease status would be necessary and albumin effect dependent on age may be negligible.

The WHO recommended growth charts only consider healthy subjects not receiving pharmacotherapy and lack data for premature neonates. Due to limited studies in pre-term infants, we included only postnatal age as age descriptor on CL. For children below two years of age, the immaturity of renal and metabolic systems largely affects the PK of small molecule drugs. Postmenstrual age (GA+PNA), was shown to correlate better with biological processes such as glomerular filtration rate and better explains the time course of sMD clearance for children until two years of age [194, 206]. The question arises to what extent this also holds true for mAbs, since they do not follow renal excretion neither classical hepatic enzymatic metabolism.

Considerable **inter-individual variability** has been reported for monoclonal antibody pharmacokinetics [86]. Thus, the objective of our analysis was also to consider IIV when comparing the model-based predictions of unspecific clearance across postnatal age using the investigated population PK models (Table A.2). Again, following question arose: How to compare variation in clearance with CL models based on different covariates and, what factors cause IIV in clearance? IIV in clearance may be related to many different aspects, e.g., differences in disease status, sex, ethnicity, age, body size, genetic polymorphisms, concomitant medication, comorbidity and immune status [86]. For sake of simplicity, we assume that IIV in clearance is based on following two levels:

i) Variation of body weight across age: using the reported percentiles of body weight across age from WHO recommended growth charts.
ii) Estimated IIV on the population parameter clearance: using the reported between-patient random effect in the investigated population PK models (Table A.2):

$$\mathrm{CL_i} = \mathrm{CL_{pop}} \cdot e^{\eta_{\mathrm{CL}}} \tag{A.20}$$

with $\mathrm{CL_i}$ being the value of the PK parameter for the ith patient and η_{CL} is the between-patient random variable corresponding to the PK parameter. In the investigated population PK models, η is assumed to be an independent, identically and normally distributed statistical error with a mean equal to zero and a standard deviation ω. The magnitude of the IIV in each pharmacokinetic parameter was expressed as % CV of the typical population value and reported in the mentioned population PK models. Standard deviation ω was calculated using the following formula [207]:

$$\frac{\mathrm{CV\%}}{100} = \sqrt{(e^{\omega^2 - 1})}. \tag{A.21}$$

The ontogeny of albumin was explicitly implemented (without variability).

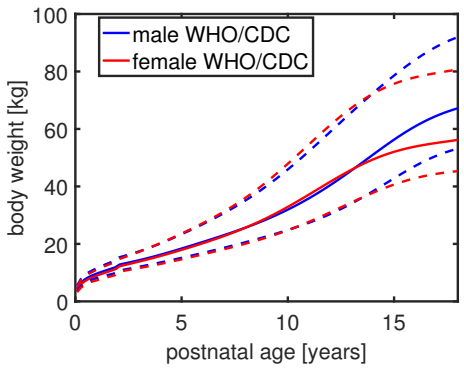

Fig. A.17.: *Body weight vs. postnatal age relationship from WHO/CDC growth charts including between subject variability.*

For the results of simulation-based comparison of mAb clearance using the examined POP-PK models, see section A.4.3.

A.4.2 PBPK modelling approaches to predict PK in paediatric populations

More and more companies are submitting PBPK modelling reports to health authorities and it is well possible that health authorities ask for PBPK modelling approaches to support paediatric drug development in neonates and infants [191]. There are several PBPK software systems commercially available and PBPK models are successfully used to predict differences in PK between adults and children for several sMDs [208].

Unlike for sMDs, there is no *consensus* on how to model monoclonal antibodies disposition for adults in a PBPK context (for details see Chapter 3). Current approaches hugely vary in their representation of physiology and its parameterisation, which poses a challenge for their application, e.g., within the pharmaceutical industry [3, 63]. Consequently, the potential of PBPK modelling for mAbs has not yet been fully exploited [4].

For sMDs and children above two years, allometric scaling and PBPK-based extrapolation to children performed very similarly [60]. Unlike for sMDs, a systematic and quantitative comparison of both approaches for mAbs (allometric scaling and PBPK-based extrapolation to children) is not available so far [179]. We cannot even expect similar predictions by published mAb PBPK models, since there is no *consensus* on how to model mAb disposition in a PBPK context.

Furthermore, for infants, maturation processes also have to be taken into account when predicting sMD PK of children [194]. The impact of maturation, e.g. on the elimination pathways, however, has not been well-characterised for mAbs [179, 195]. An allometric body weight-based model with 'maturation' of CL with age was used to describe the PK of palivizumab in adults and children [196]. The 'maturation', however, is a purely empirical description and no underlying mechanism is given.

Since mAbs do not follow renal excretion neither classical hepatic enzymatic metabolism, the established enzyme maturity paradigm that explains differences from neonates to adolescents may not apply to mAbs. Elimination of mAbs is instead considered to comprise different routes of administration namely target-mediated clearance and unspecific clearance pathway. The latter pathway is highly influenced by FcRn. Following endocytosis, both, endogenous IgG and therapeutic mAb compete for binding to FcRn that directs them from the intracellular space back to the systemic circulation and, thus, protects them from degradation. Knowledge about ontogeny

in endogenous IgG concentration and ontogenetic development of the FcRn salvage pathway (involving endocytosis rate, endosomal sorting, lysosomal degradation, FcRn concentration) may provide explanations for the maturation especially of the unspecific clearance pathway of mAbs.

Children undergo a dramatic transition at birth from a protected environment to the environment of the outside world. Most of IgG that is present at birth is of maternal origin, which declines after birth resulting in reduced albumin and IgG concentrations for children below one year of age [209]. In contrast to IgG ontogeny, there is no information on the ontogenetic development of FcRn expression, binding affinity to FcRn or FcRn uptake into endosomes. To our knowledge, there are not even any published measurements of FcRn abundance in the different tissues in human. We expect maturation processes of FcRn expression to exist, since there is a limited ability to produce an immune response in newborns. Macrophages and monocytes that are detected in umbilical cord at birth show less chemotaxis [209]. A different cytokine production in neonates and infants compared to adults might impact the ontogeny in FcRn expression since FcRn has a structural similarity to MHC class I molecules [40]. As an example, the cytokine interferon alpha is important for MHC class I expression [210]. The authors in [211], however, showed that interferon gamma has no effect on FcRn expression in human retinal pigment epithelial cells and no enhanced cell surface FcRn expression after stimulation of human keratinocytes with pro-inflammatory cytokines was observed in [212]. In addition, the median serum albumin concentration (used as a covariate in mAb POP-PK analyses) appeared to be lower in paediatric patients than in adult patients [202]. Both, IgG and albumin are protected from degradation via the FcRn salvage pathway. High baseline serum albumin concentration may indicate increased functional efficiency of FcRn, leading to reduced mAb elimination.

Mechanistic knowledge and adequate estimates on physiological ontogeny can be incorporated in physiologically-based methods to predict mAb PK in paediatric populations. Published PBPK models for mAbs, however, are quite heterogeneous, e.g., regarding the importance to explicitly account for endogenous IgG and with respect to the FcRn salvage mechanism. Furthermore, still today, there is very limited quantitative knowledge about the processes involved in the FcRn protection mechanism, e.g., fluid-phase endocytosis, endosomal sorting and FcRn expression.

Summary of features of commercial PBPK software packages

In the present section, the current (late 2016) features of commercially available PBPK software to obtain a paediatric prediction with focus on mAb unspecific

clearance are briefly examined: GASTROPLUS® 9.0 PBPK module for biologics, PK-Sim® Version 7.0, Simcyp Simulator® Version 15 Release 1.

The concentrations of the neonatal Fc receptor and of endogenous IgG are important factors that determine the unspecific clearance of mAbs. Physiological knowledge on maturation and growth processes, e.g., ontogeny in endogenous IgG concentration and ontogenetic development of the FcRn salvage pathway may provide adequate estimates of the unspecific mAb clearance. All PBPK models consider explicitly/implicitly the competition between endogenous IgG and therapeutic mAb for binding to FcRn (see Table A.3 for an overview).

Tab. A.3.: Implemented features in commercial PBPK software to predict mAb unspecific clearance in paediatric populations

	Implemented IgG ontogeny	Implemented FcRn ontogeny
PK-Sim® Version 7.0	yes	no
Simcyp ® Version 15 Release 1	yes	no
GASTROPLUS® 9.0	no	no

Ontogeny of FcRn expression and of endogenous IgG concentration is not included in the currently available version of GASTROPLUS® 9.0 PBPK module for biologics and thus, the ability to obtain PK predictions for mAbs in paediatric populations is limited (Viera Lukacova, personal communication, GastroPlus PBPK Modeling & Simulation Workshop, October 18, 2016).

A paediatric PBPK model for biologics is implemented in PK-Sim® Version 7.0. In this model, the physiological parameters of the adult biologics model were allometrically scaled to children using body weight and body height (for details, see [213]) and the scaled paediatric model was validated using literature clinical data. Processes involved in the FcRn protection mechanism were allometrically scaled from adults to children and again externally qualified with literature data for biologics exhibiting FcRn-mediated linear kinetics. However, in the paediatrics biologics PBPK model, FcRn ontogeny is not implemented [214].

The paediatric module of the Simcyp Simulator® (Version 15 Release 1) incorporates a PBPK model for biologics. The Simcyp® paediatric population database is based on a North European paediatric population of healthy individuals excluding pre-term neonates. Physiological variability is implemented in the paediatric simulator at different ages. Similar to the other software packages and in line with absence of knowledge, FcRn ontogeny is not implemented in the paediatric module of Simcyp Simulator®. Instead, FcRn abundance is fixed to a value of 40 μM over age with 10% CV. This value was estimated by [67] for FcRn abundance in mice. The ontogeny

of endogenous IgG concentration (see Figure A.18) is based on an in-house meta-analysis (Felix Stader, personal communication, October 17, 2016).

Still today, there is very limited quantitative insight about the processes involved in the FcRn protection mechanism, e.g., fluid-phase endocytosis, endosomal sorting and FcRn expression. Thus, currently available PBPK models within each of the mentioned software packages lack mechanistic knowledge to explain the processes of unspecific mAb elimination and its ontogenetic development. As a case example for PBPK-based extrapolation, Simcyp® was used to predict the unspecific mAb clearance across age. Predicted median CL by Simcyp® is then compared to clearance over age based on empirical compartmental models (from section A.4.1). For results, see section A.4.3.

Using Simcyp Simulator®, two distribution models are available for mAbs: (i) a minimal PBPK model for mAbs (mPBPK) [215] and (ii) a full PBPK model for mAbs. In the following, further details of the mPBPK model for mAbs are discussed as it is used to predict median unspecific clearance across age. Despite the same naming, the minimal PBPK model in Simcyp® is different from the minimal PBPK model proposed in [73]. The Simcyp®'s mPBPK model contains only a single tissue compartment, plasma and lymph node. All of the tissue compartments are lumped into a single CMT, which is subdivided into vascular, endothelial and interstitial space. Competition of endogenous IgG and mAb for FcRn binding in endothelial space is included based on the model for FcRn recycling in [66]. Most of the parameters are obtained from literature, except the catabolic CL of free endogenous IgG (see below), the vascular reflection coefficient of endogenous IgG and the recycling rate constant, which are manually fitted [215]. The unspecific CL in the Simcyp®'s mPBPK model has two main contributions:

i) a **catabolic CL contribution** (catabolic CL applies to unbound mAb), which represents the CL of mAb from endothelial space. It is set to 0.0175 L/h based on the intrinsic CL of endogenous IgG from endothelial space and assumed to be the same for all mAbs [215]. It reflects the total value including all tissues. The impact of the catabolic CL on the total unspecific CL is highly influenced by the binding affinity to FcRn, and the concentrations of FcRn and endogenous IgG.

ii) an **additional systemic CL contribution**, which represents a lumped CL to describe additional CL pathways of mAbs in venous plasma such as immunogenicity and Fc gamma receptor-mediated elimination. The additional systemic clearance in the Simcyp Simulator® is incorporated as a constant and compound-specific value. The impact of growth and maturation on additional systemic CL is unknown, since the value was estimated based on clinical data in adults and describes several CL pathways of mAbs. This fact also high-

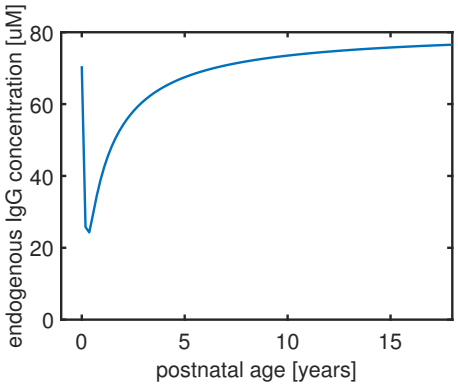

Fig. A.18.: *Ontogeny of endogenous IgG concentration based on Simcyp® Paediatric population.* Most of IgG present at birth is of maternal origin. Decline of maternal IgG levels after birth and impaired production of paediatric IgG at birth lead to low IgG levels for children < 1 year of age [216]. IgG levels stabilise by the age of approx. 5 years.

lights the difficulty when extrapolating the CL to paediatric populations. In order to generate predictions in paediatric populations, the additional systemic clearance has to be scaled by the user applying simple allometry (Felix Stader, personal communication, October 17, 2016).

A.4.3 Simulation-based comparison of mAb CL

Comparison of age-dependency of mAb unspecific clearance based on available POP-PK models

Unspecific linear mAb clearance was computed using the covariate effects on CL based on the available POP-PK models. The function of CL across age was predicted through linking body weight and albumin concentration to postnatal age (see section A.4.1). For adalimumab and omalizumab, only the apparent clearance (CL/F) was reported within the respective POP-PK models [200, 201].

The value of absolute unspecific CL varies between the mAbs at a specific age. Furthermore, the slope of the 'CL vs. age relationship' differs between the various mAbs (see Figure A.19 (top)). Note that the small discontinuity in CL at two years of age arise through the change from WHO to CDC growth charts at two years. The absolute CL of palivizumab, which was predicted using an explicit maturation function is very low in comparison to bevacizumab, where also subjects below two years of age were included in model development.

Absolute mAb CL was normalised to the CL of an 18 year-old subject of the respective mAb to better compare the trend lines between the different compounds. Pronounced differences in the overall trend of normalised CL across age are visible between different mAbs, e.g., at two years of age, CL varies up to a factor two (see Figure A.19 (bottom)). Due to differences in the slope of the 'CL vs. age relationship' between the mAbs, it may be challenging to predict the CL at younger ages solely based on the CL of an 18 year-old subject.

Potential reasons for the differences in CL between the mAbs, can be, e.g., (i) differences in modelling (purely body weight-based or including explicit age effect on CL); (ii) disease effects or (iii) different study populations. Considering the diversity of study populations of the different publications (e.g., patients with different diseases within one study), predicted clearance can be greatly influenced by disease status. Parameters such as lymph flow rate and lymph volumes are altered in several disease conditions as rheumatoid arthritis and cancer [86]. Furthermore, the abundance of Fc gamma receptors and the immune status highly differ at disease conditions. Covariates affecting infliximab PK have been reported to be different between rheumatoid arthritis and ulcerative colitis [202]. As already mentioned in section A.4.1, estimated clearance and covariates on CL can be greatly influenced by the study population used for model development.

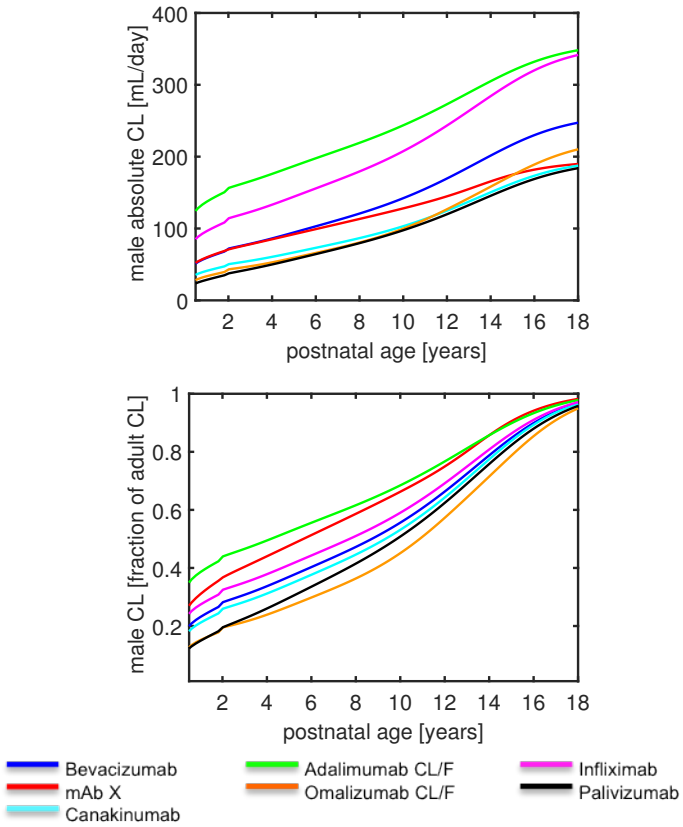

Fig. A.19.: *Predicted median absolute clearance (top) and predicted normalised median absolute clearance (bottom) for different mAbs based on available POP-PK models.* Absolute CL was normalised to CL of an 18 year-old subject.

Comparison of CL including inter-individual variability

IIV in clearance was considered when comparing the model-based predictions of unspecific linear mAb clearance across postnatal age using the investigated population PK models (Table A.2). The comparison of absolute clearance including IIV at the postnatal age of two years for four mAbs is shown in Figure A.20 (top). Data is usually sparse in infants and children $\leq$ 3 years of age. As an example, only four out of seven investigated population PK models (Table A.2) included data for children $\leq$ 3 years of age (see Figure A.20 (top)). In addition, the number of included individuals $\leq$ 3 years of age is generally very low. For example, the paediatric dataset in [198] was comprised of 7 patients $\leq$ 2 years, whereas the paediatric dataset in [196] was comprised of 1684 patients $\leq$ 2 years of age. Thus, the CL predictions of bevacizumab, mAb X and canakinumab in infants are mostly based on extrapolation except for palivizumab [196].

A marked difference between the predictions of palivizumab and the other three mAbs can be observed in Figure A.20 (top). The lower median CL of palivizumab may be related to the explicit age effect that was added to the CL model in addition to body weight effects in study [196]. The POP-PK model for palivizumab [196] was the only one including such an explicit age-based function to empirically describe mAb CL in infants. This function was termed 'maturation function', however no underlying physiological mechanism was given. It could be related to any other effect with age as surrogate such as disease. In addition, Robbie et al. [196] could probably stratify between an explicit age effect and body weight effects on CL due to the large number of individuals $\leq$ 2 years of age. Thus, it remains to be elucidated within further research whether the 'maturation' function is related to a bias in assessment due to usually sparse data in infants (except palivizumab) or due to effects of e.g. disease and study population.

The comparison of absolute mAb clearance including IIV at the postnatal age of six years is shown in Figure A.20 (bottom). The present selection of mAbs was chosen because data of individuals at six years of age were included in the population PK analyses of the presented mAbs. Since only CL/F was reported for adalimumab and omalizumab, the absolute CL is not compared with the herein presented mAbs.

Infliximab CL was computed based on different models [202]: (i) the model based on children data only ('Infliximab children') and (ii) the model also including adults data ('Infliximab children and adults'). The model for adults and children provides a larger median value than the CL based on the children model alone, and IIV was estimated lower based on children data (see Figure A.20 (bottom)). This nicely demonstrates that the study population can have a marked impact on the estimation of the clearance parameters.

In summary, differences in CL do not become negligible at six years of age compared to infants, and IIV between the different mAbs is dependent on the underlying study population (i.e., the random effect in the POP-PK models).

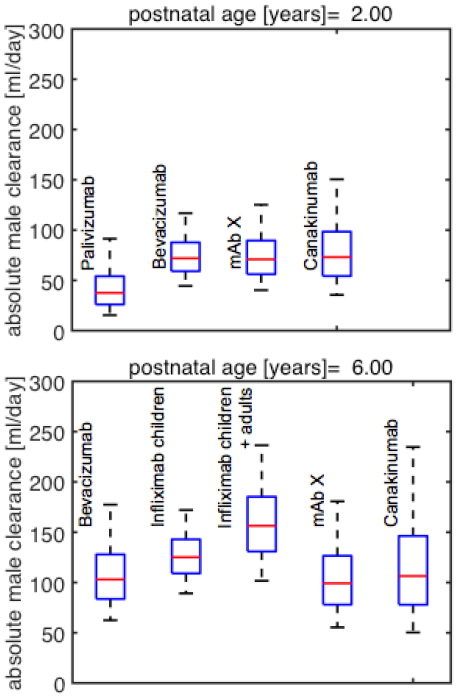

Fig. A.20.: *Predicted absolute clearance for different mAbs based on available POP-PK models including IIV on CL for two years of age (top) and six years of age (bottom).* IIV is based on variability of BW across age and on the between-patient random effect in POP-PK models. Variability on albumin ontogeny is not implemented.

Commercial PBPK software to predict mAb PK in paediatric populations

As a case example for physiologically based models, Simcyp® was used to predict the unspecific mAb clearance across age. Predicted median CL by Simcyp® was then compared to median clearance over age based on the investigated POP-PK models that mainly include purely body weight based scaling methods to predict CL in children.

In general, the adalimumab CL predicted by Simcyp® shows a stronger increase in CL for the first six years of life than compared to the other mAbs, which were mostly predicted using allometric scaling (see Figure A.21). Even for palivizumab, where a 'maturation' function was included to predict CL in infants, we see a great difference in trend line to the Simcyp® CL. Since, the Simcyp® CL prediction was based on an i.v. administration, it cannot be directly compared to the absolute adalimumab CL/F based on the respective POP-PK model [200]. Despite s.c. administration, however, the slope of adalimumab CL/F is more similar to the CL predictions of the

other mAbs than compared to the Simcyp® CL. The different trend line of Simcyp® CL across age (especially for younger children below six years) can be explained by lower endogenous IgG concentrations until six years of age at a constant FcRn expression level across age implemented into Simcyp® Simulator. This results in a larger binding capacity of mAb to FcRn and thus in reduced mAb CL.

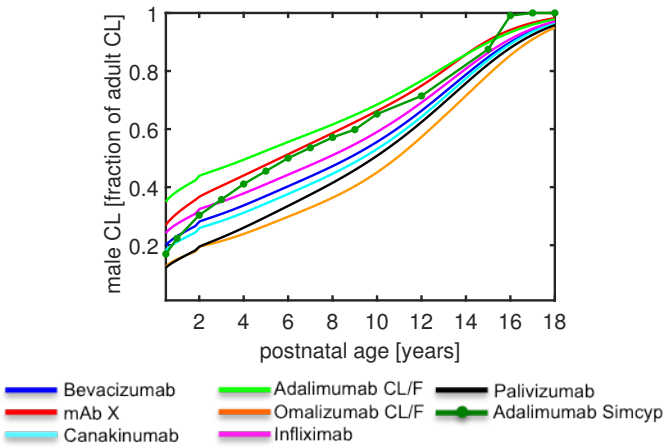

Fig. A.21.: *Predicted normalised median clearance for different mAbs based on available POP-PK models including Simcyp®-predicted adalimumab linear clearance.* CL values were normalised to CL of an 18 year-old subject.

A.4.4 Discussion

A quantitative overview of PK characteristics with focus on linear unspecific CL across age of mAbs in paediatric populations has been given. Current POP-PK models use mostly a combination of weight dependency and currently only one publication reported an explicit age-based 'maturation' function to describe the PK of mAbs in infants. Differences in the overall trend line of linear CL across age based on POP-PK analyses are visible between the investigated mAbs. This highlights the difficulty to solely extrapolate CL from the value in adults or adolescents.

So far, only a small number of subjects below three years of age were included in the model development of the investigated POP-PK models. Only two studies included subjects below two years of age. Furthermore, if individuals were included below three years, POP-PK analyses rely on usually very sparse data in young children (except for palivizumab). The absolute CL of palivizumab, which was predicted using an explicit 'maturation' function is lower in comparison to the CL of the other investigated mAbs using mainly BW-based methods to predict linear CL. It remains to be elucidated, whether the 'maturation' effect on CL is related to a bias in assessment due to sparse data or due to effects such as disease and study population. The quality of reporting information regarding model-building strategies and information of the results of the PK analyses needs to be improved. For example, detailed information on demographics and on the quality of individual estimated clearance values may provide valuable information.

Furthermore, the influence and clinical implication of maturation processes on mAb CL is still unclear. The concentrations of the neonatal Fc receptor and of endogenous IgG are important factors that determine the unspecific clearance of mAbs. Still today, there is very limited quantitative insight about the processes involved in the FcRn protection mechanism and its ontogeny. Thus currently available PBPK software lack mechanistic knowledge to explain the processes of unspecific mAb elimination and its ontogenetic development. Detailed physiological knowledge about the processes involved in the FcRn protection mechanism and its maturation is needed to investigate relevant physiological differences across age and to increase confidence using PBPK models.

Bibliography

[1] G. M. Thurber. „Tumor Effect-Site Pharmacokinetics: Mechanisms and Impact on Efficacy“. In: *ADME Transl. Pharmacokinet. Ther. Proteins. Appl. Drug Discov. Dev.* Ed. by H. Zhou and F.-P. Theil. Wiley, 2015, pp. 225–239 (cit. on pp. 1, 7, 8, 11, 73, 75, 78, 85, 101, 103).

[2] C. Rathi and B. Meibohm. „ADME for Therapeutic Biologics: Antibody-Derived Proteins and Proteins with Novel Scaffolds“. In: *ADME Transl. Pharmacokinet. Ther. Proteins. Appl. Drug Discov. Dev.* Ed. by H. Zhou and F.-P. Theil. Wiley, 2015, pp. 39–54 (cit. on pp. 1, 2, 12, 102, 107).

[3] H. M. Jones, Y. Chen, C. Gibson, et al. „Physiologically based pharmacokinetic modeling in drug discovery and development: a pharmaceutical industry perspective“. In: *Clin. Pharmacol. Ther.* 97.3 (2015), pp. 247–262 (cit. on pp. 1, 14, 19, 105, 140).

[4] H. M. Jones, K. Mayawala, and P. Poulin. „Dose selection based on physiologically based pharmacokinetic (PBPK) approaches.“ In: *AAPS J.* 15.2 (2012), pp. 377–87 (cit. on pp. 1, 15, 16, 19, 105, 140).

[5] Y. Cao and W. J. Jusko. „Mechanistic Physiologically Based Pharmacokinetic Models in Development of Therapeutic Monoclonal Antibodies“. In: *ADME Transl. Pharmacokinet. Ther. Proteins. Appl. Drug Discov. Dev.* Ed. by H. Zhou and F.-P. Theil. Wiley, 2015, pp. 159–174 (cit. on pp. 1, 19).

[6] D. K. Shah and A. M. Betts. „Antibody biodistribution coefficients Inferring tissue concentrations of monoclonal antibodies based on the plasma concentrations in several preclinical species and human“. In: *mAbs* 5.2 (2013), pp. 297–305 (cit. on pp. 1, 7, 16, 19, 23–26, 28–30, 72, 105).

[7] L. Fronton, S. Pilari, and W. Huisinga. „Monoclonal antibody disposition: a simplified PBPK model and its implications for the derivation and interpretation of classical compartment models.“ In: *J. Pharmacokinet. Pharmacodyn.* 41.2 (2014), pp. 87–107 (cit. on pp. 1, 15, 16, 19, 20, 22–24, 26, 46, 48, 50, 69).

[8] D. E. Mager and W. J. Jusko. „General pharmacokinetic model for drugs exhibiting target-mediated drug disposition.“ In: *J. Pharmacokinet. Pharmacodyn.* 28.6 (2001), pp. 507–32 (cit. on pp. 2, 16, 23).

[9] D. E. Mager and W. Krzyzanski. „Quasi-equilibrium pharmacokinetic model for drugs exhibiting target-mediated drug disposition.“ In: *Pharm. Res.* 22.10 (2005), pp. 1589–96 (cit. on pp. 2, 23).

[10]L. Gibiansky, E. Gibiansky, T. Kakkar, and P. Ma. „Approximations of the target-mediated drug disposition model and identifiability of model parameters“. In: *J. Pharmacokinet. Pharmacodyn.* 35.5 (2008), pp. 573–91 (cit. on pp. 2, 17, 23).

[11]H. P. Grimm. „Gaining insights into the consequences of target-mediated drug disposition of monoclonal antibodies using quasi-steady-state approximations.“ In: *J. Pharmacokinet. Pharmacodyn.* 36.5 (2009), pp. 407–20 (cit. on pp. 2, 23, 107).

[12]B.-F. Krippendorff, K. Kuester, C. Kloft, and W. Huisinga. „Nonlinear pharmacokinetics of therapeutic proteins resulting from receptor mediated endocytosis.“ In: *J. Pharmacokinet. Pharmacodyn.* 36.3 (2009), pp. 239–60 (cit. on pp. 2, 17, 23).

[13]B.-F. Krippendorff, D. A. Oyarzún, and W. Huisinga. „Predicting the F(ab)-mediated effect of monoclonal antibodies in vivo by combining cell-level kinetic and pharmacokinetic modelling.“ In: *J. Pharmacokinet. Pharmacodyn.* 39.2 (2012), pp. 125–39 (cit. on pp. 2, 11, 16, 23, 79–81, 85, 128).

[14]R. J. Keizer, A. D. R. Huitema, J. H. M. Schellens, and J. H. Beijnen. „Clinical pharmacokinetics of therapeutic monoclonal antibodies.“ In: *Clin. Pharmacokinet.* 49.8 (2010), pp. 493–507 (cit. on pp. 2, 10, 45).

[15]R. Kim, M. Emi, and K. Tanabe. „Cancer immunosuppression and autoimmune disease: Beyond immunosuppressive networks for tumour immunity“. In: *Immunology* 119.2 (2006), pp. 254–264 (cit. on pp. 2, 45).

[16]W. von Bernstorff, M. Voss, S. Freichel, et al. „Systemic and local immunosuppression in pancreatic cancer patients.“ In: *Clin. Cancer Res.* 7.3 (2001), 925s–932s (cit. on pp. 2, 45).

[17]I. Penn and T. E. Starzl. „Immunosuppression and Cancer“. In: *Transpl. Proc.* 5.1 (1973), pp. 943–947 (cit. on pp. 2, 45).

[18]S. I. Rudnick and G. P. Adams. „Affinity and avidity in antibody-based tumor targeting.“ In: *Cancer Biother. Radiopharm.* 24.2 (2009), pp. 155–61 (cit. on pp. 2, 7, 73).

[19]C. Cilliers, H. Guo, J. Liao, N. Christodolu, and G. M. Thurber. „Multiscale Modeling of Antibody-Drug Conjugates: Connecting Tissue and Cellular Distribution to Whole Animal Pharmacokinetics and Potential Implications for Efficacy.“ In: *AAPS J.* 18.5 (2016), pp. 1117–30 (cit. on pp. 2, 12, 13, 16, 73, 76, 84–86, 101–103, 107, 121).

[20]E. Khera, C. Cilliers, S. Bhatnagar, and G. Thurber. „Computational transport analysis of antibody-drug conjugate bystander effects and payload tumoral distribution: implications for therapy“. In: *Mol. Syst. Des. Eng.* 3 (2018), pp. 73–88 (cit. on pp. 2, 12, 13, 73, 98, 107).

[21]M. J. Eigenmann, T. V. Karlsen, B.-F. Krippendorff, et al. „Interstitial IgG antibody pharmacokinetics assessed by combined in vivo- and physiologically-based pharmacokinetic modelling approaches“. In: *J. Physiol.* 24 (2017), pp. 7311–7330 (cit. on pp. 2, 19, 21, 23–25, 27, 105).

[22]D. M. Ecker, S. D. Jones, and H. L. Levine. „The therapeutic monoclonal antibody market“. In: *mAbs* 7.1 (2015), pp. 9–14 (cit. on p. 5).

[23]H. Kaplon and J. M. Reichert. „Antibodies to watch in 2018“. In: *mAbs* 10.2 (2018), pp. 183–203 (cit. on p. 5).

[24]H. W. Schroeder and L. Cavacini. „Structure and function of immunoglobulins“. In: *J. Allergy Clin. Immunol.* 125.2 (2010), S41–52 (cit. on p. 6).

[25]J. T. Ryman and B. Meibohm. „Pharmacokinetics of Monoclonal Antibodies“. In: *CPT Pharmacometrics Syst. Pharmacol.* 6 (2017), pp. 576–588 (cit. on pp. 6–9, 13, 43, 89).

[26]D.K. Shah and A. M. Betts. „Towards a platform PBPK model to characterize the plasma and tissue disposition of monoclonal antibodies in preclinical species and human.“ In: *J. Pharmacokinet. Pharmacodyn.* 39.1 (2012), pp. 67–86 (cit. on pp. 7, 14).

[27]W. Huisinga, S. Fuhrmann, L. Fronton, and B.-F. Krippendorff. „Target-Driven Pharmacokinetics of Biotherapeutics“. In: *ADME Transl. Pharmacokinet. Ther. Proteins. Appl. Drug Discov. Dev.* Ed. by Honghui Zhou and Frank-Peter Theil. Wiley, 2015. Chap. 14, pp. 197–209 (cit. on pp. 7, 16).

[28]H. Sarin. „Physiologic upper limits of pore size of different blood capillary types and another perspective on the dual pore theory of microvascular permeability“. In: *J. Angiogenes. Res.* 2.14 (2010) (cit. on p. 7).

[29]I. Fuso Nerini, L. Morosi, M. Zucchetti, et al. „Intratumor heterogeneity and its impact on drug distribution and sensitivity.“ In: *Clin. Pharmacol. Ther.* 96.2 (2014), pp. 224–38 (cit. on pp. 7, 8, 75, 78, 99).

[30]B. S. Kuszyk, F. M. Corl, F. N. Franano, et al. „Tumor transport physiology: Implications for imaging and imaging-guided therapy“. In: *Am. J. Roentgenol.* 177.4 (2001), pp. 747–753 (cit. on pp. 7, 8).

[31]S. I. Rudnick, J. Lou, C. C. Shaller, et al. „Influence of affinity and antigen internalization on the uptake and penetration of anti-HER2 Antibodies in Solid Tumors“. In: *Cancer Res.* 71.6 (2011), pp. 2250–2259 (cit. on pp. 7, 73).

[32]G. M. Thurber, M. M. Schmidt, and K. D. Wittrup. „Factors determining antibody distribution in tumors.“ In: *Trends Pharmacol. Sci.* 29.2 (2008), pp. 57–61 (cit. on p. 7).

[33]H.-P. Gerber, P. D. Senter, and I. S. Grewal. „Antibody drug-conjugates targeting the tumor vasculature: Current and future developments.“ In: *mAbs* 1.3 (2009), pp. 247–53 (cit. on pp. 8, 12, 86, 103).

[34]R. K. Jain. „Transport of Molecules in the Tumor Interstitium : A Review Transport of Molecules in the Tumor Interstitium : A Review“. In: *Cancer Res.* 47.17 (1987), pp. 3039–3051 (cit. on pp. 8, 75, 78).

[35]P. M. Gullino, F. H. Grantham, and S. H. Smith. „The Interstitial Water Space of Tumors The Interstitial Water Space of Tumors“. In: *Cancer Res.* 25 (1965), pp. 727–731 (cit. on pp. 8, 77, 84).

[36]N. L. Dirks and B. Meibohm. „Population pharmacokinetics of therapeutic monoclonal antibodies.“ In: *Clin. Pharmacokinet.* 49.10 (2010), pp. 633–59 (cit. on pp. 8, 9, 13, 30, 40, 45, 131).

[37]D. Samineni, S. Girish, and C. Li. „Impact of Shed/Soluble targets on the PK/PD of approved therapeutic monoclonal antibodies“. In: *Expert Rev. Clin. Pharmacol.* 9.12 (2016), pp. 1557–1569 (cit. on pp. 9, 43, 44).

[38]F. Nimmerjahn and J. V. Ravetch. „Fcγ receptors as regulators of immune responses.“ In: *Nat. Rev. Immunol.* 8.1 (2008), pp. 34–47 (cit. on p. 9).

[39]W. Wang, E. Q. Wang, and J. P. Balthasar. „Monoclonal antibody pharmacokinetics and pharmacodynamics.“ In: *Clin. Pharmacol. Ther.* 84.5 (2008), pp. 548–58 (cit. on pp. 9, 10).

[40]D. C. Roopenian and S. Akilesh. „FcRn: the neonatal Fc receptor comes of age.“ In: *Nat. Rev. Immunol.* 7.9 (2007), pp. 715–25 (cit. on pp. 10, 11, 141).

[41]L. D. Hooghe, A. D. Chalmers, S. Heywood, and P. Whitley. „Cell surface dynamics and cellular distribution of endogenous FcRn“. In: *PLoS One* 12.8 (2017), pp. 1–16 (cit. on p. 10).

[42]C. Chaudhury, C. L. Brooks, D. C. Carter, J. M. Robinson, and C. L. Anderson. „Albumin binding to FcRn: distinct from the FcRn-IgG interaction.“ In: *Biochemistry* 45.15 (2006), pp. 4983–90 (cit. on p. 10).

[43]S. Latvala, B. Jacobsen, M. B. Otteneder, A. Herrmann, and S. Kronenberg. „Distribution of FcRn Across Species and Tissues“. In: *J. Histochem. Cytochem.* 65.6 (2017), pp. 321–333 (cit. on pp. 10, 71).

[44]J. P. Martins, P. J. Kennedy, H. A. Santos, C. Barrias, and B. Sarmento. „A comprehensive review of the neonatal Fc receptor and its application in drug delivery“. In: *Pharmacol. Ther.* 161 (2016), pp. 22–39 (cit. on pp. 10, 46, 107).

[45]J. T. Andersen, M. B. Daba, G. Berntzen, T. E. Michaelsen, and I. Sandlie. „Cross-species binding analyses of mouse and human neonatal Fc receptor show dramatic differences in immunoglobulin G and albumin binding.“ In: *J. Biol. Chem.* 285.7 (2010), pp. 4826–36 (cit. on pp. 10, 49).

[46]J. M. Redman, E. M. Hill, D. AlDeghaither, and L. M. Weiner. „Mechanisms of Action of Therapeutic Antibodies for Cancer“. In: *Mol. Immunol.* 67 (2015), pp. 28–45 (cit. on p. 11).

[47]Y. Yarden and B.-Z. Shilo. „SnapShot: EGFR Signaling Pathway“. In: *Cell* 131.5 (2007) (cit. on pp. 11, 128).

[48]W. Tai, R. Mahato, and K. Cheng. „The role of HER2 in cancer therapy and targeted drug delivery“. In: *J. Control. Release* 146.3 (2010), pp. 264–275 (cit. on p. 11).

[49]B. A. Teicher and R. V. J. Chari. „Antibody conjugate therapeutics: challenges and potential.“ In: *Clin. Cancer Res.* 17.20 (2011), pp. 6389–97 (cit. on p. 12).

[50]J. A. Flygare, T. H. Pillow, and P. Aristoff. „Antibody-drug conjugates for the treatment of cancer.“ In: *Chem. Biol. Drug Des.* 81.1 (2013), pp. 113–21 (cit. on p. 12).

[51]M. Kågedal, L. Gibiansky, J. Xu, et al. „Platform model describing pharmacokinetic properties of vc-MMAE antibody-drug conjugates“. In: *J. Pharmacokinet. Pharmacodyn.* 44 (2017), pp. 537–548 (cit. on pp. 12, 88).

[52]B. Zhao and T. H. Han. „Overview of ADME and PK/PD of ADCs“. In: *ADME Transl. Pharmacokinet. Ther. Proteins. Appl. Drug Discov. Dev.* Ed. by H. Zhou and F.-P. Theil. Wiley, 2015, pp. 55–65 (cit. on pp. 12, 86, 102).

[53]R. S. Zolot, S. Basu, and R. P. Million. „Antibody-drug conjugates.“ In: *Nat. Rev. Drug Disc.* 12.4 (2013), pp. 259–60 (cit. on p. 13).

[54]H. Derendorf, L. J. Lesko, P. Chaikin, et al. „Pharmacokinetic/pharmacodynamic modeling in drug research and development“. In: *J. Clin. Pharmacol.* 40 (2000), pp. 1399–1418 (cit. on p. 13).

[55]H. M. Jones, I. B. Gardner, and K. J. Watson. „Modelling and PBPK Simulation in Drug Discovery“. In: *AAPS J.* 11.1 (2009), pp. 155–166 (cit. on p. 13).

[56]R. L. Lalonde, K. G. Kowalski, M. M. Hutmacher, et al. „Model-based drug development“. In: *Clin. Pharmacol. Ther.* 82.1 (2007), pp. 21–32 (cit. on p. 13).

[57]R. P. Brown, M. D. Delp, S. L. Lindstedt, L. R. Rhomberg, and R. P. Beliles. „Physiological Parameter Values for Physiologically Based Pharmacokinetic Models“. In: *Toxicol. Ind. Health* 13.4 (1997), pp. 407–484 (cit. on pp. 13, 20, 26–28, 30).

[58]International Commission on Radiological Protection (ICRP). „Basic anatomical and physiological data for use in radiological protection: Reference values“. In: *ICRP Publ.* 89 (2002) (cit. on pp. 13, 25, 26, 29, 30).

[59]P. Poulin and F.-P. Theil. „Prediction of pharmacokinetics prior to in vivo studies. II. Generic physiologically based pharmacokinetic models of drug disposition.“ In: *J. Pharm. Sci.* 91.5 (2002), pp. 1358–1370 (cit. on pp. 14, 28).

[60]W. Huisinga, A. Solms, L. Fronton, and S. Pilari. „Modeling Interindividual Variability in Physiologically Based Pharmacokinetics and Its Link to Mechanistic Covariate Modeling“. In: *CPT Pharmacometrics Syst. Pharmacol.* 1.e4 (2012) (cit. on pp. 14, 26, 130, 132, 140).

[61]P. Poulin and F.-P. Theil. „A priori prediction of tissue: Plasma partition coefficients of drugs to facilitate the use of physiologically-based pharmacokinetic models in drug discovery“. In: *J. Pharm. Sci.* 89.1 (2000), pp. 16–35 (cit. on p. 14).

[62]M. Rowland, C. Peck, and G. Tucker. „Physiologically-based pharmacokinetics in drug development and regulatory science.“ In: *Annu. Rev. Pharmacol. Toxicol.* 51 (2011), pp. 45–73 (cit. on p. 14).

[63]G. Z. Ferl, F.-P. Theil, and H. Wong. „Physiologically based pharmacokinetic models of small molecules and therapeutic antibodies: a mini-review on fundamental concepts and applications“. In: *Biopharm. Drug Dispos.* 37 (2016), pp. 75–92 (cit. on pp. 14, 140).

[64]D. G. Covell, J. Barbet, O. D. Holton, et al. „Pharmacokinetics of Monoclonal Immunoglobulin G1, F(ab')2, and Fab' in Mice“. In: *Cancer Res.* 46 (1986), pp. 3969–3978 (cit. on pp. 14, 15, 26–29).

[65]L. T. Baxter, H. Zhu, D. G. Mackensen, and R. K. Jain. „Physiologically based pharmacokinetic model for specific and nonspecific monoclonal antibodies and fragments in normal tissues and human tumor xenografts in nude mice.“ In: *Cancer Res.* 54.6 (1994), pp. 1517–28 (cit. on pp. 14, 15, 20, 25, 26, 116).

[66]A. Garg and J. P. Balthasar. „Physiologically-based pharmacokinetic (PBPK) model to predict IgG tissue kinetics in wild-type and FcRn-knockout mice.“ In: *J. Pharmacokinet. Pharmacodyn.* 34.5 (2007), pp. 687–709 (cit. on pp. 14, 15, 26–29, 70, 72, 118, 143).

[67]G. Z. Ferl, A. M. Wu, and J. J. DiStefano. „A predictive model of therapeutic monoclonal antibody dynamics and regulation by the neonatal Fc receptor (FcRn).“ In: *Ann. Biomed. Eng.* 33.11 (2005), pp. 1640–52 (cit. on pp. 14, 72, 118, 142).

[68]S. R. Urva, V. C. Yang, and J. P. Balthasar. „Physiologically Based Pharmacokinetic Model for T84.66: A Monoclonal Anti-CEA Antibody“. In: *J. Pharm. Sci.* 99.3 (2010), pp. 1582–1600 (cit. on p. 14).

[69]Y. Chen and J. P. Balthasar. „Evaluation of a catenary PBPK model for predicting the in vivo disposition of mAbs engineered for high-affinity binding to FcRn.“ In: *AAPS J.* 14.4 (2012), pp. 850–9 (cit. on pp. 14, 15, 70, 71, 107).

[70]P. M. Glassman and J. P. Balthasar. „Physiologically-based pharmacokinetic modeling to predict the clinical pharmacokinetics of monoclonal antibodies“. In: *J. Pharmacokinet. Pharmacodyn.* 43.4 (2016), pp. 427–446 (cit. on p. 14).

[71]Patrick M Glassman, Yang Chen, and Joseph P Balthasar. „Scale-up of a physiologically-based pharmacokinetic model to predict the disposition of monoclonal antibodies in monkeys“. In: *J. Pharmacokinet. Pharmacodyn.* 42.5 (2015), pp. 527–540 (cit. on p. 14).

[72]B. Rippe and B. Haraldsson. „Transport of macromolecules across microvascular walls: the two-pore theory.“ In: *Physiol. Rev.* 74.1 (1994), pp. 163–219 (cit. on p. 15).

[73]Y. Cao, J. P. Balthasar, and W. J. Jusko. „Second-generation minimal physiologically-based pharmacokinetic model for monoclonal antibodies“. In: *J. Pharmacokinet. Pharmacodyn.* 40.5 (2013), pp. 597–607 (cit. on pp. 15, 16, 20, 43, 46, 105, 143).

[74]Y. Cao and W. J. Jusko. „Survey of monoclonal antibody disposition in man utilizing a minimal physiologically-based pharmacokinetic model.“ In: *J. Pharmacokinet. Pharmacodyn.* 41.6 (2014), pp. 571–80 (cit. on pp. 15, 43, 105).

[75]L. A. Peletier and J. Gabrielsson. „Dynamics of target-mediated drug disposition: characteristic profiles and parameter identification.“ In: *J. Pharmacokinet. Pharmacodyn.* 39.5 (2012), pp. 429–51 (cit. on p. 17).

[76]R. Kawai, M. Lemaire, J.-L. Steimer, et al. „Physiologically based pharmacokinetic study on a cyclosporin derivative, SDZ IMM 125“. In: *J. Pharmacokinet. Biopharm.* 22.5 (1994), pp. 327–365 (cit. on pp. 21, 25, 27).

[77]Y. Vugmeyster, P. Szklut, L. Tchistiakova, et al. „Preclinical pharmacokinetics, interspecies scaling, and tissue distribution of humanized monoclonal anti-IL-13 antibodies with different IL-13 neutralization mechanisms“. In: *Int. Immunopharmacol.* 8.3 (2008), pp. 477–483 (cit. on pp. 25, 32, 34).

[78]J. Haunschild, K. Steiner, H. P. Faro, and R. Senekowitsch. „Pharmacokinetics of reshaped MAb 425 in three animal species“. In: *Cell Biophys.* 26.3 (1995), pp. 167–182 (cit. on pp. 25, 32, 35).

[79]A. Garg. „Investigation of the Role of FcRn in the Absorption, Distribution, and Elimination of Monoclonal Antibodies“. PhD thesis. State University of New York at Buffalo, 2007 (cit. on pp. 25, 52, 54, 55, 59, 60, 116).

[80]L. Abuqayyas and J. P. Balthasar. „Application of PBPK modeling to predict monoclonal antibody disposition in plasma and tissues in mouse models of human colorectal cancer.“ In: *J. Pharmacokinet. Pharmacodyn.* 39.6 (2012), pp. 683–710 (cit. on pp. 25, 116).

[81]M. R. Buist, P. Kenemans, W. Den Hollander, et al. „Kinetics and tissue distribution of the radiolabeled chimeric monoclonal antibody MOv18 IgG and F(ab')$_2$ fragments in ovarian carcinoma patients“. In: *Cancer Res.* 53.22 (1993), pp. 5413–5418 (cit. on pp. 25, 36, 37, 39).

[82]U. Windberger, A. Bartholovitsch, R. Plasenzotti, K. J. Korak, and G. Heinze. „Whole blood viscosity, plasma viscosity and erythrocyte aggregation in nine mammalian species: reference values and comparison of data.“ In: *Exp. Physiol.* 88 (2003), pp. 431–440 (cit. on pp. 27, 28, 30).

[83]H. A. El-Masri and C. J. Portier. „Physiologically Based Pharmacokinetics Model of Primidone and its Metabolites Phenobarbital and Phenylethylmalonamide in Humans, Rats and Mice“. In: *Drug Metab. Dispos.* 26 (1998), pp. 585–594 (cit. on p. 27).

[84]K.-H. Diehl, R. Hull, D. Morton, et al. „A good practice guide to the administration of substances and removal of blood, including routes and volumes“. In: *J. Appl. Toxicol.* 21 (2001), pp. 15–23 (cit. on pp. 27, 28, 30).

[85]International Commission on Radiological Protection (ICRP). „Report of the Task Group on Reference Man“. In: *ICRP Publ.* 23 (1975) (cit. on p. 29).

[86]K. L. Gill, K. K. Machavaram, R. H. Rose, and M. Chetty. „Potential Sources of Inter-Subject Variability in Monoclonal Antibody Pharmacokinetics“. In: *Clin. Pharmacokinet.* 55.7 (2016), pp. 789–805 (cit. on pp. 30, 139, 145).

[87]L. R. Williams. *Reference Values for Total Blood Volume and Cardiac Output in Humans*. Tech. rep. ORNL/TM-12814 Oak Ridge National Laboratory, 1994 (cit. on p. 30).

[88]A. Chakraborty, S. Tannenbaum, C. Rordorf, et al. „Pharmacokinetic and pharmacodynamic properties of canakinumab, a human anti-interleukin-1β monoclonal antibody“. In: *Clin. Pharmacokinet.* 51.6 (2012), e1–e18 (cit. on pp. 32, 33).

[89]J. Zhao, Y. Cao, and W. J. Jusko. „Across-Species Scaling of Monoclonal Antibody Pharmacokinetics Using a Minimal PBPK Model“. In: *Pharm. Res.* 32.10 (2015), pp. 3269–3281 (cit. on pp. 32, 33, 37).

[90]F. Curtin, H. Perron, A. Kromminga, H. Porchet, and A. B. Lang. „Preclinical and early clinical development of GNbAC1, a humanized IgG4 monoclonal antibody targeting endogenous retroviral MSRV-Env protein“. In: *mAbs* 7.1 (2015), pp. 265–275 (cit. on pp. 32, 110).

[91]H. Xie, C. Audette, M. Hoffee, J. M. Lambert, and W. A. Blättler. „Pharmacokinetics and biodistribution of the antitumor immunoconjugate, cantuzumab mertansine (huC242-DM1), and its two components in mice“. In: *J. Pharmacol. Exp. Ther.* 308.3 (2004), pp. 1073–82 (cit. on pp. 32, 110).

[92]European Medicines Agency. *Assessment report - Inflectra*. 2013 (cit. on p. 32).

[93]V. Hsei, G. G. Deguzman, A. Nixon, and J. Gaudreault. „Complexation of VEGF with bevacizumab decreases VEGF clearance in rats.“ In: *Pharm. Res.* 19.11 (2002), pp. 1753–6 (cit. on p. 32).

[94]C. B. Davis, T. W. Hepburn, J. J. Urbanski, et al. „Evaluation of the Respiratory Antibody Syncytial RSHZ19“. In: *Drug Metab. Dispos.* 23.10 (1995), pp. 1028–1036 (cit. on p. 32).

[95]L. Kagan, M. R. Turner, S. V. Balu-Iyer, and D. E. Mager. „Subcutaneous absorption of monoclonal antibodies: Role of dose, site of injection, and injection volume on rituximab pharmacokinetics in rats“. In: *Pharm. Res.* 29.2 (2012), pp. 490–499 (cit. on p. 32).

[96]I. P. Nnane, Z. Xu, H. Zhou, and H. M. Davis. „Non-Clinical Pharmacokinetics, Prediction of Human Pharmacokinetics and First-in-Human Dose Selection for CNTO 5825, an Anti-Interleukin-13 Monoclonal Antibody“. In: *Basic Clin. Pharmacol. Toxicol.* 117.4 (2015), pp. 219–225 (cit. on p. 32).

[97]M. I. Bazin-Redureau, C. B. Renard, and J. M. Scherrmann. „Pharmacokinetics of heterologous and homologous immunoglobulin G, F(ab')2 and Fab after intravenous administration in the rat.“ In: *J. Pharm. Pharmacol.* 49.3 (1997), pp. 277–281 (cit. on p. 32).

[98]M. H. Weisman, L. W. Moreland, D. E. Furst, et al. „Efficacy, pharmacokinetic, and safety assessment of adalimumab, a fully human anti-tumor necrosis factor-alpha monoclonal antibody, in adults with rheumatoid arthritis receiving concomitant methotrexate: A pilot study“. In: *Clin. Ther.* 25.6 (2003), pp. 1700–1721 (cit. on p. 37).

[99]A. A. Fasanmade, O. J. Adedokun, J. Ford, et al. „Population pharmacokinetic analysis of infliximab in patients with ulcerative colitis“. In: *Eur. J. Clin. Pharmacol.* 65.12 (2009), pp. 1211–1228 (cit. on p. 37).

[100]C. Cavelti-Weder, A. Babians-Brunner, C. Keller, et al. „Effects of Gevokizumab on Glycemia and Inflammatory Markers in Type 2 Diabetes“. In: *Diabetes Care* 35 (2012) (cit. on p. 37).

[101]R. Kurzrock, A. Patnaik, J. Aisner, et al. „A phase I study of weekly R1507, a human monoclonal antibody insulin-like growth factor-I receptor antagonist, in patients with advanced solid tumors“. In: *Clin. Cancer Res.* 16.8 (2010), pp. 2458–2465 (cit. on pp. 37, 43).

[102]E. L. López, M. M. Contrini, E. Glatstein, et al. „Safety and pharmacokinetics of urtoxazumab, a humanized monoclonal antibody, against Shiga-like toxin 2 in healthy adults and in pediatric patients infected with Shiga-like toxin-producing Escherichia coli“. In: *Antimicrob. Agents Chemother.* 54.1 (2010), pp. 239–243 (cit. on p. 37).

[103]T. Puchalski, U. Prabhakar, Q. Jiao, B. Berns, and H. M. Davis. „Pharmacokinetic and pharmacodynamic modeling of an anti-interleukin-6 chimeric monoclonal antibody (siltuximab) in patients with metastatic renal cell carcinoma“. In: *Clin. Cancer Res.* 16.5 (2010), pp. 1652–1661 (cit. on p. 37).

[104]J. C. Szepietowski, S. Nilganuwong, A. Wozniacka, et al. „Phase I, randomized, double-blind, placebo-controlled, multiple intravenous, dose-ascending study of sirukumab in cutaneous or systemic lupus erythematosus“. In: *Arthritis Rheum.* 65.10 (2013), pp. 2661–2671 (cit. on p. 37).

[105]S. Hetherington, M. Texter, E. Wenzel, et al. „Phase I dose escalation study to evaluate the safety and pharmacokinetic profile of tefibazumab in subjects with end-stage renal disease requiring hemodialysis“. In: *Antimicrob. Agents Chemother.* 50.10 (2006), pp. 3499–3500 (cit. on p. 37).

[106]C. M. Ng, B. L. Lum, V. Gimenez, S. Kelsey, and D. Allison. „Rationale for fixed dosing of pertuzumab in cancer patients based on population pharmacokinetic analysis“. In: *Pharm. Res.* 23.6 (2006), pp. 1275–1284 (cit. on p. 37).

[107]D. Singh, B. Kane, N. A. Molfino, et al. „A phase 1 study evaluating the pharmacokinetics, safety and tolerability of repeat dosing with a human IL-13 antibody (CAT-354) in subjects with asthma.“ In: *BMC Pulm. Med.* 10.3 (2010), pp. 1–8 (cit. on p. 37).

[108]C. L. Kauffman, N. Aria, E. Toichi, et al. „A phase I study evaluating the safety, pharmacokinetics, and clinical response of a human IL-12 p40 antibody in subjects with plaque psoriasis“. In: *J. Invest. Dermatol.* 123.6 (2004), pp. 1037–1044 (cit. on p. 37).

[109]D. A. Smith, E. A. Minthorn, and M. Beerahee. „Pharmacokinetics and Pharmacodynamics of Mepolizumab, an Anti-Interleukin-5 Monoclonal Antibody“. In: *Clin. Pharmacokinet.* 50.4 (2011), pp. 215–227 (cit. on p. 37).

[110]E. S. Antonarakis, M. A. Carducci, M. A. Eisenberger, et al. „Phase I rapid dose-escalation study of AGS-1C4D4, a human anti-PSCA (prostate stem cell antigen) monoclonal antibody , in patients with castration-resistant prostate cancer: a PCCTC trial“. In: *Cancer Chemother. Pharmacol.* 69 (2012), pp. 763–771 (cit. on p. 37).

[111]P. Verhamme, S. Pakola, T. J. Jensen, et al. „Tolerability and pharmacokinetics of TB-402 in healthy male volunteers“. In: *Clin. Ther.* 32.6 (2010), pp. 1205–1220 (cit. on p. 37).

[112]B. White, F. Leon, W. White, and G. Robbie. „Two first-in-human, open-label, phase I dose-escalation safety trials of MEDI-528, a monoclonal antibody against interleukin-9, in healthy adult volunteers“. In: *Clin. Ther.* 31.4 (2009), pp. 728–740 (cit. on p. 37).

[113]B. van Hartingsveldt, I. P. Nnane, E. Bouman-Thio, et al. „Safety, tolerability and pharmacokinetics of a human anti-interleukin-13 monoclonal antibody (CNTO 5825) in an ascending single-dose first-in-human study“. In: *Br. J. Clin. Pharmacol.* 75.5 (2012), pp. 1289–1298 (cit. on p. 37).

[114]V. Riddle, P. Leese, D. Blanset, et al. „Phase I study evaluating the safety and pharmacokinetics of MDX-1303, a fully human monoclonal antibody against Bacillus anthracis protective antigen, in healthy volunteers.“ In: *Clin. Vaccine Immunol.* 18.12 (2011), pp. 2136–42 (cit. on p. 37).

[115]F. Curtin, A. B. Lang, H. Perron, et al. „GNbAC1, a Humanized Monoclonal Antibody Against the Envelope Protein of Multiple Sclerosis-Associated Endogenous Retrovirus: A First-in-Humans Randomized Clinical Study“. In: *Clin. Ther.* 34.12 (2012), pp. 2268–2278 (cit. on p. 37).

[116]G. M. Subramanian, P. W. Cronin, G. Poley, et al. „A Phase 1 Study of PAmAb, a Fully Human Monoclonal Antibody against Bacillus anthracis Protective Antigen, in Healthy Volunteers“. In: *Clin. Infect. Dis.* 41 (2005), pp. 12–20 (cit. on p. 37).

[117]T. A. Waldmann and W. Strober. „Metabolism of immunoglobulins“. In: *Progr. Allergy* 13 (1969), pp. 1–34 (cit. on p. 40).

[118]L. B. Avery, M. Wang, M. S. Kavosi, et al. „Utility of a human FcRn transgenic mouse model in drug discovery for early assessment and prediction of human pharmacokinetics of monoclonal antibodies“. In: *mAbs* 8.6 (2016), pp. 1064–1078 (cit. on pp. 40, 105, 107).

[119]J.-F. Lu, R. Bruno, S. Eppler, et al. „Clinical pharmacokinetics of bevacizumab in patients with solid tumors.“ In: *Cancer Chemother. Pharmacol.* 62.5 (2008), pp. 779–86 (cit. on pp. 40, 43).

[120]M. S. Gordon, K. Margolin, M. Talpaz, et al. „Phase I safety and pharmacokinetic study of recombinant human anti-vascular endothelial growth factor in patients with advanced cancer.“ In: *J. Clin. Oncol.* 19.3 (2001), pp. 843–850 (cit. on pp. 43, 44).

[121]P. M Beer, S. J. Wong, A. M. Hammad, et al. „Vitreous levels of unbound bevacizumab and unbound vascular endothelial growth factor in two patients.“ In: *Retina* 26.8 (2006), pp. 871–876 (cit. on p. 43).

[122]Y. Vugmeyster, X. Xu, F.-P. Theil, L. A. Khawli, and M. W. Leach. „Pharmacokinetics and toxicology of therapeutic proteins: Advances and challenges.“ In: *World J. Biol. Chem.* 3.4 (2012), pp. 73–92 (cit. on p. 44).

[123]R. D. Wochner, G. Drews, W. Strober, and T. A. Waldmann. „Accelerated breakdown of immunoglobulin G (IgG) in myotonic dystrophy: a hereditary error of immunoglobulin catabolism.“ In: *J. Clin Invest.* 45.3 (1966), pp. 321–329 (cit. on p. 45).

[124]D. Schuppan and N. H. Afdhal. „Liver cirrhosis“. In: *Lancet* 371 (2008), pp. 838–851 (cit. on p. 45).

[125]R. P. Junghans and C. L. Anderson. „The protection receptor for IgG catabolism is the β_2-microglobulin-containing neonatal intestinal transport receptor.“ In: *Proc. Natl. Acad. Sci. U.S.A.* 93 (1996), pp. 5512–5516 (cit. on pp. 48, 53).

[126]J. Bloemmen and H. Eyssen. „Immunoglobulin levels of sera of genetically thymusless (nude) mice“. In: *Eur. J. Immunol.* 3 (1973), pp. 117–118 (cit. on p. 48).

[127]R. Deng, Y. G. Meng, K. Hoyte, et al. „Subcutaneous bioavailability of therapeutic antibodies as a function of FcRn binding affinity in mice“. In: *mAbs* 4.1 (2012), pp. 101–109 (cit. on p. 48).

[128]J. J. Xiao. „Pharmacokinetic models for FcRn-mediated IgG disposition.“ In: *J. Biomed. Biotechnol.* 2012 (2012), p. 282989 (cit. on p. 50).

[129]W. K. Bleeker, J. L. Teeling, and C. E. Hack. „Accelerated autoantibody clearance by intravenous immunoglobulin therapy : studies in experimental models to determine the magnitude and time course of the effect“. In: *Transfus. Med.* 98.10 (2001), pp. 3136–3142 (cit. on p. 51).

[130]T. T. Kuo and V. G. Aveson. „Neonatal Fc receptor and IgG-based therapeutics.“ In: *mAbs* 3.5 (2011), pp. 422–30 (cit. on p. 51).

[131]J. Zhou, J. E. Johnson, V. Ghetie, R. J. Ober, and E. S. Ward. „Generation of mutated variants of the human form of the MHC class I-related receptor, FcRn, with increased affinity for mouse immunoglobulin G“. In: *J. Mol. Biol.* 332.03 (2003), pp. 901–913 (cit. on pp. 52, 56, 57, 70).

[132]Y.-Y. Fan and H. Neubert. „Quantitative Analysis of Human Neonatal Fc Receptor (FcRn) Tissue Expression in Transgenic Mice by Online Peptide Immuno-Affinity LC-HRMS“. In: *Anal. Chem.* 88.8 (2016), pp. 4239–4247 (cit. on p. 52).

[133]T. A. Waldmann and W. D. Terry. „Familial hypercatabolic hypoproteinemia. A disorder of endogenous catabolism of albumin and immunoglobulin“. In: *J. Clin Invest.* 86.6 (1990), pp. 2093–2098 (cit. on p. 53).

[134]S. Popov, J. G. Hubbard, J. K. Kim, et al. „The stoichiometry and affinity of the interaction of murine Fc fragments with the MHC class I-related receptor, FcRn“. In: *Mol. Immunol.* 33.6 (1996), pp. 521–530 (cit. on pp. 57, 70).

[135]R. J. Ober, C. G. Radu, V. Ghetie, and E. S. Ward. „Differences in promiscuity for antibody-FcRn interactions across species: implications for therapeutic antibodies.“ In: *Int. Immunol.* 13.12 (2001), pp. 1551–9 (cit. on pp. 57, 70).

[136]B. Gurbaxani, M. Dostalek, and I. Gardner. „Are endosomal trafficking parameters better targets for improving mAb pharmacokinetics than FcRn binding affinity?“ In: *Mol. Biol.* 56.4 (2013), pp. 660–674 (cit. on pp. 57, 70, 71).

[137]J. W. Stoop, B. J. M. Zegers, P. C. Sander, and R. E. Baillieux. „Serum immunoglobulin levels in healthy children and adults“. In: *Clin. Exp. Immunol.* 4 (1969), pp. 101–112 (cit. on p. 69).

[138]Y. N. Abdiche, Y. A. Yeung, J. Chaparro-Riggers, et al. „The neonatal Fc receptor (FcRn) binds independently to both sites of the IgG homodimer with identical affinity“. In: *mAbs* 7.2 (2015), pp. 331–343 (cit. on p. 70).

[139]T. Suzuki, A. Ishii-Watabe, M. Tada, et al. „Importance of neonatal FcR in regulating the serum half-life of therapeutic proteins containing the Fc domain of human IgG1: a comparative study of the affinity of monoclonal antibodies and Fc-fusion proteins to human neonatal FcR.“ In: *J. Immunol.* 184.4 (2010), pp. 1968–76 (cit. on p. 70).

[140]M. Dostalek, I. Gardner, B. M. Gurbaxani, R. H. Rose, and M. Chetty. „Pharmacokinetics, Pharmacodynamics and Physiologically-Based Pharmacokinetic Modelling of Monoclonal Antibodies“. In: *Clin. Pharmacokinet.* 52 (2013), pp. 83–124 (cit. on p. 70).

[141]S. Akilesh, G. J. Christianson, D. C. Roopenian, and A. S. Shaw. „Neonatal FcR Expression in Bone Marrow-Derived Cells Functions to Protect Serum IgG from Catabolism“. In: *J. Immunol.* 179.7 (2007), pp. 4580–4588 (cit. on p. 71).

[142]R. Swiercz, M. Mo, P. Khare, et al. „Loss of expression of the recycling receptor, FcRn, promotes tumor cell growth by increasing albumin consumption“. In: *Oncotarget* 8.2 (2017), pp. 3528–3541 (cit. on p. 71).

[143]V. Yip, E. Palma, D. B. Tesar, et al. „Quantitative cumulative biodistribution of antibodies in mice: Effect of modulating binding affinity to the neonatal Fc receptor“. In: *mAbs* 6.3 (2014), pp. 689–696 (cit. on p. 71).

[144]L. Liu. „Pharmacokinetics of monoclonal antibodies and Fc-fusion proteins“. In: *Protein Cell* 9.1 (2018), pp. 15–32 (cit. on pp. 73, 107).

[145]D. Xiang, C. Zheng, S. F. Zhou, et al. „Superior performance of aptamer in tumor penetration over antibody: Implication of aptamer-based theranostics in solid tumors“. In: *Theranostics* 5.10 (2015), pp. 1083–1097 (cit. on p. 73).

[146]H. Sha, Z. Zou, K. Xin, et al. „Tumor-penetrating peptide fused EGFR single-domain antibody enhances cancer drug penetration into 3D multicellular spheroids and facilitates effective gastric cancer therapy“. In: *J. Control. Release* 200 (2015), pp. 188–200 (cit. on p. 73).

[147]K. Fujimori, D. Covell, J. E. Fletcher, and J. N. Weinstein. „A Modeling Analysis of Monoclonal Antibody Percolation Through Tumors: A Binding-Site Barrier“. In: *J. Nucl. Med.* 31 (1990), pp. 1191–1198 (cit. on pp. 73, 123, 124).

[148]K. Fujimori, D. G. Covell, J. E. Fletcher, and J. N. Weinstein. „Modeling analysis of the global and microscopic distribution of immunoglobulin G, F(ab')$_2$, and Fab in tumors“. In: *Cancer Res.* 49.20 (1989), pp. 5656–5663 (cit. on pp. 73, 126).

[149]D. M. Glatt, D. R. Beckford Vera, M.C. Parrott, et al. „The Interplay of Antigen Affinity, Internalization, and Pharmacokinetics on CD44-Positive Tumor Targeting of Monoclonal Antibodies“. In: *Mol. Pharm.* 13.6 (2016), pp. 1894–1903 (cit. on p. 73).

[150]Amgen GmbH. *Fachinformation Vectibix® 20mg/mL Konzentrat*. 2016 (cit. on pp. 73, 92, 94, 95).

[151]Roche Pharma AG. *Fachinformation Herceptin® i.v.* 2017 (cit. on p. 73).

[152]C. Vasalou, G. Helmlinger, and B. Gomes. „A Mechanistic Tumor Penetration Model to Guide Antibody Drug Conjugate Design". In: *PLoS One* 10.3 (2015), pp. 1–20 (cit. on pp. 73, 76).

[153]N. Iqbal and N. Iqbal. „Human Epidermal Growth Factor Receptor 2 (HER2) in Cancers: Overexpression and Therapeutic Implications". In: *Mol. Biol. Int.* (2014), pp. 1–9 (cit. on pp. 74, 85, 86).

[154]D. Harari and Y. Yarden. „Molecular mechanisms underlying ErbB2/HER2 action in breast cancer." In: *Oncogene* 19.53 (2000), pp. 6102–6114 (cit. on pp. 74, 86).

[155]C. D. Austin, A. M. De Maziere, P. I. Pisacane, et al. „Endocytosis and Sorting of ErbB2 and the Site of Action of Cancer Therapeutics Trastuzumab and Geldamycin". In: *Mol. Biol. Cell* 15 (2004), pp. 5268–5282 (cit. on pp. 74, 86).

[156]G. M. Thurber and R. Weissleder. „A systems approach for tumor pharmacokinetics". In: *PLoS One* 6.9 (2011) (cit. on p. 76).

[157]T. L. Jackson, S. R. Lubkin, N. O. Siemers, et al. „Mathematical and experimental analysis of localization of anti-tumour antibody-enzyme conjugates." In: *Br. J. Cancer* 80.11 (1999), pp. 1747–1753 (cit. on p. 76).

[158]L. Abuqayyas. „Evaluation of the Mechanistic Determinants of Antibody Exposure in Tissues". PhD thesis. State University of New York at Buffalo, 2012 (cit. on p. 84).

[159]U. Del Monte. „Does the cell number 10^9 still really fit one gram of tumor tissue?" In: *Cell Cycle* 8.3 (2009), pp. 505–506 (cit. on p. 84).

[160]R. Chignola, M. Sega, S. Stella, V. Vyshemirsky, and E. Milloti. „From Single-Cell Dynamics to Scaling Laws in Oncology". In: *Res. Phys. Cancer*. Ed. by B. S. Gerstman. World Scientific, 2016, pp. 97–108 (cit. on p. 84).

[161]M. M. Schmidt and K. D. Wittrup. „A modeling analysis of the effects of molecular size and binding affinity on tumor targeting". In: *Mol. Cancer Ther.* 8.10 (2009), pp. 2861–2871 (cit. on pp. 84, 98).

[162]U. Moran, R. Phillips, and R. Milo. „SnapShot: Key numbers in biology". In: *Cell* 141.7 (2010), pp. 1–2 (cit. on p. 84).

[163]F. Yuan, M. Dellian, D. Fukumura, et al. „Vascular Permeability in a Human Tumor Xenograft: Molecular Size Dependence and Cutoff Size1". In: *Cancer Res.* 55 (1995), pp. 3752–3757 (cit. on p. 84).

[164]C. Starbuck and D. A. Lauffenburger. „Mathematical model for the effects of epidermal growth factor receptor trafficking dynamics on fibroblast proliferation responses." In: *Biotechnol. Progr.* 8.2 (1992), pp. 132–43 (cit. on p. 85).

[165]B.-F. Krippendorff, D. Oyarzun, and W. Huisinga. „Ligand accumulation counteracts therapeutic inhibition of receptor systems". In: *Proc. Found. Syst. Biol. Eng.* (2009), pp. 173–176 (cit. on p. 85).

[166]J. Brzezinski and A. Lewinski. „Increased plasma concentration of epidermal growth factor in female patients with non-toxic nodular goitre“. In: *Eur. J. Endocrinol.* 138.4 (1998), pp. 388–393 (cit. on p. 85).

[167]E. Tahara, H. Sumiyoshi, J. Hata, et al. „Human Epidermal Growth Factor in Gastric Carcinoma as a Biologic Marker of High Malignancy“. In: *J. Cancer. Res.* 77 (1986), pp. 145–152 (cit. on p. 85).

[168]C. Messa, F. Russo, M. G. Caruso, and A. Di Leo. „EGF, TGF-α, and EGF-R in Human Colorectal Adenocarcinoma“. In: *Acta Oncol.* 37.3 (1998), pp. 285–289 (cit. on p. 85).

[169]J. J. Lammerts van Bueren, W. K. Bleeker, H. O. Bøgh, et al. „Effect of target dynamics on pharmacokinetics of a novel therapeutic antibody against the epidermal growth factor receptor: implications for the mechanisms of action.“ In: *Cancer Res.* 66.15 (2006), pp. 7630–8 (cit. on p. 85).

[170]M. R. Schneider and E. Wolf. „The epidermal growth factor receptor ligands at a glance“. In: *J. Cell Physiol.* 218 (2009), pp. 460–466 (cit. on p. 85).

[171]L. Gibiansky and E. Gibiansky. „Target-mediated drug disposition model and its approximations for antibody-drug conjugates“. In: *J. Pharmacokinet. Pharmacodyn.* 41.1 (2014), pp. 35–47 (cit. on pp. 86, 102).

[172]Roche Pharma AG. *Fachinformation Kadcyla®*. 2017 (cit. on pp. 86, 89).

[173]M. Mano, A. Hendlisz, J. Machiels, et al. „Phase I trial of zalutumumab and irinotecan in metastatic colorectal cancer patients who have failed irinotecan- and cetuximab-based therapy“. In: *J. Clin. Oncol.* 27 (2009) (cit. on p. 94).

[174]S. C. Chen, A. Quartino, D. Polhamus, et al. „Population pharmacokinetics and exposure-response of trastuzumab emtansine in advanced breast cancer previously treated with $\geq$2 HER2-targeted regimens“. In: *Br. J. Clin. Pharmacol.* 92 (2017), pp. 2767–2777 (cit. on p. 102).

[175]P. J. Carter and P. D. Senter. „Antibody-Drug Conjugates for Cancer therapy“. In: *Cancer J.* 14 (2008), pp. 154–169 (cit. on p. 103).

[176]S. J. Demarest, K. Hariharan, and J. Dong. „Emerging antibody combinations in oncology“. In: *mAbs* 3.4 (2011), pp. 338–351 (cit. on p. 103).

[177]A. Drakaki and S. A. Hurvitz. „HER2-Positive Breast Cancer: Update on New and Emerging Agents“. In: *Am. J. Hematol. / Oncol.* 11.4 (2015), pp. 17–23 (cit. on p. 103).

[178]M. S. Braun and M. T. Seymour. „Balancing the efficacy and toxicity of chemotherapy in colorectal cancer“. In: *Ther. Adv. Med. Oncol.* 3.1 (2011), pp. 43–52 (cit. on p. 103).

[179]H. Edlund, J. Melin, Z. P. Parra-Guillen, and C. Kloft. „Pharmacokinetics and Pharmacokinetic-Pharmacodynamic Relationships of Monoclonal Antibodies in Children“. In: *Clin. Pharmacokinet.* 54.1 (2015), pp. 35–80 (cit. on pp. 106, 130, 140).

[180]J. C. Lagarias, J. A. Reeds, M. H. Wright, and P. E. Wright. „Convergence Properties of the Nelder–Mead Simplex Method in Low Dimensions“. In: *SIAM J OPTIMIZ* 9.1 (1998), pp. 112–147 (cit. on pp. 109, 117).

[181]*SCID Mice/Envigo*. URL: `http://www.envigo.com/products-services/research-models-services/research-models/mice/mutant/scid-mice/c.b-17-icrhsd-prkdcscid/` (visited on Sept. 28, 2015) (cit. on p. 116).

[182]C. Kreutz, A. Raue, D. Kaschek, and J. Timmer. „Profile likelihood in systems biology“. In: *FEBS J.* 280.11 (2013), pp. 2564–2571 (cit. on p. 117).

[183]C. Kloft, E. U. Graefe, P. Tanswell, et al. „Population pharmacokinetics of sibrotuzumab, a novel therapeutic monoclonal antibody, in cancer patients“. In: *Invest. New Drugs* 22.1 (2004), pp. 39–52 (cit. on p. 117).

[184]A. Bertuzzi, A. Fasano, A. Gandolfi, and C. Sinisgalli. „Tumour Cords and their Response to Anticancer Agents“. In: *Sel. Top. Cancer Model.* Ed. by N. Bellomo and E. de Angelis. Birkhäuser, 2008, pp. 1–24 (cit. on p. 123).

[185]R. P. Araujo and D. L. S. McElwain. „A history of the study of solid tumour growth: the contribution of mathematical modelling“. In: *Bull. Math. Biol.* 66 (2004), pp. 1039–1091 (cit. on p. 123).

[186]W. van Osdol, K. Fujimori, and J. N. Weinstein. „An Analysis of Monoclonal Antibody Distribution in Microscopic Tumor Nodules: Consequences of a ‘Binding Site Barrier’“. In: *Cancer Res.* 51.18 (1991), pp. 4776–4784 (cit. on p. 124).

[187]P. Rubin and G. Casarett. „Microcirculation of tumors. I. Anatomy, function, and necrosis“. In: *Clin. Radiol.* 17 (1966), pp. 220–229 (cit. on p. 124).

[188]R. J. Lukes and R. D. Collins. „Immunologic characterization of human malignant lymphomas“. In: *Cancer* 34 (1974), pp. 1488 –1503 (cit. on p. 124).

[189]G. Parries, K. Chen, K. S. Misono, and S. Cohen. „The human urinary epidermal growth factor (EGF) precursor“. In: *J. Biol. Chem.* 270.46 (1995), pp. 27954–27960 (cit. on p. 128).

[190]G. Hosgood. „Wound Repair and Specific Tissue Response to Injury“. In: *Textb. Small Anim. Surg.* Ed. by D. H. Slatter. Elsevier Health Sciences, 2003, pp. 66–86 (cit. on p. 128).

[191]J. Zisowsky, A. Krause, and J. Dingemanse. „Drug development for pediatric populations: Regulatory aspects“. In: *Pharmaceutics* 2.4 (2010), pp. 364–388 (cit. on pp. 130, 140).

[192]T N. Johnson and A. Rostami-Hodjegan. „Resurgence in the use of physiologically based pharmacokinetic models in pediatric clinical pharmacology: Parallel shift in incorporating the knowledge of biological elements and increased applicability to drug development and clinical practice“. In: *Paediatr. Anaesth.* 21.3 (2011), pp. 291–301 (cit. on p. 130).

[193]S. Björkman. „Prediction of drug disposition in infants and children by means of physiologically based pharmacokinetic (PBPK) modelling: Theophylline and midazolam as model drugs“. In: *Br. J. Clin. Pharmacol.* 59.6 (2004), pp. 691–704 (cit. on p. 130).

[194]B. J. Anderson and N. H. G. Holford. „Mechanism-based concepts of size and maturity in pharmacokinetics.“ In: *Annu. Rev. Pharmacol. Toxicol.* 48 (2008), pp. 303–332 (cit. on pp. 130, 132, 138, 140).

[195]R. Shi and H. Derendorf. „Pediatric dosing and body size in biotherapeutics“. In: *Pharmaceutics* 2.4 (2010), pp. 389–418 (cit. on pp. 130, 140).

[196] G. J. Robbie, L. Zhao, J. Mondick, G. Losonsky, and L. K. Roskos. „Population pharmacokinetics of palivizumab, a humanized anti-respiratory syncytial virus monoclonal antibody, in adults and children“. In: *Antimicrob. Agents Chemother.* 56.9 (2012), pp. 4927–4936 (cit. on pp. 131–135, 138, 140, 147).

[197] Food and Drug Administration. *General Clinical Pharmacology Considerations for Pediatric Studies for Drugs and Biological Products-Guidance for Industry*. 2014 (cit. on p. 132).

[198] K. Han, T. Peyret, A. Quartino, et al. „Bevacizumab dosing strategy in paediatric cancer patients based on population pharmacokinetic analysis with external validation“. In: *Br. J. Clin. Pharmacol.* 81.1 (2015), pp. 148–160 (cit. on pp. 132, 134–136, 138, 147).

[199] H. Sun, L. M. Van, D. Floch, et al. „Pharmacokinetics and Pharmacodynamics of Canakinumab in Patients With Systemic Juvenile Idiopathic Arthritis“. In: *J. Clin. Pharmacol.* 56.12 (2016), pp. 1516–1527 (cit. on pp. 132, 133).

[200] S. Sharma, D. Eckert, J. S. Hyams, et al. „Pharmacokinetics and exposure-efficacy relationship of adalimumab in pediatric patients with moderate to severe Crohn's disease: results from a randomized, multicenter, phase-3 study.“ In: *Inflamm. Bowel Dis.* 21.4 (2015), pp. 783–792 (cit. on pp. 132, 133, 138, 145, 148).

[201] P. J. Lowe and D. Renard. „Omalizumab decreases IgE production in patients with allergic (IgE-mediated) asthma“. In: *Br. J. Clin. Pharmacol.* 72.2 (2011), pp. 306–320 (cit. on pp. 132, 145).

[202] A. A. Fasanmade, O. J. Adedokun, M. Blank, H. Zhou, and H. M. Davis. „Pharmacokinetic Properties of Infliximab in Children and Adults with Crohn's Disease: A Retrospective Analysis of Data from 2 Phase III Clinical Trials“. In: *Clin. Ther.* 33.7 (2011), pp. 946–964 (cit. on pp. 132–134, 141, 145, 147).

[203] Centers for Disease Control and Prevention. *WHO and CDC growth charts*. URL: `https://www.cdc.gov/growthcharts/` (visited on Sept. 10, 2016) (cit. on p. 136).

[204] D. Dubois and E.F. Dubois. „A Formula To Estimate The Approximate Surface Area If Height and Weight Be Known“. In: *Arch. Intern. Med.* (1916), pp. 863–871 (cit. on p. 136).

[205] T. N. Johnson, A. Rostami-Hodjegan, and G. T. Tucker. „Prediction of the clearance of eleven drugs and associated variability in neonates, infants and children“. In: *Clin. Pharmacokinet.* 45.9 (2006), pp. 931–956 (cit. on pp. 137, 138).

[206] A. L. Sumpter and N. H. G. Holford. „Predicting weight using postmenstrual age – neonates to adults“. In: *Pediatr. Anesth.* 21.3 (2011), pp. 309–315 (cit. on p. 138).

[207] J. Elassaiss-Schaap and S. H. Heisterkamp. *Variability as constant coefficient of variation: Can we right two decades in error?* PAGE, Lissabon, Portugal, 2009. URL: `www.page-meeting.org/?abstract=1508` (cit. on p. 139).

[208] J. S. Barrett, O. Della Casa Alberighi, S. Läer, and B. Meibohm. „Physiologically based pharmacokinetic (PBPK) modeling in children.“ In: *Clin. Pharmacol. Ther.* 92.1 (2012), pp. 40–9 (cit. on p. 140).

[209] P. G. Holt and C. A. Jones. „The development of the immune system during pregnancy and early life.“ In: *Allergy* 55.8 (2000), pp. 688–697 (cit. on p. 141).

[210]O. Levy. „Innate immunity of the newborn: basic mechanisms and clinical correlates“. In: *Nat. Rev. Immunol.* 7.5 (2007), pp. 379–390 (cit. on p. 141).

[211]K. van Bilsen, P. M. van Hagen, J. Bastiaans, et al. „The neonatal Fc receptor is expressed by human retinal pigment epithelial cells and is downregulated by tumour necrosis factor-alpha“. In: *Br.J.Ophthalmol.* 95.6 (2011), pp. 864–868 (cit. on p. 141).

[212]K. Cauza, G. Hinterhuber, R. Dingelmaier-Hovorka, et al. „Expression of FcRn, the MHC class I-related receptor for IgG, in human keratinocytes“. In: *J. Invest. Dermatol.* 124.1 (2005), pp. 132–139 (cit. on p. 141).

[213]S. Willmann, K. Höhn, A. Edginton, et al. „Development of a physiology-based whole-body population model for assessing the influence of individual variability on the pharmacokinetics of drugs“. In: *J. Pharmacokinet. Pharmacodyn.* 34.3 (2007), pp. 401–431 (cit. on p. 142).

[214]S. Basu, C. Niederalt, H. Yang, et al. *Development and Quantification of a Pediatric Population-based Pharmacokinetic Model for Biologics in PK-Sim®*. Annual Meeting of the American College of Clinical Pharmacology, Bethesda, MD, 2016 (cit. on p. 142).

[215]L. Li, I. Gardner, R. Rose, and M. Jamei. „Incorporating Target Shedding Into a Minimal PBPK-TMDD Model for Monoclonal Antibodies.“ In: *CPT Pharmacometrics Syst. Pharmacol.* 3.e96 (2014) (cit. on p. 143).

[216]C.-A. Siegrist and R. Aspinall. „B-cell responses to vaccination at the extremes of age.“ In: *Nat. Rev. Immunol.* 9.3 (2009), pp. 185–194 (cit. on p. 144).

List of Figures

List of Tables

Declaration

I hereby declare that I have completed the work solely and only with the help of the mentioned references.

Potsdam, October 23, 2018

Saskia Fuhrmann